NONLINEAR OPTICS WITH STRUCTURED LIGHT

EDITED BY: Zhi-Han Zhu, Antonio Zelaquett Khoury, Bao-Sen Shi and
Carmelo Rosales-Guzmán
PUBLISHED IN: Frontiers in Physics

frontiers Research Topics

ISSN 1664-8714
ISBN 978-2-88976-082-4
DOI 10.3389/978-2-88976-082-4

About Frontiers

Frontiers is more than just an open-access publisher of scholarly articles: it is a pioneering approach to the world of academia, radically improving the way scholarly research is managed. The grand vision of Frontiers is a world where all people have an equal opportunity to seek, share and generate knowledge. Frontiers provides immediate and permanent online open access to all its publications, but this alone is not enough to realize our grand goals.

Frontiers Journal Series

The Frontiers Journal Series is a multi-tier and interdisciplinary set of open-access, online journals, promising a paradigm shift from the current review, selection and dissemination processes in academic publishing. All Frontiers journals are driven by researchers for researchers; therefore, they constitute a service to the scholarly community. At the same time, the Frontiers Journal Series operates on a revolutionary invention, the tiered publishing system, initially addressing specific communities of scholars, and gradually climbing up to broader public understanding, thus serving the interests of the lay society, too.

Dedication to Quality

Each Frontiers article is a landmark of the highest quality, thanks to genuinely collaborative interactions between authors and review editors, who include some of the world's best academicians. Research must be certified by peers before entering a stream of knowledge that may eventually reach the public - and shape society; therefore, Frontiers only applies the most rigorous and unbiased reviews.
Frontiers revolutionizes research publishing by freely delivering the most outstanding research, evaluated with no bias from both the academic and social point of view.
By applying the most advanced information technologies, Frontiers is catapulting scholarly publishing into a new generation.

What are Frontiers Research Topics?

Frontiers Research Topics are very popular trademarks of the Frontiers Journals Series: they are collections of at least ten articles, all centered on a particular subject. With their unique mix of varied contributions from Original Research to Review Articles, Frontiers Research Topics unify the most influential researchers, the latest key findings and historical advances in a hot research area! Find out more on how to host your own Frontiers Research Topic or contribute to one as an author by contacting the Frontiers Editorial Office: frontiersin.org/about/contact

NONLINEAR OPTICS WITH STRUCTURED LIGHT

Topic Editors:
Zhi-Han Zhu, Harbin University of Science and Technology, China
Antonio Zelaquett Khoury, Fluminense Federal University, Brazil
Bao-Sen Shi, University of Science and Technology of China, China
Carmelo Rosales-Guzmán, Harbin University of Science and Technology, China

Citation: Zhu, Z.-H., Khoury, A. Z., Shi, B.-S., Rosales-Guzmán, C., eds. (2022). Nonlinear Optics With Structured Light. Lausanne: Frontiers Media. doi: 10.3389/978-2-88976-082-4

Table of Contents

frontiers
in Physics

ORIGINAL RESEARCH
published: 24 June 2021
doi: 10.3389/fphy.2021.690721

Generation of High-Order Vortex States From Two-Mode Squeezed States

Graciana Puentes[1,2]* *and Anindya Banerji*[3]

[1]Departamento de Fsica, Facultad de Ciencias Exactas y Naturales, Universidad de Buenos Aires, Ciudad Universitaria, Buenos Aires, Argentina, [2]CONICET-Universidad de Buenos Aires, Instituto de Fsica de Buenos Aires (IFIBA), Ciudad Universitaria, Buenos Aires, Argentina, [3]Centre for Quantum Technologies, National University of Singapore, Singapore, Singapore

We report a scheme for generation of high-order quadrature vortex states using two-mode photon-number squeezed states, generated via the non-linear process of Spontaneous Parametric Down Conversion. By applying a parametric rotation in the quadratures $(\widehat{X}, \widehat{Y})$, using a ϕ converter, the Gaussian profile of the photon-number squeezed input state can be mapped into a superposition of Laguerre-Gauss modes in the quadratures with N vortices or singularities, for an input state containing $2N$ photons, thus mapping photon-number fluctuations to interference effects in the quadratures. Our scheme has the potential to improve measurement sensitivity beyond the Standard uantum Limit (SQL $\propto \sqrt{N}$), by exploiting the advantages of optical vortices, such as high dimensionality or topological properties, for applications requiring reduced uncertainty, such as quantum cryptography, quantum metrology and sensing.

Keywords: orbital angular momentum, photon-number squeezed states, optical vortices, structured light, spontaneous parametric down conversion

Edited by:
Antonio Zelaquett Khoury,
Fluminense Federal University, Brazil

Reviewed by:
Rafael Barros,
Tampere University, Finland
Luis Sanchez Soto,
Complutense University of Madrid,
Spain

***Correspondence:**
Graciana Puentes
gpuentes@df.uba.ar

Specialty section:
This article was submitted to
Optics and Photonics,
a section of the journal
Frontiers in Physics

Received: *04 April 2021*
Accepted: *31 May 2021*
Published: *24 June 2021*

Citation:
Puentes G and Banerji A (2021)
Generation of High-Order Vortex
States From Two-Mode
Squeezed States.
Front. Phys. 9:690721.
doi: 10.3389/fphy.2021.690721

1 INTRODUCTION

In quantum optics, a beam of light is in a squeezed state if its electric field amplitude has a reduced uncertainty, in relation to that of a coherent state. Thus, the term squeezing refers to squeezed uncertainty. In general, for a classical coherent state with N particles, the sensitivity of a measurement is limited by shot noise to the Standard Quantum Limit (SQL $\propto \sqrt{N}$). On the other hand, quantum states, such as photon-number squeezed states, hold the promise of improving measurement precision beyond the SQL. Squeezed states of light find a myriad of applications, such as in precision measurements, radiometry, calibration of quantum efficiencies, or entanglement-based quantum cryptography, to mention only a few [1–10].

An optical vortex is a singularity or zero point intensity of an optical field. More specific, a generic Laguerre-Gauss beam of order m of the form $\psi \propto e^{im\phi}e^{-r^2}$, with ϕ its azymuthal phase and $r = \sqrt{x^2 + y^2}$ its radial coordinate, has an optical vortex in its center for $m > 0$. The phase in the field circulates around such singularity giving rise to vortices. Integrating around a path enclosing a vortex yields an integer number, multiple of π. This integer is known as the topological charge. There is a broad range of applications of optical vortices in diverse areas, such as in astronomy for detection of extra-solar planets, in optical tweezers for manipulation of cells and micro-particles, in optical communication to improve the spectral efficiency, in Orbital Angular Momentum (OAM) multiplexing, and in quantum cryptography to increase communication bandwidth [11–20].

In this article, we report a scheme for generation of high-order **quadrature** vortex states using two-mode photon-number squeezed states generated *via* the non-linear process of Spontaneous

Parametric Down Conversion (SPDC). By applying a parametric rotation in the quadratures $(\widehat{X}, \widehat{Y})$ using a ϕ converter, the quadrature representation of the photon-number squeezed input state can be mapped into a vortex state in the quadratures containing N vortices or singularities, for an input state containing $2N$ photons, thus mapping photon-number fluctuations to interference effects in the quadrature, giving rise to the emergence of a state with a well-defined number of vortices. Our scheme has the potential of exploiting the advantages of optical vortices, such as high dimensionality or topological properties, for applications requiring precision beyond the SQL $\propto \sqrt{N}$, such as quantum cryptography, quantum metrology and sensing.

A ϕ converter, also called mode converter, is customarily used in classical optics to convert two orthogonal Hermite-Gauss modes into a Laguerre-Gauss mode. The main motivation of the present work is to explore if an equivalent operation exists that can transform a Hermite-Gauss quadrature representation into a Laguerre-Gauss representation. We found such operation indeed exists. A remarkable feature of this operation is that it can be experimentally realized by using a balanced 50:50 beam splitter. A key application of the scheme reported here is in generation of photon-number squeezed states from quadrature vortex states, by implementation of the inverse protocol.

The article is structured as follows: First, in **Section 2** we review the properties of two-mode photon-number squeezed states such as their quadrature representation and photon-number distribution, second in **Section 3** we introduce the concept of quadrature rotation. Next, in **Section 4**, we present the quadrature representation of the rotated states in terms of Laguerre-Gauss modes. In **Section 5**, we present numerical simulations confirming the creation of N vortices for a squeezed input state containing $2N$ photons. In **Section 6**, we present analytical and numerical derivations for the photon-number distribution of the resulting quadrature vortex states, revealing super-Poissonian photon statistics. Finally, in **Section 7**, we present our conclusions.

2 2-MODE PHOTON-NUMBER SQUEEZED STATE

Consider a truncated two-mode photon-number squeezed state, produced by SPDC, in the Fock state representation of the form [21]:

$$|\psi\rangle = \frac{D}{\cosh r} \sum_{j=0}^{N} (\tanh r)^j |j\rangle_a |j\rangle_b \tag{1}$$

where (a, b) are modes labels, D is a normalization factor and r is the squeezing parameter. In what follows, we consider $|j\rangle_a |j\rangle_b = |j, j\rangle$. The wave-vector and polarization for each mode will be determined by the specific type of SPDC process and configuration being used. For example, in the case of non-collinear type-I SPDC, the two modes would correspond to distinct directions governed by the wave-vectors of signal and idler photons. In order to keep our description as general as possible, we do not limit to a particular SPDC process.

To obtain a quadrature representation of the wavefunction for the state in **Eq. 1**, we use the standard representation of Fock states $(\{|n\rangle\})$ in the position basis $(\{|x\rangle\})$ which, up to a scaling factor, is equivalent to the Hermite-Gauss polynomial of order n, of the form $\langle x|n\rangle = \sqrt{\frac{1}{\pi 2^n n!}} H_n(x) e^{-(x^2)/2}$ [24]. A 2D representation can be obtained by ascribing orthogonal bases $(\{|x, y\rangle\})$ to each mode, where $|x, y\rangle = |x\rangle|y\rangle$ are the eigenvectors of the quadrature operators $\widehat{X} = \frac{\hat{a}+\hat{a}^\dagger}{\sqrt{2}}$ and $\widehat{Y} = \frac{\hat{b}+\hat{b}^\dagger}{\sqrt{2}}$, with eigenvalues x and y, respectively. Here $(\hat{a}, \hat{b})$ are annihilation operators for the two modes (a, b) [24]. In this notation, the two-mode photon-number states $|n_x, n_y\rangle$ can be written in the quadrature representation as $\langle x, y|n_x, n_y\rangle = \sqrt{\frac{1}{\pi 2^{(n_x+n_y)} n_x! n_y!}} H_{n_x}(x) H_{n_y}(y) e^{-(x^2+y^2)/2}$ [22–25]. Using these expressions, the two-mode photon-number squeezed input state $|\psi\rangle$ has a quadrature representation of the form $\langle x, y|\psi\rangle = \psi(x, y)$:

$$\begin{aligned}\psi(x, y) = \frac{D}{\cosh r} \sum_{j=0}^{N} (\tanh r)^j \times \\ \sqrt{\frac{1}{\pi 4^j (j!)^2}} H_j(x) H_j(y) e^{-(x^2+y^2)/2}.\end{aligned} \tag{2}$$

The quadrature representation of the input state $|\psi\rangle$ is depicted in **Figure 1B** and **Figure 1C**. Such quadrature representation reveals a Gaussian profile, with no vortices or singularities for squeezing parameter $r = 1$. Note that the quadrature profile is not equivalent to the transverse profile of the beam, since $\widehat{X}$ and $\widehat{Y}$ are quadrature operators, not transvese coordinates. Moreover, the plots in **Figures 1B,C** correspond to the quadrature representation of the wavefunction of the input state $\psi(x, y)$, which is not equivalent to the Wigner function in phase space. The photon-number distribution for the input state $P(n, n) = |\langle n, n|\psi\rangle|^2$ can be calculated obtaining the well known sub-Poissonian quantum statistics. Tracing over one mode we obtain $P(n) = \left|\frac{\tanh r^n}{\cosh r}\right|^2$. Photon-number distributions for different values of the squeezing parameter $r = 1, 0.5, 0.1$ are displayed in **Figure 1D**, revealing thermal statistics when tracing over one mode, while the overall photon-number statistics for the 2-mode squeezed states is sub-Poissonian.

3 QUADRATURE ROTATION

The photon-number squeezed state depicted in **Figure 1** displays a standard Gaussian profile in the quadratures $(\widehat{X}, \widehat{Y})$, with no topological charges or phase singularities. In order to imprint a vortex in the quadratures $(\widehat{X}, \widehat{Y})$, we introduce a rotation $\widehat{C}$ by an angle ϕ, represented by a unitary operator of the form:

$$\widehat{C} = e^{i2\phi\left[\hat{a}^\dagger \hat{b} + \hat{b}^\dagger \hat{a}\right]}, \tag{3}$$

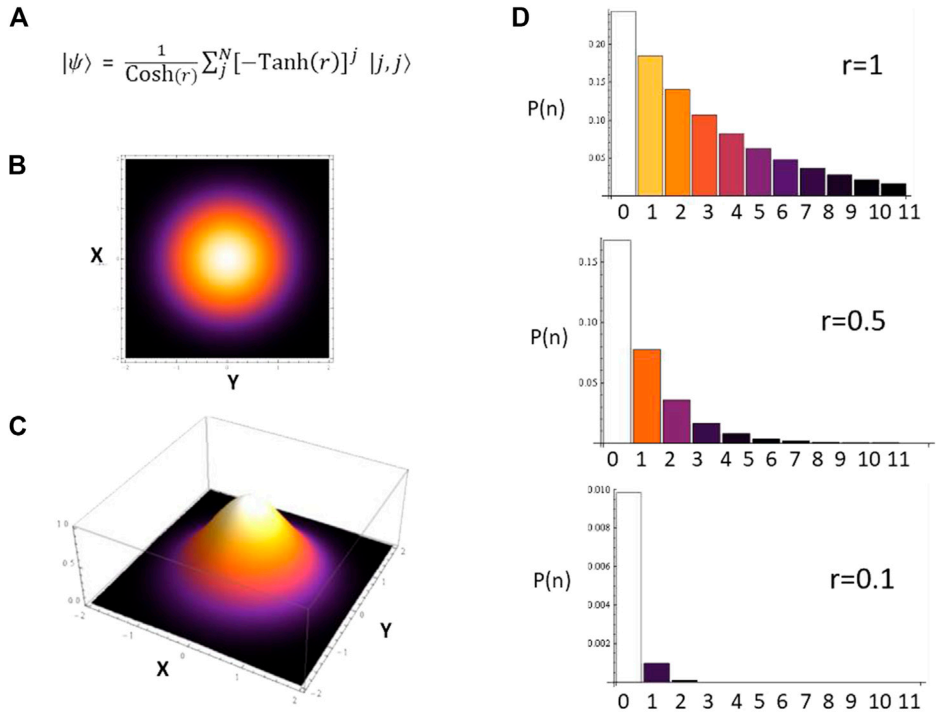

FIGURE 1 | (A) Two-mode photon-number squeezed input state $|\psi\rangle$. **(B,C)** Quadrature representation of input state (not Wigner function) displaying a Gaussian profile with no vortices or singularities, for squeezing parameter $r = 1$. **(D)** Photon-number distribution for different values of squeezing parameter $r = 1, 0.5, 0.1$, revealing thermal statistics by tracing over one mode (see text for details).

where $(\hat{a}^\dagger, \hat{a})$ and $(\hat{b}^\dagger, \hat{b})$ are creation and destruction operators for modes (a, b), which satisfy the standard commutation rules $[\hat{a}^\dagger, \hat{a}] = 1$ and $[\hat{b}^\dagger, \hat{b}] = 1$. Interestingly, $\hat{C}$ is mathematically equivalent to the unitary operator describing the action of a beam splitter in Fock space [1], therefore it can be easily implemented in the laboratory.

The input state transformed under the unitary operator $\hat{C}$ becomes $|\psi'\rangle$:

$$|\psi'\rangle = \hat{C}|\psi\rangle, \tag{4}$$

which represents a rotation of the quadrature by an angle ϕ. In the Heisenberg picture, considering standard commutation rules for creation and annhiliation operators, we obtain the following expression (see **Appendix A**):

$$|\psi'\rangle = \frac{D}{\cosh r}\sum_{j=0}^{N} (\tanh r)^j \times \left(\frac{\hat{a}^\dagger}{\sqrt{2}} + i\frac{\hat{b}^\dagger}{\sqrt{2}}\right)^j \left(\frac{\hat{b}^\dagger}{\sqrt{2}} + i\frac{\hat{a}^\dagger}{\sqrt{2}}\right)^j |0,0\rangle \tag{5}$$

By a binomial expansion in **Eq. 5** we obtain:

$$|\psi'\rangle = \frac{D}{\cosh r}\sum_{j=0}^{N} A_j^{r,N} \times \sum_{k=0}^{j}\sum_{l=0}^{j} B_{k,l}^{\phi} C_{kl}^{Nj} |j-(l-k), j+(l-k)\rangle. \tag{6}$$

where D is the normalization factor. The coefficients in the sums are of the form $A_j^{r,N} = (\tanh r)^j \sqrt{\frac{(j)!(j)!}{2^N}}$, $B_{k,l}^{\phi} = (i2\phi)^{l+k}$, while $C_{k,l}^{Nj}$ takes the form (see **Appendix A**):

$$C_{lk}^{Nj} = \frac{\sqrt{(j-l+k)!(j+l-k)!}}{k!(j-k)!l!(j-l)!}. \tag{7}$$

In order to observe the action of the rotation $\hat{C}$ in the quadratures we turn to the quadrature representation of the transformed ket $\langle x, y|\psi'\rangle = \psi'(x, y)$.

4 LAGUERRE-GAUSS MODE EXPANSION

The quadrature representation of the rotated state $\psi'(x, y)$ results in:

$$\psi'(x,y) = \frac{D}{\cosh r}\sum_{j=0}^{N} A_j^{r,N} \times \sum_{k=0}^{j}\sum_{l=0}^{j} B_{k,l}^{\phi} C_{lk}^{Nj} H_{j-(l-k)}(x) H_{j+(l-k)}(y) e^{-\left(x^2+y^2\right)/2}, \tag{8}$$

where $H_{j-(l-k)}(x) = \langle x|j-l+k\rangle$ and $H_{j+(l-k)}(y) = \langle y|j+l-k\rangle$ are Hermite-Gauss polynomials of order $(j-l+k)$ and $(j+l-k)$, respectively.

It is well known that Hermite-Gauss (HG) modes with spatial dependence $H_p(x)H_q(y)$ may become a single Laguerre-Gauss

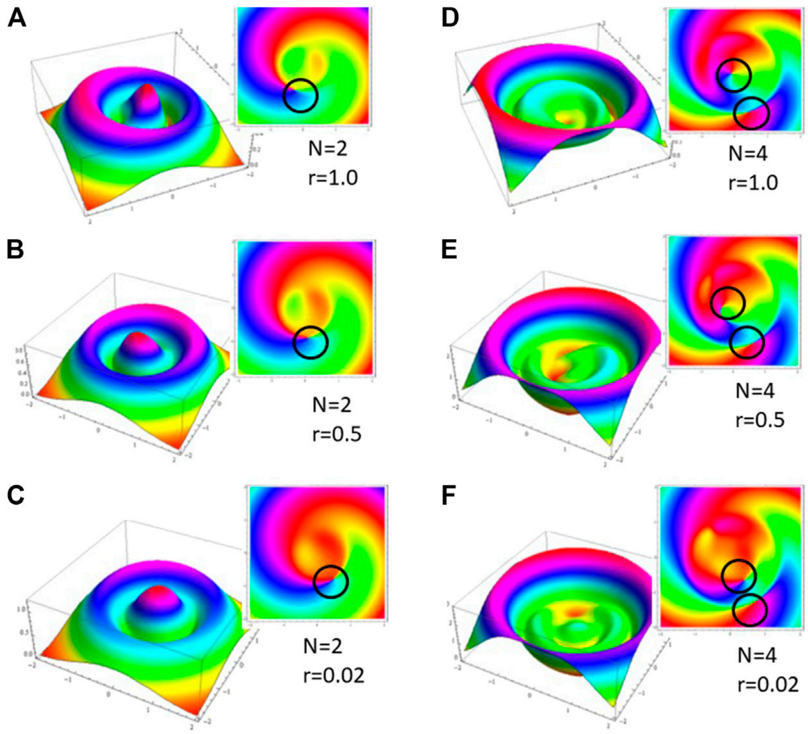

FIGURE 2 | 3D plots of amplitude $|\psi_{LG}(x, y)|$ for resulting Laguerre-Gauss mode in the quadrature representation, depicting the impact of the squeezing parameter r on the formation of vortices, for different values of squeezing parameter r and total photon-number N. Insets correspond to phase profiles $|\phi_{LG}(x, y)|$ for resulting Laguerre-Gauss mode revealing vortices or singularities in the quadratures (not in the transverse profile of the beam). **(A)** $N = 2$, $r = 1$, **(B)** $N = 2$, $r = 0.5$, **(C)** $N = 2$, $r = 0.02$, **(D)** $N = 4$, $r = 1$, **(E)** $N = 4$, $r = 0.5$, **(F)** $N = 4$, $r = 0.02$. As the squeezing parameter decreases, the formation of $N/2$ vortices in the quadratures becomes apparent (see text for details).

(LG) mode of order $L_q^{p-q}(x^2 + y^2)$ provided a phase change of $\pi/2$ in the mode profile is achieved [11]. Such Laguerre-Gauss mode is associated with a quadrature vortex number of $(p - q)$ [16, 21–24, 26–34].

By choosing the rotation parameter $\phi = \pi/4$, we may obtain the required phase change to convert the Hermite-Gauss modes into a single Laguerre-Gauss mode. By relabeling the indices $(l - k) = m$, with $m = 0, \ldots, N/2$, we note the quadrature profile can be written as a sum of products of HG modes of the form $H_{j-m}(x)H_{j+m}(y)$. Selecting $\phi = \pi/4$, the quadrature profile can be written in terms of LG modes of the form $L_{j-m}^{2m}(r^2)$, thus resulting in a superposition of LG modes of order $2m$ in the quadrature representation.

5 NUMERICAL RESULTS

To explore the resulting mode-profile in the quadrature $(\widehat{X}, \widehat{Y})$, we performed numerical simulations for a superposition of LG modes of the form:

$$\psi_{LG}(x, y) = \frac{1}{\cosh r}\sum_{j=0}^{N}\sum_{m=0}^{j} A_j^{r,N} C_{kl}^{Nj} \times L_{j-m}^{2m}(x^2 + y^2)e^{-(x^2+y^2)/2}, \tag{9}$$

where r is the squeezing parameter and the coefficients take the form $A_j^{r,N} = (\tanh r)^j \sqrt{\frac{(j)!(j)!}{2^N}}$, $C_{lk}^{Nj} = \frac{\sqrt{(j-l+k)!(j+l-k)!}}{k!(j-k)!l!(j-l)!}$.

We performed numerical simulations in the quadrature for different values of squeezing parameter r, and different values of photon-number N. The results are depicted in **Figure 2** and **Figure 3**. The main result we observe is that, for a sufficiently small squeezing parameter r, the resulting quadrature profile exhibits $N/2$ vortices for an input state with $N/2$ photons *per mode*. In this way, we have mapped the reduced uncertainty in photon-number in Fock space, to a reduced uncertainty in vortex-number in the quadrature.

5.1 Dependence on Squeezing Parameter *r*

In order to better understand the impact of the squeezing parameter r in the formation of vortices in the quadrature, we performed numerical simulations for different squeezing parameters, and for different total number of photons N. This is displayed in **Figures 2A–F**. **Figure 2** left column corresponds to $N = 2$ total photon number and right column corresponds to $N = 4$ total number of photons. Different rows in decreasing order correspond to squeezing parameters $r = 1, 0.5, 0.02$. Numerical simulations clearly reveal that vortices are formed as r decreases, thus as the uncertainty in photon-number decreases, as expected. Thus confirming that the reduced

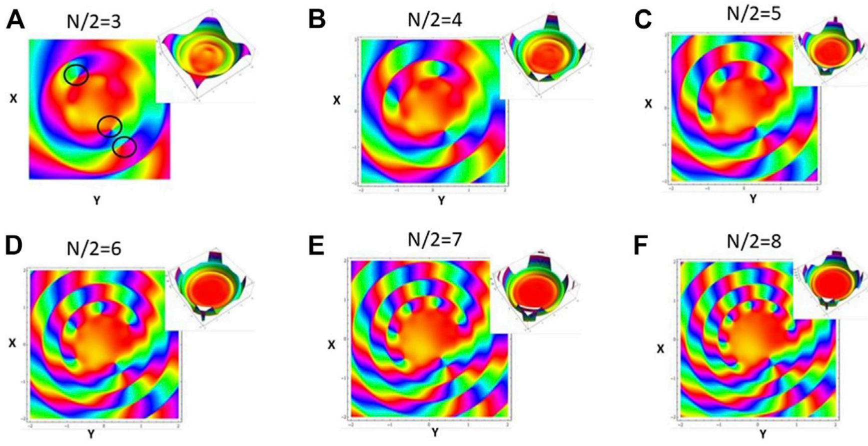

FIGURE 3 | Phase profile $|\phi_{LG}(x,y)|$ of resulting Laguerre-Gauss quadrature representation for a squeezing parameter $r = 0.02$, exploring the impact of the photon-number ($N/2$ per mode) in the formation of vortices. Insets correspond to amplitude plots $|\psi_{LG}(x,y)|$. The numerical results confirm creation of $N/2$ vortices for N total input photons. **(A)** $N/2 = 3$, **(B)** $N/2 = 4$, **(C)** $N/2 = 5$, **(D)** $N/2 = 6$, **(E)** $N/2 = 7$, **(F)** $N/2 = 8$, with $N/2$ input photons per mode (see text for details).

uncertainty in Fock space is mapped to reduced uncertainty in vortex number, in the quadrature.

5.2 Dependence on Photon-Number *N*

To confirm the viability of generation of high-order vortex states in the quadratures we performed numerical simulations for larger total number of photons ($N > 2$). This is depicted in **Figure 3**, for a squeezing parameter $r = 0.02$. **Figures 3A–F** display plots of phase profile associated with $\psi_{LG}(x,y)$, calculated *via* $\phi_{LG}(x,y) = \tan^{-1}\left[\frac{\Im[\psi_{LG}(x,y)]}{\Re[\psi_{LG}(x,y)]}\right]$, for $N/2 = 3, 4, 5, 6, 7, 8$ input photons per mode, further confirming the azymuthal charge and vorticity in quadrture space increases with the number of photons. Insets display 3D plots of mode amplitude $|\psi_{LG}(x,y)|$. As predicted, in all cases the number of vortices is equal to thel number of photons per mode $N/2$ in the initial 2-mode photon-number squeezed state containing N photons, thus confirming the mapping of photon-number in Fock space to quadrature vortex-number in quadrature.

6 PHOTON-NUMBER DISTRIBUTION OF QUADRATURE VORTEX STATES

The generation of vortices in the quadrature can be considered an interference effect arising from photon-number fluctuations, therefore it is expected that the photon-number distribution should be modified for **quadrature** vortex states. To further confirm that photon-number fluctuations are mapped into interference effects in the quadratures, resulting in the emergence of vortices, for a two-mode photon-number squeezed input state, we calculated the photon-number distribution for the resulting vortex states $P(n_1, n_2) = |\langle n_1, n_2|\psi'\rangle|^2$. Using orthogonality of Fock states, the sums in **Eq. 6** collapse into a single sum, of the form:

$$P(n_1, n_2) = \left|\frac{D}{\cosh r}\sum_{k=0}^{n_1+n_2} A_{n_1,n_2}^{N,r} B_{n_1,n_2}^{\phi,k} C_{n_1,n_2}^{N,k}\right|^2, \tag{10}$$

where $A_{n_1,n_2}^{N,r} = \tanh(r)^{\frac{n_1+n_2}{2}}\sqrt{\frac{(n_1+n_2)!\,(n_1+n_2)!}{2^N}}$, $B_{n_1,n_2}^{\phi,k} = (i2\phi)^{2k+\frac{n_2-n_1}{2}}$, and $C_{n_1,n_2}^{N,k}$ results in:

$$C_{n_1,n_2}^{N,k} = \frac{\sqrt{(n_1)!\,(n_2)!}}{\sqrt{k!\left(\frac{n_1+n_2}{2}-k\right)!\left(k+\frac{(n_2-n_1)}{2}\right)!\,(n_1-k)!}}. \tag{11}$$

Equation 11 reveals the photon-number fluctuations which give rise to the emergence of vortices. Numerical results for the photon-number distributions of quadrature vortex states are presented in **Figure 4** and **Figure 5**, confirming the predicted photon-number fluctuations and super-Poissonian statistics.

In order to further illustrate the photon-number imbalance between the two modes, introduced by the rotation in the quadratures, we performed numerical simulations for the two-mode photon number distribution $P(n_1, n_2)$ for vortex states, taking $n_1 \geq n_2$ and a truncation parameter of N *total* photons in the two-mode state, for a rotation parameter $\phi = \pi/4$. Numerical results for different squeezing parameter values are displayed in **Figure 5**: (a) $N = 6$ and $r = 1.0$, (b) $N = 6$ and $r = 0.5$, (c) $N = 10$ and $r = 1.0$, (d) $N = 10$ and $r = 0.5$. For a sufficiently large squeezing parameter, the photon-number distribution peaks for $n_1 = n_2 \approx N/2$.

7 DISCUSSION

We presented a scheme for generation of high-order quadrature vortex states starting from a two-mode photon-number squeezed state generated *via* the non-linear process of Spontaneous Parametric Down Conversion (SPDC). By applying a parametric rotation in the quadratures $(\hat{X}, \hat{Y})$ using a ϕ converter, the quadrature representation of the photon-number squeezed input state is transformed into a high-order **quadrature** vortex state, with N vortices, for an input state containing $2N$ photons, thus mapping the fluctuations in photon-number to interference effects in the quadrature as

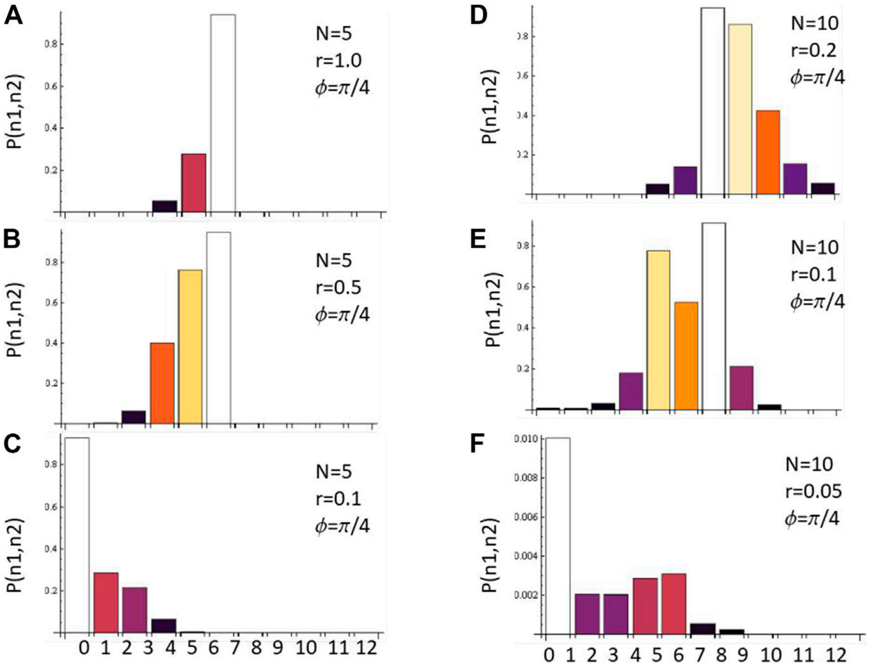

FIGURE 4 | Photon-number statistics $P(n_1,n_2)$ for quadrature vortex states considering $n_1 = n_2$ and a truncation parameter given by N photons *per mode*. Left column $N = 5$ and $\phi = \pi/4$, right column $N = 10$ and $\phi = \pi/4$. Different rows correspond to squeezing parameters **(A)** $r = 1.0$, **(B)** $r = 0.5$, **(C)** $r = 0.1$, **(D)** $r = 0.2$, **(E)** $r = 0.1$, **(F)** $r = 0.05$. The photon-number fluctuations due to quadrature vortex formation is revealed (see text for details).

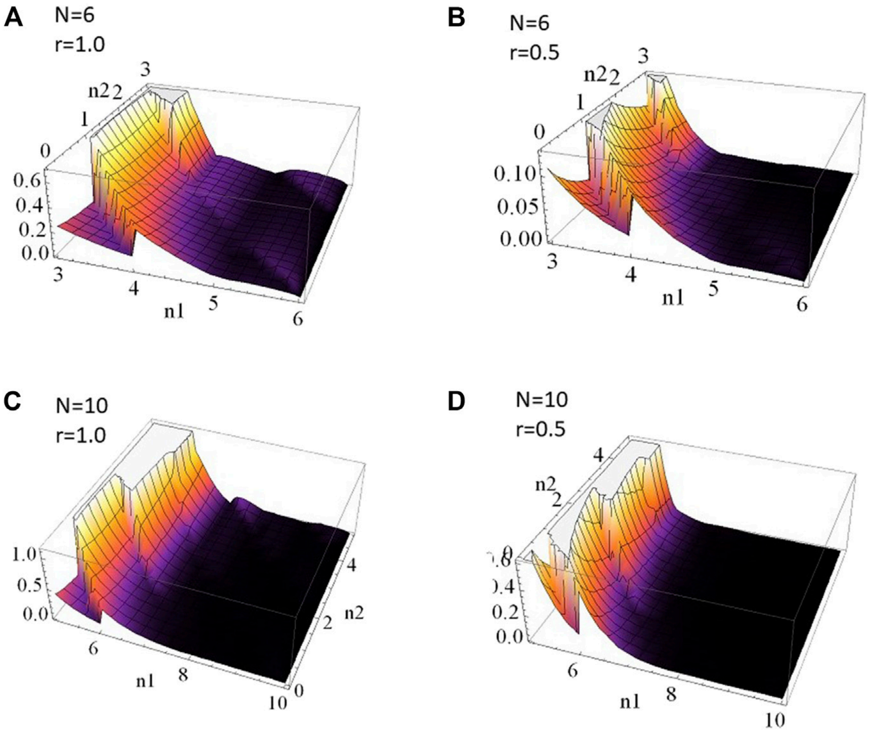

FIGURE 5 | Numerical simulations of photon-number statistics $P(n_1,n_2)$ for quadrature vortex states, taking $n_1 \geq n_2$, and a truncation parameter given by *N total photons* in the two-mode state, for a rotation parameter $\phi = \pi/4$. Numerical results are displayed in Panel 5 for: **(A)** $N = 6$ and $r = 1$, **(B)** $N = 6$ and $r = 0.5$, **(C)** $N = 10$ and $r = 1$, **(D)** $N = 10$ and $r = 0.5$. The photon-number distribution peaks at $n_1 = n_2 \approx N/2$.

depicted by optical singularities with zero-point intensity and singular phase. Furthermore, we obtained analytical and numerical expressions for the super-Poissonian photon-number statistics and fluctuations, giving rise to vortex formation in the quadratures.

Vortex states are customarily generated using various tools, such as Dove prisms, spiral plates, fork holograms, or astigmatic mode converters such as a cylindrical lenses. The important distinction is that these operations act on the transverse profile of the input beam. In the context of the present article, the rotation is performed on the quadrature representation of the state, which can be readily implemented in the lab by a balanced beam splitter. A key application of our scheme is in generation of two-mode photon-number squeezed states from two-mode quadrature vortex states, by implementing the inverse protocol.

Our scheme has the potential of exploiting the advantages of optical vortices, such as high dimensionality and topological properties, for quantum applications requiring squeezed uncertainty beyond the SQL limit ($\sqrt{N}$), such as quantum cryptography, quantum metrology and quantum sensing [35–42].

DATA AVAILABILITY STATEMENT

The data and numerical codes are available upon request.

AUTHOR CONTRIBUTIONS

GP and AB conceived the idea and performed analytical derivations. GP and AB performed numerical simulations. GP wrote the manuscript. All authors provided critical feedback and helped shape the research, analysis and manuscript.

FUNDING

GP acknowledges financial support *via* grants PICT Startup 2015 0710 and UBACyT PDE 2017.

REFERENCES

1. Loudon R. *The Quantum Theory of Light*. 3rd ed. Oxford, United Kingdom: Oxford University Press (2000).
2. Xiao M, Wu L-A, and Kimble HJ. Precision Measurement beyond the Shot-Noise Limit. *Phys Rev Lett* (1987) 59:278–81. doi:10.1103/physrevlett.59.278
3. Walther P, Pan J-W, Aspelmeyer M, Ursin R, Gasparoni S, and Zeilinger A. De Broglie Wavelength of a Non-local Four-Photon State. *Nature* (2004) 429:158–61. doi:10.1038/nature02552
4. McKenzie K, Shaddock DA, McClelland DE, Buchler BC, and Lam PK. Experimental Demonstration of a Squeezing-Enhanced Power-Recycled Michelson Interferometer for Gravitational Wave Detection. *Phys Rev Lett* (2002) 88:231102. doi:10.1103/physrevlett.88.231102
5. Goda K, Miyakawa O, Mikhailov EE, Saraf S, Adhikari R, McKenzie K, et al. A Quantum-Enhanced Prototype Gravitational-Wave Detector. *Nat Phys* (2008) 4:472–6. doi:10.1038/nphys920
6. Ourjoumtsev A, Tualle-Brouri R, Laurat J, and Grangier P. Generating Optical Schrödinger Kittens for Quantum Information Processing. *Science* (2006) 312:83. doi:10.1126/science.1122858
7. Vahlbruch H, Chelkowski S, Hage B, Franzen A, Danzmann K, and Schnabel R. Demonstration of a Squeezed-Light-Enhanced Power- and Signal-Recycled Michelson Interferometer. *Phys Rev Lett* (2005) 95:211102. doi:10.1103/physrevlett.95.211102
8. Wagner K, Janousek J, Delaubert V, Zou H, Harb C, Treps N, et al. Entangling the Spatial Properties of Laser Beams. *Science* (2008) 321:541–3. doi:10.1126/science.1159663
9. Jain N, Huisman SR, Bimbard E, and Lvovsky AI. A Bridge between the Single-Photon and Squeezed-Vacuum States. *Opt Express* (2010) 18:18254–9. doi:10.1364/oe.18.018254
10. Neergaard-Nielsen S, Melholt Nielsen B, Hettich C, Molmer K, and Polzik ES. *Phys Rev Lett* (2006) 97:083604. doi:10.1103/physrevlett.97.083604
11. Allen L, Beijersbergen MW, Spreeuw RJC, and Woerdman JP. Orbital Angular Momentum of Light and the Transformation of Laguerre-Gaussian Laser Modes. *Phys Rev A* (1992) 45:8185–9. doi:10.1103/physreva.45.8185
12. Krenn M, Handsteiner J, Fink M, Fickler R, Ursin R, Malik M, et al. Twisted Light Transmission over 143 Km. *Proc Natl Acad Sci USA* (2016) 113:13648–53. doi:10.1073/pnas.1612023113
13. Paterson L, MacDonald MP, Arlt J, Sibbett W, Bryant PE, and Dholakia K. Controlled Rotation of Optically Trapped Microscopic Particles. *Science* (2001) 292:912. doi:10.1126/science.1058591
14. Wang J, Yang J-Y, Fazal IM, Ahmed N, Yan Y, Huang H, et al. Terabit Free-Space Data Transmission Employing Orbital Angular Momentum Multiplexing. *Nat Photon* (2012) 6:488–96. doi:10.1038/nphoton.2012.138
15. Tian N, Fu L, and Gu M. Resolution and Contrast Enhancement of Subtractive Second Harmonic Generation Microscopy with a Circularly Polarized Vortex Beam. *Sci Rep* (2015) 5:13580. doi:10.1038/srep13580
16. Fickler R, Lapkiewicz R, Plick WN, Krenn M, Schaeff C, Ramelow S, et al. Quantum Entanglement of High Angular Momenta. *Science* (2012) 338:640–3. doi:10.1126/science.1227193
17. Korobchevskaya K, Peres C, Li Z, Antipov A, Sheppard CJR, Diaspro A, et al. Intensity Weighted Subtraction Microscopy Approach for Image Contrast and Resolution Enhancement. *Sci Rep* (2016) 6:25816. doi:10.1038/srep25816
18. Emile O, and Emile J. Naked Eye Picometer Resolution in a Michelson Interferometer Using Conjugated Twisted Beams. *Opt Lett* (2017) 42:354. doi:10.1364/ol.42.000354
19. Fickler R, Campbell G, Buchler B, Lam PK, and Zeilinger A. Quantum Entanglement of Angular Momentum States with Quantum Numbers up to 10,010. *Proc Natl Acad Sci USA* (2016) 113:13642–7. doi:10.1073/pnas.1616889113
20. Padgett MJ. Orbital Angular Momentum 25 Years on [Invited]. *Opt Express* (2017) 25:11265. doi:10.1364/oe.25.011265
21. Caves CM, Zhu C, Milburn GJ, and Schleich W. Photon Statistics of Two-Mode Squeezed States and Interference in Four-Dimensional Phase Space. *Phys Rev A* (1991) 43:3854–61. doi:10.1103/physreva.43.3854
22. Karimi E, Boyd RW, de la Hoz P, de Guise H, Řeháček J, Hradi Z, et al. Radial Quantum Number of Laguerre-Gauss Modes. *Phys Rev A* (2014) 89:8185. doi:10.1103/PhysRevA.89.063813
23. Nienhuis G, and Visser J. Angular Momentum and Vortices in Paraxial Beams. *J Opt A: Pure Appl Opt* (2004) 6:S248–S250. doi:10.1088/1464-4258/6/5/020
24. Agarwal GS, Puri RR, and Singh RP. Vortex States for the Quantized Radiation Field. *Phys Rev A* (1997) 56:4207–15. doi:10.1103/physreva.56.4207
25. Nienhuis G, and Visser J. Angular Momentum and Vortices in Paraxial Beams. *J Opt A: Pure Appl Opt* (2004) 6:S248–S250. doi:10.1088/1464-4258/6/5/020
26. Sanchez-Soto L, Klimov AB, de la Hoz P, Rigas I, Řeháček J, Hradil Z, et al. *Phys Rev A* (2013) 88:053839. doi:10.1103/physreva.88.053839
27. Hemsing E, Knyazik A, Dunning M, Xiang D, Marinelli A, Hast C, et al. Coherent Optical Vortices from Relativistic Electron Beams. *Nat Phys* (2013) 9:549–53. doi:10.1038/nphys2712
28. Mair A, Vaziri A, Weihs G, and Zeilinger A. Entanglement of the Orbital Angular Momentum States of Photons. *Nature* (2001) 412:313–6. doi:10.1038/35085529

29. Oemrawsingh SSR, Aiello A, Eliel ER, Nienhuis G, and Woerdman JP. How to Observe High-Dimensional Two-Photon Entanglement with Only Two Detectors. *Phys Rev Lett* (2004) 92:217901. doi:10.1103/physrevlett.92.217901
30. Marrucci L, Karimi E, Slussarenko S, Piccirillo B, Santamato E, Nagali E, et al. Spin-to-orbital Conversion of the Angular Momentum of Light and its Classical and Quantum Applications. *J Opt* (2011) 13:064001. doi:10.1088/2040-8978/13/6/064001
31. Molina-Terriza G, Rebane L, Torres JP, Torner L, and Carrasco S. *J Eur Opt Soc* (2007) 2:07014. doi:10.2971/jeos.2007.07014
33. Karimi E, and Santamato E. Radial Coherent and Intelligent States of Paraxial Wave Equation. *Opt Lett* (2012) 37:2484. doi:10.1364/ol.37.002484
34. Plick WN, Lapkiewicz R, Ramelow S, and Zeilinger A. The Forgotten Quantum Number: A Short Note on the Radial Modes of Laguerre-Gauss Beams. *arXiv: 1306.6517*.
35. Salomaa MM, and Volovik GE. Quantized Vortices in superfluidHe3. *Rev Mod Phys* (1987) 59:533–613. doi:10.1103/revmodphys.59.533
36. Puentes G, LundeenBranderhorst JSM, Coldesstrodt-Ronge H, Smith B, and Walmsley IA. *Phys Rev Lett* (2009) 102:080404. doi:10.1103/physrevlett.102.080404
37. Puentes G, Datta A, Feito A, Eisert J, Plenio MB, and Walmsley IA. Entanglement Quantification from Incomplete Measurements: Applications Using Photon-Number-Resolving Weak Homodyne Detectors. *New J Phys* (2010) 12:033042. doi:10.1088/1367-2630/12/3/033042
38. Puentes G, Waldherr G, Neumann P, Balasubramanian G, and Wrachtrup J. *Scientific Rep* (2014) 4:1–6. doi:10.1038/srep04677
39. Puentes G, Aiello A, Voigt D, and Woerdman JP. *Phys Rev A* (2007) 75:032319. doi:10.1103/physreva.75.032319
40. Puentes G, Colangelo G, Sewell RJ, and Mitchell MW. Planar Squeezing by Quantum Non-demolition Measurement in Cold Atomic Ensembles. *New J Phys* (2013) 15:103031. doi:10.1088/1367-2630/15/10/103031
41. Moulieras S, Lewenstein M, and Puentes G. Entanglement Engineering and Topological protection by Discrete-Time Quantum Walks. *J Phys B: Mol Opt Phys* (2013) 46:104005. doi:10.1088/0953-4075/46/10/104005
42. Takayama O, and Puentes G. Enhanced Spin Hall Effect of Light by Transmission in a Polymer. *Opt Lett* (2018) 43:1343–6. doi:10.1364/ol.43.001343

Conflict of Interest: The authors declare that the research was conducted in the absence of any commercial or financial relationships that could be construed as a potential conflict of interest.

APPENDIX A

The starting point of the derivation is **Eq. 5**, which defines a $\pi/4$ mode converter:

$$\widehat{C} = \frac{1}{2}\left(\widehat{a}^{\dagger}\widehat{b}^{\dagger} + \widehat{a}^{\dagger}\widehat{b}^{\dagger}\right) \tag{12}$$

where $\widehat{a}^{\dagger}$ $(\widehat{b}^{\dagger})$ are the bosonic mode operators acting on orthogonal modes and follow regular bosonic commutation relations. Also, let us consider the initial state of the two mode system to be the following

$$|\psi\rangle = \sum_j A_j |j\rangle_a |j\rangle_b \tag{13}$$

The above describes a general two-mode state in the Fock basis with total number of particles N distributed between the two modes. Now **Eq. 13** can be written in terms of the mode operators as follows

$$|\psi\rangle = \sum_j A_j \left(\widehat{a}^{\dagger}\right)^j \left(\widehat{b}^{\dagger}\right)^j |0\rangle_a |0\rangle_b \tag{14}$$

where it is understood that the operator $\widehat{a}^{\dagger}$ $(\widehat{b}^{\dagger})$ acts on mode $|0\rangle_a$ $(|0\rangle_b)$. We want to find how the state $|\psi\rangle$ transforms under the action of $\widehat{C}$. Moving to the Heisenberg picture, the mode operators $\widehat{a}^{\dagger}$ $(\widehat{b}^{\dagger})$ evolve under $\widehat{C}$ as

$$\widehat{a}^{\dagger} \rightarrow \exp\left(i2\phi\widehat{C}\right)\widehat{a}^{\dagger} \exp\left(-i2\phi\widehat{C}^{\dagger}\right) \tag{15}$$

Using the Baker-Hausdorff lemma, we can write **Eq. 15** as follows

$$\exp\left(i2\phi\widehat{C}\right)\widehat{a}^{\dagger} \exp\left(-i2\phi\widehat{C}^{\dagger}\right) = \widehat{a}^{\dagger} + i2\phi\left[\widehat{C}, \widehat{a}^{\dagger}\right] + \tag{16}$$

$$\frac{(i2\phi)^2}{2!}\left[\widehat{C}, \left[\widehat{C}, \widehat{a}^{\dagger}\right]\right] + \ldots \tag{17}$$

Solving for the commutators, we see that $[\widehat{C}, \widehat{a}] = -\widehat{b}^{\dagger}/2$ and. Plugging these values back into **Eq. 16**, we see that we can group the terms as

$$\widehat{a}^{\dagger}\left(1 - \frac{(\phi)^2}{2!} + \ldots\right) - i\widehat{b}^{\dagger}\left(\phi - \frac{\phi^3}{3!} + \ldots\right)$$

$$= \widehat{a}^{\dagger}\cos\phi - i\widehat{b}^{\dagger}\sin\phi \tag{18}$$

Now for a $\pi/4$ mode converter, we put $\phi = \pi/4$ resulting in the transformation

$$\widehat{a}^{\dagger} \rightarrow \frac{1}{\sqrt{2}}\left(\widehat{a}^{\dagger} - i\widehat{b}^{\dagger}\right) \tag{19}$$

and similarly for $\widehat{b}^{\dagger}$. Therefore, **Eq. 14** is transformed to

$$|\psi\rangle_v = \sum_j A_j \left(\widehat{a}^{\dagger} + i\widehat{b}^{\dagger}\right)^j \left(\widehat{b}^{\dagger} + i\widehat{a}^{\dagger}\right)^j |0\rangle_a |0\rangle_b$$

under the effect of the $\pi/4$ mode converter. It is understood in **Eq. 20** that factors $1/\sqrt{2}$ have been absorbed into A_j. **Equation 6** follows from here by a binomial expansion of the terms.

frontiers
in Physics

BRIEF RESEARCH REPORT
published: 05 July 2021
doi: 10.3389/fphy.2021.671559

Numerical Simulation of Long-Wave Infrared Generation Using an External Cavity Diamond Raman Laser

Hui Chen[1,2], Zhenxu Bai[1,2,3]*, Chen Zhao[1,2], Xuezong Yang[4], Jie Ding[1,2], Yaoyao Qi[1,2], Yulei Wang[1,2] and Zhiwei Lu[1,2]

[1]Center for Advanced Laser Technology, Hebei University of Technology, Tianjin, China, [2]Hebei Key Laboratory of Advanced Laser Technology and Equipment, Tianjin, China, [3]MQ Photonics Research Centre, Department of Physics and Astronomy, Macquarie University, Sydney, NSW, Australia, [4]Hangzhou Institute for Advanced Study, UCAS, Hangzhou, China

Diamond has a broad spectral transmission range (>0.2 μm) and the largest Raman frequency shift (1,332 cm^{-1}) among known Raman crystals. Hence, the diamond Raman laser has the potential to achieve lasing in the long-wave infrared (LWIR) range, which is difficult to reach via other crystalline lasers. Here, we report a new approach to achieve LWIR output using diamond Raman conversion and provide the corresponding analysis model and simulation results. The conversion efficiency is analyzed as function of the pump waist size, output-coupler transmission, and crystal length, at constant pump power. The maximum output power at which a diamond of relatively large size can be operated without damage is predicted. This study paves a way for high-power LWIR lasing in diamond.

Keywords: long-wave infrared, diamond, Raman laser, external cavity, numerical simulation

OPEN ACCESS

Edited by:
Zhi-Han Zhu,
Harbin University of Science and Technology, China

Reviewed by:
Quan Sheng,
Tianjin University, China
Zhiyuan Zhou,
University of Science and Technology of China, China

****Correspondence:***
Zhenxu Bai
baizhenxu@hotmail.com

Specialty section:
This article was submitted to Optics and Photonics, a section of the journal Frontiers in Physics

Received: *24 February 2021*
Accepted: *21 June 2021*
Published: *05 July 2021*

Citation:
Chen H, Bai Z, Zhao C, Yang X, Ding J, Qi Y, Wang Y and Lu Z (2021) Numerical Simulation of Long-Wave Infrared Generation Using an External Cavity Diamond Raman Laser. Front. Phys. 9:671559. doi: 10.3389/fphy.2021.671559

INTRODUCTION

The long-wave infrared (LWIR) range (>8 μm) falls in the atmospheric window, where has lower atmospheric absorption and scattering loss compared with that of the near-infrared region, as shown in **Figure 1**. Hence, LWIR lasers are able to strongly penetrate fog and smoke. Therefore, these lasers have important applications in defense, laser remote sensing, and biochemical detection [1, 2]. Limitations on crystal growth (viz. limited size, limited transmission spectrum range, low damage threshold, or low gain coefficient, etc.) pose a limitation on the performance of the inversion lasers in the LWIR band. At present, the common approaches toward 10 μm band lasing include CO_2 laser, quantum cascade laser (QCL), free-electron laser, as well as frequency conversion via nonlinear optical techniques. Among these methods, the optical parametric oscillator (OPO) based on nonlinear frequency conversion is one of the most well-known techniques to realize all-solid-state LWIR lasing [3, 4]. However, it is very difficult to obtain high-power LWIR output by using OPO because of its large quantum defect and low optical conversion efficiency. Owing to the limited depth of quantum wells, the output power of QCLs in LWIR is usually less than hundreds of milliwatts, and it is difficult to achieve high peak power output [5]. The CO_2 laser is a mature method to generate tunable laser output in the range from 9.2 to 10.8 μm. However, continuous CO_2 gas injection is required for the operation of CO_2 lasers, and this results in large footprint and high operational cost. As a third-order nonlinear frequency conversion technology, stimulated Raman scattering (SRS) is automatic phase-matched and not affected by the "spatial hole burning" effect existing in traditional inversion lasers. Wideband laser output can be achieved by controlling the pump wavelength and cascade process in a Raman oscillator [6]. In addition, the "beam cleanup" effect makes SRS an effective technical method to obtain a high beam quality laser source [7–9].

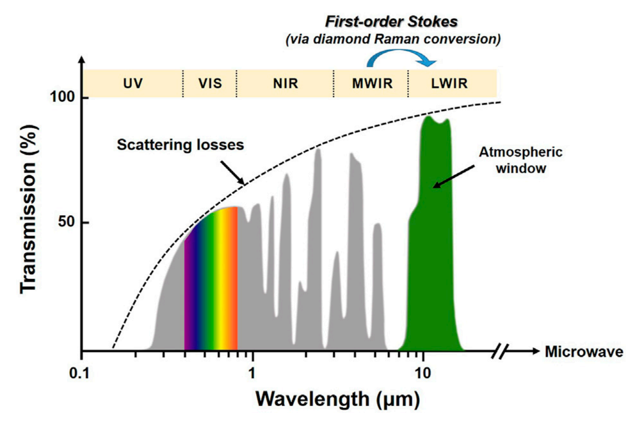

FIGURE 1 | Atmospheric windows (inset: LWIR laser generation via diamond Raman conversion).

Diamond is an excellent Raman crystal with an extremely high Raman gain coefficient, wide spectral transmission range (from 0.2 to >50 μm), large Raman frequency shift (1,332.3 cm^{-1}), and extremely high thermal conductivity (>2000 $W\ m^{-1}\ K^{-1}$) [10–13]. The thermal conductivity of diamond is dozens or even hundreds of times that of common laser host materials (thermal conductivity of $Y_3Al_5O_{12}$ is 14 $W\ m^{-1}\ K^{-1}$ and that of quartz fiber is 1.17 $W\ m^{-1}\ K^{-1}$) and widely used mid-infrared OPO crystals (thermal conductivity of $ZnGeP_2$ is 35 $W\ m^{-1}\ K^{-1}$ and that of $KTiOAsO_4$ is 2 $W\ m^{-1}\ K^{-1}$). The near infrared 1.5 μm (eye-safe) [14] and mid-infrared 3–5 μm [15] band laser outputs have been achieved through diamond Raman conversion. Combined with the excellent photothermal properties of the diamond crystal and the many significant advantages of the SRS process, the diamond Raman laser (DRL) has become a potentially effective means to obtain LWIR lasing output. Utilizing the large Raman frequency shift of diamond and a 4.3 μm laser as the pump source, a 10 μm LWIR lasing output can be obtained through the first-order diamond Raman conversion, as shown in the inset of **Figure 1**.

In this paper, we propose a model of a first-order Raman laser with 10 μm output by utilizing diamond Raman conversion. Based on the steady-state model of the DRL, the relationships between the cavity parameters, crystal length, and output characteristics, such as the conversion rate are simulated and analyzed. The optimal pump waist size, output coupler transmission, and crystal length are determined. In addition, the intensity changes of pump and Stokes in the time domain during the Raman conversion are analyzed.

NUMERICAL SIMULATION AND ANALYSIS

Model for Simulation

The experimental setup for the simulation analysis in this study is shown in **Figure 2**. Pump wavelength 4.3 μm (no challenge to realize in an OPO at present) was applied in the simulation for >10 μm Raman lasing. The long-band pumped far-infrared Raman laser has a larger intrinsic mode size under the condition of certain cavity parameters compared to the traditional short-band pumped Raman lasers; meanwhile, the Raman gain coefficient is inversely proportional to the wavelength [6]. Therefore, these increase the pump threshold of LWIR generation, the maximum pump power that the crystal can bear, and the maximum output power that can be obtained. The Raman oscillator adopts a near-concentric cavity structure. The curvature radius of the input and output couplers is 50 mm. The surface of the input coupler is antireflection-coated at the pump (4.3 μm) and high-reflection-coated at the Stokes (10 μm); the surface of the output coupler is high-reflection-coated at 4.3 μm. The total length of the cavity is 102 mm, and the corresponding intrinsic beam waist size is 251 μm (380 μm at the *t*-plane and 122 μm at the *s*-plane). As the refractive index of diamond is constant ($n = 2.38$) at wavelengths greater than 2 μm [11], a Brewster-cut (~67.2°) single-crystal diamond is applied for the transmittance of both pump and Stokes beams, while avoiding the problems caused by crystal coating and film damage. The

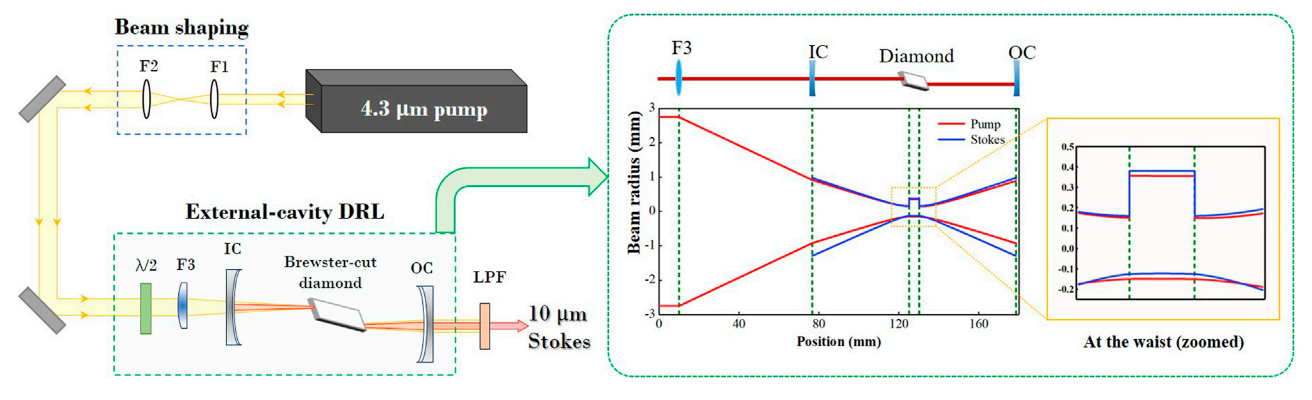

FIGURE 2 | Schematic of 10 μm external-cavity DRL (inset: pump and intrinsic mode of diamond Raman resonator).

diamond is 5 mm in length and placed at the beam waist of the Stokes. To achieve better mode matching to improve the conversion efficiency, a focusing lens F3 with a focal length of 100 mm is used to focus the pump beam to the center of the diamond, and the corresponding pump waist size is 252 μm, as shown in the inset of **Figure 2**.

Simulation Analysis

For crystalline Raman gain materials, the time of Raman phase transition is usually in the order of picosecond. This means that the pump pulse duration in tens of nanoseconds is consistent with the steady-state operating conditions [16, 17]. However, affected by the build-up and amplification time of Stokes, usually the pulse duration of Stokes is often shorter than that of the pump until the pump pulse width is longer than hundreds of nanoseconds. Therefore, based on the resonator structure proposed above, we first used the steady-state model of an external cavity Raman laser to simulate and analyze the output characteristics (conversion efficiency, output power, etc.) under different resonators and pump parameters. Subsequently, time-domain characteristics of a short pulse pumped DRL is discussed to better understand the effect of oscillator parameters on the output pulse.

When the Raman laser operates in a steady-state, the following relationship is satisfied [18, 19].

$$P_p = \frac{T + 2\alpha L}{\eta T} P_s \left[1 - \exp\left(-\frac{2G}{T} P_s\right)\right]^{-1} \tag{1}$$

$$P_{res} = P_p - \frac{(T + 2\alpha L) P_s}{\eta T} \tag{2}$$

where T is the output coupler transmittance, α (=0.03 cm^{-1}) and L (=5 mm) are the absorption coefficient and the length of the diamond crystal, respectively; η is the quantum defect in the Raman conversion process ($\eta = \lambda p/\lambda s$); G is the Raman power gain in the focused geometry; P_p, P_s and P_res are the powers of pump, Stokes, and the residual pump, respectively.

$$G = \frac{g_s \arctan\left(\frac{L}{2}\sqrt{\frac{\left(w_p/z_p\right)^2 + \left(w_s/z_s\right)^2}{w_p^2 + w_s^2}}\right)}{\eta \frac{\pi}{4}\sqrt{\left(w_p^2 + w_s^2\right)^2\left[\left(w_p/z_p\right)^2 + \left(w_s/z_s\right)^2\right]}} \tag{3}$$

$$z_{p,s} = \frac{\pi n_{p,s} w_{p,s}^2}{M_{p,s}^2 \lambda_{p,s}} \tag{4}$$

where g_s is the Raman gain coefficient of the diamond crystal, $n_\mathrm{p,s}$ ($n_\mathrm{p} = n_\mathrm{s} = 2.38$), $w_\mathrm{p,s}$ ($w_\mathrm{p} = 252$ μm and $w_\mathrm{s} = 251$ μm) and $M_{p,s}^2$ ($M_p^2 = 2$ and $M_s^2 = 1.1$) are the indices of refraction, waist size and beam quality factors of the pump and Stokes, respectively. As the gain coefficient is inversely proportional to the wavelength, the gain coefficient is set to be 1 cm/GW in the simulation, based on the previous reports g_s = ~10 cm/GW at 1 μm [6]. According to **Eq. 2**, when the pump power increases to infinity, the slope efficiency of Stokes light (σ) is equal to the maximum conversion efficiency of Raman generation, i.e.,

$$\sigma = \frac{\eta T}{T + 2\alpha L} \tag{5}$$

When Stokes output power approaches zero infinitely, the threshold P_thr of Raman generation is calculated by **Eq. 1**:

$$P_{thr} = \frac{\pi(T + 2\alpha L)\sqrt{\left(w_p^2 + w_s^2\right)^2\left[\left(w_p/z_p\right)^2 + \left(w_s/z_s\right)^2\right]}}{8 g_s \arctan\left(\frac{L}{2}\sqrt{\frac{\left(w_p/z_p\right)^2 + \left(w_s/z_s\right)^2}{w_p^2 + w_s^2}}\right)} \tag{6}$$

According to **Eqs. 5**, **6**, we can obtain the maximum conversion efficiency and Raman generation threshold at different output coupler transmittances. As shown in **Figures 3A,B**, the Raman generation threshold of DRL is much higher than that in the near-infrared band owing to its relatively low Raman gain and high absorption loss in the LWIR band [11]. The Raman generation threshold increases linearly with the output coupler transmittance. When the output coupler transmittance increases to about 60%, the maximum conversion efficiency can approach the quantum conversion limit (~43%). Using **Eqs. 1**, **2**, the output power and the residual pump curves when T = 0.5% are obtained for the double-pass pump mode. As shown in **Figure 3C**, when T = 0.5%, the corresponding Stokes generation threshold is 34.8 kW. When the pump power is greater than this value, owing to the consumption of Raman conversion, the residual pump power rapidly reduces, and the Stokes power generated increases accordingly.

The output transmittance, pump waist size, and crystal length are three key factors that affect the output power of the DRL. Utilizing **Eq. 1**, we obtained the relationship between the output power of Stokes and the output transmittance, the size of the pump waist, and the crystal length under different pump powers, as shown in **Figure 3**. When the pump waist size and the crystal length are fixed, different pump powers correspond to different values of the optimal output transmittance. As shown in **Figure 3D**, the optimal output transmittance increases with the increase in pump power. The threshold of Stokes generation corresponds to a fixed pump power density, and the size of the pump focus is directly related to the power density. When the pump power is constant, the smaller the pump focus size (corresponding to the higher power density), and the easier it is to obtain Stokes output, as shown in **Figure 3E**. However, the pump spot size cannot be infinitely small, which is particularly difficult for LWIR lasers. Thus, there is an experimental optimum beam waist size that is small enough to get close to the maximum output power and yet not be experimentally problematic, for example, by shortening the length of the Raman oscillator combining with a shorter pump focus lens (F3, as illustrated in **Figure 1**). Even if the pump waist size is smaller than this value, the improvement of the output Stokes power is very limited. Meanwhile, the small size of the pump waist may increase the risk of diamond damage and aggravate the thermal effect. The crystal length is another key factor affecting the output power of the Raman laser, which affects the absorption loss of the crystal, as well as the interaction length of the pump and Stokes beams during the Raman conversion. As shown in **Figure 3F**, the Stokes power increases with the increase of diamond length in the initial stage, however, decreases when the diamond length increases

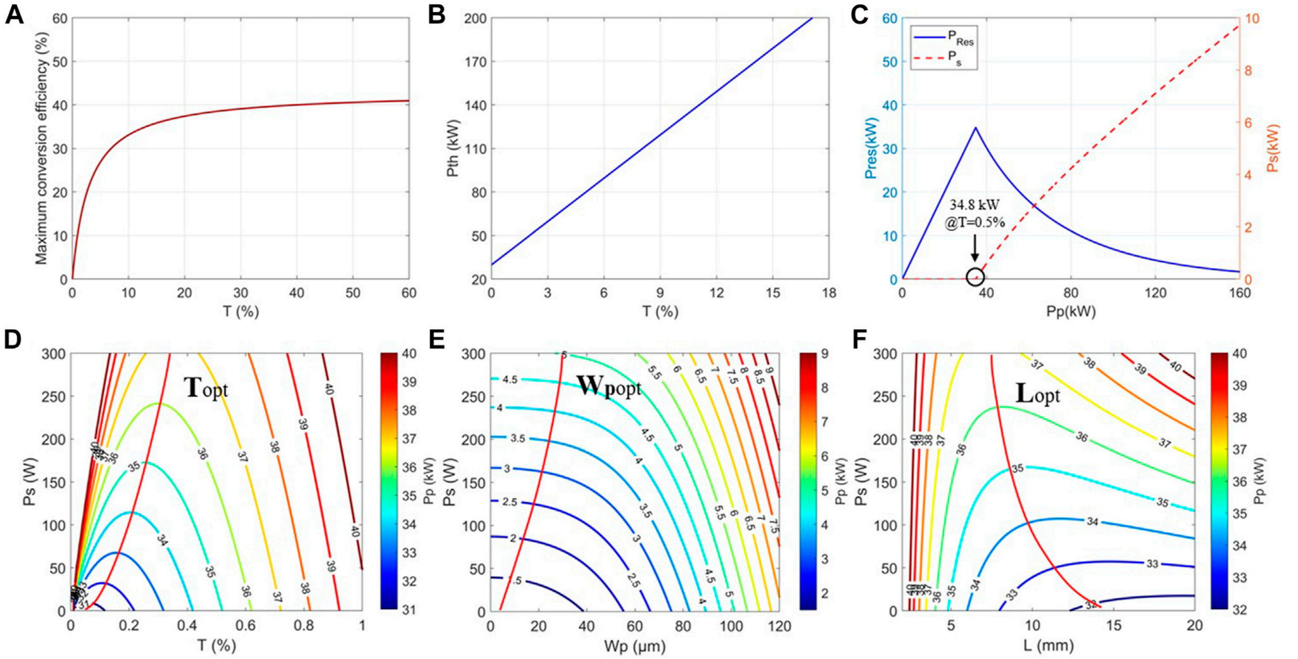

FIGURE 3 | Numerical simulation results. **(A)** Maximum conversion efficiency, and **(B)** Raman generation threshold as a function of output coupler transmittance at Stokes; **(C)** output and residual pump curves at T = 0.5%. Stokes output power as a function of **(D)** output coupling transmittance, **(E)** pump waist radius, and **(F)** the crystal length, for different pump powers. The red line indicates optimal values of output coupler transmission, pump waist radius, and length of the crystal, respectively.

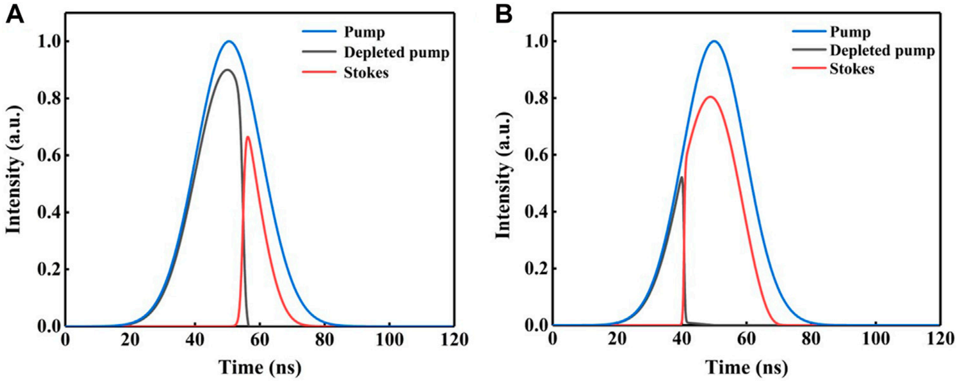

FIGURE 4 | Tracings diagram of pump, depleted pump and Stokes with **(A)** small gain, and **(B)** large gain.

continuously due to the relatively large absorption loss in the pump band. Therefore, it is critical to choose an optimal length of the crystal, especially for LWIR Raman lasing.

Theoretically, as the dephasing time of the vibrational excitation is of order of 10 ps for crystals [20], the Stokes pulse width is close to that of the pump when the overall gain of the oscillator is large enough for a crystalline Raman laser pumped by tens of nanoseconds pulse (or longer). However, restricted by Raman gain coefficient, crystal length, intracavity diffraction loss, as well as resonator structure, Stokes beam cannot oscillate and output in a very short time, which leads to an obvious pulse compression effect during Raman conversion [21, 22]. In view of this situation, we simply analyze the changes of pump and Stokes intensity in time domain in a Raman oscillator. It is assumed that the time-domain distribution of the pump pulse is Gaussian and only the first order Stokes generation is existed, as shown in **Figure 4**. At the beginning, the pump pulse remains in the input state before reaching the Raman threshold. When reaches the Stokes generation threshold, Stokes pulse is amplified rapidly with pump pulse depleted until the end of the pump cycle. It can be seen from the comparison of **Figures 4A,B**, when the overall gain of the Raman oscillator is small, a relatively long time is required to Stokes generation, showing low output power intensity and strong pulse width compression effect. By contrast, Stokes with high power intensity and negligible pulse compression effect is presented, while the gain is high. As gain coefficient in the specific operating wavelength and waist radii of the pump and Stokes beams, are the main parameters that the overall gain of a Raman oscillator depended on, it can be predicted that relatively strong pulse width compression will occur in a LWIR-DRL if the pump pulse width is in the order of nanoseconds. Therefore, compared with short pulse pumping (~ns), increasing the pump pulse width in a certain range is an alternative way to improve the pump efficiency of LWIR-DRLs.

CONCLUSION AND OUTLOOK

In this paper, we proposed a new scheme to realize LWIR lasing output through diamond Raman conversion by utilizing the excellent photothermal properties of diamond crystals and the advantages of SRS. Based on the large Raman frequency shift of the diamond crystal, a 10 μm far-infrared laser was obtained by using a 4.3 μm laser as the pump source through the first-order Raman conversion. Using the diamond Raman steady-state model, we simulated the relationship between the output transmittance and the maximum conversion efficiency, Raman generation threshold, and residual pump power. The relationship between the relevant parameters (the size of the pump waist, output transmittance, and crystal length) and the output power was analyzed. And the pulse compression effect as the function of the oscillator gain in the process of Raman conversion is discussed. It can be predicted that when the diamond size is $1 \times 1 \times 1\ \mathrm{cm}^3$, the maximum Stokes peak power output close to 123 MW can be generated with the transmittance of 40%. However, since the steady-state Raman gain coefficient is inversely proportional to the linewidth [23, 24], considering the intrinsic gain linewidth of the diamond (~40 GHz), it is necessary to control the linewidth of the mid-wave infrared (MWIR) pump beam in the experiment to ensure the Raman conversion efficiency.

The simulation results in this study provide important theoretical guidance and prediction for the subsequent development of LWIR lasers based on the DRL. In addition, due to the excellent thermophysical properties of diamond, stable LWIR Raman operation without heat accumulation can be realized when the pump pulse width is in the order of 100 microseconds, meanwhile, the repetition rate can be up to kHz-level [10, 25], even if its quantum defect is significantly higher than that of the short wave. As there is no spatial hole burning effect in the process of Raman conversion [26–29], the theoretical study also provides a preliminary reference for realizing the operation of narrow linewidth LWIR lasing. Besides, the excellent Brillouin characteristics of diamond also make it possible to realize low-noize LWIR Brillouin lasing and Brillouin frequency combs in the future [30, 31].

DATA AVAILABILITY STATEMENT

The raw data supporting the conclusion of this article will be made available by the authors, without undue reservation.

AUTHOR CONTRIBUTIONS

HC: Methodology, Formal analysis, Writing - original draft. ZB: Conceptualization, Writing - review and editing, Formal analysis, Supervision, Funding acquisition. CZ: Investigation, Writing - original draft. XY: Writing - review and editing, Formal analysis. JD: Writing - review and editing. YQ: Writing - review and editing. YW: Conceptualization, Supervision. ZL: Conceptualization, Supervision.

FUNDING

This work was supported by the National Natural Science Foundation of China (61905061 and 61927815), Key Laboratory of Functional Crystals and Laser Technology Foundation (FCLT202004), and Postgraduate Innovation Ability Training Program of Hebei Province (CXZZSS2021039).

REFERENCES

1. Shaw LB, Cole B, Thielen PA, Sanghera JS, and Aggarwal ID. Mid-Wave IR and Long-Wave IR Laser Potential of Rare-Earth Doped Chalcogenide Glass Fiber. *IEEE J Quan Electron* (2001) 37:1127–37. doi:10.1109/3.945317
2. Miyamoto K, and Ito H. Wavelength-agile Mid-infrared (5-10 μm) Generation Using a Galvano-Controlled KTiOPO_4 Optical Parametric Oscillator. *Opt Lett* (2007) 32:274–6. doi:10.1364/ol.32.000274
3. Badikov VV, Laptev VB, Panyutin VL, Ryabov EA, and Shevyrdyaeva GS. Study of Nonlinear-Optical Characteristics of AgGa1-xInxSe2crystals. *Quan Electron* (2005) 35(3):263–7. doi:10.1070/qe2005v035n03abeh002795
4. Watson MA, O'Connor MV, Shepherd DP, and Hanna DC. Synchronously Pumped CdSe Optical Parametric Oscillator in the 9-10 μm Region. *Opt Lett* (2003) 28(20):1957–9. doi:10.1364/ol.28.001957
5. Razeghi M, Zhou W, Slivken S, Lu Q-Y, Wu D, and McClintock R. Recent Progress of Quantum cascade Laser Research from 3 to 12 μm at the Center for Quantum Devices [Invited]. *Appl Opt* (2017) 56(31):H30–H44. doi:10.1364/ao.56.000h30
6. Williams RJ, Kitzler O, Bai Z, and Sarang S. High Power diamond Raman Lasers. *IEEE J Selected Top Quan Electronics* (2018) 24(5):1602214. doi:10.1109/jstqe.2018.2827658
7. Murray JT, Austin WL, and C. Powell R. Intracavity Raman Conversion and Raman Beam Cleanup. *Opt Mater* (1999) 11(4):353–71. doi:10.1016/s0925-3467(98)00033-0
8. Bai Z, Williams RJ, Jasbeer H, Sarang S, Kitzler O, Mckay A, et al. Large Brightness Enhancement for Quasi-Continuous Beams by diamond Raman Laser Conversion. *Opt Lett* (2018) 43(3):563–6. doi:10.1364/ol.43.000563
9. Bai Z, Williams RJ, Kitzler O, Sarang S, Spence DJ, and Mildren RP. 302 W Quasi-Continuous Cascaded diamond Raman Laser at 15 Microns with Large Brightness Enhancement. *Opt Express* (2018) 26(16):19797–803. doi:10.1364/oe.26.019797
10. Williams RJ, Kitzler O, Mckay A, and Mildren RP. Investigating diamond Raman Lasers at the 100 W Level Using Quasi-Continuous-Wave Pumping. *Opt Lett* (2014) 39(14):4152–5. doi:10.1364/ol.39.004152

11. Mildren RP. Intrinsic Optical Properties of Diamond. *Optical Engineering of Diamond*. New Jersey: John Wiley&Sons (2013) p. 1–34. doi:10.1002/9783527648603.ch1
12. Balmer RS, Brandon JR, Clewes SL, Dhillon HK, Dodson JM, Friel I, et al. Chemical Vapour Deposition Synthetic diamond: Materials, Technology and Applications. *J Phys Condens Matter* (2009) 21(36):364221. doi:10.1088/0953-8984/21/36/364221
13. Friel I, Geoghegan SL, Twitchen DJ, and Scarsbrook GA. Development of High Quality Single crystal diamond for Novel Laser Applications [C]. *Proc SPIE* (2010) 13:783819. doi:10.1117/12.864981
14. Li Y, Bai Z, Chen H, Jin D, Yang X, Qi Y, et al. Eye-safe diamond Raman Laser. *Results Phys* (2020) 16:102853. doi:10.1016/j.rinp.2019.102853
15. Sabella A, Piper JA, and Mildren RP. Diamond Raman Laser with Continuously Tunable Output from 3.38 to 3.80 μm. *Opt Lett* (2014) 39(13):4037–40. doi:10.1364/ol.39.004037
16. Piper JA, and Pask HM. Crystalline Raman Lasers. *IEEE J Select Top Quan Electron* (2007) 13(3):692–704. doi:10.1109/jstqe.2007.897175
17. Warrier AM, Lin J, Pask HM, Mildren RP, Coutts DW, and Spence DJ. Highly Efficient Picosecond diamond Raman Laser at 1240 and 1485 nm. *Opt Express* (2014) 22(3):3325–33. doi:10.1364/oe.22.003325
18. Kitzler O, McKay A, Spence DJ, and Mildren RP. Modelling and Optimization of Continuous-Wave External Cavity Raman Lasers. *Opt Express* (2015) 23: 8590–602. doi:10.1364/oe.23.008590
19. Boyd G, Johnston W, and Kaminow I. Optimization of the Stimulated Raman Scattering Threshold. *IEEE J Quan Electron* (1969) 5(4):203–6. doi:10.1109/jqe.1969.1075751
20. Pask HM. The Design and Operation of Solid-State Raman Lasers. *Prog Quan Electronics* (2003) 27(1):3–56. doi:10.1016/s0079-6727(02)00017-4
21. Wang Y, Peng W, Yang X, and Peng J. Efficient Operation Near the Quantum Limit in External Cavity diamond Raman Laser. *Laser Phys* (2020) 30(9): 095002. doi:10.1088/1555-6611/ab9d76
22. Ma S, Tu H, Lu D, Hu Z, Jiang N, Wang X, et al. Efficient Raman Red Laser with Second-Order Stokes Effect of diamond crystal. *Opt Commun* (2020) 22: 126399. doi:10.1016/j.optcom.2020.126399
23. Spence DJ. Spectral Effects of Stimulated Raman Scattering in Crystals. *Prog Quan Electronics* (2017) 51:1–45. doi:10.1016/j.pquantelec.2016.11.001
24. Sheng Q, Lee A, Spence D, and Pask H. Wavelength Tuning and Power Enhancement of an Intracavity Nd:GdVO$_4$-BaWO$_4$ Raman Laser Using an Etalon. *Opt Express* (2018) 26(24):32145–55. doi:10.1364/oe.26.032145
25. Bai Z, Zhang Z, Wang K, Gao J, Zhang Z, Yang X, et al. Comprehensive thermal Analysis of diamond in a High-Power Raman Cavity Based on FVM-FEM Coupled Method. *Nanomaterials* (2021) 11(6):1572. doi:10.3390/nano11061572
26. Lux O, Sarang S, Kitzler O, Spence DJ, and Mildren RP. Intrinsically Stable High-Power Single Longitudinal Mode Laser Using Spatial Hole Burning Free Gain. *Optica* (2016) 3(8):876–81. doi:10.1364/optica.3.000876
27. Sheng Q, Li R, Lee AJ, Spence DJ, and Pask HM. A Single-Frequency Intracavity Raman Laser. *Opt Express* (2019) 27(6):8540–53. doi:10.1364/oe.27.008540
28. Yang X, Kitzler O, Spence DJ, Williams RJ, Bai Z, Sarang S, et al. Single-frequency 620 Nm diamond Laser at High Power, Stabilized via Harmonic Self-Suppression and Spatial-hole-burning-free Gain. *Opt Lett* (2019) 44(4): 839–42. doi:10.1364/ol.44.000839
29. Yang X, Kitzler O, Spence DJ, Bai Z, Feng Y, and Mildren RP. Diamond Sodium Guide star Laser. *Opt Lett* (2020) 45(7):1898–901. doi:10.1364/ol.387879
30. Bai Z, Robert JW, Ondrej K, and Kitzler O. Diamond Brillouin Laser in the Visible. *APL Photon* (2020) 5(3):031301. doi:10.1063/1.5134907
31. Williams RJ, Bai Z, Sarang S, Kitzler O, Spence DJ, and Mildren RP. *Diamond Brillouin Lasers*. arXiv preprint arXiv:1807.00240 (2018).

Conflict of Interest: The authors declare that the research was conducted in the absence of any commercial or financial relationships that could be construed as a potential conflict of interest.

frontiers
in Physics

BRIEF RESEARCH REPORT
published: 16 August 2021
doi: 10.3389/fphy.2021.727109

A Narrow-Linewidth Linearly Polarized 1018-nm Fiber Source for Pumping Diamond Raman Laser

Xuezong Yang[1,2]*, *Zhenxu Bai*[3,4], *Huawei Jiang*[2], *Richard P. Mildren*[3] *and Yan Feng*[1,2]

[1]*Hangzhou Institute for Advanced Study, University of Chinese Academy of Sciences, Hangzhou, China,* [2]*Shanghai Institute of Optics and Fine Mechanics, Chinese Academy of Sciences, Shanghai, China,* [3]*MQ Photonics Research Centre, Department of Physics and Astronomy, Macquarie University, Sydney, NSW, Australia,* [4]*Center for Advanced Laser Technology, Hebei University of Technology, Tianjin, China*

A 7.8-GHz linewidth ytterbium-doped fiber (YDF) laser with an output power of 75 W at 1,018 nm is demonstrated based on narrow-bandwidth fiber Bragg gratings. Effective suppression of spectral broadening and amplified spontaneous emission is achieved by optimizing the resonator structure and active fiber parameters. An 1,178-nm diamond Raman output pumped by this narrow-linewidth 1,018 nm source is addressed in this study, which shows a promising application of generating the sodium guide star laser at 589 nm. A single-longitudinal-mode Stokes with an output power of 0.6 W is obtained using this multimode 1,018 nm laser at the pump power of 13 W. The impact of pump spectral linewidth on the effective Raman gain coefficient is analyzed, and the laser threshold of the diamond Stokes resonator increases with the broadening of the pump linewidth.

Keywords: fiber laser, stimulated Raman scattering, second harmonic generation, solid state laser, diamond Raman laser

Edited by:
Zhi-Han Zhu,
Harbin University of Science and Technology, China

Reviewed by:
Shijie Fu,
University of Arizona, United States
Li Fan,
Yangzhou University, China
Hanwei Zhang,
National University of Defense Technology, China

***Correspondence:**
Xuezong Yang
xuezong.yang@ucas.ac.cn

Specialty section:
This article was submitted to Optics and Photonics, a section of the journal Frontiers in Physics

Received: *18 June 2021*
Accepted: *12 July 2021*
Published: *16 August 2021*

Citation:
Yang X, Bai Z, Jiang H, Mildren RP and Feng Y (2021) A Narrow-Linewidth Linearly Polarized 1018-nm Fiber Source for Pumping Diamond Raman Laser. Front. Phys. 9:727109. doi: 10.3389/fphy.2021.727109

INTRODUCTION

High-power 1,018 nm ytterbium-doped fiber (YDF) lasers [1–7] are attractive pump sources. In tandem-pumping configurations, 1,018 nm fiber lasers have been widely harnessed to pump YDF amplifiers and random fiber lasers, due to their advantages of low quantum defect, high beam brightness, and high efficiency. Besides, narrow spectral-linewidth 1,018 nm lasers are of intense interest for many applications in beam combining laser subsystem [8], frequency converted to 509 and 254 nm for laser spectroscopy [9] and atom trapping [10].

A promising application using high-power narrow-linewidth 1,018 nm fiber lasers is as the pump for a diamond Raman laser to generate 1,178 nm output through the first-order diamond Raman shift (39.99 THz). Frequency-doubled 1,178 nm lasers [11, 12] provide a crucial application for the adaptive optics system, acting as sodium laser beacon. The Raman gain profile of the diamond pumped by a single frequency source is a Lorentzian shape with a full-width at half-maximum (FWHM) linewidth of 45 GHz [13]. Pumped with a narrow-linewidth laser, a single-longitudinal-mode (SLM) Stokes output was directly available in a diamond Raman resonator due to the homogeneous Raman gain profile and the absence of spatial hole burning effect [14]. The combination of diamond's ability to rapidly dissipate heat [15] and its gain nature of spatial hole burning free provides a pathway toward high-power SLM lasers. Our recently reported work, where SLM powers of 11.8 W at 1,240 nm and 38 W at 620 nm were achieved in a simple standing-wave diamond Raman frequency-doubling cavity pumped by a 1,064-nm laser with 3.3 GHz linewidth [16], brings forth a promising approach to demonstrate a high-power SLM 589 nm laser by exploiting a narrow-linewidth 1,018 nm pump.

For optical fiber lasers, spectral linewidth broadening, induced by fiber nonlinearity and dispersion [17–20], is the main challenge of generating narrow-linewidth lasers with a high output power. The output spectral linewidth of 1,018 nm emitting with an output power of around 100 W has been still more than 75 GHz [21, 22]. Another main challenge is the amplified spontaneous emission (ASE) at around 1,030 nm due to its higher gain in YDF than that at 1,018 nm. This is understood as follows. In a homogeneously broadened gain medium such as Yb-doped silica fiber, the gain at one wavelength is uniquely determined by the gain at two other wavelengths [23, 24]. Assuming pumping at 976 nm, the ASE gain at 1,030 nm is calculated by, $G^{1030} = 1.41G^{1018} - 0.0324\frac{1}{\beta}G^{976}$ where β is approximately equal to the ratio of fiber core to cladding. Therefore, the ASE gain at 1,030 nm decreases rapidly with increasing the fiber core-to-cladding ratio.

In this article, a linewidth of 7.8 GHz linearly polarized 1,018 nm YDF laser is demonstrated. At a pump power of 118 W, output power of 75 W was achieved corresponding to an optical to optical conversion efficiency of 64%. To the best of our knowledge, this is the narrowest linewidth reported of 1,018 nm fiber laser at this output power level. The 1,018 nm fiber laser was successfully used to generate the first-order Stokes laser at 1,178 nm in a standing-wave diamond Raman resonator. The 1,178 nm output characteristics were also experimentally investigated.

EXPERIMENTAL SETUP

The schematic of experimental setup is shown in **Figure 1**. The 1,018 nm YDF laser is formed with a fiber resonator and a one-stage of YDF amplifier. A 27-W 976-nm laser diode (LD) was coupled into the fiber resonator as the pump through a combiner. The linear fiber resonator consisted of a pair of fiber Bragg gratings (FBGs) and 1.5 m long active fiber. The reflectivities of the high reflecting (HR) and output coupling (OC) FBGs were 98.5 and 17%, respectively. The center wavelengths of two FBGs were both located at about 1,017.9 nm with bandwidths of 0.4 and 0.08 nm, respectively, shown in the inset of **Figure 1**. The active fiber was a large core-to-cladding ratio Yb-doped double-cladding fiber with core and cladding diameters of 15 and 130 μm (LMA-YDF-15/130), and an absorption of 5.40 dB/m at 976 nm. A length of 50 m passive fiber (LMA-GDF-15/130) was fused between the active fiber and OC-FBG in order to increase the optical length of the oscillator. A fast-axis blocked polarization-maintaining (PM) optical isolator was inserted

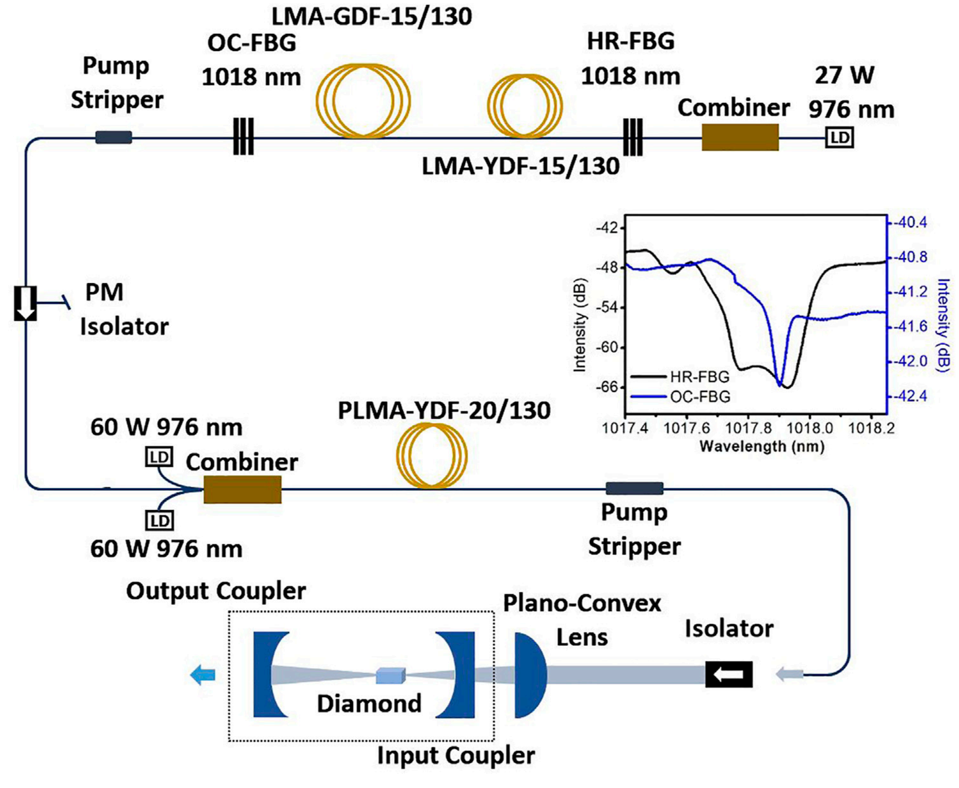

FIGURE 1 | Diagram of 1,018 nm fiber laser and 1,178 nm diamond Raman laser (dotted box). LD: laser diode; PM: polarization maintaining; PLMA: polarized large mode area; YDF: Yb^{3+}-doped fiber; GDF: germanium-doped fiber; HR FBG: highly reflective fiber Bragg grating; OC FBG: output-coupling fiber Bragg grating; 15/130 and 20/130: fiber core diameter of 15 or 20 μm, and a fiber-cladding diameter of 130 μm. The inset is the transmission spectra of HR (black) and OC (blue) FBGs.

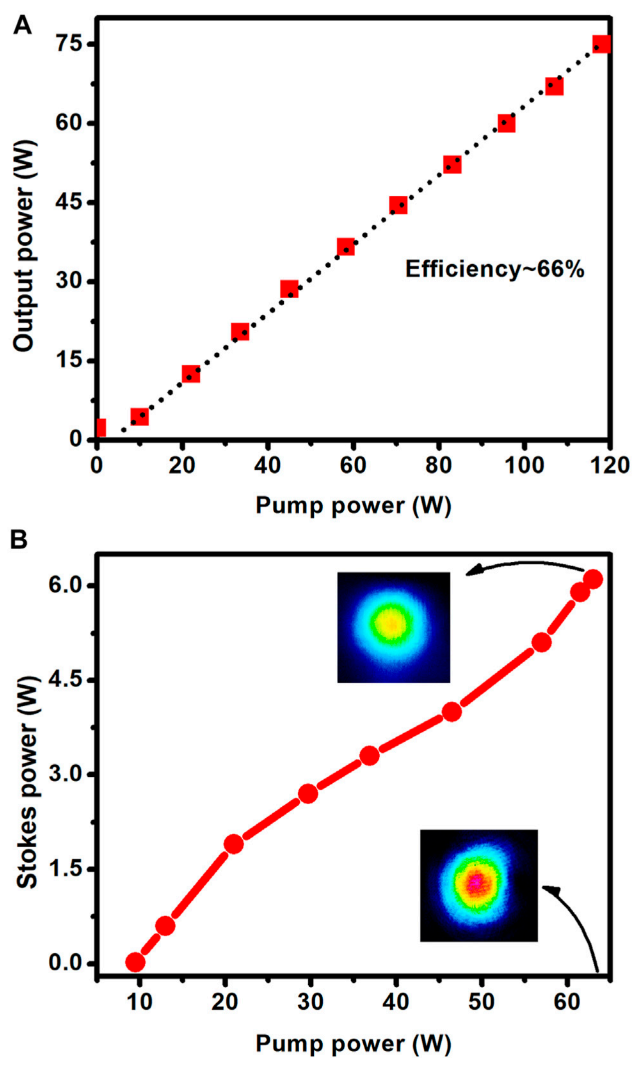

FIGURE 2 | (A) The output power of the fiber amplifier as a function of pump power. **(B)** Measured 1,178 nm Stokes power as a function of the incident pump power; inset: beam profiles for Stokes **(top)** and pump **(bottom)** at the maximum power.

between the resonator and amplifier to enable only slow-axis polarized light passing and prevent the backward feedback into the resonator. In the fiber amplifier, two 60 W 976 nm LDs and a length of 0.9 m with core/cladding diameters of 20/130 μm PM LMA Yb-doped double cladding fiber (10 dB/m at 976 nm) were used to provide the pump and gain, respectively. Two pump strippers were used to remove the residual pump of the resonator and amplifier.

RESULTS AND DISCUSSION

- The 1,018 nm resonator was an all non-PM fiber connected linear structure. The length of active fiber was optimized to 1.5 m. The fast-axis blocked isolator acting as a polarizer enabled a linearly polarized output. The output power of the

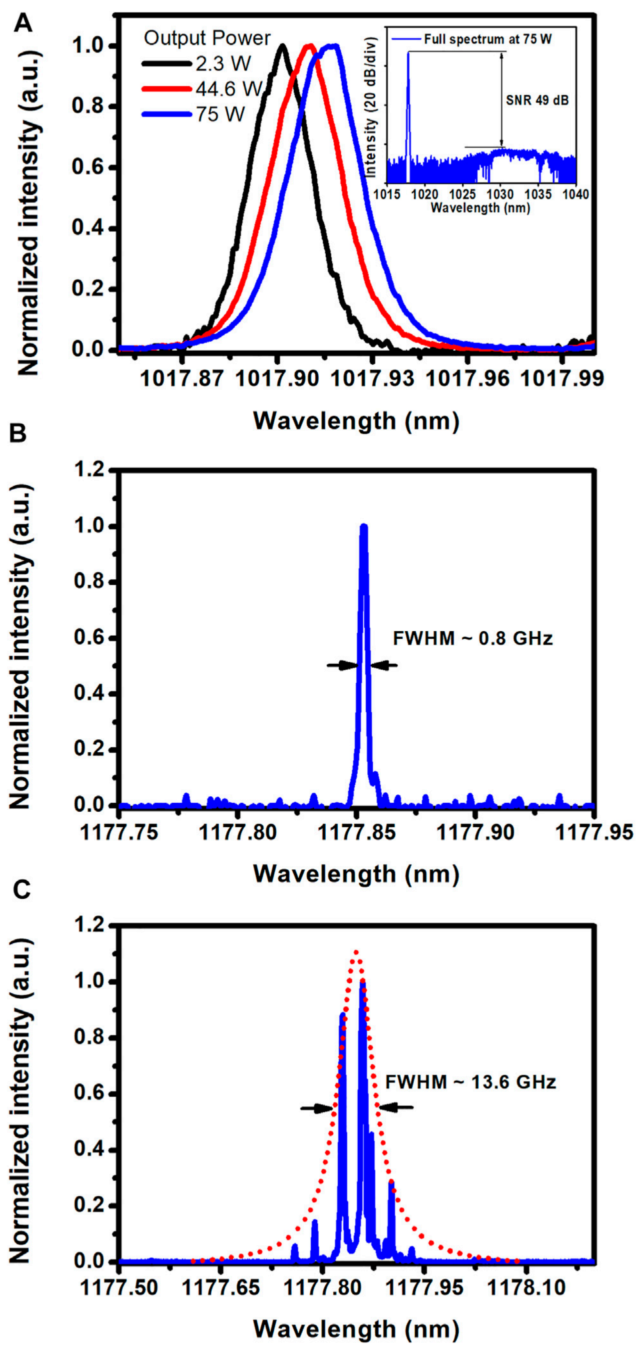

FIGURE 3 | (A) Output spectra of the 1,018 nm fiber laser at the output power of 2.3, 44.5, and 75 W; inset: a broad output spectrum at the output power of 75 W. **(B)** An SLM Stokes spectrum at the output powers of 0.6 W. **(C)** The Stokes spectrum at the output powers of 6.1 W; The Lorentzian curve of the Stokes spectrum (dotted red).

1,018 nm seed laser was measured after the PM isolator. The threshold was about 1.5 W, and the output power increased to 2.6 W at the pump power of 11.8 W. **Figure 2A** depicts the output power of the amplifier as a function of pump power. When the pump power increased up to 118 W, the

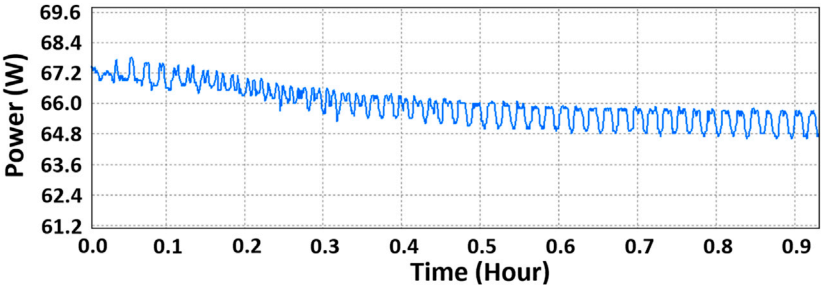

FIGURE 4 | Output power stability evolution of the 1,018 nm fiber laser after the free-space isolator.

output power of 75 W was achieved corresponding to an optical-to-optical conversion efficiency of 64%. The maximum output power was limited by the available pump power. The output polarization extinction ratio was only about 12 dB at the output power of 75 W due to the insufficient polarization extinction ratio of the PM isolator.

- The output spectra of the 1,018 nm laser were analyzed using a spectrometer (HF-8997-2, LightMachinery; resolution of 0.8 GHz) equipped with an InGaAs camera. As is shown in **Figure 3A**, the spectrum of the seed laser was centered at 1,017.90 nm and had a FWHM linewidth of 6.6 GHz. The longitudinal mode spacing of the seed laser spectrum was about 1.9 MHz, corresponding to an oscillator length of about 53 m. The narrow spectral linewidth was generated by exciting partial longitudinal modes within the FBG reflection bandwidth due to a low-power pumping. In order to suppress spectral broadening and ASE, the length of the large core-cladding ratio gain fiber (PLMA 20/130) in the amplifier was shortened to 0.9 m. The spectral FWHM linewidth was slightly broadened from 6.6 to 7.8 GHz as the output power was increased from 2.3 to 75 W, as shown in **Figure 3A**. The slight redshift of central wavelength was observed due to the thermal induced refractive index decrease of the silica fiber. A broad spectrum at output power of 75 W was measured using an optical spectrum analyzer (YOKOGAWA, AQ6370B) with a resolution of 0.02 nm. The inset in **Figure 3A** depicts that the signal-to-noise ratio (SNR) between 1,018 and 1,030 nm was 49 dB, indicating excellent suppression of the ASE.
- A FBG resonator-based fiber laser usually has a temporal profile with high intensity fluctuation due to longitudinal modes beating. The intensity fluctuations of the pump laser is transferred to the stimulated Raman scattering process due to the short response time [25]. The resonator consists of a spool of 50 m passive fiber to decrease the longitudinal mode spacing and thus increase the number of longitudinal modes. Due to the longitudinal modes with random phases, the intensity fluctuations caused by modes beating decreased with the increase of the number of modes. The amplified 1,018 nm laser was collimated by a commercial pigtailed collimator which delivered an output beam diameter of 1.3 mm.
- The collimated continuous-wave (CW) 1,018 nm laser was injected into a standing-wave diamond Raman cavity after passing through a free-space isolator and a plano-convex focusing lens (f = 50 mm), shown in the dotted box in **Figure 1**. The output power evolution of the pump laser, measured after the free-space isolator, in about 1 h is shown in **Figure 4**. The starting power was 67.4 W, corresponding to a total loss of 10% that resulted from the collimator and isolator. The output power decreased slowly from 67.4 to 65.4 W in the first half hour, during which the laser diode and the gain fiber of the amplifier reached thermal stability. In the next half hour, the average output power stabilized at about 65.4 W. Note that there were periodic power fluctuations, due to the slow variation of the polarization state of the non-PM fiber seed oscillator. In a non-PM fiber, the state of the polarization is sensitive to the fiber birefringence which varies with temperature, pressure, and mechanical disturbances [26, 27]. The periodic variation (~1.8 min) of the polarization state is likely to result from the periodic temperature fluctuation of the water chiller. One solution to the power fluctuations is to substitute the seed laser with an all-PM fiber oscillator.
- The diamond Raman resonator consisted of two plano-concave mirrors as the input coupler and output coupler, respectively. The input coupler with 50 mm radius curvature was highly transmissive (>98%) at 1,018 nm and highly reflective (>99.9%) at 1,178 nm. The OC had a 100-mm radius of curvature, was highly reflective (>99.9%) at 1,018 nm, and provided approximately 0.1% transmission at 1,178 nm. The diamond (Element Six Ltd., low-birefringence, low-nitrogen, CVD-grown single crystal) with dimensions of 8 mm × 4 mm × 1.2 mm was inserted at the waist of the near-concentric resonator.

The output power of 1,178 nm Stokes is plotted in **Figure 2B** as a function of the incident 1,018 nm pump power. The threshold was 9.3 W, beyond which the 1,178 nm output only attained power of 6.1 W at the incident pump power of 63 W since the transmittance of the OC at 1,178 nm was only 0.1%. The effective Raman gain coefficient g_{eff} is proportional to $g_0\omega_R/(\omega_R + \omega_P + \omega)$, where g_0 is the Raman gain coefficient, and ω_R, ω_P, and ω are the FWHM linewidths of Raman gain profile, pump, and Stokes, respectively [28]. Therefore, a pump with much narrower linewidth than Raman gain profile (e.g., $\omega_P \ll$ 45 GHz) is required to achieve a highly effective Raman gain coefficient. In order to further investigate the impact of pump linewidth on effective Raman gain and thus the threshold of diamond Raman laser, a second pump laser with a linewidth of 20 GHz was employed. The calculated g_{eff} for a pump linewidth of 7.8 GHz is approximately 16% higher than for a 20 GHz pump, assuming that ω_R is 45 GHz and Stokes linewidth of ω is neglected at threshold. The laser threshold for the broad bandwidth laser was 11.4 W and 22.5% higher than that for the 7.8 GHz pump.

- The beam profiles of pump and Stokes at maximum power are included in **Figure 2B**, which depicts an evidence of beam cleaning during stimulated Raman scattering in diamond [29]. **Figure 3B** shows the evolution of Stokes output spectrum through SLM to multi-longitudinal modes with the increasing of pump power due to the thermal drift in cavity length and nonlinear spectral broadening. Those spectra were measured by using a cavity mode–spacing resolved spectrometer (HF-8997-2, LightMachinery). **Figure 3B** shows an SLM spectrum with an output power of 0.6 W at the pump power 13 W, and the FWHM bandwidth is 0.8 GHz, which is the limitation of the spectrometer resolution. At the highest output power of 6.1 W, a multi-longitudinal mode Stokes spectrum was observed with a Lorentzian FWHM linewidth of 13.6 GHz, as shown in **Figure 3C**.

CONCLUSION

In summary, a high-power linearly polarized 1,018 nm fiber laser with 7.8 GHz linewidth is demonstrated based on a pair of narrow-bandwidth FBGs. The highest output power was 75 W, corresponding to an optical efficiency of 64%, and the spectral trace had a contrast of approximately 49 dB against the noise floor. One of the important applications for a narrow-linewidth 1,018 nm laser is to pump a diamond Raman laser for generating the first-order Stokes at 1,178 nm which can be frequency doubled to 589 nm for a sodium guide star laser. Here, the 1,018 nm fiber laser was successfully utilized in a standing-wave diamond Raman cavity to generate a power of 6.1 W and near-diffraction limit 1,178 nm output. And the spectral evolution of Stokes from a single mode to multimodes with the increase of pump power was observed.

DATA AVAILABILITY STATEMENT

The raw data supporting the conclusions of this article will be made available by the authors, without undue reservation.

AUTHOR CONTRIBUTIONS

All authors listed have made a substantial, direct, and intellectual contribution to the work and approved it for publication.

FUNDING

This work was funded by the National Natural Science Foundation of China (62005073) and the Natural Science Foundation of Hebei Province (F2020202026).

ACKNOWLEDGMENTS

We are thankful for the support from Key Laboratory of OptoElectronic Information Technology, Ministry of Education (Tianjin University).

REFERENCES

1. Stiles E. New Developments in IPG Fiber Laser Technology. *Presented in 5th International Workshop on Fiber Lasers*. Germany: Dresden (2009).
2. Zhu J, Zhou P, Ma Y, Xu X, and Liu Z. Power Scaling Analysis of Tandem-Pumped Yb-Doped Fiber Lasers and Amplifiers. *Opt Express* (2011) 19: 18645–54. doi:10.1364/oe.19.018645
3. Du X, Zhang H, Xiao H, Zhou P, and Liu Z. Temporally Stable Random Fiber Laser Operates at 1070 Nm. *IEEE Photon J.* (2015) 7:1–7. doi:10.1109/JPHOT.2015.2477279
4. Yu W, Xiao Q, Wang L, Zhao Y, Qi T, Yan P, et al. 2196 W Large-Mode-Area Er:Yb Codoped Fiber Amplifier Operating at 1600 Nm Pumped by 1018 Nm Fiber Lasers. *Opt Lett* (2021) 46:2192–5. doi:10.1364/OL.424368
5. Yan P, Wang X, Li D, Huang Y, Sun J, Xiao Q, et al. High-power 1018 Nm Ytterbium-Doped Fiber Laser with Output of 805 W. *Opt Lett* (2017) 42: 1193–6. doi:10.1364/OL.42.001193
6. Xiao H, Zhou P, Wang XL, Xu XJ, and Liu ZJ. High Power 1018 Nm Ytterbium Doped Fiber Laser with an Output Power of 309 W. *Laser Phys Lett* (2013) 10: 065102. doi:10.1088/1612-2011/10/6/065102
7. Zhou P, Xiao H, Leng J, Xu J, Chen Z, Zhang H, et al. High-power Fiber Lasers Based on Tandem Pumping. *J Opt Soc Am B* (2017) 34:A29–A36. doi:10.1364/JOSAB.34.000A29
8. Khitrov V, Farley K, Leveille R, Galipeau J, Majid I, Christensen S, et al. kW Level Narrow Linewidth Yb Fiber Amplifiers for Beam Combining. *SPIE Defense, Security, and Sensing*, 8. Bellingham WA: SPIE (2010). doi:10.1117/12.862648
9. Rye HS, Yue S, Wemmer DE, Quesada MA, Haugland RP, Mathies RA, et al. Stable Fluorescent Complexes of Double-Stranded DNA with Bis-Intercalating Asymmetric Cyanine Dyes: Properties and Applications. *Nucl Acids Res* (1992) 20:2803–12. doi:10.1093/nar/20.11.2803
10. Villwock P, Siol S, and Walther T. Magneto-optical Trapping of Neutral Mercury. *Eur Phys J D* (2011) 65:251–5. doi:10.1140/epjd/e2011-20064-9
11. Feng Y, Taylor LR, and Calia DB. 25 W Raman-Fiber-Amplifier-Based 589 Nm Laser for Laser Guide star. *Opt Express* (2009) 17:19021–6. doi:10.1364/oe.17.019021
12. Yang X, Zhang L, Cui S, Fan T, Dong J, and Feng Y. Sodium Guide star Laser Pulsed at Larmor Frequency. *Opt Lett* (2017) 42:4351–4. doi:10.1364/ol.42.004351
13. Mildren RP. *Intrinsic Optical Properties of Diamond*. Wiley-VCH, Wiley (2013). doi:10.1002/9783527648603.ch1
14. Lux O, Sarang S, Kitzler O, Spence DJ, and Mildren RP. Intrinsically Stable High-Power Single Longitudinal Mode Laser Using Spatial Hole Burning Free Gain. *Optica* (2016) 3:876–81. doi:10.1364/optica.3.000876
15. Bai Z, Zhang Z, Wang K, Gao J, Zhang Z, Yang X, et al. Comprehensive Thermal Analysis of Diamond in a High-Power Raman Cavity Based on

FVM-FEM Coupled Method. *Nanomaterials* (2021) 11:1572. doi:10.3390/nano11061572

16. Yang X, Kitzler O, Spence DJ, Williams RJ, Bai Z, Sarang S, et al. Single-frequency 620 Nm diamond Laser at High Power, Stabilized *via* Harmonic Self-Suppression and Spatial-hole-burning-free Gain. *Opt Lett* (2019) 44: 839–42. doi:10.1364/ol.44.000839
17. Babin SA, Churkin DV, Ismagulov AE, Kablukov SI, and Podivilov EV. Spectral Broadening in Raman Fiber Lasers. *Opt Lett* (2006) 31:3007–9. doi:10.1364/ol.31.003007
18. Kablukov SI, Zlobina EA, Podivilov EV, and Babin SA. Output Spectrum of Yb-Doped Fiber Lasers. *Opt Lett* (2012) 37:2508–10. doi:10.1364/OL.37.002508
19. Soh DBS, Koplow JP, Moore SW, Schroder KL, and Hsu WL. The Effect of Dispersion on Spectral Broadening of Incoherent Continuous-Wave Light in Optical Fibers. *Opt Express* (2010) 18:22393–405. doi:10.1364/oe.18.022393
20. Liu W, Miao Y, Ma P, Zhou P, and Jiang Z. Theoretical Study of Narrow-Linewidth Hybrid Rare-Earth-Raman Fiber Amplifiers. *Opt Express* (2019) 27: 14523–35. doi:10.1364/oe.27.014523
21. Jiang M, Zhou P, Xiao H, and Ma P. A High-Power Narrow-Linewidth 1018 Nm Fiber Laser Based on a Single-Mode-Few-Mode-Single-Mode Structure. *High Pow Laser Sci Eng* (2015) 3:e25. doi:10.1017/hpl.2015.24
22. Midilli Y, Efunbajo OB, şimşek B, and Ortaç B. 1018 Nm Yb-Doped High-Power Fiber Laser Pumped by Broadband Pump Sources Around 915 Nm with Output Power above 100 W. *Appl Opt* (2017) 56:7225–9. doi:10.1364/ao.56.007225
23. Palma-Vega G, Walbaum T, Heinzig M, Kuhn S, Hupel C, Hein S, et al. Ring-up-doped Fiber for the Generation of More Than 600 W Single-Mode Narrow-Band Output at 1018 Nm. *Opt Lett* (2019) 44:2502–5. doi:10.1364/OL.44.002502
24. Nilsson J, Minelly JD, Paschotta R, Tropper AC, and Hanna DC. Ring-doped Cladding-Pumped Single-Mode Three-Level Fiber Laser. *Opt Lett* (1998) 23: 355–7. doi:10.1364/ol.23.000355
25. Krause M, Cierullies S, Renner H, and Brinkmeyer E. Pump-to-Stokes RIN Transfer in Raman Fiber Lasers and its Impact on the Performance of Co-pumped Raman Amplifiers. *Opt Commun* (2006) 260:656–61. doi:10.1016/j.optcom.2005.10.077
26. Ulrich R. Polarization Stabilization on Single-mode Fiber. *Appl Phys Lett* (1979) 35:840–2. doi:10.1063/1.90999
27. Kidoh Y, Suematsu Y, and Furuya K. Polarization Control on Output of Single-Mode Optical Fibers. *IEEE J Quan Electron.* (1981) 17:991–4. doi:10.1109/JQE.1981.1071206
28. Sabella A, Spence DJ, and Mildren RP. Pump-Probe Measurements of the Raman Gain Coefficient in Crystals Using Multi-Longitudinal-Mode Beams. *IEEE J Quan Electron.* (2015) 51:1–8. doi:10.1109/JQE.2015.2503404
29. Bai Z, Williams RJ, Jasbeer H, Sarang S, Kitzler O, McKay A, et al. Large Brightness Enhancement for Quasi-Continuous Beams by diamond Raman Laser Conversion. *Opt Lett* (2018) 43:563–6. doi:10.1364/OL.43.000563

Conflict of Interest: The authors declare that the research was conducted in the absence of any commercial or financial relationships that could be construed as a potential conflict of interest.

frontiers
in Physics

REVIEW
published: 14 September 2021
doi: 10.3389/fphy.2021.747272

Developments of Picosecond Lasers Based on Stimulated Brillouin Scattering Pulse Compression

Chen Cao[1,2], Yulei Wang[1,2], Zhenxu Bai[1,2,3], Yunfei Li[1,2], Yu Yu[1,2] and Zhiwei Lu[1,2]*

[1]Center for Advanced Laser Technology, Hebei University of Technology, Tianjin, China, [2]Hebei Key Laboratory of Advanced Laser Technology and Equipment, Tianjin, China, [3]MQ Photonics Research Centre, Department of Physics and Astronomy, Macquarie University, Sydney, NSW, Australia

Pulse compression based on stimulated Brillouin scattering (SBS) is a nonlinear optical approach that efficiently converts high-energy nanosecond pulses into the picosecond. Since the first observation of SBS pulse compression, different compression structures for different input and output parameters were developed to optimize the characteristics of pulse compression in the past decades. Here, a comprehensive review of the development status of SBS pulse compression schemes is provided, meanwhile, methods and trends to the optimization of SBS pulse compression are proposed.

Keywords: stimulated Brillouin scattering, pulse compression, high energy, picosecond, structure

Edited by:
Zhi-Han Zhu,
Harbin University of Science and Technology, China

Reviewed by:
Wei Gao,
Harbin University of Science and Technology, China
Yanping Xu,
Shandong University, China
Xing Fu,
Tsinghua University, China

****Correspondence:***
Yulei Wang
wyl@hebut.edu.cn

Specialty section:
This article was submitted to Optics and Photonics, a section of the journal Frontiers in Physics

Received: *26 July 2021*
Accepted: *30 August 2021*
Published: *14 September 2021*

Citation:
Cao C, Wang Y, Bai Z, Li Y, Yu Y and Lu Z (2021) Developments of Picosecond Lasers Based on Stimulated Brillouin Scattering Pulse Compression. Front. Phys. 9:747272. doi: 10.3389/fphy.2021.747272

INTRODUCTION

High-energy picosecond pulse lasers have attracted significant attention for their extensive and important applications, such as satellite laser ranging [1–3], laser processing [4–6], and medical laser treatment [7, 8]. In the field of satellite laser ranging, ultra-high-precision remote ranging can be achieved using picosecond lasers. For example, measurement of the distance between the earth and the moon [9], the geosynchronous orbit satellite with ranging accuracy of sub-centimeter [10], and BeiDou navigation satellite system with single ranging accuracy of 8.5 mm [11]. For laser processing, due to the shorter pulse duration compared to that of the nanosecond, picosecond lasers can effectively inhibit the formation of heat-affected zones, realizing higher precision in processing materials. In addition, the higher peak power density can greatly improve the material removal rate and the quality of the burnt surface while the material is surface-textured [12–14]. Mode-locking is the most common approach to generate picosecond pulses, which demonstrates extremely low single pulse energy (~nJ to μJ) [15–18]. Q-switching is another method to generate short pulses, but it is difficult to obtain pulses narrower than 300 ps due to the limitation of cavity length and switching speed [19–22]. Even though picosecond pulses can be achieved via mode-locking and Q-switching techniques, the lower power amplification efficiency induced by the short pulse duration limits their applications. Namely, the generation of picosecond pulses with high-energy directly from laser cavities and amplifiers is still a challenge.

Nonlinear optics technique provides another approach to control the temporal and spatial modes of pulses exiting a laser system. Among them, stimulated Brillouin scattering (SBS) [23], one of the strongest nonlinear light-matter interactions occurring in transparency media, has been widely studied for converting the temporal mode into a shorter one, or rather, pulse compression [24]. Today, many laser systems for high-energy picosecond pulses are realized by using pulse compression based on SBS. A key advantage of the SBS technique is generating time-reversal beam at the Stokes frequency, thus, some SBS compressors are also called SBS phase conjugate mirrors (SBS-PCMs). By appropriately using SBS-PCMs, except for realizing picosecond pulses, one can also compensate wavefront distortions caused by optical elements during laser transmission and amplification processes, leading to a higher beam quality output [25, 26]. For this reason, today, the combination of SBS-PCMs and master oscillator power amplifier (MOPA) is a common method to achieve high peak power, high beam quality, and narrow pulse width lasers [27]. Although showed that the distortion with vortex wavefront will lead to the input "donut-like" pump pluses into peta-like Stokes pluses [28], SBS is always the most effective phase conjugation method for conventional lasers with the fundamental (i.e., TEM_{00}) spatial mode.

SBS-based beam amplification technology, or named stimulated Brillouin amplification (SBA), is another effective method to obtain high-energy pulses. In this "three-wave" mixing process, the energy in the pump wave is transferred to a pre-prepared and counter-propagating Stokes wave, and parametrically generating an acoustic wave to hold the energy conservation. Compared with nonlinear crystals for optical parametric amplification (OPA), SBS media, usually are liquids, can provide a much higher limitation on the power loading. Therefore, energy of up to tens of joules can be obtained through the "beam splitting-amplification-beam combination" method [29–31]. Additionally, optical limiters, a technique for transmitting a low-intensity beam, made by SBS technology have also been widely used in high-power lasers, which can effectively protect optical elements and improve the stability of the laser system [32, 33]. Especially, based on SBS pulse compression has been demonstrated to be an effective method to convert nanosecond long pulses into picosecond short pulses due to the advantages of low cost, simple operation, and high efficiency. High-power short-pulse with peak power of ~GW and pulse width of hundreds of picoseconds can be obtained through this technology [34, 35].

Besides, driven by the recent advances in the field of structured light during the last two decades, generation and application of laser beams or pulses with high-order (scalar and vector) spatial modes have gained increasing attention [36, 37]. Although the study on shaping light's spatial modes via nonlinear interactions can be traced back to the dawn of the field [38], the SBS involves structured light was theoretically considered until the last decade and only explored experimentally in recent years, yet demonstrating a series of impressive results [28, 39–44]. For years, detailed research works on SBS-based pulse compression technology had been hotly pursued by several groups. Although many overviews on the research progress of SBS media have been reviewed, there are few reports on summarizing the structures of SBS pulse compressors [45, 46]. In this paper, recent research progress using different SBS pulse compression structures for picosecond pulse generation were reviewed. Meanwhile, both the advantages and disadvantages of different structures were compared and analyzed. Finally, the optimized pulse compression structure that can be applied in the future was proposed, which provided a reference for the development of a high-energy laser.

PRINCIPLE OF PULSE COMPRESSION TECHNOLOGY BASED ON STIMULATED BRILLOUIN SCATTERING

SBS is a physical process of three-wave coupling formed by the interaction of strong light and matter. The physical process of SBS is depicted in **Figure 1A**. The backward propagating Stokes beam is generated by the interaction of the high-intensity pump and the medium under the periodically changing acoustic grating. Then the Stokes is continuously amplified with time by the scattering effect of the acoustic grating on the pump. The process shows the characteristics of high-efficient pulse compression by the energy transfer from the pump to Stokes directly with the peak power density greatly enhanced. However, it should be noted that the efficiency of the energy transfer process (pulse compression process) will be affected by many factors, for example, the interaction length of the pump and Stokes beams. Too short interaction length will lead to low pulse compression efficiency and low energy conversion efficiency. However, too long interaction length can also result in negative effects including tail modulation and pulse width broadening. Therefore, choosing an appropriate interaction length is critical to realize high-efficiency SBS pulse compression with high quality. The electrostriction effect produced by the polarization of the molecules in the medium causes the change of refractive index or density. Then, pump light is scattered by periodically changing density fluctuations which are also called moving gratings and its transmission direction is changed, enhancing the intensity of backward propagating Stokes light.

The diagram of the SBS-based pulse compression is shown in **Figure 1B**. The leading edge of the backward-propagating Stokes light meets the forward-propagating pumping light firstly. The energy of the pump light is transferred to the Stokes light through the phonon field vibrated in the three-wave coupling process. At this moment, the leading edge of Stokes light is magnified and the trailing edge remains unchanged. Because the energy of the pump light has almost been exhausted by the leading edge of Stokes light, and it has almost no amplification ability when it meets the trailing edge. This process is manifested as the steepening of the leading edge of the Stokes light waveform and the narrowing of the overall pulse width of the laser pulse, which is the so-called pulse compression technology. A large number of research groups have carried out exploration works for pulse compressors based on stimulated Raman scattering (SRS) and SBS [47–61]. Maier et al. and Chiao et al. successfully observed backward Raman scattering caused by forwarding Stokes radiation scattering and Brillouin scattering, which was based on noise [47, 61]. In 1972, Stolen et al. achieved the SRS-based pulse compression in glass optical waveguide for the first time [53].

REASERCH PROGRESS OF STIMULATED BRILLOUIN SCATTERING PLUSE COMPRESSORS

Tapered Waveguide

In the early stage, most of the pulse compression based on SBS was fulfilled in tapered waveguides. In 1980, Hon et al. for the first time realized the SBS pulse compression in a tapered waveguide filled with methane at a pressure of 130 atm [60]. **Figure 2** illustrates the basic structure of the tapered waveguide pulse compressor [62]. In such a tapered fiber, the Stokes light is

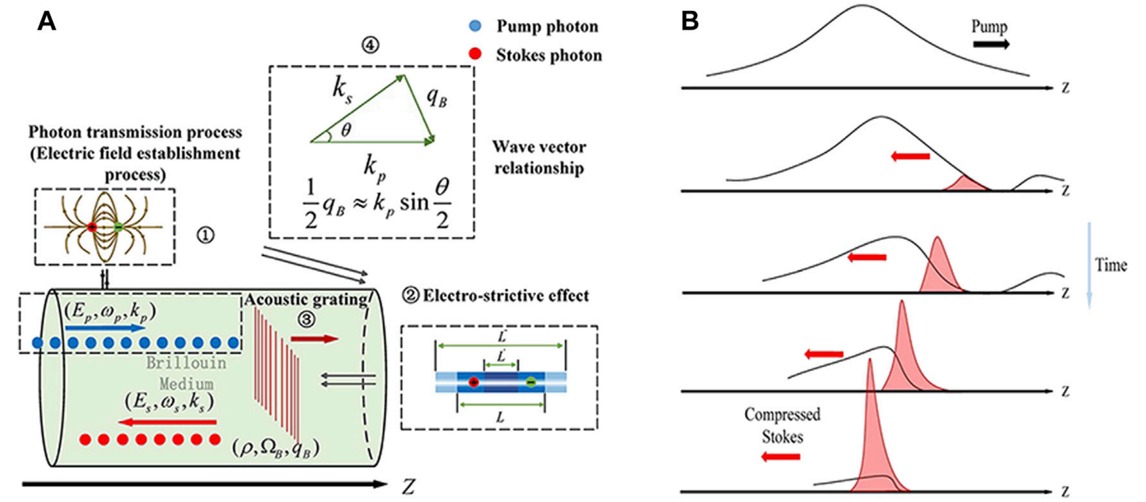

FIGURE 1 | (A) The physical process of SBS, **(B)** Principle diagram of pulse compression based on SBS.

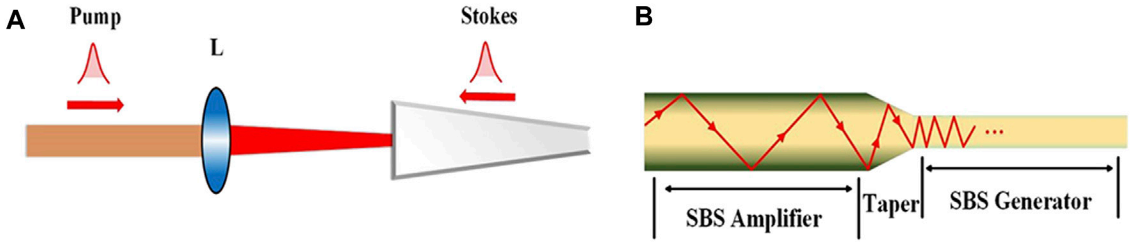

FIGURE 2 | Schematic diagram of tapered waveguide. **(A)** Tapered waveguide pulse compressor, **(B)** Schematic diagram of tapered waveguide structure [62].

first generated in the smaller core of the generator section and the main power reflection takes place in the amplifier. With this specific structure, the SBS gain is enhanced due to the smaller diameter of the optical fiber in the SBS generator. During the tapering process, both the length and angle of the taper can be controlled to obtain optimal results for a given system. For instance, a longer tapered region can effectively decrease the power coupling loss between the generator and the amplifier [63]. However, although this structure has a lower SBS threshold, it cannot be applied in SBS pulse compression experiments with high energy peak power due to the limitations of fiber material [127]. Therefore, more universal structures are required for pulse compression.

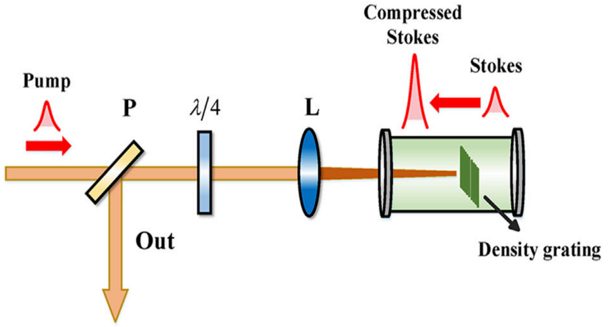

FIGURE 3 | Schematic diagram of focusing single cell structure.

Focusing Single Cell

Compared with tapered waveguide, lens focusing structure has advantages of high stability and lower cost. In the 1980s, the focusing single-cell structure was first proposed by Damzen et al., and the basic structure was shown in **Figure 3**. They obtained the compressed pulse with a width of 4 ns in methane [64]. Since then, a large number of groups have used the structure to perform compression in different media [65–73] (as shown in **Table 1**). For instance, Kmetik et al. compressed the pulse width from 10 to 0.9 ns with an energy of 0.57 J in ultra-filtered FC-75 liquid medium and obtained up to 94% energy reflectivity [71]. Yoshida et al. proved for the first time that a 1,064 nm pump pulse and its second harmonic (532 nm), third harmonic (335 nm), and fourth harmonic (266 nm) could be compressed to hundreds of picoseconds based on a single-cell structure that demonstrated over 80% energy [72, 73]. The above two experimental results prove that due to the advantages of

TABLE 1 | Typical experimental results in single cell structure.

Author (Year)	Medium	Pump pulse width/ns	Compressed pulse width/ns	Output energy/mJ	Energy efficiency
Damzen et al. (1983) [62]	Methane	27	4	10	70%
Gorbunov et al. (1983) [64]	Ar	20	1	500	80%
Tomov et al. (1985) [65]	Freon−12	25	1.5	180	35%
Buzyalis et al. (1985) [67]	Carbon tetrachloride	12	0.7	1	\
Davydov et al. (1986) [68]	Carbon tetrachloride	30	1.2	40	90%
Kmetik et al. (1998) [70]	FC-75	10	0.9	570	94%
Yoshida et al. (2004, 2007) [71, 72]	Fused Silica	8	1	1,000	40%, 95%

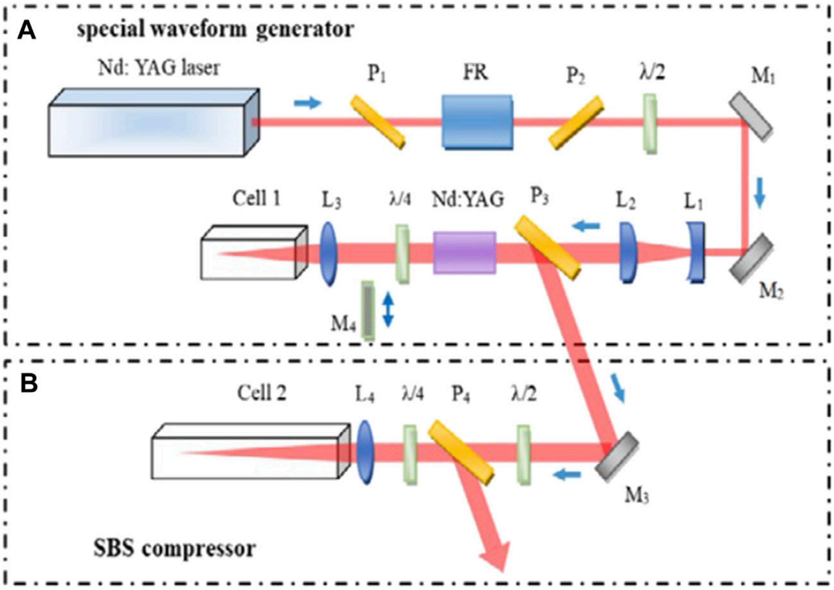

FIGURE 4 | Schematic diagram of experimental setup: **(A)** special waveform generator, **(B)** single-pass SBS compressor [74].

compact structure and easy adjustment, using the focusing single cell is easy to obtain high energy reflectivity. In 2016, Liu et al. conducted comparative experiments on pulse compression of pump light with different waveforms, and the results showed that the pulse width of the step pulse could be compressed to half of the phonon lifetime with a single-cell with energy efficiency exceeding 65%. The schematic diagram of the experimental device is shown in **Figure 4** [74]. Bai et al. developed a picosecond laser with <450 ps pulse width and single pulse energy of 400 mJ by combining MOPA with SBS pulse compression [75]. In 2018, Liu et al. applied a single-cell structure based on an interferometric scheme to break through the pulse compression limit (the phonon lifetime of the medium). They obtained a compressed pulse output of $0.36\tau_B$ with energy efficiency of 65% in FC-3283, and a compressed pulse output of $0.12\tau_B$ with energy efficiency of 40% in Acetone, which was close to one-tenth of the phonon lifetime [76].

The focusing single-cell structures have the advantages of simple structure and easy operation. However, with the increasing of injected energy, the low load capacity of this structure will lead to the phenomena of optical breakdown, hindering the generation of Stokes seed light in severe cases. Therefore, the single-cell structure is mostly used in small and low-energy commercial laser systems. Piskarskas et al. theoretically analyzed the space-time characteristics of the Stokes beam formed when the pump light intensity was unevenly distributed in spatial cross-sectional. They proposed that the two-cell generator-amplifier setup should be preferred to realize a compression ratio higher than 10 [77].

Focusing Two-Cell Structure

To overcome the shortcomings of the focusing single-cell structure, the two-cell structure was introduced to separate the compression part and the generating part of the original single cell into two independent cells. The design enables the control of the energy which is injected into the generator, thereby improving the load capacity and stability of the entire system. In addition, the interaction length between pump light and Stokes seed light is increased, which is beneficial to obtain a high compression ratio.

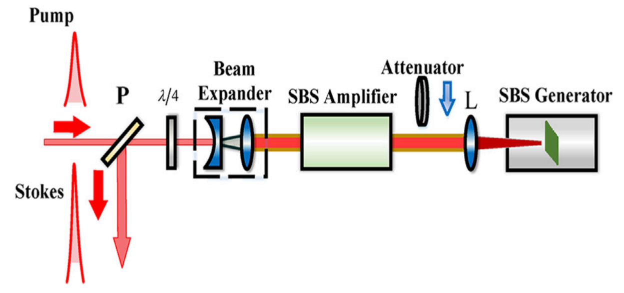

FIGURE 5 | Schematic diagram of compact two-cell structure.

Compact two-cell and independent two-cell are the two most used structures.

Compact Two-Cell

Figure 5 illustrates the schematic diagram of a compact two-cell structure. In general, an attenuator is placed in front of the focusing lens to reduce the energy entering the generator, or a beam expander system is placed in front of the amplifier to reduce the intensity of the pump pulse. This is to avoid irreversible damage to components caused by optical breakdown. Schiemann et al. conducted compression experiments in three liquid media: water, methanol, and carbon tetrachloride. The minimum pulse width of 270 ps (central part of the beam) was obtained with a reflectivity of 75% [78].

In recent years, great breakthroughs have been made in pulse compression ratio and energy efficiency [79–89] (as shown in **Table 2**). Yoshida et al. compressed the pulse width from 13 to 160 ps with a central wavelength of 1,064 nm in an FC-40 liquid medium. The beam brightness was increased by nearly 65 times, and the highest energy efficiency exceeded 80% without optical breakdown (the experimental setup is shown in **Figure 6**) [84]. Wang et al. proposed a new type of cyclic compact two-cell structure for realizing SBS-PCM with a high-energy and high-repetition rate. Energy reflectivity of 84.7% was obtained with an incident energy of 1.1 J at a repetition rate of 10 Hz [79]. Hasi et al. compressed the 10 ns to 116 ps in different perfluorocarbon liquid media, generating the single pulse energy over several hundred millijoules with energy reflectivity over 80% [80, 81, 85].

In 2015, Wang et al. proposed an interferometric scheme to generate standing waves in the focal area to improve energy stability. The pulse was compressed from 8 ns to 393 ps with a single pulse energy of 40 mJ with high stability [87, 88]. In 2017, Bai et al. achieved picosecond ultraviolet (355 nm) output with compact two-cell structure. The pulse width was compressed from 6.3 ns to 168 ps with an output energy of 100 mJ and the energy efficiency of about 35% [89]. In 2019, Wang et al. obtained a short pulse of 820 ps at kHz repetition rate in HT270 liquid medium with energy efficiency of 52.2% for the first time [90].

Due to the advantages of higher load capacity and longer effective interaction length, the compact two-cell structure can obtain shorter pulse width and higher energy efficiency with different SBS active media. But the energy stability becomes worse with the increase of pump energy, which is similar to the focusing single cell structure. Controlling energy through the attenuator also has several defects, such as low energy efficiency and adjustment accuracy. In 2006, Mitra et al. proposed a new type of "one-cell, dual-purpose" compact two-cell structure [91]. Their results show that more than 90% energy efficiency can be obtained with the pulse width close to 1 ns at the injected energy reaching above 1-J level without inserting an attenuator. The minimum pulse duration of 600 ps could be obtained when the attenuation was 45%, while the energy efficiency was only 55%. Kmetik et al. designed the compact dual-cell compressor which was applied to the GEKKO-XII laser device, realizing high-energy pulse compression with a large-diameter laser system [92]. The pulse was compressed from 13 ns to 600 ps at the output energy up to 30 J approximately with the low energy efficiency. Therefore, the compact two-cell structure is unsuitable to be applied in the situation of high energy. At this time, an independent two-cell structure was proposed which could flexibly adjust the injected energy of two-cell, respectively.

Independent Two-Cell

The independent two-cell structure is actually a kind of light splitting structure, which divides the pump light into two parts: seeding pump light and amplifying pump light (as shown in **Figure 7**). The utilizing of optical elements such as waveplates and polarizers can flexibly control the meeting position, meeting time, and intensity ratio of the two beams. The structure effectively improves the load capacity of the entire system under high energy. In 1984, Fedosejevs et al. first proposed an independent two-cell structure and using KrF laser to compress long pulses from 24 ns to 440 ps with the energy efficiency of about 40% [93, 94].

Compared with other structures, the obvious advantage of the independent two-cell structure is adjusting the pulse intensity in the two cells arbitrarily, resulting in avoiding nonlinear effects such as an optical breakdown. In the follow-up research, more detailed research and optimization of the optical path structure

TABLE 2 | Typical experiments of compact two-cell structure.

Author (Year)	Medium	Pump pulse width/ns	Compressed pulse width/ns	Output energy/mJ	Energy efficiency (%)
I.Daito et al. (2012) [79]	FC-40	8	0.2	300	80
Hasi W et al. (2013) [80]	FC-770	8	0.116	260	80
Zhu et al. (2014) [81]	FC-40	8	0.136	300	80
Ogino et al. (2014) [82]	FC-40	4	0.4	34	75

TABLE 3 | Summary of the advantages and disadvantages of each structure.

Name of structure	Advantage	Disadvantage
Tapered waveguide	Simple structure, easy to control	High cost, poor universality
Focusing single cell	Simple optic path, more controllable compression	Poor stability under high-energy condition
Compact two-cell	Longer effective interaction length, can obtain higher compression ratio	Poor stability under high-energy condition
Independent two-cell	Strong flexibility	Complicated optical path, large loss
Non-focusing structure	Strong stability, suitable for high-power large-aperture laser system	There are pump source modulation problems and threshold problems

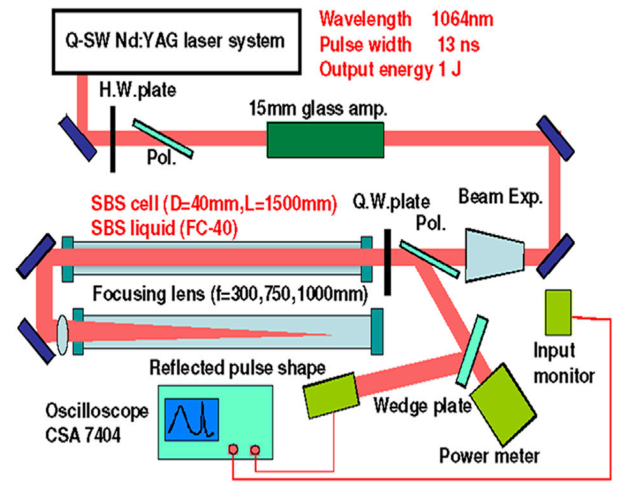

FIGURE 6 | Schematic diagram of typical experiment design of compact two-cell [84].

were carried out to achieve more precise and stable control of the beam intensity [128].

Dane et al. added an adjustable delay light path for changing the relative delay time of the seeding pump light and the amplifying pump light in the independent two-cell structure for the first time. The scheme obtained output energy of 2.5 J, and proposed a new optimization direction for compression characteristics [95]. From 2014 to 2017, Xu et al. conducted a series of pulse compression experiments. Compressed pulse width from 12 ns to 580 ps at the center wavelength of 1,064 nm in FC-72 was performed. At the center wavelength of 532 nm in water, the pulse width was compressed from 9 ns to 170 ps which was close to the phonon life limit of the medium. At the same time, they explored the relationship between the meeting position of the two light and the magnification effect in the independent two cell structure. In the two experiments, the energy reached 1 J level with the peak power over 1 GW [97–99, 129, 130].

The independent two-cell structure can largely avoid the non-linear effects such as optical breakdown, self-focusing, and self-defocusing under high-energy conditions, which inclines it to obtain better compression output characteristics and beam quality. However, introduced additional optical elements directly cause considerable transmission energy losses. Consequently, it is unfavorable for obtaining high energy efficiency. At the same time, the complexity of the optical path and the adjustment difficulty cannot be ignored, especially in the application of large-scale laser systems.

Other Structures

Multi-Stage Compression Structure

The multi-stage compression method provides the possibility to compress the pulse width to below 100 ps [100–108]. From 2003 to 2006, Wang et al. compressed the pulse width from 8 ns to 153 ps with two-stage compression in FC-75 [102, 103]. Pivinskii et al. proposed a new three-stage pulse compression structure for the first time. It was composed of a two-stage SBS compression system and a terminal SRS compression system. The original pump pulse of 8 ns was compressed to the ultrashort pulse of 20 ps in carbon tetrachloride liquid with an output energy of 6 mJ. At the same time, it was proposed that pulses below 10 ps could be obtained with lower output energy [106]. **Figure 8** illustrates the schematic diagram of the two-stage compression.

Generally, large-aperture laser systems rely heavily on beam quality. Although the multi-stage compression structure has made a great breakthrough with pulse width, the problems such as wavefront distortion and poor stability caused by the increasing of components have seriously affected the beam quality and energy efficiency. Therefore, improving the beam quality is the core issue for this structure to be applied in large-aperture high-power laser systems in the future.

Non-focusing Structure

For a long time, reports on the structure of SBS pulse compressor have basically focused on the lens focusing structure [72, 81, 98, 109]. To improve the stability under high-energy conditions, Neshev et al. proposed a new non-focusing single-cell structure for the first time and compressed the pulse width from 4 ns to 200 ps [108]. In 2015, our group obtained a short pulse of ~360 ps with a single pulse energy of 3.02 J, and there was no thermal effect or other nonlinear effects during the compression process [109]. **Figure 9** provides a schematic diagram of the experimental device and principle of the non-fousing method. The high reflectivity mirror was used to reflect the Stokes component of the sideband component of the super-Gaussian pump light to form the "feedback-initiated" Stokes seed light, and then compressing and amplifying. This method can suppress the generation of seed light originating from randomly distributed thermal noise. Thereby it reduces the probability of phase distortion and improves the stability of the system and the beam quality of the output pulse. Although this structure can

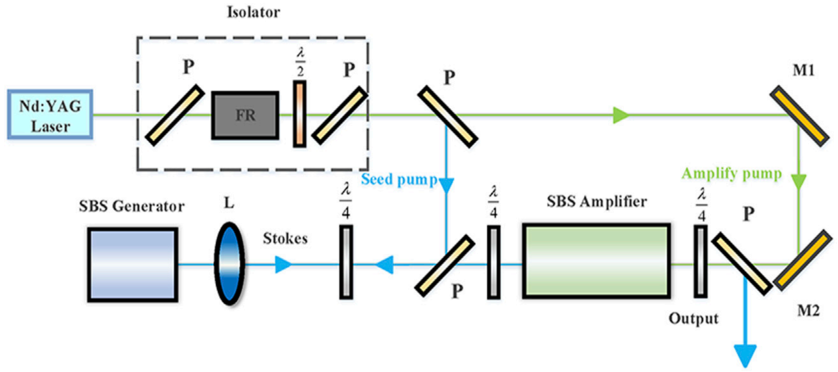

FIGURE 7 | Schematic diagram of basic independent two-cell structure.

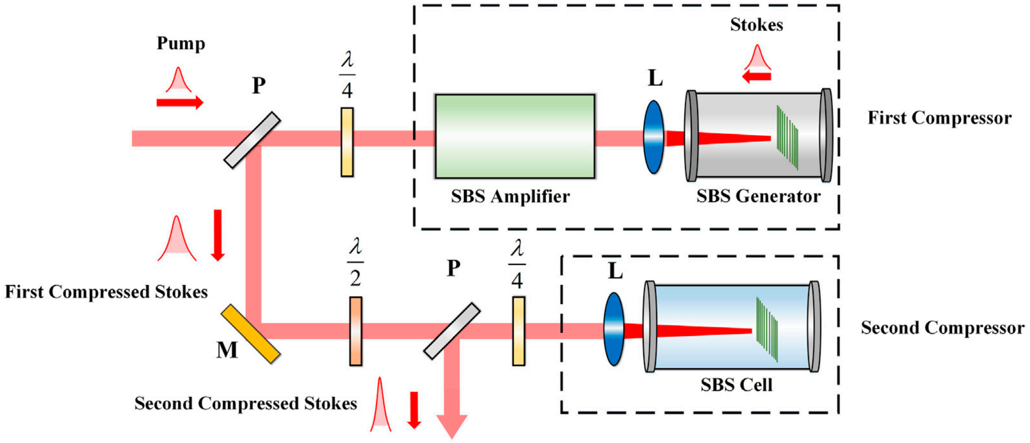

FIGURE 8 | Schematic of the two-stage compression structure.

be used for high-energy pulse compression characteristics research experiments, its injection energy will be limited by the noise-initiated SBS threshold in the medium cell. In addition to the mentioned challenges, the modulation procedure of the pump pulse cannot be removed because of the non-conjugation in this process. **Table 3** lists the advantage and disadvantages of different structures.

Unfolding the Hidden Spatial Degree of Freedoms

Plasma-Based Stimulated Brillouin Scattering

In recent years, some research groups use plasma as the new SBS active medium for pulse compression and amplification. Due to the advantage of its non-destructive property, SBS pulse compression based on plasma can obtain extremely high peak power up to the order of 10^{15} W and ultrashort pulse of the order of femtosecond [96, 110–114]. In 2010, Lancia et al. achieved the energy transfer from a long (3.5 ps) pump pulse to a short (400 fs) seed pulse due to stimulated Brillouin backscattering in the strong-coupling regime with output energy of 60 mJ in N_2 and Ar plasmas. The interaction process is shown in the **Figure 10**. They found that increasing the uniformity of plasma density can effectively reduce energy attenuation. At the same time, maintaining a high plasma density can increase the maximum amplification factor [96]. In 2013, Weber et al. used the strong coupling stimulated Brillouin technology in the plasma to obtain an amplified seed light with a peak power of 10^{18} W/cm^{2}and a pulse width of 10 fs [113].

Stimulated Brillouin Scattering With Structured Light

To date, the great majority of SBS studies, as reviewed in above, neglected the spatial dimensions of paraxial light. This is because most commercial laser systems are designed to generate the TEM_{00} mode with a linear polarization for highly efficient generation. More recently, progress in the study on structured light, both in fundamental and application aspects, has significantly gained the research intertest in techniques for generation and manipulation of high-order spatial modes [36, 37]. For the nonlinear approach, OAM transfer between light fields in varies optical parametric processes have been intensively studied over 20 years [38], and the community is recently focus

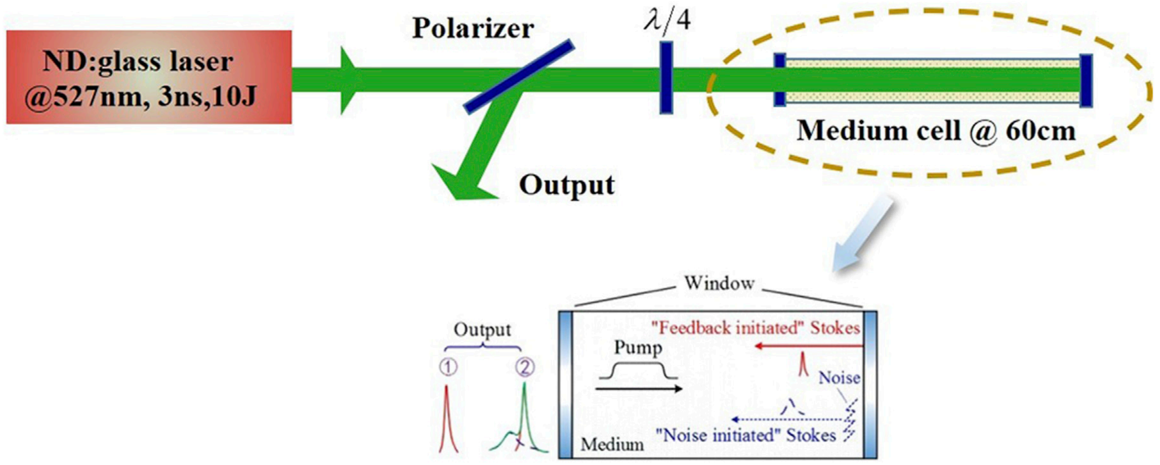

FIGURE 9 | The schematic diagram of "feedback-initiated" non-focus structure experimental device and principle: ①represents the "feedback-initiated" Stokes reflected pulse waveform; ② represents the coexist of "double peak" reflected pulse waveform of "noise-initiated" Stokes and "feedback-initiated" Stokes [109].

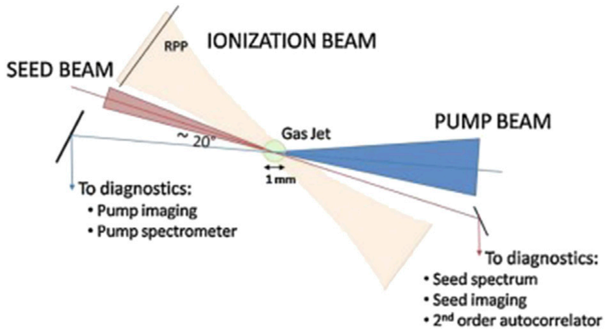

FIGURE 10 | Experimental scheme showing the three laser beams focused at the center of a supersonic gas jet [96].

on nonlinear generation and transformation generalized spatial modes and associated full-field selection rules [39, 115], as well as the effect of spin-orbit coupling [116]. By contrast, SBS involving OAM carrying light was first studied in theory until 2009 [40], and the corresponding experimental demonstration only appeared the 5 years later [41]. Particularly, Zhu *et al.* systematically studied OAM selection rules in varies SBS processes, and first realized OAM interconversion between light and acoustic fields, a high-dimension light memory, and revealed the underlying physics for the fragmentation of vortex beams in SBS-PCMs [28, 39], as shown in **Figure 11**.

For vectorial spatial modes, the first theoretically study for amplification of cylindrical vector (CV) modes was provided by Vieira *et al.* [42], only 1 year later, Zhu experimentally realized a strong (100 mJ at 300 ps) CV-mode laser output via SBA [43]. Besides, it is worthy to note that the structured acoustic wave generated in SBS excited by structured light, owing to its 0-spin and low group velocity, has a great potential for generation and transformation of structured light, and especially for applications regarding to strong laser pulses. For instance, ref. 120 predicted a "high OAM harmonic generation in cascading SBS/SRS on a specific acoustic wave. Remarkably, some novel nonlinear optical phenomena have been revealed in these few works, yet the underlying physics for the transformation of spatial modes in SBS has not been fully understanded to date. In a word, the SBS science with structured light is still in its infancy.

SUMMARIES

Due to the advantages of simple structure, low cost, and excellent beam quality of output pulse among others, pulse compression based on SBS has become one of the effective means to obtain picosecond pulses. This review gives a comprehensive overview of the research progress of SBS pulse compression with different structures. In addition, gain media also have a significant impact on the compression characteristics of SBS. At present, the more common Brillouin media are mainly solid media such as fused silica, K8 glass and liquid media such as perfluorocarbon series and water. Among them, the solid media has good thermal conductivity and no thermal convection effect, but its damage threshold is relatively low. As a new solid gain medium discovered in recent years, diamond crystal has attracted extensive attention because of its high Brillouin gain coefficient, high thermal conductivity, and wide spectral transmission range [117–120]. Once it breaks through the size limit, its application prospect in SBS pulse compression will be very promising. As a new type of Brillouin medium discovered in the last decades, the perfluorocarbon series of liquids have excellent performance and low cost, therefore are currently the mainstream Brillouin medium in high energy pulse compression. In general, since Stokes beam with narrow pulse width can be easily obtained, media with short phonon lifetime and high gain coefficient are popular. However, based on recent experimental results, our research group found that the medium which has a

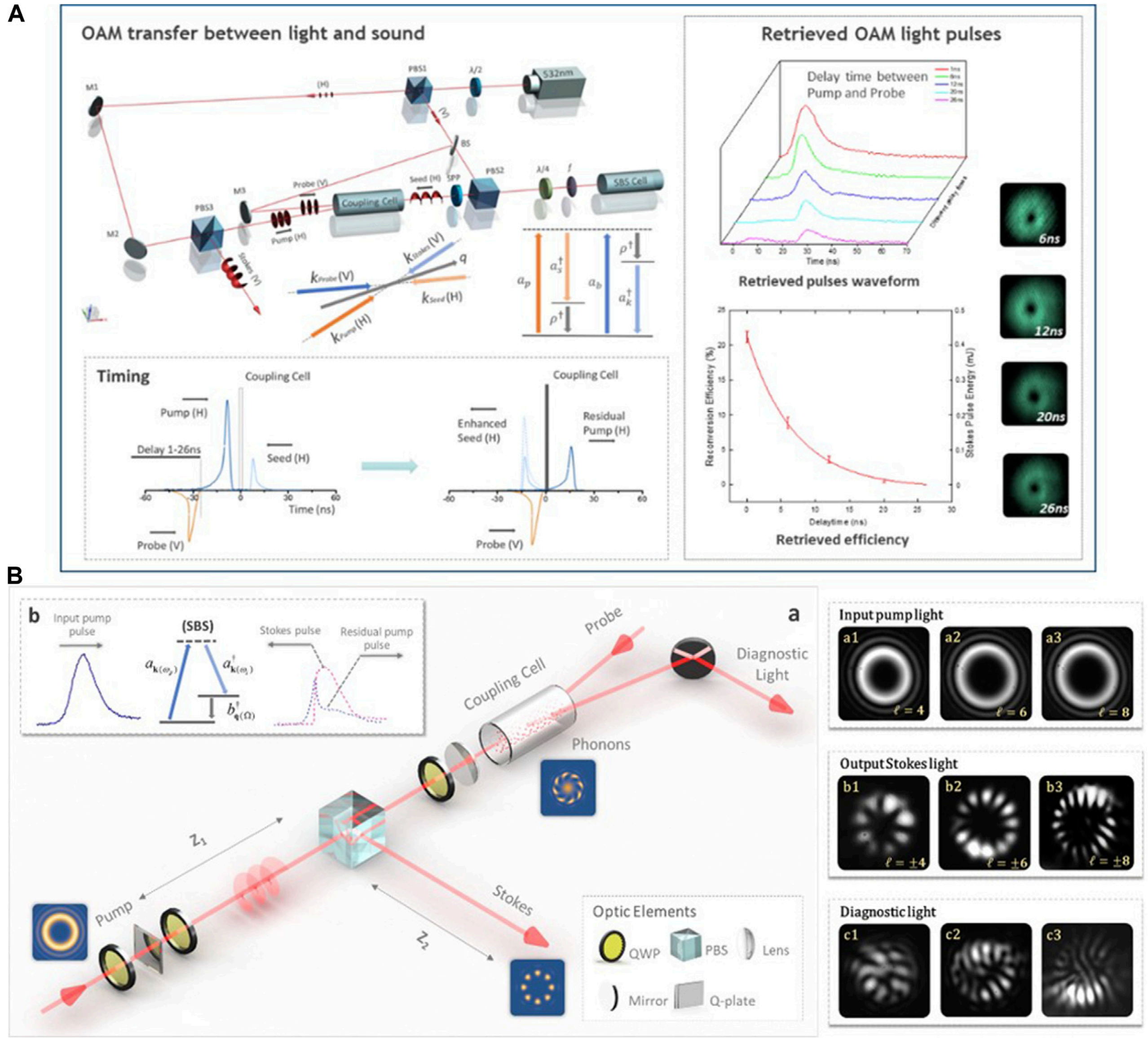

FIGURE 11 | Realization of OAM interconversion between light and sound waves via SBS **(A)** and demonstration of fragmentation of vortex beams in an SBS-PCM **(B)** [28, 39].

short phonon lifetime and high gain (such as HT-230) will cause the compression limit point to be generated prematurely, and then the pulse width broadening phenomenon and even the cascaded SBS phenomenon will occur.

At present, more attention to SBS-based pulse compression and amplification studies has been paid to narrower pulse width output with higher repetition rate and higher energy. Since the traditional focusing structure and active medium are limited by the damage threshold, it is difficult to make major breakthroughs with an aspect of pulse intensity. Therefore, the researches on non-focusing structures and new active media have guiding significance. The non-focusing structure can greatly improve the stability of the entire system and the injected energy, and obtain short pulses with high beam quality. It is extremely suitable for high-power large-aperture laser systems. Chirped-pulse amplification technology (CPA) and optical parametric chirped-pulse amplification technology (OPCPA) have been unable to achieve further breakthroughs because of the limitation of the optical damage threshold of compressed gratings [121–125]. At the same time, the reversibility of photoacoustic conversion in the SBS process has been reported, and it also has application value in communication [126]. Although the above-mentioned strong coupling stimulated Brillouin scattering technology implemented in plasma has obtained extremely high peak power and ultra-short pulse width, this method is hard to manipulate, and has extremely high requirements for the experimental environment and the precision of the devices. Therefore, the plasma-based SBS pulse compression technology still needs in-depth research. The breakthroughs of this technology will significantly promote research work and practical applications in the field of basic science.

AUTHOR CONTRIBUTIONS

CC: Writing-Original Draft, Writing-Review and Editing. YW: Supervision, Funding acquisition, Writing-Review and Editing. ZB: Supervision, Writing-Review and Editing. YL: Writing—Review and Editing. YY: Writing—Review and Editing. ZL: Supervision, Funding acquisition.

FUNDING

This work was supported by the National Natural Science Foundation of China (Nos. 62075056, 61927815, and 61905061).

REFERENCES

1. Bury G, Sośnica K, Zajdel R. Multi-GNSS Orbit Determination Using Satellite Laser Ranging. *J Geod* (2018) 93(12):2447–63. doi:10.1007/s00190-018-1143-1
2. Loomis BD, Rachlin KE, Wiese DN, Landerer FW, Luthcke SB. Replacing GRACE/GRACE-FO with Satellite Laser Ranging: Impacts on Antarctic Ice Sheet Mass Change. *Geophys Res Lett* (2020) 47(3):e2019GL085488. doi:10.1029/2019GL085488
3. McGarry JF, Hoffman ED, Degnan JJ, Cheek JW, Clarke CB, Diegel IF, et al. NASA's Satellite Laser Ranging Systems for the Twenty-First Century. *J Geod* (2018) 93(11):2249–62. doi:10.1007/s00190-018-1191-6
4. Samanta A, Wang Q, Singh G, Shaw SK, Toor F, Ratner A, et al. Nanosecond Pulsed Laser Processing Turns Engineering Metal Alloys Antireflective and Superwicking. *J Manuf Process* (2020) 54:28–37. doi:10.1016/j.jmapro.2020.02.029
5. Sugioka K. Progress in Ultrafast Laser Processing and Future Prospects. *Nano-photonics* (2017) 6(2):393–413. doi:10.1515/nanoph-2016-0004
6. Zheng Z, Wu C, Liu S, Yang X. Analysis of Energy Occupying Ratio of Coulomb Explosion and Thermal Effect in Picosecond Pulse Laser Processing. *Opt Commun* (2018) 424:190–7. doi:10.1016/j.optcom.2018.04.045
7. Zhan SY, Li HT, Yang RY. New Progress in Laser Treatment of Chloasma. *J Pract Dermatol* (2018) 11(3):158–61. doi:10.11786/sypfbxzz.1674-1293.20180309
8. Li M, Huang Y, Zhu W. Clinical Application Progress of Picosecond Laser. *J Pract Dermatol* (2019) 12(4):223–6. doi:10.11786/sypfbxzz.1674-1293.20190409
9. Huang Y, Zhang H, Yan X, Guo G, Bai Z, Lin W, et al. High-Brightness 100 Hz/363 mJ Picosecond Nd:YAG Laser System for Ultra-remote Laser Ranging. *IEEE J Quan Electron.* (2020) 56(5):1700310. doi:10.1109/JQE.2020.3004139
10. Zhang H, Cheng Z, Long M, Deng H, Meng W, Wu Z, et al. Applications of Satellite Laser Ranging and Laser Time Transfer in BeiDou Navigation Satellite System. *Optik* (2019) 188:251–62. doi:10.1016/j.ijleo.2019.04.131
11. Sośnica K, Bury G, Zajdel R, Strugarek D, Drożdżewski M, Kazmierski K. Estimating Global Geodetic Parameters Using SLR Observations to Galileo, GLONASS, BeiDou, GPS, and QZSS. *Earth Planets Space* (2019) 71(11):20. doi:10.1186/s40623-019-1000-3
12. Benocci R, Batani D, Roman HE. Incubation Models for Under-threshold Laser Ablation with Thermal Dissipation. *Appl Phys B* (2019) 125(2):22. doi:10.1007/s00340-019-7132-0
13. Mustafa H, Matthews DTA, Römer GRBE. The Role of Pulse Repetition Rate on Picosecond Pulsed Laser Processing of Zn and Zn-Coated Steel. *Opt Laser Technol* (2020) 131:106408. doi:10.1016/j.optlastec.2020.106408
14. Mustafa H, Pohl R, Bor TC, Pathiraj B, Matthews DTA, Römer GRBE. Picosecond-pulsed Laser Ablation of Zinc: Crater Morphology and Comparison of Methods to Determine Ablation Threshold. *Opt Express* (2018) 26(14):18664–83. doi:10.1364/OE.26.018664
15. Yoshida M, Yoshida K, Kasai K, Nakazawa M, et al. *A 0.95ps, 10GHz, 60mW HCN Frequency-Stabilized and Mode-Locked Fiber Laser at 1.55 μm*. San Jose: Lasers and Electro-optics (2016). doi:10.1364/CLEO_SI.2016.Stu1P.3
16. Bourne OL, Alcock AJ. Simplified Technique for Subnanosecond Pulse Generation and Injection Mode-Locking of a XeCl Laser. *Appl Phys B* (1985) 36(4):181–5. doi:10.1007/BF00704572
17. Li X, Wang H, Qiao ZL, Guo X, Wang WJ, Ng GI, et al. Investigation of Regime Switching from Mode Locking to Q-Switching in a 2 μm InGaSb/AlGaAsSb Quantum Well Laser. *Opt Express* (2018) 26(7):8289. doi:10.1364/OE.26.008289
18. Perego AM, Garbin B, Gustave F, Barland S, Prati F, de Valcárcel GJ. Coherent Master Equation for Laser Modelocking. *Nat Commun* (2020) 11(1):311. doi:10.1038/s41467-019-14013-4
19. Li Y, Tu W, Wang B, Zong N, Yang F, Zhang F, et al. High-Power Narrow-Linewidth Q-Switched TEM00 Mode 355-nm Laser. *IEEE Photon J.* (2018) 10(3):1502509. doi:10.1109/JPHOT.2018.2825238
20. Zayhowski JJ, Dill C. Diode-pumped Passively Q-Switched Picosecond Microchip Lasers. *Opt Lett* (1994) 19(18):1427–9. doi:10.1364/OL.19.001427
21. Yang X, Zhang P, Xie W, Li L Double Q-Switch Ho:Sc$_2$ SiO$_5$ Laser by Acousto-Optic Modulator Combined with Cr $^{2+}$:ZnSe Saturable Absorber. *Opt Laser Technol* (2018) 98:19–22. doi:10.1016/j.optlastec.2017.07.038
22. Cole B, Goldberg L, Hays AD. High-efficiency 2 μm Tm:YAP Laser with a Compact Mechanical Q-Switch. *Opt Lett* (2018) 43(2):170–3. doi:10.1364/OL.43.000170
23. Boyd RW, Rzązewski K, Narum P. Noise Initiation of Stimulated Brillouin Scattering. *Phys Rev A* (1990) 42(9):5514–21. doi:10.1103/PhysRevA.42.5514
24. Crofts GJ, Lamb RA, Damzen MJ. Experimental and Theoretical Investigation of Two-Cell Stimulated-Brillouin-Scattering Systems. *J Opt Soc Am B* (1991) 8(11):2282–8. doi:10.1364/JOSAB.8.002282
25. Wang HL, Cha S, Kong HJ, Wang YL, Lu ZW. Rotating Off-Centered Lens in SBS Phase Conjugation Mirror for High-Repetition-Rate Operation. *Opt Express* (2019) 27(7):9895–905. doi:10.1364/OE.27.009895
26. Tsubakimoto K, Yoshida H, Miyanaga N. High-average-power green Laser Using Nd:YAG Amplifier with Stimulated Brillouin Scattering Phase-Conjugate Pulse-Cleaning Mirror. *Opt Express* (2016) 24(12):12557–64. doi:10.1364/OE.24.012557
27. Kang ZJ, Fan ZW, Huang YT, Zhang HB, Ge WQ, Li MS, et al. High-repetition-rate, High-Pulse-Energy, and High-Beam-Quality Laser System Using an Ultraclean Closed-type SBS-PCM. *Opt Express* (2018) 26(6):6560–71. doi:10.1364/OE.26.006560
28. Zhu Z-H, Chen P, Li H-W, Zhao B, Zhou Z-Y, Hu W, et al. Fragmentation of Twisted Light in Photon-Phonon Nonlinear Propagation. *Appl Phys Lett* (2018) 112(16):161103. doi:10.1063/1.5020082
29. Kong HJ, Park S, Cha S, Ahn H, Lee H, Oh J, et al. Conceptual Design of the Kumgang Laser: a High-Power Coherent Beam Combination Laser Using SC-SBS-PCMs towards a Dream Laser. *High Pow Laser Sci Eng* (2015) 3(1):19–31. doi:10.1017/hpl.2014.49
30. Park S, Cha S, Oh J, Lee H, Ahn H, Churn KS, et al. Coherent Beam Combination Using Self-phase Locked Stimulated Brillouin Scattering Phase Conjugate Mirrors with a Rotating Wedge for High Power Laser Generation. *Opt Express* (2016) 24(8):8641–6. doi:10.1364/OE.24.008641
31. Cui C, Wang YL, Lu ZW, Yuan H, Wang Y, Chen Y, et al. Demonstration of 25 J, 10 Hz, Nanosecond Laser Beam Combination System Based on Non-collinear Brillouin Amplification. *Opt Express* (2018) 26(25):32717–27. doi:10.1364/OE.26.03272710.1364/oe.26.032717
32. Hasi WLJ, Lu ZW, Gong S, Lin DY, He WM, Fan RQ. Investigation on the Output Energy Characteristic of Optical Limiting Based on Stimulated Brillouin Scattering. *Appl Phys B* (2008) 92:599–602. doi:10.1007/s00340-008-3115-2
33. Lu ZW, Lu YL, Yang J. Optical Limiting Effect Based on Stimulated Brillouin Scattering in CCl$_4$. *Chin Phys.* (2003) 12(5):507–13. doi:10.1088/1009-1963/12/5/308

34. Kang ZJ, Zhang HB, Yan XC, Lang Y, Bai ZA, Fan ZW. 200 Hz High Repetition Frequency SBS Pulse Width Compression experiment. *Chin Opt* (2018) 11(5):736–44. doi:10.3788/CO.20181105.0736
35. Wang H, Cha S, Wang Y, Kong HJ, Lu Z. SBS Pulse Compression Using Bulk Fused Silica by Diode-Pumped Solid-State Lasers at 1 kHz Repetition Rate. *Opt Laser Technol* (2020) 128:106258. doi:10.1016/j.optlastec.2020.106258
36. Forbes A, de Oliveira M, Dennis MR. Structured Light. *Nat Photon* (2021) 15: 253–62. doi:10.1038/s41566-021-00780-4
37. Rubinsztein-Dunlop H, Forbes A, Berry MV, Dennis MR, Andrews DL, Mansuripur M, et al. Roadmap on Structured Light. *J Opt* (2017) 19:013001. doi:10.1088/2040-8978/19/1/013001
38. Courtial J, Dholakia K, Allen L, Padgett MJ. Second-harmonic Generation and the Conservation of Orbital Angular Momentum with High-Order Laguerre-Gaussian Modes. *Phys Rev A* (1997) 56:4193–6. doi:10.1103/PhysRevA.56.4193
39. Wu H-J, Mao L-W, Yang Y-J, Rosales-Guzmán C, Gao W, Shi B-S, et al. Radial Modal Transitions of Laguerre-Gauss Modes during Parametric Up-Conversion: Towards the Full-Field Selection Rule of Spatial Modesfield Selection Rule of Spatial Modes. *Phys Rev A* (2020) 101:063805. doi:10.1103/PhysRevA.101.063805
40. Mendonça JT, Thidé B, Then H. Stimulated Raman and Brillouin Backscattering of Collimated Beams Carrying Orbital Angular Momentum. *Phys Rev Lett* (2009) 102(18):185005. doi:10.1103/PhysRevLett.102.185005
41. Gao W, Mu C, Li H, Yang Y, Zhu Z. Parametric Amplification of Orbital Angular Momentum Beams Based on Light-Acoustic Interaction. *Appl Phys Lett* (2015) 107(4):041119. doi:10.1063/1.4927699
42. Vieira J, Trines RMGM, Alves EP, Fonseca RA, Mendonça JT, Bingham R, et al. Amplification and Generation of Ultra-intense Twisted Laser Pulses via Stimulated Raman Scattering. *Nat Commun* (2016) 7(3):10371. doi:10.1038/ncomms10371
43. Zhu Z-H, Chen P, Sheng L-W, Wang Y-L, Hu W, Lu Y-Q, et al. Generation of strong Cylindrical Vector Pulses via Stimulated Brillouin Amplification. *Appl Phys Lett* (2017) 110(14):141104. doi:10.1063/1.4979588
44. Vieira J, Trines RMGM, Alves EP, Fonseca RA, Mendonça JT, Bingham R, et al. High Orbital Angular Momentum Harmonic Generation. *Phys Rev Lett* (2016) 117(26):265001. doi:10.1103/PhysRevLett.117.265001
45. Liu HX, Li YL, Gu XK, Hu WW, Zhang YP, Zhang YM. Research on Medium for Ultrashort Pulse Laser by SBS. *Laser and Infrared* (2019) 49(004):387–94. doi:10.3969/j.issn.1001-5078.2019.04.001
46. Bai Z, Yuan H, Liu Z, Xu P, Gao Q, Williams RJ, et al. Stimulated Brillouin Scattering Materials, Experimental Design and Applications: A Review. *Opt Mater* (2018) 75:626–45. doi:10.1016/j.optmat.2017.10.035
47. Maier M, Kaiser W, Giordmaine JA. Intense Light Bursts in the Stimulated Raman Effect. *Phys Rev Lett* (1966) 17(26):1275–7. doi:10.1103/PhysRevLett.17.1275
48. Glass A. Design Considerations for Raman Lasers. *IEEE J Quan Electron.* (1967) 3(6):516–20. doi:10.1109/JQE.1967.1074552
49. Minck RW, Hagenlocker EE, Rado WG. Simultaneous Occurrence of and Competition between Stimulated Optical-Scattering Processes in Gases. *J Appl Phys* (1967) 38(5):2254–60. doi:10.1063/1.1709865
50. Culver WH, Vanderslice JTA, Townsend VWT. Controlled Generation of Intense Light Pulses in Reverse-pumped Raman Lasers. *Appl Phys Lett* (1968) 12(5):189–90. doi:10.1063/1.1651946
51. Rahn O, Maier M, Kaiser W. Stimulated Raman, Librational, and Brillouin Scattering in Water. *Opt Commun* (1969) 1(3):109–10. doi:10.1016/0030-4018(69)90022-4
52. Maier M, Kaiser W, Giordmaine JA. Backward Stimulated Raman Scattering. *Phys Rev* (1969) 177(2):580–99. doi:10.1103/PhysRev.177.580
53. Stolen RH, Ippen EP, Tynes AR. Raman Oscillation in Glass Optical Waveguide. *Appl Phys Lett* (1972) 20(2):62–4. doi:10.1063/1.1654046
54. Lowdermilk WH, Kachen GI. Stokes Pulse Growth in Transient Stimulated Raman Scattering. *Appl Phys Lett* (1975) 27(3):133–5. doi:10.1063/1.88381
55. Tan-No N, Shirahata T, Yokoto K, Inaba H. Coherent Transient Effect in Raman Pulse Propagation. *Phys Rev A* (1975) 12(1):159–68. doi:10.1103/PhysRevA.12.159
56. Heuer A, Menzel R. Phase-conjugating Stimulated Brillouin Scattering Mirror for Low Powers and Reflectivities above 90% in an Internally Tapered Optical Fiber. *Opt Lett* (1998) 23(11):834–6. doi:10.1364/OL.23.000834
57. Ewing J, Haas R, Swingle J, George E, Krupke W. Optical Pulse Compressor Systems for Laser Fusion. *IEEE J Quan Electron.* (1979) 15(5):368–79. doi:10.1109/JQE.1979.1070010
58. Murray J, Goldhar J, Eimerl D, Szoke A. Raman Pulse Compression of Excimer Lasers for Application to Laser Fusion. *IEEE J Quan Electron.* (1979) 15(5):342–68. doi:10.1109/JQE.1979.1070009
59. Chiao RY, Townes CH, Stoicheff BP. Stimulated Brillouin Scattering and Coherent Generation of Intense Hypersonic Waves. *Phys Rev Lett* (1964) 12(21):592–5. doi:10.1103/PhysRevLett.12.592
60. Hon DT. Pulse Compression by Stimulated Brillouin Scattering. *Opt Lett* (1980) 5(12):516–8. doi:10.1364/OL.5.000516
61. Yuan H, Wang Y, Lu Z, Liu Z, Bai Z, Liu R, et al. SRS Characteristics and its Influence on SBS Pulse Compression in a Fluorocarbon Liquid. *Laser Part Beams* (2017) 35(1):114–9. doi:10.1017/S026303461600094X
62. Damzen M, Hutchinson H. Laser Pulse Compression by Stimulated Brillouin Scattering in Tapered Waveguides. *IEEE J Quan Electron.* (1983) 19(1):7–14. doi:10.1109/JQE.1983.1071718
63. Zhao Z, Dong Y, Pan S, Liu C, Chen J, Tong L, et al. Performance of Large Aperture Tapered Fiber Phase Conjugate Mirror with High Pulse Energy and 1-kHz Repetition Rate. *Opt Express* (2012) 20(2):1896–902. doi:10.1364/OE.20.001896
64. Damzen MJ, Hutchinson MHR. High-efficiency Laser-Pulse Compression by Stimulated Brillouin Scattering. *Opt Lett* (1983) 8(6):313–5. doi:10.1364/OL.8.000313
65. Gorbunov VA, Papernyĭ SB, Petrov VF, Startsev VR. Time Compression of Pulses in the Course of Stimulated Brillouin Scattering in Gases. *Sov J Quan Electron.* (1983) 13(7):900–5. doi:10.1070/QE1983v013n07ABEH004367
66. Tomov IV, Fedosejevs R, Mcken DCD. High-efficiency Stimulated Brillouin Scattering of KrF Laser Radiation in SF_6. *Opt Lett* (1984) 9(9):405–7. doi:10.1364/OL.9.000405
67. Tomov I, Fedosejevs R, Mcken D. Stimulated Brillouin Scattering of KrF Laser Radiation in Dichlorodifluoromethane. *IEEE J Quan Electron.* (1985) 21(1):9–11. doi:10.1109/JQE.1985.1072533
68. Buzyalis RR, Dementjev AS, Kosenko EK. Formation of Subnanosecond Pulses by Stimulated Brillouin Scattering of Radiation from a Pulse-Periodic YAG:Nd Laser. *Sov J Quan Electron.* (1985) 15(10):1335–7. doi:10.1070/QE1985v015n10ABEH007759
69. Davydov MA, Shipilov KF, Shmaonov TA. Formation of Highly Compressed Stimulated Brillouin Scattering Pulses in Liquids. *Sov J Quan Electron.* (1986) 16(10):1402–3. doi:10.1070/QE1986v016n10ABEH007597
70. Gaĭzhauskas É, Krushas V, Nedbaev NY, Petrenko RA, Piskarskas A, Smil'gyavichyus V. Generation of Picosecond Pulses as a Result of Stimulated Brillouin Scattering in Liquids. *Sov J Quan Electron.* (1986) 16(6):854–5. doi:10.1070/QE1986v016n06ABEH006956
71. Kmetik V, Fiedorowicz H, Andreev AA, Witte KJ, Daido H, Fujita H, et al. Reliable Stimulated Brillouin Scattering Compression of Nd:YAG Laser Pulses with Liquid Fluorocarbon for Long-Time Operation at 10 Hz. *Appl Opt* (1998) 37(30):7085–90. doi:10.1364/AO.37.007085
72. Yoshida H, Fujita H, Nakatsuka M, Fujinoki A. Temporal Compression by Stimulated Brillouin Scattering of Q-Switched Pulse with Fused Quartz Glass. *Jpn J Appl Phys* (2004) 43(8B):L1103–L1105. doi:10.1143/JJAP.43.L1103
73. Yoshida H, Fujita H, Nakatsuka M, Ueda T, Fujinoki A. Temporal Compression by Stimulated Brillouin Scattering of Q-Switched Pulse with Fused-Quartz and Fused-Silica Glass from 1064 nm to 266 nm Wavelength. *Laser Part Beams* (2007) 25(03):481–8. doi:10.1017/S0263034607000596
74. Liu Z, Wang Y, Wang Y, Li S, Bai Z, Lin D, et al. Pulse-shape Dependence of Stimulated Brillouin Scattering Pulse Compression to Sub-phonon Lifetime. *Opt Express* (2018) 26(5):5701–10. doi:10.1364/OE.26.005701
75. Bai Z, Wang Y, Lu Z, Yuan H, Jiang L, Tan T, et al. Efficient KDP Frequency Doubling SBS Pulse Compressed 532 nm Hundred Picosecond Laser. *Optik* (2016) 127(20):9201–5. doi:10.1016/j.ijleo.2016.07.021
76. Liu Z, Wang Y, Bai Z, Wang Y, Jin D, Wang H, et al. Pulse Compression to One-Tenth of Phonon Lifetime Using Quasi-Steady-State Stimulated Brillouin Scattering. *Opt Express* (2018) 26(18):23051–60. doi:10.1364/OE.26.023051
77. Gaĭzhauskas É, Piskarskas A, Smil'gyavichyus V, Stalyunas K. Space and Time Structure of Ultrashort Pulses Formed by Opposed Stimulated

Scattering of Laser Beams. *Sov J Quan Electron.* (1987) 17(5):650–3. doi:10.1070/QE1987v017n05ABEH009067

78. Schiemann S, Ubachs W, Hogervorst W. Efficient Temporal Compression of Coherent Nanosecond Pulses in a Compact SBS Generator-Amplifier Setup. *IEEE J Quan Electron.* (1997) 33(3):358–66. doi:10.1109/3.556004
79. Wang Y., Lu Z, Guo Q, Wu P, Zheng Z, He W A New Circulating Two-Cell Structure for Stimulated Brillouin Scattering Phase Conjugation Mirrors with 1-J Load and 10-Hz Repetition Rate. *Chin Opt Lett* (2010) 8(11):1064–6. doi:10.3788/COL20100811.1064
80. Zheng ZX, Hasi WLJ, Zhao H, Cheng SX, Wang XY, Lin DY, et al. Compression Characteristics of Two New SBS Mediums to Generate 100-ps Pulse for Shock Ignition. *Appl Phys B* (2014) 116(3):659–63. doi:10.1007/s00340-013-5749-y
81. Hasi WLJ, Qiao Z, Cheng SX, Wang XY, Zhong ZM, Zheng ZX, et al. Characteristics of SBS Hundreds Picosecond Pulse Compression and Influence of Energy on Pulse Stability in FC-770. *Opt Commun* (2013) 311:375–9. doi:10.1016/j.optcom.2013.05.056
82. Ogino J, Miyamoto S, Matsuyama T, Sueda K, Yoshida H, Tsubakimoto K, et al. Two-stage Optical Parametric Chirped-Pulse Amplifier Using Sub-nanosecond Pump Pulse Generated by Stimulated Brillouin Scattering Compression. *Appl Phys Express* (2014) 7(12):122702. doi:10.7567/APEX.7.122702
83. Yoshida H, Fujita H, Nakatsuka M, Ueda T, Fujinoki A. Compact Temporal-Pulse-Compressor Used in Fused-Silica Glass at 1064 nm Wavelength. *Jpn J Appl Phys* (2007) 46(3):L80–L82. doi:10.1143/JJAP.46.L80
84. Yoshida H, Hatae T, Fujita H, Nakatsuka M, Kitamura S. A High-Energy 160-ps Pulse Generation by Stimulated Brillouin Scattering from Heavy Fluorocarbon Liquid at 1064 nm Wavelength. *Opt Express* (2009) 17(16): 13654–62. doi:10.1364/OE.17.013654
85. Daito I, Kando M, Kotaki H, Hayashi Y, Kizugawa J, Shizuma T, et al. *High Flux Laser-Compton Scattered Gamma-Ray Source by Compressed Nd:YAG Laser Pulse*. New Orleans: International Particle Accelerator Conference (2012).
86. Zhu X, Lu Z, Wang Y. High Stability, Single Frequency, 300 mJ, 130 Ps Laser Pulse Generation Based on Stimulated Brillouin Scattering Pulse Compression. *Laser Part Beams* (2015) 33(01):11–5. doi:10.1017/S0263034614000597
87. Wang Y, Liu Z, Yuan H, Bai Z, Wang H, Zhu X, et al. A Promotion of Stability for Temporal Compression Based on SBS in an Interferometric Scheme. *J Mod Opt* (2016) 63(17):1734–40. doi:10.1080/09500340.2016.1171406
88. Bai Z, Wang Y, Lu Z, Yuan H, Zheng Z, Li S, et al. High Compact, High Quality Single Longitudinal Mode Hundred Picoseconds Laser Based on Stimulated Brillouin Scattering Pulse Compression. *Appl Sci* (2016) 6(1):29. doi:10.3390/app6010029
89. Bai Z, Wang Y, Lu Z, Jiang L, Yuan H, Liu Z. Demonstration of an Ultraviolet Stimulated Brillouin Scattering Pulse Compressed Hundred Picosecond Laser in LiB3O5crystals. *J Opt* (2017) 19(8):085502. doi:10.1088/2040-8986/aa74d6
90. Wang H, Cha S, Kong HJ, Wang Y, Lu Z. Sub-nanosecond Stimulated Brillouin Scattering Pulse Compression Using HT270 for kHz Repetition Rate Operation. *Opt Express* (2019) 27(21):29789–802. doi:10.1364/OE.27.029789
91. Mitra A, Yoshida H, Fujita H, Nakatsuka M. Sub Nanosecond Pulse Generation by Stimulated Brillouin Scattering Using FC-75 in an Integrated Setup with Laser Energy up to 1.5 J. *Jpn J Appl Phys* (2006) 45(3A):1607–11. doi:10.1143/JJAP.45.1607
92. Kmetik V, Yoshida H, Fujita H, Nakatsuka M, Yamanaka T. Very High Energy SBS Phase Conjugation and Pulse Compression in Fluorocarbon Liquids. *Proc SPIE-The Int Soc Opt Eng* (2000) 3889:818–26. doi:10.1117/12.380865
93. Fedosejevs R, Tomov IV, Mcken DCD, Offenberger AA. Experimental Study of an SF6Brillouin Amplifier Pumped by KrF Laser Radiation. *Appl Phys Lett* (1984) 45(4):340–2. doi:10.1063/1.95262
94. Fedosejevs R, Offenberger A. Subnanosecond Pulses from a KrF Laser Pumped SF6Brillouin Amplifier. *IEEE J Quan Electron.* (1985) 21(10): 1558–62. doi:10.1109/JQE.1985.1072567
95. Dane CB, Neuman WA, Hackel LA. High-energy SBS Pulse Compression. *IEEE J Quan Electron.* (1994) 30(8):1907–15. doi:10.1109/3.301654
96. Lancia L, Marquès J-R, Nakatsutsumi M, Riconda C, Weber S, Hüller S, et al. Experimental Evidence of Short Light Pulse Amplification Using Strong-Coupling Stimulated Brillouin Scattering in the Pump Depletion Regime. *Phys Rev Lett* (2010) 104(2):025001. doi:10.1103/PhysRevLett.104.025001
97. Feng C, Xu X, Diels J-C. Generation of 300 ps Laser Pulse with 12 J Energy by Stimulated Brillouin Scattering in Water at 532 nm. *Opt Lett* (2014) 39(12): 3367–70. doi:10.1364/OL.39.003367
98. Xu X, Feng C, Diels J-C. Optimizing Sub-ns Pulse Compression for High Energy Application. *Opt Express* (2014) 22(11):13904–15. doi:10.1364/OE.22.013904
99. Feng C, Xu X, Diels J-C. High-energy Sub-phonon Lifetime Pulse Compression by Stimulated Brillouin Scattering in Liquids. *Opt Express* (2017) 25(11):12421–34. doi:10.1364/OE.25.012421
100. Takahashi E, Kuwahara K, Matsumoto Y, Owadano Y. High-intensity Short KrF Laser-Pulse Generation by Saturated Amplification of Truncated Leading-Edge Pulse. *Opt Commun* (2000) 185(4-6):431–7. doi:10.1016/S0030-4018(00)01042-7
101. Kuwahara K, Takahashi E, Matsumoto Y, Kato S, Owadano Y, Kato S, et al. Short-pulse Generation by Saturated KrF Laser Amplification of a Steep Stokes Pulse Produced by Two-step Stimulated Brillouin Scattering. *J Opt Soc Am B* (2000) 17(11):1943–7. doi:10.1364/JOSAB.17.001943
102. Wang C, Lu ZW, He WM. Picosecond Pulse Generation by Stimulated Brillouin Scatte-Ring Compressor. *Powerful Laser Part Beam* (2003) 15(012): 1184–6. doi:10.1023/A:1022289509702
103. Wang C, Lu ZW, Lin DY, He WM. Laser Pulse with Duration Shorter Than 1/4 of Hypersound Oscillation Period of Medium Achieved by Stimulated Brillouin Compressor. *Chin J Lasers* (2006) 33:226–8.
104. Marcus G, Pearl S, Pasmanik G. Stimulated Brillouin Scattering Pulse Compression to 175ps in a Fused Quartz at 1064nm. *J Appl Phys* (2008) 103(10):103105. doi:10.1063/1.2931001
105. Hasi WLJ, Zhao H, Lin DY, He WM, Lu ZW. Characteristics of Perfluorinated Amine Media for Stimulated Brillouin Scattering in Hundreds of Picoseconds Pulse Compression at 532 nm. *Chin Opt Lett* (2015) 13: 061901–5. *English version*. doi:10.3788/COL201513.061901
106. Pivinskii EG, Akulinichev VV, Gorbunov VA. Nd:YAG Laser Pulse Compression by Three-Stage Stimulated Brillouin and Raman Scatterings. *Proc SPIE Int Soc Opt Eng* (1997) 2986:231–8. doi:10.1117/12.270002
107. Liu Z, Wang Y, Wang H, Bai Z, Li S, Zhang H, et al. Pulse Temporal Compression by Two-Stage Stimulated Brillouin Scattering and Laser-Induced Breakdown. *Appl Phys Lett* (2017) 110(24):241108. doi:10.1063/1.4986437
108. Neshev D, Velchev I, Majewski WA, Hogervorst W, Ubachs W. SBS Pulse Compression to 200 ps in a Compact Single-Cell Setup. *Appl Phys B: Lasers Opt* (1999) 68(4):671–5. doi:10.1007/s00340990145410.1007/s003400050684
109. Wang Y, Zhu X, Lu Z, Zhang H. Generation of 360 ps Laser Pulse with 3 J Energy by Stimulated Brillouin Scattering with a Nonfocusing Scheme. *Opt Express* (2015) 23(18):23318–28. doi:10.1364/OE.23.023318
110. Andreev AA, Sutyagin AN. Feasibility of Optical Pulse Compression by Stimulated Brillouin Scattering in a Plasma. *Sov J Quan Electron.* (1989) 19(12):1579–82. doi:10.1070/QE1989v019n12ABEH009826
111. Andreev AA, Riconda C, Weber S. Generation and Amplification of Ultra-short Light Pulses in the Strongly Coupled Regime of SBS in Plasma. *Phys Plasmas* (2005) 41(3):414–7. doi:10.1021/je9501853
112. Andreev AA, Riconda C, Tikhonchuk VT, Weber S. Short Light Pulse Amplification and Compression by Stimulated Brillouin Scattering in Plasmas in the Strong Coupling Regime. *Phys Plasmas* (2006) 13(5): 053110. doi:10.1063/1.2201896
113. Weber S, Riconda C, Lancia L, Marquès J-R, Mourou GA, Fuchs J. Amplification of Ultrashort Laser Pulses by Brillouin Backscattering in Plasmas. *Phys Rev Lett* (2013) 111(5):055004. doi:10.1103/PhysRevLett.111.055004
114. Peng H, Wu ZH, Zuo YL, Zhang ZM, Zhou KN, Su JQ. Single Laser Pulse Compression via Strongly Coupled Stimulated Brillouin Scattering in Plasma. *Phys Plasmas* (2016) 23(7):073516. doi:10.1063/1.4959173
115. Buono WT, Santos A, Maia MR, Pereira LJ, Tasca DS, Dechoum K, et al. Chiral Relations and Radial-Angular Coupling in Nonlinear Interactions of Optical Vortices. *Phys Rev A* (2020) 101:043821. doi:10.1103/PhysRevA.101.043821
116. Wu H-J, Yang H-R, Rosales-Guzmán C, Gao W, Shi B-S, Zhu Z-H. Vectorial Nonlinear Optics: Type-II Second-Harmonic Generation Driven by Spin-

Orbit-Coupled Fieldsfields. *Phys Rev A* (2019) 100:053840. doi:10.1103/PhysRevA.100.053840

117. R Mildren J Rabeau, editors. *Optical Engineering of Diamond*. John Wiley & Sons (2013).
118. Bai Z, Williams RJ, Kitzler O, Sarang S, Spence DJ, Wang Y, et al. Diamond Brillouin Laser in the Visible. *APL Photon* (2020) 5(3):031301. doi:10.1063/1.5134907
119. Bai Z, Zhang Z, Wang K, Gao J, Zhang Z, Yang X, et al. Comprehensive Thermal Analysis of Diamond in a High-Power Raman Cavity Based on FVM-FEM Coupled Method. *Nanomaterials* (2021) 11(6):1572. doi:10.3390/nano11061572
120. Williams RJ, Kitzler O, Bai Z, Sarang S, Jasbeer H, McKay A, et al. High Power diamond Raman Lasers. *IEEE J Select Top Quan Electron.* (2018) 24(5):1602214. doi:10.1109/JSTQE.2018.2827658
121. Pessot M, Maine P, Mourou G. 1000 Times Expansion/compression of Optical Pulses for Chirped Pulse Amplification. *Opt Commun* (1987) 62(6):419–21. doi:10.1016/0030-4018(87)90011-3
122. Pessot M, Harter DJ, Squier J, Mourou G. Chirped-pulse Amplification of 100-fsec Pulses. *Opt Lett* (1989) 14(15):797–9. doi:10.1364/OL.14.000797
123. Perry MD, Mourou G. Terawatt to Petawatt Subpicosecond Lasers. *Science* (1994) 264(5161):917–24. doi:10.1126/science.264.5161.917
124. Morin P, Dubertrand J, Beaure d'Augeres P, Quiquempois Y, Bouwmans G, Mussot A, et al. μJ Level Raman-Assisted Fiber Optical Parametric Chirped-Pulse Amplification. *Opt Lett* (2018) 43(19):4683–86. doi:10.1364/OL.43.004683
125. Guo Z, Yu L, Wang J, Wang C, Liu Y, Gan Z, et al. Improvement of the Focusing Ability by Double Deformable Mirrors for 10-PW-level Ti: Sapphire Chirped Pulse Amplification Laser System. *Opt Express* (2018) 26(20):26776–86. doi:10.1364/OE.26.026776
126. Zhu Z, Gao W, Mu C, Li H. Reversible Orbital Angular Momentum Photon-Phonon Conversion. *Optica* (2016) 3(2):212–7. doi:10.1364/OPTICA.3.000212
127. Lombardi GG. *Pulse Compression by Stimulated Brillouin Scattering*. Boston: O-E/Fiber Laser (1989). doi:10.1364/OL.5.000516
128. Offenberger AA, Thompson DC, Fedosejevs R, Harwood B, Santiago J, Manjunath HR. Experimental and Modeling Studies of a Brillouin Amplifier. *IEEE J Quan Electron.* (1993) 29(1):207–16. doi:10.1109/3.199261
129. Yuan H, Wang YL, Lu ZW, Zheng ZX. Small-Scale Self-Focusing of 200 ps Laser Pulses in Brillouin Amplification. *Chin Phys. B* (2015) 24(009):094210–270. doi:10.1088/1674-1056/24/9/094210
130. Yuan H, Lu ZW, Wang YL, Zheng ZX, Chen Y. Hundred Picoseconds Laser Pulse Amplification Based on Scalable Two-Cells Brillouin Amplifier. *Laser Part Beams* (2014) 32(03):369–74. doi:10.1017/S0263034614000238

Conflict of Interest: The authors declare that the research was conducted in the absence of any commercial or financial relationships that could be construed as a potential conflict of interest.

ORIGINAL RESEARCH
published: 22 September 2021
doi: 10.3389/fphy.2021.752081

Engineering Entangled Photons for Transmission in Ring-Core Optical Fibers

G. Cañas[1], **E. S. Gómez**[2,3], **E. Baradit**[1], **G. Lima**[2,3] **and S. P. Walborn**[2,3]*

[1]Departamento de Física, Universidad del Bío-Bío, Concepción, Chile, [2]Departamento de Física, Universidad de Concepción, Concepción, Chile, [3]Millennium Institute for Research in Optics, Universidad de Concepción, Concepción, Chile

The capacity of optical communication channels can be increased by space division multiplexing in structured optical fibers. Radial core optical fibers allows for the propagation of twisted light–eigenmodes of orbital angular momentum, which have attracted considerable attention for high-dimensional quantum information. Here we study the generation of entangled photons that are tailor-made for coupling into ring core optical fibers. We show that the coupling of photon pairs produced by parametric down-conversion can be increased by close to a factor of three by pumping the non-linear crystal with a perfect vortex mode with orbital angular momentum ℓ, rather than a gaussian mode. Moreover, the two-photon orbital angular momentum spectrum has a nearly constant shape. This provides an interesting scenario for quantum state engineering, as pumping the crystal with a superposition of perfect vortex modes can be used in conjunction with the mode filtering properties of the ring core fiber to produce simple and interesting quantum states.

Keywords: parametric down conversion, ring-core fiber, entangled photons, orbital angular momentum, perfect vortex beam

Edited by:
Bao-Sen Shi,
University of Science and Technology of China, China

Reviewed by:
Jianming Wen,
Kennesaw State University, United States
Bi-Heng Liu,
University of Science and Technology of China, China
Mingtao Cao,
National Time Service Center (CAS), China

***Correspondence:**
S. P. Walborn
swalborn@udec.cl

Specialty section:
This article was submitted to Optics and Photonics, a section of the journal Frontiers in Physics

Received: *02 August 2021*
Accepted: *07 September 2021*
Published: *22 September 2021*

Citation:
Cañas G, Gómez ES, Baradit E, Lima G and Walborn SP (2021) Engineering Entangled Photons for Transmission in Ring-Core Optical Fibers. Front. Phys. 9:752081. doi: 10.3389/fphy.2021.752081

1 INTRODUCTION

Distribution of photonic entangled states is a cornerstone of future quantum networks. Most likely, this will need to be realized within the same optical infrastructure as standard telecommunications networks. Recent developments in optical fiber technology have resulted in novel fiber core structures, which allow for the propagation of multiple spatial modes. These fibers are expected to play an important role in increasing the transmission capacity of future telecommunications networks through space division multiplexing (SDM) [1]. Examples of SDM fiber candidates include multi-mode fibers [2,3], multi-core fibers [4], and ring core fibers [5], among others. In the quantum regime, SDM technology has attractive features. The multiple spatial modes are a straightforward way to increase the dimension of quantum systems, which has several advantages in quantum key distribution (QKD) [6–11], and have shown to be more resistant to some types of noise [12]. Additional applications can be found in a recent review [13]. In addition to providing multiple channels, it is expected that these fibers will offer more phase stability, when compared to superposition states of several modes propagating in independent fibers [14,15].

Ring-core fibers (RCFs) allow for the propagation of orbital angular momentum (OAM) eigenmodes [16–25], which have attracted considerable attention as they allow for the encoding of high-dimensional quantum information [26–28]. To date, the principal source of entangled photons has been spontaneous parametric down-conversion (SPDC). A beautiful and useful characteristic of SPDC is that the two

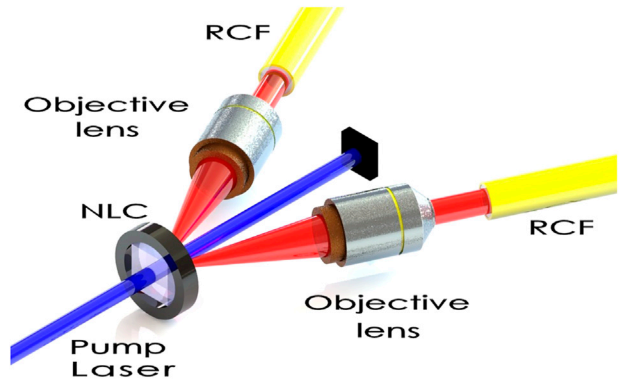

FIGURE 1 | Sketch of the basic idea. SPDC at a thin non-linear crystal (NLC) produces down-converted photon pairs, which are then coupled into ring-core fibers. The angle between the down-converted beams and the pump beam is exaggerated in the Panel for visual clarity. In the calculations, it is assumed to be small enough so that the setup can be treated as co-linear. The optical systems are such that the image plane of the crystal coincides with the entrance face of the fibers, with appropriate magnification factors.

photon spatial state can be engineered by manipulating the pump beam [29–35]. This has led to the production of quantum states with interesting properties [36–40]. The entanglement properties of these states are determined by the mode decomposition of the two-photon state, in which one has the freedom to choose between quite a few families of transverse modes. Of particular interest are those decompositions onto OAM eigen-modes such as Laguerre-Gauss [41–44] or Bessel-Gauss [45–47], which comprise a set of Schmidt modes of the two-photon state [48,49].

In this paper we study the coupling of down-converted photons into RCFs and the two-photon state that is produced, as sketched in **Figure 1**. We consider the decomposition of the two-photon state in terms of perfect vortex (PV) modes, which can have near-perfect fidelity with the eigen-modes of RCFs [25]. We show that by pumping the down-conversion crystal with a PV pump beam, the amplitude of the most relevant down-converted PV modes can be increased while maintaining a high degree of entanglement. While the two-photon OAM mode spectrum is wider for a gaussian pump beam, leading to larger Schmidt numbers, this increase in entanglement is irrelevant when coupling into RCFs or similar optical devices, as only a finite set of lower-order PV modes excite the fiber eigen-modes. In addition, the shape of the mode spectrum is nearly independent of the OAM of the PV pump beam. The combination of the two-photon state engineering using PV pump beams and the mode filtering provided by the RCF can be a powerful tool, providing a simple method to generate interesting two-photon states, some examples of which are discussed in **section 4**.

2 PERFECT VORTEX BEAMS AND RING CORE FIBERS

An illustration of a RCF is shown in **Figure 2**. It is described by a ring-shaped core, with interior radius b and exterior radius a. A set of eigenmodes of the RCF (circularly symmetric LP modes) have an azimuthal phase dependence $e^{i\ell\phi}$, and thus carry OAM [50]. In Ref. 25 it was shown that an example of a commercially available RCF supports 13 LP modes with OAM $\ell = 0, \pm1, \pm2, \cdots \pm 6$. Moreover, depending on the fiber properties, they can have near perfect (~ 0.995) overlap with the so-called PV modes with the same value of ℓ. PV modes are the Fourier transform of Bessel-Gaussian beams, carrying OAM with eigenvalue ℓ. They are given by [51].

$$\mathcal{U}_\ell(\boldsymbol{r}) = N \exp(i\ell\phi) u_\ell(r), \tag{1}$$

where N is a normalization constant and the radial component is given by

$$u_\ell(r) = \exp\left(-\frac{(r^2 + r_r^2)}{w_0^2}\right) I_\ell\left(\frac{2rr_r}{w_0^2}\right), \tag{2}$$

with I_ℓ the modified Bessel function of the first kind. The parameters r_r and w_0 are the ring radius and the Gaussian beam waist at the focus. As shown in Ref. 51, with certain parameter relations, the radial function can be approximated by

$$u_\ell(r) \approx u(r) = \exp\left(-\frac{(r - r_r)^2}{w_0^2}\right), \tag{3}$$

which presents the interesting property that it is independent of ℓ. Numerical evaluation of the overlap between normalized versions of **(2)** and **(3)** is near unity when $\ell \lesssim 3r_r/w_0$. The ring-shape with constant radius makes these modes attractive for coupling into RCFs [25,51–53]. Thus, entangled photons in perfect vortex modes are an interesting candidate for distribution of entanglement in RCFs.

3 SPONTANEOUS PARAMETRIC DOWN-CONVERSION WITH PV MODES

The two-photon state produced from SPDC using a continuous-wave, monochromatic pump beam incident on a thin non-linear crystal, is given by [29,54–56].

$$|\psi\rangle = \iint d\boldsymbol{q}_1 d\boldsymbol{q}_2 \psi(\boldsymbol{q}_1, \boldsymbol{q}_2) |\boldsymbol{q}_1\rangle |\boldsymbol{q}_2\rangle, \tag{4}$$

where $\boldsymbol{q}_l$ ($l = 1, 2$) are transverse components of the down-converted wave vectors. The single photons with transverse wave vector q_l and frequency ω_l are written as $|\boldsymbol{q}_l\rangle$. The two-photon amplitude in the paraxial regime, written in wave vector coordinates at the exit face of the crystal is given by

$$\psi(\boldsymbol{q}_1, \boldsymbol{q}_2) = \mathcal{V}(\boldsymbol{q}_1 + \boldsymbol{q}_2) \mathrm{sinc}[(k_{1z} + k_{2z} - k_{pz})L/2]. \tag{5}$$

Here L is the length of the non-linear crystal and k_{pz} is the z-component of the pump beam wavevector. The function $\mathcal{V}(\boldsymbol{q})$ is the angular spectrum of the pump beam [29], and the sinc function is known as the phase matching function [55]. For simplicity, all modes are assumed to be polarized. If narrowband filters are used to detect the photons, we can assume monochromatic down-converted fields, and apply the Fresnel approximation $k_z \approx k(1{-}q^2/2k^2)$, which gives

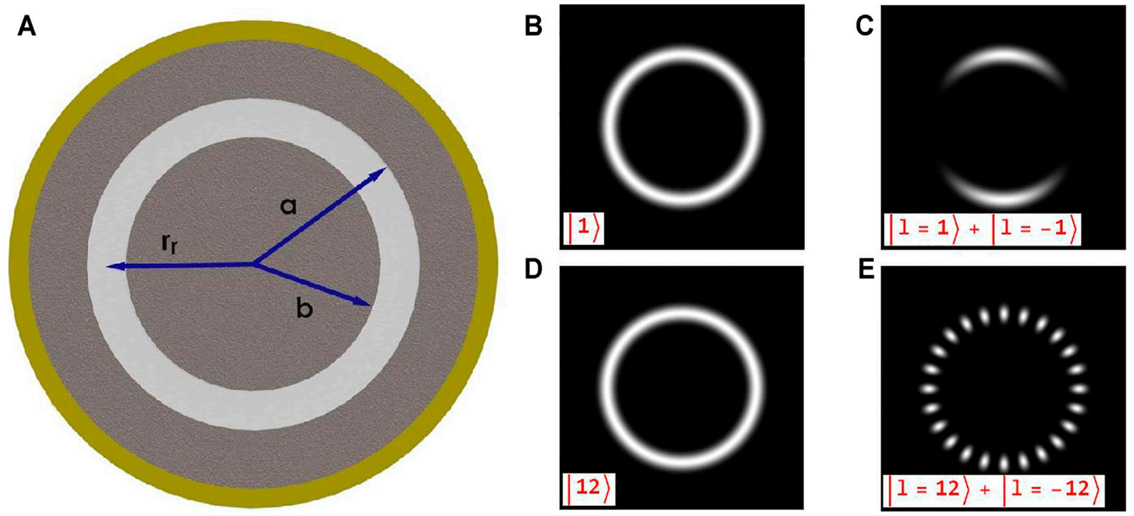

FIGURE 2 | (A) Illustration of a Ring-Core Fiber (RCF). **(B)**, **(D)** Profiles of perfect vortex modes and **(C)**, **(E)** superpositions of perfect vortex modes.

$$k_{1z} + k_{2z} - k_{pz} \approx -\frac{1}{2k_p}\left[\delta_1 \boldsymbol{q}_1 - \delta_2 \boldsymbol{q}_2\right]^2, \tag{6}$$

where we define $k_p \equiv |\boldsymbol{k}_p|$ as the wavenumber of the pump beam, and $\delta_1 = \sqrt{k_2/k_1}$, $\delta_2 = \sqrt{k_1/k_2}$. We can rewrite the two-photon amplitude as:

$$\psi(\boldsymbol{q}_1, \boldsymbol{q}_2) = \mathcal{V}(\boldsymbol{q}_1 + \boldsymbol{q}_2)\mathcal{S}\left(\left[\delta_1 \boldsymbol{q}_1 - \delta_2 \boldsymbol{q}_2\right]^2\right), \tag{7}$$

where $\mathcal{S}(\boldsymbol{q}) = A\mathrm{sinc}\left(Lq^2/4k_p\right)$. Defining the variables

$$\boldsymbol{Q}_\pm = \boldsymbol{q}_1 \pm \boldsymbol{q}_2, \tag{8}$$

$$\boldsymbol{R}_\pm = \frac{1}{2}(\boldsymbol{r}_1 \pm \boldsymbol{r}_2) \tag{9}$$

$$\delta_\pm = \frac{1}{2}(\delta_1 \pm \delta_2), \tag{10}$$

and taking the Fourier transform of **Eq. 7**, the two-photon amplitude can be written in position coordinates $\boldsymbol{r}_1$, $\boldsymbol{r}_2$ as

$$\Psi(\boldsymbol{r}_1, \boldsymbol{r}_2) = \frac{1}{2}\iint d\boldsymbol{Q}_+ d\boldsymbol{Q}_- e^{i\boldsymbol{Q}_+\boldsymbol{R}_+} e^{i\boldsymbol{Q}_-\boldsymbol{R}_-}\mathcal{V}(\boldsymbol{Q}_+) \times \mathcal{S}\left(\left[\delta_+ \boldsymbol{Q}_+ + \delta_- \boldsymbol{Q}_-\right]^2\right). \tag{11}$$

By integrating **Eq. 11**, we obtain

$$\Psi(\boldsymbol{r}_1, \boldsymbol{r}_2) = \frac{1}{2}\mathcal{W}\left(\boldsymbol{R}_+ - \frac{\delta_+}{\delta_-}\boldsymbol{R}_-\right)\Gamma(\boldsymbol{R}_-), \tag{12}$$

where $\mathcal{W}$ and Γ are the Fourier transforms of the angular spectrum of the pump beam $\mathcal{V}(q)$ and the phase matching function $\mathcal{S}(q)$, respectively.

3.1 Projection Onto PV Modes

The amplitude to project the two-photon state onto a product state of PV modes is given by

$$\mathcal{A}(\ell_1, \ell_2) = \frac{1}{2}\iint d\boldsymbol{r}_1 d\boldsymbol{r}_2 \Gamma\left(\frac{\boldsymbol{r}_1 - \boldsymbol{r}_2}{2}\right)\mathcal{U}^*_{\ell_1}(\boldsymbol{r}_1)\mathcal{U}^*_{\ell_2}(\boldsymbol{r}_2) \times \mathcal{W}\left(\frac{\boldsymbol{r}_1 + \boldsymbol{r}_2}{2} - \frac{\delta_+}{\delta_-}\frac{\boldsymbol{r}_1 - \boldsymbol{r}_2}{2}\right). \tag{13}$$

In the thin crystal approximation, such that $L \ll z_R$, where z_R is the Rayleigh range of the pump beam, we can approximate $\Gamma\left(\frac{\boldsymbol{r}_1 - \boldsymbol{r}_2}{2}\right) \approx 2\delta(\boldsymbol{r}_1 - \boldsymbol{r}_2)$, where $\delta(x)$ is the Dirac delta function. The amplitude becomes

$$\boldsymbol{\mathcal{A}}(\ell_1, \ell_2) = \int d\boldsymbol{r}\mathcal{U}^*_{\ell_1}(\boldsymbol{r})\mathcal{U}^*_{\ell_2}(\boldsymbol{r})\mathcal{W}(\boldsymbol{r}). \tag{14}$$

Assuming now that the pump beam is an OAM eigenstate, it can be written as $\mathcal{W}(\boldsymbol{r}) = M\exp(i\ell\phi)w_\ell(r)$, with M a normalization constant. Then, using expression **(1)** for the PV modes, we have

$$\mathcal{A}(\ell_1, \ell_2, \ell) = (N^*)^2 M \int dr\, r u^\star_{\ell 1}(r) u^\star_{\ell_2}(r) w_\ell(r) \times \int d\phi e^{i\phi(\ell - \ell_1 - \ell_2)}, \tag{15}$$

which leads to

$$\mathcal{A}(\ell_1, \ell_2, \ell) = \delta_{\ell, \ell_1 + \ell_2}(N^*)^2 M' \int dr\, r u^\star_{\ell_1}(r) u^\star_{\ell_2}(r) w_\ell(r), \tag{16}$$

where $M' = 2\pi M$. The appearance of the Kronecker delta function guarantees that the OAM winding numbers of the down-converted photons are correlated. These OAM correlations are typically observed in OAM mode decompositions of the two photon state, and corresponds to conservation of the orbital angular momentum [41–46,48,49,57].

3.2 Limited OAM Spectra: Optimizing Into RCF Modes

Let us consider now that the OAM spectra of the down-converted photons are limited by the optical system, such as is the case when

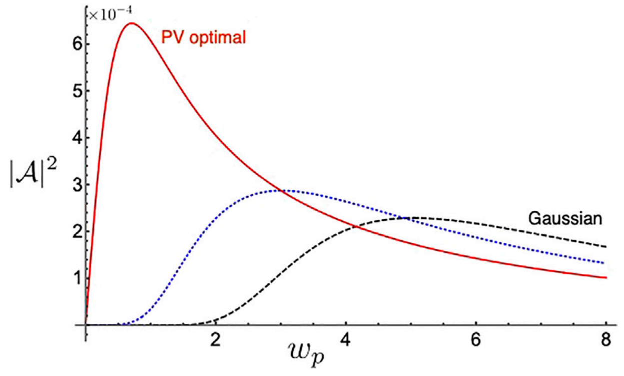

FIGURE 3 | Overlap squared $|\mathcal{A}|^2$ as a function of the pump beam width w_p (in arbitrary units of length) for a gaussian pump beam $r_{rp} = 0$ (black dashed curve), and for a PV pump beam with ring radius $r_{rp} = 2w_0 \approx 0.57r_r$ (blue dotted curve) and ring radius $r_{rp} = r_r = 3.53w_0$ (PV optimal, red solid curve) for best coupling into a commercially available RCF [25]. The optimal PV pump beam increases the probability to produce relevant down-converted modes by a factor of ~ 2.8.

coupling into a RCF, which supports a finite set $\{L\}$ of OAM eigenmodes. We assume that $\ell_j \in \{L\}$ and the ratio r_r/w_0 of the down-converted modes permits approximation of $u_\ell(r) \approx u(r)$, where we recall that this is valid when $\ell_j \lesssim r_r/w_0$. Then, we can write the PV mode product

$$u^*_{\ell_1}(r)u^*_{\ell_2}(r) \approx [u^*(r, r_r, w_0)]^2 = u^*(r, r_r, w_0/\sqrt{2}), \tag{17}$$

where the RCF ring radius and beam width are included explicitly in the argument of these functions for clarity. The integral **(16)** is thus the overlap of a PV radial mode function described by a gaussian ring centered at r_r and ring thickness $w_0/\sqrt{2}$, with the pump radial mode function $w_\ell(r)$. It is thus expected that the amplitude integral is maximized when the pump beam is also a PV beam, with the same ring thickness and ring width. Let us also consider that the pump is prepared in a PV mode and that $w_\ell(r) \approx u(r) \equiv u\ (r, r_{rp}, w_p)$. The amplitude integral **(16)** becomes

$$\mathcal{A} = (N^*)^2 M' \int dr\, r\, u^*(r, r_r, w_0/\sqrt{2})\, u(r, r_{rp}, w_p), \tag{18}$$

which has the very appealing characteristic that it depends neither on ℓ nor ℓ_1, ℓ_2. In **Figure 3** we show a plot of $|\mathcal{A}|^2$ as a function of the pump beam width w_p for several pump beams, where we used $r_r = 3.53w_0$, corresponding to the parameters of PV modes that are most efficiently coupled into a commercially available RCF [25]. The red solid curve and the blue dotted curve correspond to PV pump beams with ring radii $r_{rp} = r_r$ and $r_{rp} = 2w_0 \approx 0.57r_r$. As a comparison, we also show the squared amplitude when the pump beam is described by a gaussian beam $w(r) = \sqrt{2/(\pi w_p^2)}\exp(-r^2/w_p^2)$. We can see that the amplitude to produce down-converted photons in these eigenmodes can be increased by using a PV pump beam, and reaches a maximum when $w_p = w_0/\sqrt{2}$. In principle, this corresponds to an a factor of ~ 2.8 increase in generation of the relevant down-converted modes. We note that we have considered nearly co-linear SPDC, in which the pump beam and photon pair propagate in the same direction. It has been shown that non-colinear SPDC can lead to asymmetry when the pump beam is a PV mode [58]. Recently, it was shown that the heralding efficiency of a twisted down-converted photon with $\ell_2 = \ell$ (with $\ell_1 = 0$) can be increased by pumping with a PV mode Anwar et al. [47].

An important characteristic here is that, aside from the OAM correlation provided by the Kronecker delta function, the amplitude of the overlap coefficients does not depend upon ℓ_1, ℓ_2 nor ℓ. Thus, considering a post-selected set of PV modes in both the down-converted fields, the two-photon state can be written

$$|\psi\rangle = \frac{\mathcal{A}}{\sqrt{C}} \sum_{\ell-\ell_1, \ell_1 \in \{L\}} |\ell_1\rangle_1 |\ell - \ell_1\rangle_2, \tag{19}$$

where the states $|\ell\rangle$ represent single photon PV modes, i.e., $\langle \mathbf{r}|\ell\rangle = \mathcal{U}_\ell(\mathbf{r})$, C is a normalization constant, and $\{L\}$ is the set of OAM supported by the fibers. This is a maximally entangled state, whose entanglement depends upon the number of terms in the summation. We emphasize here the fact that **(19)** is valid in the case where the characteristics of the pump and down-converted photons allow the modes to be written in form **(3)**. Typically, this approach is restricted to smaller OAM values. In the next section, we consider the complete two-photon OAM spectrum.

3.3 Unlimited OAM Spectra

When the optical system does not severely limit the OAM spectra of the down-converted photons, such as emission into free space, we can evaluate the amplitude integral **(16)** numerically using **Eq. 2** to describe the modes. Plots of $|\mathcal{A}(\ell_1, \ell - \ell_1, \ell)|^2$ as a function of ℓ_1 are shown in **Figure 4** for $\ell = 0, \pm 3, \pm 12$. To compare the relative weights, we have normalized to the value $|\mathcal{A}(0,0,0)|^2$. We can see that the curves have similar forms and magnitudes, but are shifted along the ℓ_1 axis by an amount equal to ℓ.

To compare between a PV and a gaussian pump beam, we evaluated the OAM mode spectra and the entanglement of the two-photon state. **Figure 5A**) shows the normalized probabilites $|\mathcal{A}_{\ell_1}|^2/\sum_{\ell_1}|\mathcal{A}_{\ell_1}|^2$ for a PV pump beam given by **(2)** with the optimal parameters $w_p = w/\sqrt{2}$ and $r_{rp} = r_r = 3.53w_0$, and a gaussian beam with $w_p = 5w$, similar to **section 3.2**. We can see that the probability to produce down-converted PV modes in the range $|\ell_j| \lesssim 15$ $(j = 1, 2)$ is larger for the PV pump beam than the gaussian pump beam, and nearly constant for $|\ell_j| \lesssim 6$. Moreover, the probabilities approach zero for $|\ell_j| \sim 30$. The gaussian pump mode, on the other hand, results in an OAM spectrum with much more spread, giving negligible probabilities only when $|\ell_j| \gtrsim 100$ (not shown). The narrower mode spectrum produced by the PV pump beam concentrates the probability in a smaller group of OAM modes, leading to better efficiency when one is working within this finite subspace. For example, looking at the subset of modes corresponding to $|\ell| \leq 15$ (a 31×31 dimensional bipartite system) in **Figure 5A**, this corresponds to 81% of the state produced with the PV pump beam, and only 41% percent of the state produced by the gaussian pump beam. Likewise, for

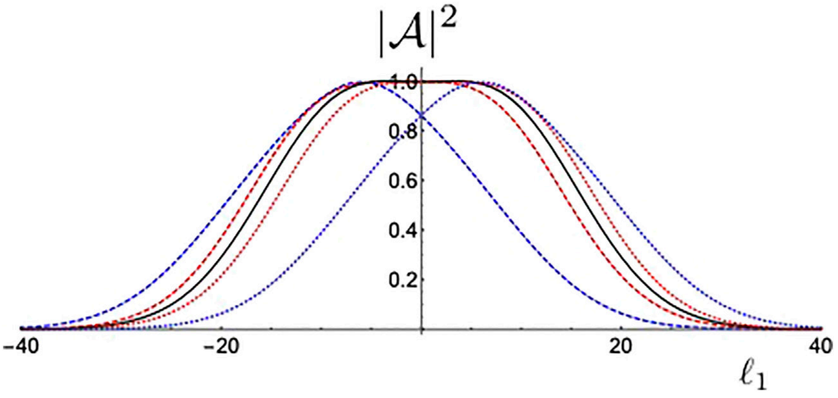

FIGURE 4 | Mode probabilities $|\mathcal{A}(\ell_1, \ell - \ell_1, \ell)|^2$, normalized by $|\mathcal{A}(0,0,0)|^2$, as a function of ℓ_1 for a PV pump beams with optimal width $w_p = w_0/\sqrt{2}$ and ring radius $r_{rp} = r_r$, and OAM number $\ell = 0$ (black solid line), $\ell = \pm 3$ (red dashed and dotted lines) and $\ell = \pm 12$ (blue dashed and dotted lines). The curves are centered at $\ell_1 = \ell$.

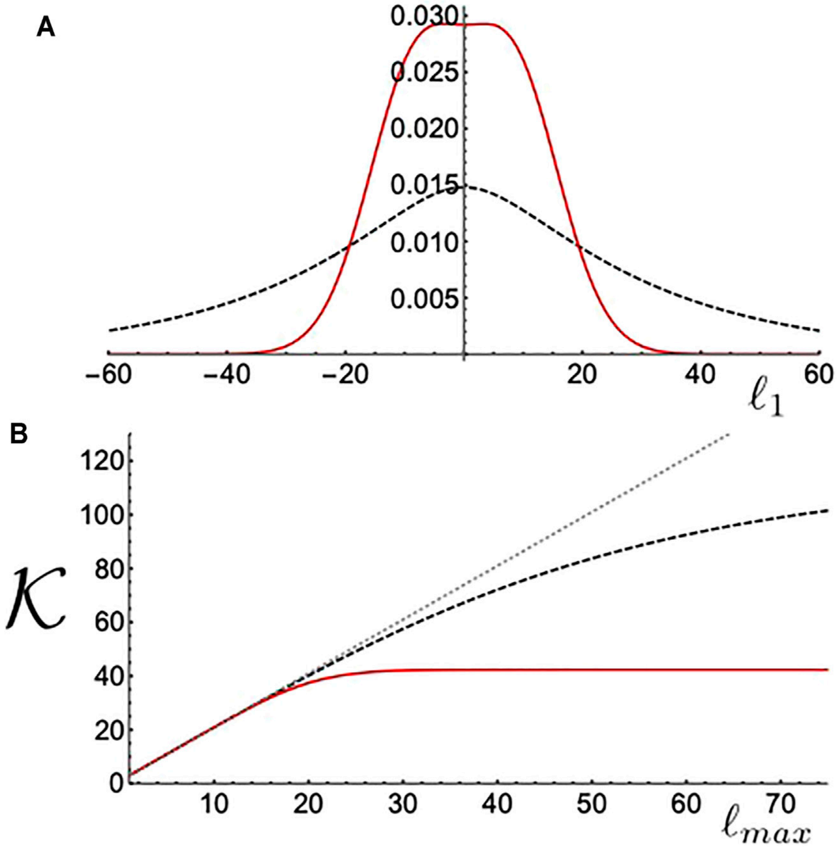

FIGURE 5 | (A) Normalized probabilities for an optimal PV pump beam with $\ell = 0$ (red solid line) and a gaussian pump beam with $w_p = 5w_0$ (black dashed line). The PV pump mode concentrates the probability in lower OAM modes. **(B)** The Schmidt number $\mathcal{K}$ for the two photon state, truncated at ± ℓ_{max} for the same pump beams. The grey dotted line corresponds to the maximum allowable Schmidt number, given by $d = 2\ell_{max} + 1$.

generating the 13 OAM modes ($|\ell| \leq 6$) of the RCF fiber studied in Ref. 25, the PV pump beam concentrates 38% of the probability in these modes, compared to 19% for the gaussian pump beam.

It is known that SPDC can produce high-dimensional entanglement in transverse spatial modes [13,26–28,36,59]. Let us see how the PV pump beam compares with a gaussian pump beam for high-dimensional entanglement generation. The

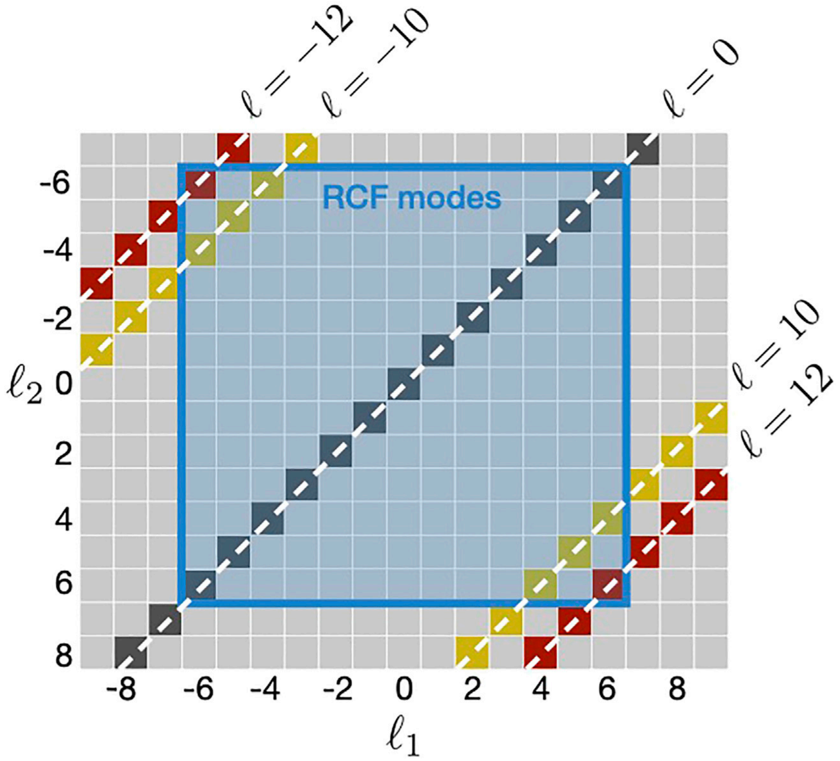

FIGURE 6 | Illustration of state engineering using OAM correlations from SPDC and mode filtering provided by ring core fibers (RCF). OAM correlations between the pump beam and down-converted photons produce photons with OAM distributed along the diagonal directions. The RCF selects modes within the shaded blue square. Thus, only OAM mode pairs along the diagonals within the square will propagate.

entanglement in PV modes can be evaluated by calculating the Schmidt number, given by

$$\mathcal{K}=\frac{\left(\sum\limits_{\ell_1=-\ell_{max}}^{\ell_{max}}\mathcal{A}_{\ell_1}\right)^2}{\sum\limits_{\ell_1=-\ell_{max}}^{\ell_{max}}\mathcal{A}_{\ell_1}^2}, \tag{20}$$

where we assume that the relevant OAM spectrum is limited by ± ℓ_{max}, so that the overall dimension of the system is $d=2\ell_{max}+1$. In **Figure 5B** we calculate $\mathcal{K}$ for different values of ℓ_{max} for the same pump beams as in **Figure 5A**. The dotted grey line shows the maximum allowable $\mathcal{K}=d$ for comparison. We can see that the PV pump beam results in a Schmidt number that saturates at around $\mathcal{K}\sim 42$, while the gaussian pump beam saturates at $\mathcal{K}\sim 128$ for $\ell_{max}\sim 150$ (not shown). For smaller values of ℓ_{max}, the PV beam and gaussian beam give almost equivalent Schmidt number, and nearly saturate the maximum allowed value of d. We also calculated the largest Schmidt numbers for PV pump modes with $|\ell|\leq 12$, and obtained nearly constant results in the range $\mathcal{K}\sim 40-43$. Thus, if the optical system imposes no practical limit on the system dimension, the Gaussian beam allows for higher-dimensional entanglement. Nonetheless, for the more realistic scenario in which the optical system supports a finite set of modes with smaller values of $|\ell_j|$, a PV pump beam concentrates the probability into a smaller set of modes, resulting in a more efficient source, and near maximal entanglement.

4 APPLICATION TO QUANTUM STATE ENGINEERING

Engineering of quantum states with different properties is both a challenge and a goal in quantum information science. In SPDC, this can be achieved by manipulation of the properties of the pump beam, as well as through mode filtering of the individual photons. In this regard, integrating the SPDC results from the last sections together with the transmission properties of RCFs presents several interesting possibilities.

As shown in **Figures 4**, **5**, the PV pump mode concentrates the two-photon probability into a smaller set of joint OAM modes, which is particularly interesting when the photons are coupled into devices that support a finite number of eigen-modes. Let us consider that both down-converted photons are coupled to RCFs that support OAM eigenmodes with $|\ell_1|, |\ell_2|\leq 6$, as was studied in Ref. 25. Thus, each down-converted photon has an OAM spectrum that is truncated in the shaded blue square region shown in **Figure 6**. When the pump beam is described by a single PV mode with OAM ℓ, the two-photon state is described by **(19)**. The important point here is that the state **(19)** contains joint OAM modes with $\ell_2=\ell-\ell_1$, non-zero overlap integral **(18)**, and with $|\ell_1|, |\ell_2| \le 6$. These three conditions can be used to engineer the quantum state. **Figure 6** illustrates the allowable joint OAM spectra for different pump beams, where allowed mode combinations appear on the diagonals, as a function of the pump OAM number ℓ, and within the blue square region, corresponding to the mode selection of the RCF. Since for this set of modes the overlap integral is approximately given by **(18)**, which is independent of the OAM of the pump and down-converted fields, the pump OAM ℓ can be used as a parameter to control the entanglement, where the Schmidt number of the state is essentially determined by the number of OAM components distributed along diagonals and within the RCF square. Thus, one can achieve a 13-dimensional entangled state by pumping with $\ell = 0$. Alternatively, a separable product state can be achieved by pumping with $\ell = \pm 12$, which gives a two-photon state $|\psi\rangle = |\pm 6\rangle_1 |\pm 6\rangle_2$, since these are the only joint OAM modes that are both produced in SPDC and supported by the RCF.

A maximally entangled pair of qubits is arguably the most useful quantum state, with numerous applications in quantum information, such as teleportation and quantum key distribution. This state can be created by using a pump beam that is a superposition of PV modes. For example, using a pump beam described by a PV mode superposition $\mathcal{E}(\boldsymbol{r}) = \alpha \mathcal{U}_{12}(\boldsymbol{r}) + \beta \mathcal{U}_{-12}(\boldsymbol{r})$, with intensity profile illustrated in **Figure 2E**, the two-photon state that propagates in the RCFs modes is

$$|\psi_{\pm 12}\rangle = \alpha |6\rangle_1 |6\rangle_2 + \beta |-6\rangle_1 |-6\rangle_2. \tag{21}$$

Maximal entanglement is achieved when $|\alpha| = |\beta|$. Similar Bell-type states have been prepared in OAM modes from SPDC, however, they rely on post-selection at the detection system [57,60]. Moreover, we note that here the OAM numbers are correlated ($\ell_1 = \ell_2$), as opposed to anti-correlated ($\ell_1 = -\ell_2$), as is usually the case due to OAM conservation. Correlated OAM states have been shown to be useful for quantum metrology [61].

By the same rationale, pumping with an equally weighted superposition of ±10, we have

$$\begin{aligned}|\psi_{\pm 10}\rangle = \frac{1}{\sqrt{6}} (&|4\rangle_1 |6\rangle_2 + |5\rangle_1 |5\rangle_2 + |6\rangle_1 |4\rangle_2 + |-4\rangle_1 |-6\rangle_2 \\ &+ |-5\rangle_1 |-5\rangle_2 + |-6\rangle_1 |-4\rangle_2),\end{aligned} \tag{22}$$

which is a 6 × 6 maximally entangled state. Higher-dimensional states can provide higher key transmission rates in quantum key distribution [6–11], as well as increased resilience to noise [12] and other applications [13,27,28]. These are just a few simple examples of how the dimension and entanglement of the two-photon state can be controlled by manipulating the PV pump beam and post-selection capabilities of the ring-core fiber. More complex quantum states can be created by considering different linear combinations of PV pump beams.

5 CONCLUSION

The generation of entangled photons in perfect vortex modes was studied in the spontaneous parametric down-conversion process. Perfect vortex modes carry orbital angular momentum, and have very high fidelity with the eigen-modes of ring-core optical fibers. We show that pumping the non-linear crystal with a perfect-vortex beam, leads to an output two-photon state that is concentrated in a smaller set of modes, when compared to that of a Gaussian pump beam. It is shown that a near three-fold increase in the coupling efficiency into ring-core fibers could be achieved. Moreover, the two-photon mode spectrum can have near constant magnitude, allowing for a high degree of entanglement.

The use of ring-core fibers as mode filters together with pump beam engineering can be a powerful tool for crafting novel quantum states. Several examples are given, ranging from product states to 13 × 13 dimensional entangled states. These can be produced by changing a single pump beam parameter. Though we focus only on OAM modes, our findings can be combined with correlations in other degrees of freedom, such as polarization. We expect our results will be important for integrating entangled photon sources with future optical fiber networks that employ structured optical fibers.

DATA AVAILABILITY STATEMENT

The original contributions presented in the study are included in the article/Supplementary Material, further inquiries can be directed to the corresponding author.

AUTHOR CONTRIBUTIONS

GC, EG, EB, GL, and SW conceived the work, GC and SW performed the calculations, all authors analyzed results and wrote the manuscript.

FUNDING

This work was supported by the Chilean agencies Fondo Nacional de Desarrollo Científico y Tecnológico (FONDECYT) (1190933, 1190901, 1200266, 1200859) and ANID–Millennium Science Initiative Program–ICN17_012.

ACKNOWLEDGMENTS

The authors thank S. E. Restrepo for valuable discussions.

REFERENCES

1. Richardson DJ, Fini JM, and Nelson LE. Space-division Multiplexing in Optical Fibres. *Nat Photon* (2013) 7:354–62. doi:10.1038/nphoton.2013.94
2. Sillard P, Bigot-Astruc M, and Molin D. Few-mode Fibers for Mode-Division-Multiplexed Systems. *J Lightwave Technol* (2014) 32:2824–9. doi:10.1109/jlt.2014.2312845
3. Rademacher G, Luís RS, Puttnam BJ, Eriksson TA, Ryf R, Agrell E, et al. High Capacity Transmission with Few-Mode Fibers. *J Lightwave Technol* (2019) 37: 425–32. doi:10.1109/jlt.2018.2870038
4. Saitoh K, and Matsuo S. Multicore Fiber Technology. *J Lightwave Technol* (2016) 34:55–66. doi:10.1109/jlt.2015.2466444
5. Brunet C, Ung B, Wang L, Messaddeq Y, LaRochelle S, and Rusch LA. Design of a Family of Ring-Core Fibers for OAM Transmission Studies. *Opt Express* (2015) 23:10553–63. doi:10.1364/OE.23.010553
6. Bourennane M, Karlsson A, and Bjork G. Quantum Key Distribution Using Multilevel Encoding. *Phys Rev A (Atomic, Mol Opt Physics)* (2001) 64:012306. doi:10.1103/physreva.64.012306
7. Collins D, Gisin N, Linden N, Massar S, and Popescu S. *Phys Rev Lett* (2002) 88:040404. doi:10.1103/physrevlett.88.040404
8. Cerf NJ, Bourennane M, Karlsson A, and Gisin N. Security of Quantum Key Distribution Usingd-Level Systems. *Phys Rev Lett* (2002) 88:127902. doi:10.1103/physrevlett.88.127902
9. Walborn SP, Lemelle DS, Almeida MP, and Ribeiro PH. Quantum Key Distribution with Higher-Order Alphabets Using Spatially Encoded Qudits. *Phys Rev Lett* (2006) 96:090501. doi:10.1103/PhysRevLett.96.090501
10. Huber M, and Pawłowski M. Weak Randomness in Device-independent Quantum Key Distribution and the Advantage of Using High-Dimensional Entanglement. *Phys Rev A* (2013) 88:032309. doi:10.1103/PhysRevA.88.032309
11. Cañas G, Vera N, Cariñe J, González P, Cardenas J, Connolly PWR, et al. High-dimensional Decoy-State Quantum Key Distribution over Multicore Telecommunication Fibers. *Phys Rev A* (2017) 96:022317. doi:10.1103/physreva.96.022317
12. Zhu F, Tyler M, Valencia NH, Malik M, and Leach J. Is High-Dimensional Photonic Entanglement Robust to Noise? *AVS Quan Sci* (2021) 3:011401. doi:10.1116/5.0033889
13. Erhard M, Krenn M, and Zeilinger A. Advances in High-Dimensional Quantum Entanglement. *Nat Rev Phys* (2020) 2:365–81. doi:10.1038/s42254-020-0193-5
14. Ding Y, Bacco D, Dalgaard K, Cai X, Zhou X, Rottwitt K, et al. High-dimensional Quantum Key Distribution Based on Multicore Fiber Using Silicon Photonic Integrated Circuits. *Npj Quan Inf* (2017) 3:25. doi:10.1038/s41534-017-0026-2
15. Xavier GB, and Lima G. Quantum Information Processing with Space-Division Multiplexing Optical Fibres. *Commun Phys* (2020) 3:9. doi:10.1038/s42005-019-0269-7
16. Bozinovic N, Yue Y, Ren Y, Tur M, Kristensen P, Huang H, et al.Terabit-scale Orbital Angular Momentum Mode Division Multiplexing in Fibers. *Science* (2013) 340:1545–8. doi:10.1126/science.1237861
17. Nejad RM, Allahverdyan K, Vaity P, Amiralizadeh S, Brunet C, Messaddeq Y, et al.Mode Division Multiplexing Using Orbital Angular Momentum Modes over 1.4-km Ring Core Fiber. *J Lightwave Technol* (2016) 34:4252–8. doi:10.1109/jlt.2016.2594698
18. Gregg P, Kristensen P, and Ramachandran S. Conservation of Orbital Angular Momentum in Air-Core Optical Fibers. *Optica* (2015) 2:267–70. doi:10.1364/optica.2.000267
19. Ramachandran S, Gregg P, Kristensen P, and Golowich SE. On the Scalability of Ring Fiber Designs for Oam Multiplexing. *Opt Express* (2015) 23:3721–30. doi:10.1364/oe.23.003721
20. Gregg P, Kristensen P, and Ramachandran S. 134km OAM State Propagation by Recirculating Fiber Loop. *Opt Express* (2016) 24:18938–47. doi:10.1364/oe.24.018938
21. Zhu L, Zhu G, Wang A, Wang L, Ai J, Chen S, et al. 18 Km Low-Crosstalk OAM + WDM Transmission with 224 Individual Channels Enabled by a Ring-Core Fiber with Large High-Order Mode Group Separation. *Opt Lett* (2018) 43:1890–3. doi:10.1364/OL.43.001890
22. Zhu G, Hu Z, Wu X, Du C, Luo W, Chen Y, et al. Scalable Mode Division Multiplexed Transmission over a 10-km Ring-Core Fiber Using High-Order Orbital Angular Momentum Modes. *Opt Express* (2018) 26:594–604. doi:10.1364/oe.26.000594
23. Cozzolino D, Bacco D, Da Lio B, Ingerslev K, Ding Y, Dalgaard K, et al. Orbital Angular Momentum States Enabling Fiber-Based High-Dimensional Quantum Communication. *Phys Rev Appl* (2019) 11:064058. doi:10.1103/physrevapplied.11.064058
24. Zhang J, Liu J, Shen L, Zhang L, Luo J, Liu J, et al.Mode-division Multiplexed Transmission of Wavelength-Division Multiplexing Signals over a 100-km Single-Span Orbital Angular Momentum Fiber. *Photon Res* (2020) 8:1236–42. doi:10.1364/prj.394864
25. Rojas-Rojas S, Cañas G, Saavedra G, Gómez ES, Walborn SP, and Lima G. Evaluating the Coupling Efficiency of Oam Beams into Ring-Core Optical Fibers. *Opt Express* (2021) 29:23381–92. doi:10.1364/OE.425419
26. Bavaresco J, Herrera Valencia N, Klöckl C, Pivoluska M, Erker P, Friis N, et al.Measurements in Two Bases Are Sufficient for Certifying High-Dimensional Entanglement. *Nat Phys* (2018) 14:1032–7. doi:10.1038/s41567-018-0203-z
27. Erhard M, Fickler R, Krenn M, and Zeilinger A. Twisted Photons: New Quantum Perspectives in High Dimensions. *Light Sci Appl* (2018) 7:17146. doi:10.1038/lsa.2017.146
28. Forbes A, and Nape I. Quantum Mechanics with Patterns of Light: Progress in High Dimensional and Multidimensional Entanglement with Structured Light. *AVS Quan Sci* (2019) 1:011701. doi:10.1116/1.5112027
29. Monken CH, Ribeiro PHS, and Pádua S. Transfer of Angular Spectrum and Image Formation in Spontaneous Parametric Down-Conversion. *Phys Rev A* (1998) 57:3123–6. doi:10.1103/physreva.57.3123
30. Torres JP, Deyanova Y, Torner L, and Molina-Terriza G. Preparation of Engineered Two-Photon Entangled States for Multidimensional Quantum Information. *Phys Rev A* (2003) 67:052313. doi:10.1103/physreva.67.052313
31. Miatto FM, Yao AM, and Barnett SM. Full Characterization of the Quantum Spiral Bandwidth of Entangled Biphotons. *Phys Rev A* (2011) 83:033816. doi:10.1103/physreva.83.033816
32. Yao AM. Angular Momentum Decomposition of Entangled Photons with an Arbitrary Pump. *New J Phys* (2011) 13:053048. doi:10.1088/1367-2630
33. Kovlakov EV, Bobrov IB, Straupe SS, and Kulik SP. Spatial bell-state Generation without Transverse Mode Subspace Postselection. *Phys Rev Lett* (2017) 118:030503. doi:10.1103/PhysRevLett.118.030503
34. Liu S, Zhou Z, Liu S, Li Y, Li Y, Yang C, et al.Coherent Manipulation of a Three-Dimensional Maximally Entangled State. *Phys Rev A* (2018) 98:062316. doi:10.1103/PhysRevA.98.062316
35. Kovlakov EV, Straupe SS, and Kulik SP. Quantum State Engineering with Twisted Photons via Adaptive Shaping of the Pump Beam. *Phys Rev A* (2018) 98:060301. doi:10.1103/PhysRevA.98.060301
36. Walborn SP, and Monken CH. Transverse Spatial Entanglement in Parametric Down-Conversion. *Phys Rev A* (2007) 76:062305. doi:10.1103/physreva.76.062305
37. Nogueira WA, Walborn SP, Pádua S, and Monken CH. Generation of a Two-Photon Singlet Beam. *Phys Rev Lett* (2004) 92:043602. doi:10.1103/PhysRevLett.92.043602
38. Vicuña Hernández V, Santiago JT, Jerónimo-Moreno Y, Ramírez-Alarcón R, Cruz-Ramírez H, U'Ren AB, et al. Double Transverse Wave-Vector Correlations in Photon Pairs Generated by Spontaneous Parametric Down-Conversion Pumped by Bessel-Gauss Beams. *Phys Rev A* (2016) 94:063863.
39. Gutiérrez-López D, Maldonado-Terrón M, Hernández RJ, Vicuña-Hernández V, Ramírez-Alarcón R, Cruz-Ramírez H, et al. Spatial Control of Spontaneous Parametric Down-Conversion Photon Pairs through the Use of Apertured Bessel-Gauss Pump Beams. *Phys Rev A* (2019) 100:013802. doi:10.1103/PhysRevA.100.013802
40. Baghdasaryan B, and Fritzsche S. Enhanced Entanglement from Ince-Gaussian Pump Beams in Spontaneous Parametric Down-Conversion. *Phys Rev A* (2020) 102:052412. doi:10.1103/PhysRevA.102.052412
41. Arnaut HH, and Barbosa GA. *Phys Rev Lett* (2001) 85:286.
42. Franke-Arnold S, Barnett SM, Padgett MJ, and Allen L. Two-photon Entanglement of Orbital Angular Momentum States. *Phys Rev A* (2002) 65: 033823. doi:10.1103/physreva.65.033823
43. Torres JP, Alexandrescu A, and Torner L. Quantum Spiral Bandwidth of Entangled Two-Photon States. *Phys Rev A* (2003) 68:050301. doi:10.1103/physreva.68.050301

44. Walborn SP, de Oliveira AN, Thebaldi RS, and Monken CH. Entanglement and Conservation of Orbital Angular Momentum in Spontaneous Parametric Down-Conversion. *Phys Rev A* (2004) 69:023811. doi:10.1103/physreva.69.023811
45. McLaren M, Agnew M, Leach J, Roux FS, Padgett MJ, Boyd RW, et al.Entangled Bessel-Gaussian Beams. *Opt Express* (2012) 20:23589–97. 10.1364/OE.20.023589.
46. McLaren M, Romero J, Padgett MJ, Roux FS, and Forbes A. Two-photon Optics of Bessel-Gaussian Modes. *Phys Rev A* (2013) 88:033818. doi:10.1103/PhysRevA.88.033818
47. Anwar A, Prabhakar S, and Singh RP. Size Invariant Twisted Optical Modes for Efficient Generation of Higher Dimensional Quantum States (2021). Available at: https://www.osapublishing.org/josab/upcoming_pdf.cfm?id=436088 (Accessed August 17, 2021).
48. Law CK, and Eberly JH. Analysis and Interpretation of High Transverse Entanglement in Optical Parametric Down Conversion. *Phys Rev Lett* (2004) 92:127903. doi:10.1103/physrevlett.92.127903
49. Straupe SS, Ivanov DP, Kalinkin AA, Bobrov IB, and Kulik SP. Angular Schmidt Modes in Spontaneous Parametric Down-Conversion. *Phys Rev A* (2011) 83. doi:10.1103/PhysRevA.83.060302
50. Allen L, Beijersbergen MW, Spreeuw RJC, and Woerdman JP. Orbital Angular Momentum of Light and the Transformation of Laguerre-Gaussian Laser Modes. *Phys Rev A* (1992) 45:8185–9. doi:10.1103/physreva.45.8185
51. Vaity P, and Rusch L. Perfect Vortex Beam: Fourier Transformation of a Bessel Beam. *Opt Lett* (2015) 40:597–600. doi:10.1364/OL.40.000597
52. Brunet C, Vaity P, Messaddeq Y, LaRochelle S, and Rusch LA. Design, Fabrication and Validation of an Oam Fiber Supporting 36 States. *Opt Express* (2014) 22:26117–27. doi:10.1364/OE.22.026117
53. Vaity P, Brunet C, Messaddeq Y, LaRochelle S, and Rusch LA. Exciting Oam Modes in Annular-Core Fibers via Perfect Oam Beams. The European Conference on Optical Communication. Bordeaux, France. Cannes, France: ECOC (2014). p. 1–3. doi:10.1109/ECOC.2014.6964195
54. Hong CK, and Mandel L. Theory of Parametric Frequency Down Conversion of Light. *Phys Rev A* (1985) 31:2409–18. doi:10.1103/physreva.31.2409
55. Walborn SP, Monken CH, Pádua S, and Souto Ribeiro PH. Spatial Correlations in Parametric Down-Conversion. *Phys Rep* (2010) 495:87–139. doi:10.1016/j.physrep.2010.06.003
56. Schneeloch J, and Howell JC. Introduction to the Transverse Spatial Correlations in Spontaneous Parametric Down-Conversion through the Biphoton Birth Zone. *J Opt* (2016) 18:053501. doi:10.1088/2040-8978/18/5/053501
57. Mair A, Vaziri A, Weihs G, and Zeilinger A. Entanglement of the Orbital Angular Momentum States of Photons. *Nature* (2001) 412:313–6. doi:10.1038/35085529
58. Jabir MV, Apurv Chaitanya N, Aadhi A, and Samanta GK. Generation of "perfect" Vortex of Variable Size and its Effect in Angular Spectrum of the Down-Converted Photons. *Sci Rep* (2016) 6:21877. doi:10.1038/srep21877
59. Schneeloch J, Tison CC, Fanto ML, Alsing PM, and Howland GA. Quantifying Entanglement in a 68-Billion-Dimensional Quantum State Space. *Nat Commun* (2019) 10:2785. doi:10.1038/s41467-019-10810-z
60. Langford NK, Dalton RB, Harvey MD, O'Brien JL, Pryde GJ, Gilchrist A, et al. *Phys Rev Lett* (2004) 93:053601. doi:10.1103/physrevlett.93.053601
61. D'Ambrosio V, Spagnolo N, Re LD, Slussarenko S, Li Y, Kwek LC, et al.Photonic Polarization Gears for Ultra-sensitive Angular Measurements. *Nat Commun* (2013) 4:2432.

Conflict of Interest: The authors declare that the research was conducted in the absence of any commercial or financial relationships that could be construed as a potential conflict of interest.

frontiers in Physics

ORIGINAL RESEARCH
published: 30 September 2021
doi: 10.3389/fphy.2021.752137

Optical Frequency Down-Conversion With Bandwidth Compression Based on Counter-Propagating Phase Matching

Dong-Jie Guo, Ran Yang, Yi-Chen Liu, Jia-Chen Duan, Zhenda Xie*, Yan-Xiao Gong* and Shi-Ning Zhu

National Laboratory of Solid State Microstructure, School of Physics, School of Electronic Science and Engineering, and Collaborative Innovation Center of Advanced Microstructures, Nanjing University, Nanjing, China

Edited by:
Bao-Sen Shi,
University of Science and Technology of China, China

Reviewed by:
Qiang Zhang,
University of Science and Technology of China, China
Yunfeng Huang,
University of Science and Technology of China, China

****Correspondence:***
Zhenda Xie
xiezhenda@nju.edu.cn
Yan-Xiao Gong
gongyanxiao@nju.edu.cn

Specialty section:
This article was submitted to Optics and Photonics, a section of the journal Frontiers in Physics

Received: *02 August 2021*
Accepted: *15 September 2021*
Published: *30 September 2021*

Citation:
Guo D-J, Yang R, Liu Y-C, Duan J-C, Xie Z, Gong Y-X and Zhu S-N (2021) Optical Frequency Down-Conversion With Bandwidth Compression Based on Counter-Propagating Phase Matching. Front. Phys. 9:752137. doi: 10.3389/fphy.2021.752137

Optical quantum network plays an important role in large scale quantum communication. However, different components for photon generation, transmission, storage and manipulation in network usually cannot interact directly due to the wavelength and bandwidth differences, and thus interfaces are needed to overcome such problems. We propose an optical interface for frequency down-conversion and bandwidth compression based on the counter-propagating quasi-phase-matching difference frequency generation process in the periodically-poled lithium niobate on insulator waveguide. We prove that a separable spectral transfer function can be obtained only by choosing proper pump bandwidth, thus relaxing the limitation of material, dispersion, and working wavelength as a result of the counter-propagation phase-matching configuration. With numerical simulations, we show that our design results in a nearly separable transfer function with the Schmidt number very close to 1. With proper pump bandwidth, an photon at central wavelength of 550 nm with a bandwidth ranging from 50 GHz to 5 THz can be converted to a photon at central wavelength of 1,545 nm with a much narrower bandwidth of 33 GHz.

Keywords: frequency conversion, bandwidth compression, counter-propagating quasi-phase-matching, periodically-poled lithium niobate on insulator waveguide, difference frequency generation

1 INTRODUCTION

Photons play an important role in quantum information science, such as long distance quantum communication [1,2], linear optical quantum computation [3,4] and interface to quantum memories [5,6]. However, in these applications, different devices and systems usually require different photon central frequencies and bandwidths. In order to combine all these systems in one quantum network, photon frequency interface capable of converting frequency and bandwidth is indispensable.

Electro-optical modulation is an efficient way to shift photon frequency [7–9], which is commonly used in pulse manipulation, however, its conversion range is limited to several GHz. Sum frequency generation (SFG) [10–12] and difference-frequency generation (DFG) [13] in nonlinear optical process are beneficial to frequency conversion between different frequency bands and have been utilized as an interface between the visible and communication wavelength bands [14–16]. Moreover, a bandwidth compression factor of 40 was achieved by utilizing SFG process with chirped input photon and anti-chirped strong pump laser [17]. However, interfaces generated by this way usually

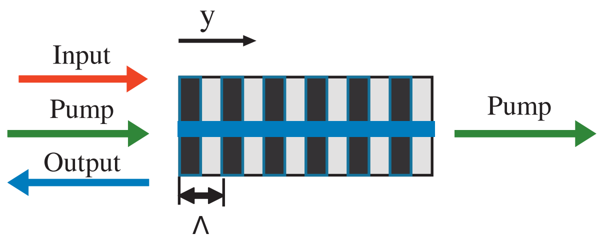

FIGURE 1 | Geometry of a counter-propagating quasi-phase-matching difference frequency generation process in a y-direction waveguide with a poling period of Λ. The input and pump light propagate in the same direction, while the output light propagates in the opposite direction.

suffer from low conversion efficiency due to the need of ultra wide phase-matching bandwidth. How to convert frequency and compress bandwidth effectively at the same time is a big challenge. Recently, Allgaier *et al.* made an approach towards both goals with dispersion-engineered SFG [18], where photon at communication wavelength was converted to the visible range with a bandwidth compression factor of 7.47 and an internal conversion efficiency of 61.5%. Such method relies on modulating the dispersion and group velocity relationship among the input, pump, and output photons, and thus has limited choices on the working wavelengths and materials.

On the other hand, counter-propagating quasi-phase-matching (QPM) spontaneous parametric down-conversion (SPDC) process has been extensively studied due to its unique spectral properties [19,20], such as narrow bandwidth [21,22] and frequency uncorrelated [23–26] photon pairs. In contrast to the traditional co-propagating process, in the counter-propagating process the phase-matching function is greatly affected by the counter propagation of the signal and idler photons, and hence such method can be applied in a large range of nonlinear materials and working wavelengths. In this paper, we propose to use the counter-propagating QPM DFG to realize an optical interface for frequency down-conversion and bandwidth compression. We design an experimental feasible waveguide structure based on the thin-film lithium niobate on insulator (LNOI) platform, which has been considered as a revolutionary platform for integrated photonics [27] and aroused a great deal of interest in recent years, as it allows a strong optical confinement and thus brings strong nonlinear effects [28–30].

2 METHODS

The configuration of a counter-propagating QPM DFG process is shown in **Figure 1**. With a pulse laser as the pump in a y-direction waveguide, a co-propagating high-frequency input photon is converted into a low-frequency output photon in the counter-propagation direction. In the undepleted pump approximation, the effective Hamiltonian describing the DFG process can be written as [31].

$$H = \int dt\hat{H}(t) = \theta \iint d\omega_i d\omega_o f(\omega_i, \omega_o)\hat{a}_i(\omega_i)\hat{a}_o^\dagger(\omega_o) + H.c., \quad (1)$$

where θ is the coupling parameter having absorbed all the constants, and the frequencies are constrained by the energy-conservation relation of $\omega_i - \omega_p = \omega_o$, with the subscripts i, p, and o representing the input, pump, and output photons, respectively. The normalized DFG transfer function can be expressed as $f(\omega_i, \omega_o) = \alpha(\omega_i - \omega_o)\Phi(\omega_i, \omega_o)$, where $\alpha(\omega_i - \omega_o)$ is the spectral amplitude of pump light and $\Phi(\omega_i, \omega_o)$ denotes the phase matching function.

With broadband pump laser, the transfer function can be written as Schmidt decomposition form [32].

$$f(\omega_i, \omega_o) = \sum_{j=1}^{K} \kappa_j \phi_j(\omega_i)\psi_j(\omega_o), \quad (2)$$

where $\{\phi_j(\omega_i)\}$ and $\{\psi_j(\omega_o)\}$ are two sets of orthogonal spectral amplitude functions and κ_j are the real Schmidt coefficients satisfying $\sum_j \kappa_j^2 = 1$. Thus the effective Hamiltonian can be rewritten as

$$H = \theta \sum_j \kappa_j A_j C_j^\dagger + H.c., \quad (3)$$

with broadband mode operators $A_j = \int d\omega\phi_j(\omega)\hat{a}_i(\omega)$ and $C_j = \int d\omega\psi_j(\omega)\hat{a}_o(\omega)$. Compared with the effective Hamiltonian of an optical beam splitter (BS) $H_{BS} = \theta\hat{a}\hat{c}^\dagger + H.c.$[33], the DFG process can be considered as a set of independent BSs which convert A_j to C_j with effective coupling parameter $\theta\kappa_j$, namely, $A_j \rightarrow \cos(\theta\kappa_j)A_j + i\sin(\theta\kappa_j)C_j$ with conversion efficiency $\sin^2(\theta\kappa_j)$ [31]. Hence, for the multi-mode input photon $\sum_j \alpha_j A_j^\dagger|0\rangle$, with $\sum \alpha_j^2 = 1$, the total conversion efficiency is given by $\sum_j |\alpha_j|^2 \sin^2(\theta\kappa_j)$. We can see that, given a fixed pump light power, the maximum total conversion efficiency is achieved when the Schmidt number $K = 1$, i.e., the transfer function is separable, according to the Cauchy-Schwarz inequality. Hence, it is important to design a separable transfer function for efficient frequency conversion. In the following, we propose a method to obtain a separable transfer function by using the counter-propagating QPM DFG process.

The phase matching function can be expressed as

$$\Phi(\omega_i, \omega_o) = \mathrm{sinc}\left(\frac{\Delta kL}{2}\right)e^{i\frac{\Delta kL}{2}}, \quad (4)$$

with L denoting the poling length. For the counter-propagating DFG process, the phase mismatch Δk is given by

$$\Delta k = k_i - k_p + k_o - k_G, \quad (5)$$

where $k_G = 2\pi m/\Lambda$ is the mth order reciprocal wave vector with Λ denoting the poling period.

We define frequency offsets $\Delta\omega_j \equiv \Omega_j - \omega_j$, with $j = i, p, o$, where Ω_j are central frequencies satisfying perfect phase-matching condition $\Delta k = 0$. Thus, according to the energy-conservation relation, we have $\Omega_i - \Omega_p = \Omega_o$, and $\Delta\omega_i - \Delta\omega_p = \Delta\omega_o$. Then, by expanding Δk to the first order in $\Delta\omega_j$ and $\Delta\omega_o$ around central frequencies, we obtain

$$\Delta k = \left(u_i^{-1} - u_p^{-1}\right)\Delta\omega_i + \left(u_o^{-1} + u_p^{-1}\right)\Delta\omega_o, \quad (6)$$

where $u_j, j = i, o, p$ are the group velocities at central frequencies. For comparison, the phase mismatch of the co-propagating DFG process given by $\Delta k_{\text{co}} = k_i - k_p - k_o - k_G$, can be expanded as

$$\Delta k_{\text{co}} = \left(u_i^{-1} - u_p^{-1}\right)\Delta\omega_i + \left(u_p^{-1} - u_o^{-1}\right)\Delta\omega_o. \tag{7}$$

We can see that in the traditional co-propagating process the coefficients of frequency offsets only depend on the difference of the reciprocal of group velocities, and thus in such process the phase-matching function is usually engineered by selecting working frequencies and structures to control the dispersion and group velocities [34]. While, in the counter-propagating process, the coefficients also depend on the sum of the group velocities, enabling intrinsic features for phase-matching engineering [20–26].

To further characterize the transfer function, we define two characteristic bandwidth scales

$$\delta\omega_1 = \frac{2}{\left(u_i^{-1} - u_p^{-1}\right)L}, \qquad \delta\omega_2 = \frac{2}{\left(u_o^{-1} + u_p^{-1}\right)L}. \tag{8}$$

Thus, the phase matching function given by **Eq. 4** can be rewritten as

$$\tilde{\Phi}\left(\frac{\Delta\omega_i}{\delta\omega_1} + \frac{\Delta\omega_o}{\delta\omega_2}\right) = \operatorname{sinc}\left(\frac{\Delta\omega_i}{\delta\omega_1} + \frac{\Delta\omega_o}{\delta\omega_2}\right)e^{-i\left(\frac{\Delta\omega_i}{\delta\omega_1} + \frac{\Delta\omega_o}{\delta\omega_2}\right)}, \tag{9}$$

where we defined a function of $\tilde{\Phi}(x) \equiv \operatorname{sinc}(x)e^{-ix}$. By rewriting the pump amplitude function $\alpha(\omega_i - \omega_o)$ as $\tilde{\alpha}(\Delta\omega_i - \Delta\omega_o)$, we can write the transfer function against frequency offsets as

$$\tilde{f}(\Delta\omega_i, \Delta\omega_o) = \tilde{\alpha}(\Delta\omega_i - \Delta\omega_o)\tilde{\Phi}\left(\frac{\Delta\omega_i}{\delta\omega_1} + \frac{\Delta\omega_o}{\delta\omega_2}\right) \tag{10}$$

In the following, we prove that when the pump light bandwidth $\delta\omega_p$ satisfies $\delta\omega_2 \ll \delta\omega_p \ll \delta\omega_1$, the transfer function can approach a separable function of $\Delta\omega_i$, $\Delta\omega_o$. In analogy to the analysis in Ref. [20], we first recast the argument of function $\tilde{\Phi}$

$$\frac{\Delta\omega_i}{\delta\omega_1} + \frac{\Delta\omega_o}{\delta\omega_2} = \frac{\Delta\omega_p}{\delta\omega_1} + \left(\frac{\Delta\omega_o}{\delta\omega_1} + \frac{\Delta\omega_o}{\delta\omega_2}\right) \approx \frac{\Delta\omega_o}{\delta\omega_3}, \tag{11}$$

with

$$\delta\omega_3 = \frac{2}{\left(u_i^{-1} + u_o^{-1}\right)L}, \tag{12}$$

where $\Delta\omega_p/\delta\omega_1$ has been neglected because it is on the order $\delta\omega_p/\delta\omega_1 \ll 1$. Then we recast the argument of function $\tilde{\alpha}$ as

$$\Delta\omega_i - \Delta\omega_o = \Delta\omega_i\left(1 + \frac{\delta\omega_2}{\delta\omega_1}\right) - \delta\omega_2\left(\frac{\Delta\omega_i}{\delta\omega_1} + \frac{\Delta\omega_o}{\delta\omega_2}\right). \tag{13}$$

where $\Delta\omega_i/\delta\omega_1 + \Delta\omega_o/\delta\omega_2$ is the argument of the sinc function in $\tilde{\Phi}$ as given in **Eq. 9**, and thus it is limited to values on the order of ~ 10, namely, inside the bandwidth of sinc function, due to the product relationship of $\tilde{\alpha}$ and $\tilde{\Phi}$ shown in **Eq. 10**. Consequently, provided that $\delta\omega_2/\delta\omega_p$ is small enough, we can have $\delta\omega_2\,(\Delta\omega_i/\delta\omega_1 + \Delta\omega_o/\delta\omega_2)$ much smaller than $\delta\omega_p$, the bandwidth of $\tilde{\alpha}$, and therefore this term is negligible in the argument of $\tilde{\alpha}$. Hence we have the following approximation

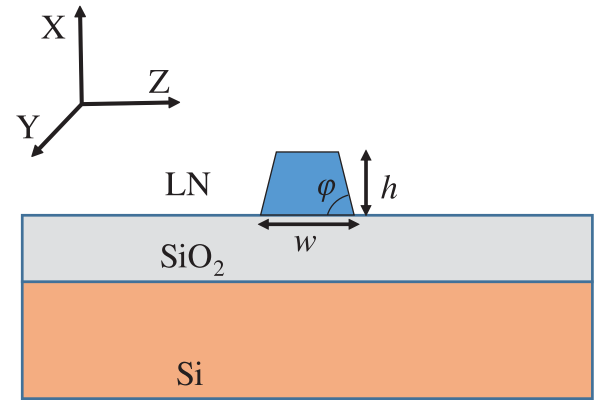

FIGURE 2 | Schematic of the X-cut LNOI waveguide structure. The parameters φ, w, and h denote sidewall angle, bottom ridge width, and hight of the waveguide, respectively.

$$\tilde{\alpha}(\Delta\omega_i - \Delta\omega_o) \approx \tilde{\alpha}\left[\Delta\omega_i\left(1 + \frac{\delta\omega_2}{\delta\omega_1}\right)\right]. \tag{14}$$

In addition, considering $\delta\omega_2/\delta\omega_1 \ll 1$, we can further make approximation on **Eq. 14** as

$$\tilde{\alpha}(\Delta\omega_i - \Delta\omega_o) \approx \tilde{\alpha}(\Delta\omega_i). \tag{15}$$

Consequently, the transfer function given by **Eq. 10** approaches the factorized form

$$\tilde{f}(\Delta\omega_i, \Delta\omega_o) \approx \tilde{\alpha}(\Delta\omega_i)\tilde{\Phi}\left(\frac{\Delta\omega_o}{\delta\omega_3}\right). \tag{16}$$

Such separable function also means that the correlation between the input and output photons is eliminated. It is clear that the frequency of the input photon can vary within the bandwidth of the pump light, and thus the bandwidth of the input photon can be as large as that of the pump light, namely, $\delta\omega_i = \delta\omega_p$. While, the bandwidth of the output photon is only determined by the phase-matching function irrespective of the pump bandwidth, which can be obtained from the full width at half maximum of the spectral density function $|\tilde{\Phi}(\Delta\omega_o/\delta\omega_3)|^2 = |\operatorname{sinc}(\Delta\omega_o/\delta\omega_3)|^2$, given by

$$\delta\omega_o = 2.78\delta\omega_3 = \frac{5.56}{\left(u_i^{-1} + u_o^{-1}\right)L}. \tag{17}$$

Hence, we can get the bandwidth compression factor as

$$\eta = \frac{\delta\omega_i}{\delta\omega_o} = \frac{1}{5.56}\delta\omega_p L\left(u_i^{-1} + u_o^{-1}\right). \tag{18}$$

3 RESULTS

The schematic of the LNOI waveguide is shown in **Figure 2** consisting of three layers of silicon (Si), silica (SiO_2), and lithium

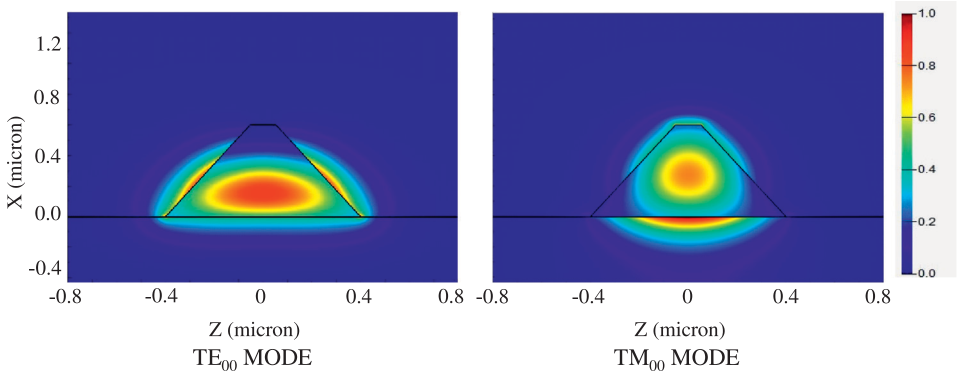

FIGURE 3 | Field distribution of TM_{00} mode and TE_{00} mode at 1,545 nm.

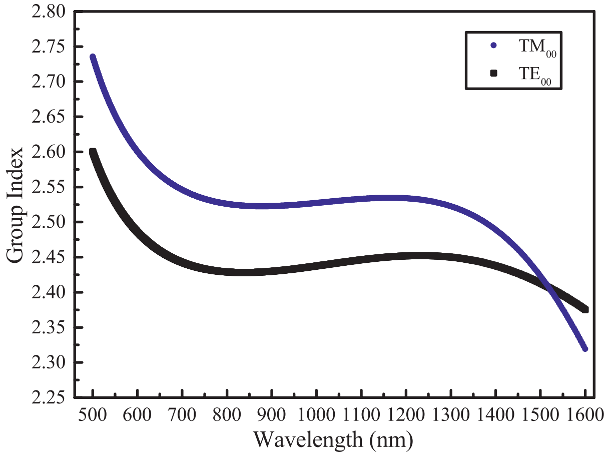

FIGURE 4 | Group index of TE_{00} and TM_{00} modes in LNOI waveguide with wavelength ranging from 500 to 1,600 nm.

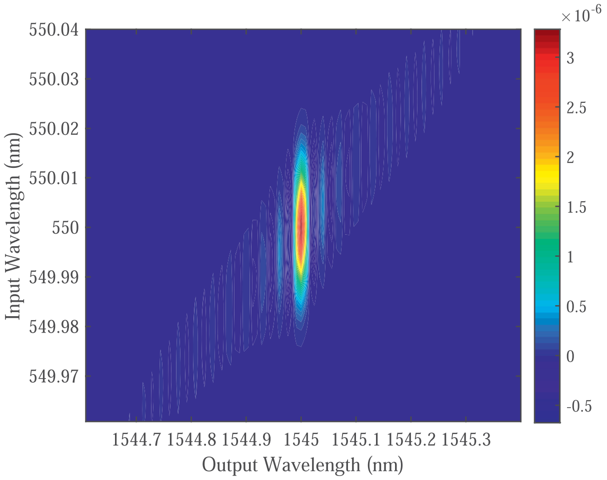

FIGURE 5 | Simulated transfer function when the pump bandwidth $\delta\omega_p$ is 50 GHz.

niobate (LN), respectively. The LN layer is made from X-cut LNOI film and the waveguide propagates in y-direction with a sidewall angle of $\varphi = 60^\circ$, and a length of $L = 10$ mm. The waveguide height h and its bottom ridge width w restrict the transverse distribution of the guide mode and can be adjusted in structure design and fabrication process. By varying the height and width, light dispersion can be tuned in the LNOI waveguide. In order to characteristic the property of the bandwidth compressor, numerically simulations of group index and effective refractive index are obtained by utilizing the Mode Solution software with the material dispersion of LN given by Ref. [35].

Here we aim to design a counter-propagating DFG process that converts the broadband input photons centered at 550 nm in TE_{00} mode to narrowband output photons centered at 1,545 nm in TM_{00} mode with a pulsed laser light centered at 854 nm in TM_{00} mode as the pump. Such frequency conversion process with the chosen wavelengths may connect the quantum communication channels with single-photon emitters around 550 nm, such as the charge-neutral nitrogen-vacancy center in diamond [36] and the CdSe quantum dots [37, 38]. The structure parameters are $h = 0.6$ μm and $w = 0.8$ μm. Single mode condition can be achieved at 1,545 nm with the field distribution of TE_{00} and TE_{00} modes shown in **Figure 3**. With simulated effective index of the waveguide, we can calculate the poling period to be $\Lambda = 0.402$ μm for satisfying the first-order QPM condition of $\Delta k = 0$ according to **Eq. 5**. The simulated results of group index $n_g = c/u$ of TE_{00} and TM_{00} modes with wavelength ranging from 500 to 1,600 nm are shown in **Figure 4**. Explicitly, the simulated group indexes of the pump light at 854 nm in TM_{00} mode, the input light at 550 nm in TE_{00} mode, and the output light at 1,545 nm in TM_{00} mode are $n_{g,p} = 2.533$, $n_{g,i} = 2.532$, and $n_{g,o} = 2.401$, respectively. Therefore, we can obtain $\delta\omega_1 = 60$ THz and $\delta\omega_2 = 12.2$ GHz.

In order to show the spectrum relation between the input and output photons, we simulate the transfer function given by **Eq. 10**. By assuming a Gaussian spectrum pump, the simulation

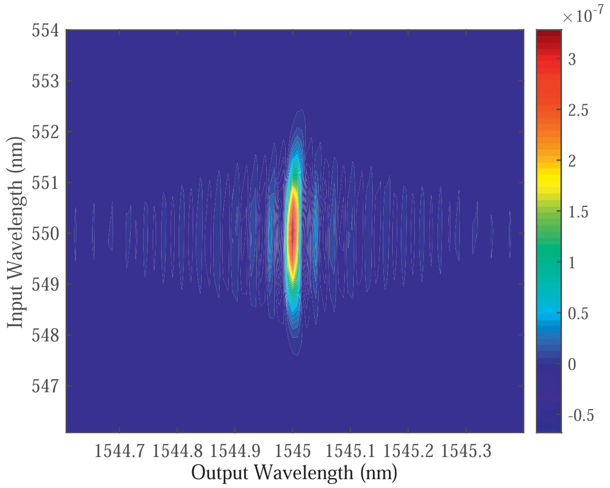

FIGURE 6 | Simulated transfer function when the pump bandwidth $\delta\omega_p$ is 5 THz.

results when pump bandwidths $\delta\omega_p = 50$ GHz and $\delta\omega_p = 5$ THz are shown in **Figure 5**, **6**, respectively. The corresponding Schmidt numbers K are estimated to be 1.037, and 1.041, respectively. Hence, we can see that the transfer function is very close to a separable one. The bandwidth of the output photon can be estimated from **Eq. 17**, namely, $\delta\omega_o = 33$ GHz. Then according to **Eq. 18** we can express the bandwidth compression factor as

$$\eta = \frac{\delta\omega_i}{\delta\omega_o} = \frac{\delta\omega_p}{33\ \text{GHz}}, \tag{19}$$

and consequently, in our simulation range of $\delta\omega_p = 50$ GHz ~ 5 THz, we can obtain a compression factor ranging from 1.5 to 150.

Then we give a simulation of the conversion efficiency. The DFG process with a separable transfer function can be treated as a BS model and the conversion efficiency is given by $sin^2\theta$ [31]. Here the coupling parameter can be expressed as

$$\theta = \frac{2d\pi^2 LN}{c}\sqrt{\frac{2P_p\omega_{i0}\omega_{o0}}{c\varepsilon_0 n_{p0}n_{i0}n_{o0}\left|\int d\omega_p\alpha\left(\omega_p\right)\right|^2 B}}, \tag{20}$$

where $d = 2d_{31}/(m\pi)$ is the nonlinear coefficient, and P_p is the pump peak power, with n_j $(j = p, i, o)$ representing the effective refractive index of pump, input and output lights at central frequencies, respectively. The parameter N is the normalization factor of transfer function given by

$$N = \sqrt{\iint d\omega_i d\omega_o |f(\omega_i, \omega_o)|^2}. \tag{21}$$

The effective interaction area B can be written as

$$B = \left[\iint dxdz g_p(x,z) g_i(x,z) g_o^*(x,z)\right]^{-2}, \tag{22}$$

where $g_j(x, z)$ $(j = p, i, o)$ is the normalized spatial distribution of the cross-sectional area of pump, input and output fields, respectively. Through numerical simulation using the Mode solution software, we estimated B to be 0.472 μm^2. With these calculations, we can estimate a pump peak power of 2.04 W in the case of unity conversion efficiency. If setting the pump pulse width to be 200 fs with a repetition rate of 80 MHz, we can calculate the average pump power to be 0.032 mW, which is much lower than the previous experiment results [39, 40].

It should be noted that the ideal unity conversion efficiency in a single process could be achieved only in the limit of short interaction length or long pump pulse [41]. In broadband mode case, time-ordering corrections may affect the conversion efficiency [42, 43], which are resulted from the noncommutativity of the interaction Hamiltonian at different times. A maximum conversion efficiency of 87.7% has been obtained in a SFG process [44]. Moreover, Reddy *et al.* [45] proposed a scheme to overcome the time-ordering correction limitation by cascading two frequency conversion processes with 50% conversion efficiency.

4 DISCUSSION

We would like to discuss the experimental feasibility of our design. The LNOI waveguide structure is experimentally feasible with current LNOI fabrication techniques [27–30]. The poling period on the order of 0.402 μm is still challenging at present. However, we can use a higher-order reciprocal wave vector to obtain a bigger poling period at the cost of lower efficiency. For example, if using the third-order reciprocal wave vector, we would get a poling period of 1.206 μm with the nonlinear coefficient reduced to $d/3$. Such poling period is possible with current fabrication techniques [46].

In conclusion, we proposed a scheme to realize optical frequency down-conversion and bandwidth compression via the counter-propagating QPM DFG process, which can provide a quantum network interface for devices working at different central frequencies and bandwidths. We proved that, due to the counter-propagation configuration, a separable spectrum transfer function can be obtained only by choosing the pump bandwidth in a range between two characteristic bandwidth scales, rather than satisfying constrained dispersion and group velocity relations, and thus this method is not strictly limited by the material, dispersion, and working wavelength. Moreover, under this condition, the input photon can have a bandwidth the same with that of the pump light, while the bandwidth of the out photon is only determined by the phase-matching function irrespective of the pump bandwidth. Such feature enables a large bandwidth compression factor as well as facilitates the application in the interface between photons with different spectral shapes. We designed a periodically-poled LNOI waveguide to realize the scheme. The simulation result shows a nearly separable transfer function with the Schmidt number estimated very close to 1. By changing the pump bandwidth, a bandwidth compression factor ranging from 1.5 to 150 can be obtained. We also calculate a pump average power of 0.032 mW to achieve unit conversion efficiency. In addition, the counter-propagating output feature is also of great benefit to compressing co-propagating noises. Finally, our approach opens up a way for efficient optical interface connecting photons with different frequency and spectrum bandwidth benefiting from the counter-propagating nonlinear process. We hope our approach can stimulate more such investigations.

DATA AVAILABILITY STATEMENT

The original contributions presented in the study are included in the article/Supplementary Material, further inquiries can be directed to the corresponding authors.

AUTHOR CONTRIBUTIONS

D-JG designed the scheme and performed the calculations with the help of RY. Y-XG, and ZX supervised the project. All authors discussed the results and reviewed the manuscript.

FUNDING

This work was supported by the National Key R&D Program of China (No. 2019YFA0705000), Key R&D Program of Guangdong Province (No. 2018B030329001), Leading-edge technology Program of Jiangsu Natural Science Foundation (No. BK20192001), National Natural Science Foundation of China (51890861, 11690031, 11674169, 11974178).

REFERENCES

1. Duan L-M, Lukin MD, Cirac JI, and Zoller P. Long-distance Quantum Communication With Atomic Ensembles and Linear Optics. *Nature* (2001) 414:413–8. doi:10.1038/35106500
2. Boaron A, Boso G, Rusca D, Vulliez C, Autebert C, Caloz M, et al. Secure Quantum Key Distribution Over 421 Km of Optical Fiber. *Phys Rev Lett* (2018) 121:190502. doi:10.1103/PhysRevLett.121.190502
3. Knill E, Laflamme R, and Milburn GJ. A Scheme for Efficient Quantum Computation With Linear Optics. *nature* (2001) 409:46–52. doi:10.1038/35051009
4. Kok P, Munro WJ, Nemoto K, Ralph TC, Dowling JP, and Milburn GJ. Linear Optical Quantum Computing With Photonic Qubits. *Rev Mod Phys* (2007) 79: 135–74. doi:10.1103/RevModPhys.79.135
5. Lvovsky AI, Sanders BC, and Tittel W. Optical Quantum Memory. *Nat Photon* (2009) 3:706–14. doi:10.1038/nphoton.2009.231
6. Kozhekin AE, Mølmer K, and Polzik E. Quantum Memory for Light. *Phys Rev A* (2000) 62:033809. doi:10.1103/PhysRevA.62.033809
7. Karpiński M, Jachura M, Wright LJ, and Smith BJ. Bandwidth Manipulation of Quantum Light by an Electro-Optic Time Lens. *Nat Photon* (2017) 11:53–7. doi:10.1038/nphoton.2016.228
8. Wright LJ, Karpiński M, Söller C, and Smith BJ. Spectral Shearing of Quantum Light Pulses by Electro-Optic Phase Modulation. *Phys Rev Lett* (2017) 118: 023601. doi:10.1103/PhysRevLett.118.023601
9. Sośnicki F, and Karpiński M. Large-Scale Spectral Bandwidth Compression by Complex Electro-Optic Temporal Phase Modulation. *Opt Express* (2018) 26: 31307–16. doi:10.1364/OE.26.031307
10. Vandevender AP, and Kwiat PG. High Efficiency Single Photon Detection *via* Frequency Up-Conversion. *J Mod Opt* (2004) 51:1433–45. doi:10.1080/09500340408235283
11. Albota MA, and Wong FNC. Efficient Single-Photon Counting at 155 Mm by Means of Frequency Upconversion. *Opt Lett* (2004) 29:1449–51. doi:10.1364/ol.29.001449
12. Kobayashi T, Ikuta R, Yasui S, Miki S, Yamashita T, Terai H, et al. Frequency-Domain Hong-Ou-Mandel Interference. *Nat Photon* (2016) 10:441–4. doi:10.1038/nphoton.2016.74
13. Ikuta R, Kobayashi T, Yasui S, Miki S, Yamashita T, Terai H, et al. Frequency Down-Conversion of 637 Nm Light to the Telecommunication Band for Non-Classical Light Emitted From Nv Centers in diamond. *Opt Express* (2014) 22: 11205–14. doi:10.1364/OE.22.011205
14. Vollmer CE, Baune C, Samblowski A, Eberle T, Händchen V, Fiurášek J, et al. Quantum Up-Conversion of Squeezed Vacuum States from 1550 to 532 Nm. *Phys Rev Lett* (2014) 112:073602. doi:10.1103/PhysRevLett.112.073602
15. Rakher MT, Ma L, Slattery O, Tang X, and Srinivasan K. Quantum Transduction of Telecommunications-Band Single Photons From a Quantum Dot by Frequency Upconversion. *Nat Photon* (2010) 4:786–91. doi:10.1038/nphoton.2010.221
16. Walker T, Miyanishi K, Ikuta R, Takahashi H, Vartabi Kashanian S, Tsujimoto Y, et al. Long-Distance Single Photon Transmission From a Trapped Ion via Quantum Frequency Conversion. *Phys Rev Lett* (2018) 120:203601. doi:10.1103/physrevlett.120.203601
17. Lavoie J, Donohue JM, Wright LG, Fedrizzi A, and Resch KJ. Spectral Compression of Single Photons. *Nat Photon* (2013) 7:363–6. doi:10.1038/nphoton.2013.47
18. Allgaier M, Ansari V, Sansoni L, Eigner C, Quiring V, Ricken R, et al. Highly Efficient Frequency Conversion With Bandwidth Compression of Quantum Light. *Nat Commun* (2017) 8:1–6. doi:10.1038/ncomms14288
19. Harris SE. Proposed Backward Wave Oscillation in the Infrared. *Appl Phys Lett* (1966) 9:114–6. doi:10.1063/1.1754668
20. Gatti A, Corti T, and Brambilla E. Temporal Coherence and Correlation of Counterpropagating Twin Photons. *Phys Rev A* (2015) 92:053809. doi:10.1103/physreva.92.053809
21. Gong YX, Xie ZD, Xu P, Yu XQ, Xue P, and Zhu SN. Compact Source of Narrow-Band Counterpropagating Polarization-Entangled Photon Pairs Using a Single Dual-Periodically-Poled Crystal. *Phys Rev A* (2011) 84: 053825. doi:10.1103/physreva.84.053825
22. Duan J-C, Zhang J-N, Zhu Y-J, Sun C-W, Liu Y-C, Xu P, et al. Generation of Narrowband Counterpropagating Polarization-Entangled Photon Pairs Based on Thin-Film Lithium Niobate on Insulator. *J Opt Soc Am B* (2020) 37: 2139–45. doi:10.1364/josab.395108
23. Christ A, Eckstein A, Mosley PJ, and Silberhorn C. Pure Single Photon Generation by Type-I Pdc With Backward-Wave Amplification. *Opt Express* (2009) 17:3441–6. doi:10.1364/OE.17.003441
24. Luo K-H, Ansari V, Massaro M, Santandrea M, Eigner C, Ricken R, et al. Counter-Propagating Photon Pair Generation in a Nonlinear Waveguide. *Opt Express* (2020) 28:3215–25. doi:10.1364/OE.378789
25. Cai W-H, Wei B, Wang S, and Jin R-B. Counter-propagating Spectrally Uncorrelated Biphotons at 1550 Nm Generated From Periodically Poled MTiOXO4 (M = K, Rb, Cs; X = P, as). *J Opt Soc Am B* (2020) 37:3048–54. doi:10.1364/JOSAB.401157
26. Liu Y-C, Guo D-J, Ren K-Q, Yang R, Shang M, Zhou W, et al. Observation of Frequency-Uncorrelated Photon Pairs Generated by Counter-propagating Spontaneous Parametric Down-Conversion. *Sci Rep* (2021) 11:1–6. doi:10.1038/s41598-021-92141-y
27. Boes A, Corcoran B, Chang L, Bowers J, and Mitchell A. Status and Potential of Lithium Niobate on Insulator (Lnoi) for Photonic Integrated Circuits. *Laser Photon Rev* (2018) 12:1700256. doi:10.1002/lpor.201700256
28. Wang C, Langrock C, Marandi A, Jankowski M, Zhang M, Desiatov B, et al. Ultrahigh-Efficiency Wavelength Conversion in Nanophotonic Periodically Poled Lithium Niobate Waveguides. *Optica* (2018) 5:1438–41. doi:10.1364/optica.5.001438
29. Chen J-Y, Ma Z-H, Sua YM, Li Z, Tang C, and Huang Y-P. Ultra-Efficient Frequency Conversion in Quasi-Phase-Matched Lithium Niobate Microrings. *Optica* (2019) 6:1244–5. doi:10.1364/OPTICA.6.001244

30. Lu J, Surya JB, Liu X, Bruch AW, Gong Z, Xu Y, et al. Periodically Poled Thin-Film Lithium Niobate Microring Resonators With a Second-Harmonic Generation Efficiency of 250,000%/w. *Optica* (2019) 6:1455–60. doi:10.1364/OPTICA.6.001455
31. Eckstein A, Brecht B, and Silberhorn C. A Quantum Pulse Gate Based on Spectrally Engineered Sum Frequency Generation. *Opt Express* (2011) 19: 13770–8. doi:10.1364/OE.19.013770
32. Law CK, Walmsley IA, and Eberly JH. Continuous Frequency Entanglement: Effective Finite hilbert Space and Entropy Control. *Phys Rev Lett* (2000) 84: 5304–7. doi:10.1103/PhysRevLett.84.5304
33. Prasad S, Scully MO, and Martienssen W. A Quantum Description of the Beam Splitter. *Opt Commun* (1987) 62:139–45. doi:10.1016/0030-4018(87)90015-0
34. Baronavski AP, Ladouceur HD, and Shaw JK. Analysis of Cross Correlation, Phase Velocity Mismatch and Group Velocity Mismatches in Sum-Frequency Generation. *IEEE J Quan Electron.* (1993) 29:580–9. doi:10.1109/3.199312
35. Zelmon DE, Small DL, and Jundt D. Infrared Corrected Sellmeier Coefficients for Congruently Grown Lithium Niobate and 5 mol.% Magnesium Oxide–Doped Lithium Niobate. *JOSA B* (1997) 14:3319–22. doi:10.1364/JOSAB.14.003319
36. Aharonovich I, Castelletto S, Simpson DA, Su C-H, Greentree AD, and Prawer S. Diamond-Based Single-Photon Emitters. *Rep Prog Phys* (2011) 74:076501. doi:10.1088/0034-4885/74/7/076501
37. Chen O, Zhao J, Chauhan VP, Cui J, Wong C, Harris DK, et al. Compact High-Quality CdSe-CdS Core-Shell Nanocrystals With Narrow Emission Linewidths and Suppressed Blinking. *Nat Mater* (2013) 12:445–51. doi:10.1038/nmat3539
38. Lin X, Dai X, Pu C, Deng Y, Niu Y, Tong L, et al. Electrically-Driven Single-Photon Sources Based on Colloidal Quantum Dots With Near-Optimal Antibunching at Room Temperature. *Nat Commun* (2017) 8:1132–7. doi:10.1038/s41467-017-01379-6
39. Tanzilli S, Tittel W, Halder M, Alibart O, Baldi P, Gisin N, et al. A Photonic Quantum Information Interface. *Nature* (2005) 437:116–20. doi:10.1038/nature04009
40. Roussev RV, Langrock C, Kurz JR, and Fejer MM. Periodically Poled Lithium Niobate Waveguide Sum-Frequency Generator for Efficient Single-Photon Detection at Communication Wavelengths. *Opt Lett* (2004) 29:1518–20. doi:10.1364/OL.29.001518
41. Donohue JM, Mazurek MD, and Resch KJ. Theory of High-Efficiency Sum-Frequency Generation for Single-Photon Waveform Conversion. *Phys Rev A* (2015) 91:033809. doi:10.1103/PhysRevA.91.033809
42. Christ A, Brecht B, Mauerer W, and Silberhorn C. Theory of Quantum Frequency Conversion and Type-Ii Parametric Down-Conversion in the High-Gain Regime. *New J Phys* (2013) 15:053038. doi:10.1088/1367-2630/15/5/053038
43. Quesada N, and Sipe JE. High Efficiency in Mode-Selective Frequency Conversion. *Opt Lett* (2016) 41:364–7. doi:10.1364/ol.41.000364
44. Brecht B, Eckstein A, Ricken R, Quiring V, Suche H, Sansoni L, et al. Demonstration of Coherent Time-Frequency Schmidt Mode Selection Using Dispersion-Engineered Frequency Conversion. *Phys Rev A* (2014) 90: 030302. doi:10.1103/physreva.90.030302
45. Reddy DV, Raymer MG, and McKinstrie CJ. Efficient Sorting of Quantum-Optical Wave Packets by Temporal-Mode Interferometry. *Opt Lett* (2014) 39: 2924–7. doi:10.1364/ol.39.002924
46. Younesi M, Kumar P, Stanicki BJ, Geiss R, Chang WK, and Chen YH. Periodic Poling With Short Period for Thin Film Lithium Niobate Waveguides. In: Lasers and Electro-Optics Europe & European Quantum Electronics Conference (2019) IEEE. doi:10.1109/cleoe-eqec.2019.8871472

Conflict of Interest: The authors declare that the research was conducted in the absence of any commercial or financial relationships that could be construed as a potential conflict of interest.

frontiers in Physics

ORIGINAL RESEARCH
published: 04 October 2021
doi: 10.3389/fphy.2021.751963

Dispersion Characteristic of Spatiotemporal Sharply Autofocused Vector Airy-Circular Airy Gaussian Vortex Wave Packets

Dong Li, Xin Chen, Chengquan Wei, Peng Li and Jianlin Zhao**

MOE Key Laboratory of Material Physics and Chemistry under Extraordinary Conditions and Shaanxi Key Laboratory of Optical Information Technology, School of Physical Science and Technology, Northwestern Polytechnical University, Xi'an, China

OPEN ACCESS

Edited by:
Zhi-Han Zhu,
Harbin University of Science and Technology, China

Reviewed by:
Yijie Shen,
University of Southampton, United Kingdom
Pei Zhang,
Xi'an Jiaotong University, China

****Correspondence:***
Dong Li
dongli@nwpu.edu.cn
Jianlin Zhao
jlzhao@nwpu.edu.cn

Specialty section:
This article was submitted to Optics and Photonics, a section of the journal Frontiers in Physics

Received: *02 August 2021*
Accepted: *20 September 2021*
Published: *04 October 2021*

Citation:
Li D, Chen X, Wei C, Li P and Zhao J (2021) Dispersion Characteristic of Spatiotemporal Sharply Autofocused Vector Airy-Circular Airy Gaussian Vortex Wave Packets. Front. Phys. 9:751963. doi: 10.3389/fphy.2021.751963

The spatiotemporal vector Airy-Circular Airy Gaussian vortex wave packet is constructed by solving the (3 + 1)D Schrodinger equation in free space. The wave packet can simultaneously autofocus in space and time by setting the appropriate initial pulse velocity v and the initial position of the main lobe T_0. This kind of wave packet has low intensity before focusing, but the intensity at focus is about 80 times of the initial plane intensity. Our results may have potential applications in particle manipulation, laser processing, and other fields. Furthermore, the influence of the third-order dispersion coefficient on the evolution trajectory, the focus position, and the main peak intensity at the focus of the focusing pulse vector field is analyzed. The results show that the change of the initial velocity, the initial position, and the third-order dispersion coefficient can accurately control the evolution trajectory and the focus position, while the main peak intensity at the focus can only be controlled by adjusting the third-order dispersion coefficient. This means that the pulse vector light field can be manipulated precisely for precise processing by adjusting the third-order dispersion effect.

Keywords: vector beam, vortex, wave packets, optical pulse, dispersion

INTRODUCTION

Spatiotemporal wave packet theory [1] and ultrashort laser pulses [2–7] have received considerable attention by the researchers in the field of laser technology for the past decades. Hellwarth et al. have studied the focused one-cycle electromagnetic pulses to introduce focused vector wave packets [8]. Due to the characteristic of self-acceleration [9], Airy beams propagates along a quadratic trajectory on the transverse plane, and the main lobe remains basically unchanged. The sudden autofocus ability of a circular Airy beams in a linear region has been theorized and experimentally demonstrated [10–12]. This characteristic can be used to improve the performance of optical tweezers. Richards-wolf vector diffraction integral theory can accurately describe the focal field distribution of the tightly focused vector light field [13], and has been widely used to analyze the tightly focused field of the vector light field [14, 15]. Compared with the traditional beam, the circular Airy Gaussian beam can focus automatically without lens. Due to the obvious advantages of Airy beams, such as self-healing, self-acceleration and non-diffraction, the spatiotemporal wave packet research related to Airy beams has attracted the attention of many researchers. Georgios et al. firstly proposed light bullets produced by Airy pulses [16]. Eichelkrant et al. studied the oblique spatiotemporal Airy packet in doubly dispersive optical media [17]. Zhong et al. investigated the

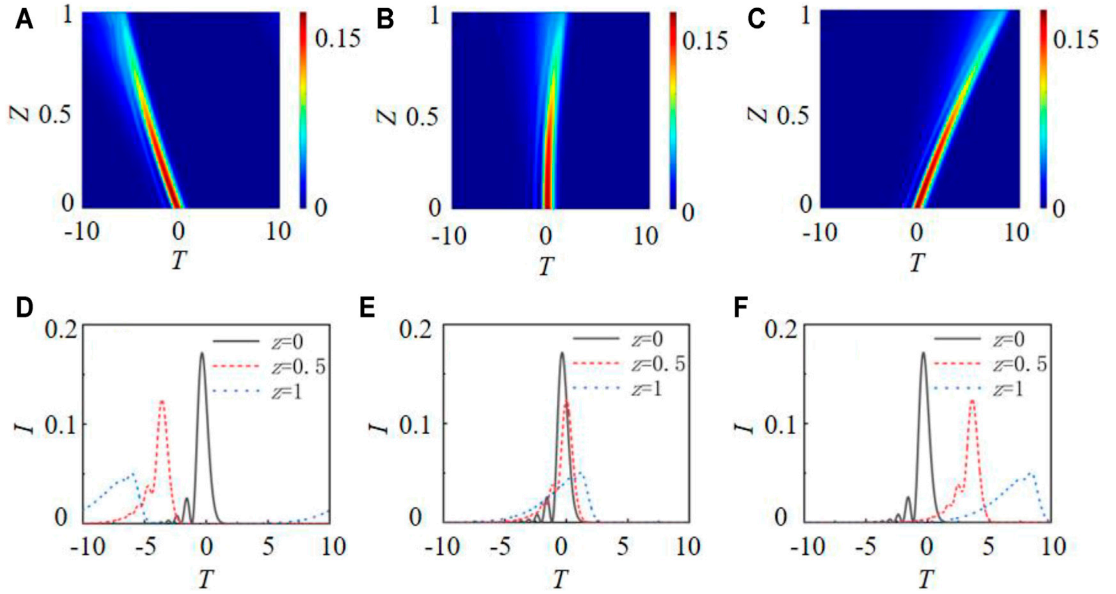

FIGURE 1 | The propagation process of Airy pulse intensity at **(A)** υ = -3.6, **(B)** υ = 0, **(C)** υ = 3.6; The intensity distribution of Airy pulse after different distances at **(D)** υ = -3.6, **(E)** υ = 0 and **(F)** υ = 3.6.

three-dimensional finite energy self-accelerating Airy parabolic light projector [18] and the Airy-Laguerre-Gaussian wave packet [19]. Peng et al. researched the chirped Airy Gaussian vortex packets in a secondary index medium [20]. Chong et al. have achieved a three-dimensional Airy-Bessel wave packet experimentally by combining a temporal Airy pulse with a spatial Bessel beam [21]. Besides, other spatiotemporal wave packets, such as Airy-Hermite-Gaussian packets and Airy-vortex packets [22, 23] were also been demonstrated. The spatial distribution of the spatiotemporal wave packets above is scalar light field. Chong et al. proposed a universal linear spatiotemporal light wave packet called Airy-Bessel light bullet, which was first proposed as a vector light field [21]. Generating spatiotemporal wave packets that are neither affected by dispersion nor diffraction has always been a fascinating challenge. In this paper, we study the spatiotemporal autofocusing properties of the vector-Airy-circular Airy Gaussian vortex (VAi) and the vector-symmetry Airy-circular Airy Gaussian vortex (VSAi) wave packet in free space.

MODEL OF 3D VSAI WAVE PACKETS

Since the radial symmetry of the VAi and VSAi wave packet, the Schrodinger equation in cylindrical coordinates is more suitable as following [19, 24].

$$\mathrm{i}\frac{\partial U}{\partial Z}+\frac{1}{2}\left(\frac{\partial^2 U}{\partial R^2}+\frac{1}{R}\frac{\partial U}{\partial R}+\frac{1}{R^2}\frac{\partial^2 U}{\partial \varphi^2}+\frac{\partial^2 U}{\partial T^2}\right)=0 \qquad (1)$$

Where, $R=(X^2+Y^2)^{1/2}$, and azimuth $\varphi = \arctan(Y/X)$. Here, $X = x/\omega_0$, $Y = y/\omega_0$ and $T = t/t_0$ are normalized coordinates, and ω_0 is the spatial scaling parameter, t_0 is the temporal scaling parameter, Z is the normalized propagation distance. The wave packet can be separated as.

$$U(R,\varphi,T,Z)=M(R,\varphi,Z)P(T,Z) \qquad (2)$$

So the Schrodinger equation can be described as.

$$\mathrm{i}\frac{\partial P}{\partial Z}+\frac{1}{2}\frac{\partial^2 P}{\partial T^2}=0 \qquad (3)$$

$$\mathrm{i}\frac{\partial M}{\partial Z}+\frac{1}{2}\left(\frac{\partial^2 M}{\partial R^2}+\frac{1}{R}\frac{\partial M}{\partial R}+\frac{1}{R^2}\frac{\partial^2 M}{\partial \varphi^2}\right)=0 \qquad (4)$$

The two equations describe the propagation characteristics of wave packets in time domain and space domain respectively. Based on this, we will further analyze the influence of dispersion effect on the evolution characteristics of VAi and VSAi wave packets.

RESULTS AND DISCUSSIONS

Based on the analysis above, the influence of initial velocity on the evolution trajectory and the intensity of Airy pulse during the self-focusing process of circular Airy light can be analyzed following. **Figures 1A–C** present the evolution trajectory and **Figures 1D–F** show the intensity distribution of Airy pulse after different propagation distances with various initial velocities υ. The parameters adopted as $\omega_0 = 1$, $t_0 = 1$, the temporal and spatial attenuation coefficient $a_t = 0.3$, the time distribution factor $b_t = 0.5$, the attenuation coefficient of spatial domain $a_s = 0.05$, the spatial distribution factor $b_s = 0.2$ and the radius of the initial circular Airy Gaussian light $R_0 = 2$. It can be seen that the

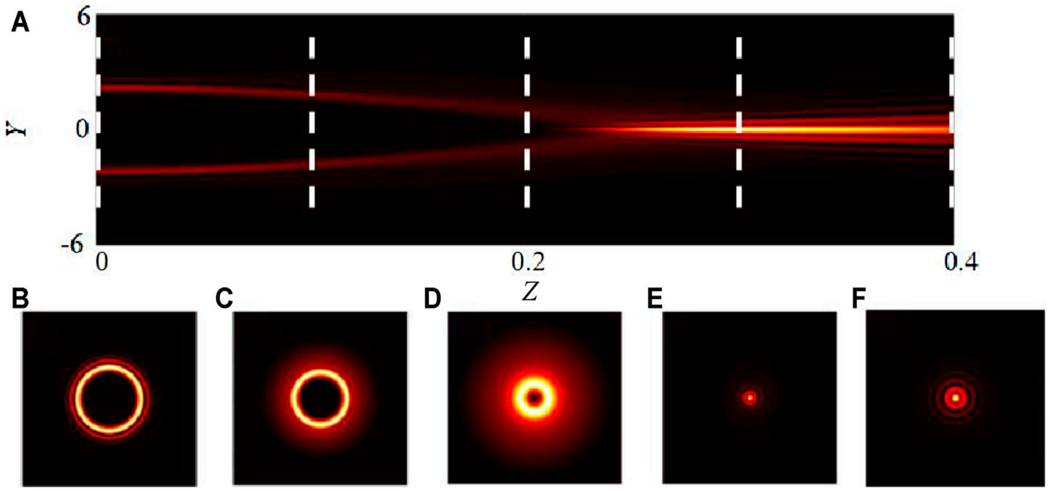

FIGURE 2 | Longitudinal propagation characteristics of self-focusing of a radially-polarized circular Airy Gauss vortex bam in free space when R_0 = 2. **(A)** Longitudinal intensity distribution from Z = 0 to Z = 0.4 .**(B)–(F)** transverse intensity distribution of the beam at the dotted lines in **(A)**.

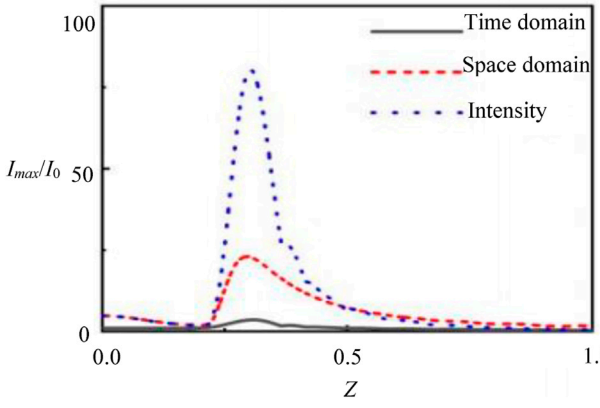

FIGURE 3 | Variation of I_{max}/I_0 of VSAi wave packet with the propagation distance.

evolution trajectory of Airy pulse can be controlled by changing the initial velocity, and the initial velocity of Airy pulse has no effect on the intensity distribution during the propagation. The self-accelerating trajectory of **Figure 1B,E** is the same as the evolution trajectory of conventional Airy pulse for $\upsilon = 0$. But when the initial velocity is negative, Airy pulse will initially propagate in the negative direction and then propagate in the positive direction for $\upsilon = -3.6$ as in **Figure 1A,D**. When the initial velocity of the Airy pulse is in the opposite direction from the self-acceleration, it will slow down and then accelerate. Furthermore, the direction of the initial velocity of the Airy pulse is the same as the direction of the self-acceleration, and it will continue to accelerate when $\upsilon = 3.6$ as in **Figure 1C,F** That means the evolution trajectory of Airy pulse can be modulated by its initial velocity, and the speed of the pulse will become faster versus the absolute value of the initial velocity increasing.

At the same time, the longitudinal self-focusing propagation characteristics of a radially polarized circular Airy Gauss vortex in free space when $R_0 = 2$ is also analyzed. **Figure 2A** shows the longitudinal intensity distribution of incident light from $Z = 0$ to $Z = 0.4$. The dotted lines represent propagation positions at $Z = 0$, 0.1, 0.2, 0.3 and 0.4 successively. It can be found that the circular Airy Gauss vortex will focus at $Z = 0.2$, and the intensity peak will increase first rapidly and then decrease gradually versus the propagation distance, and the intensity maximum $I_{max} = 5.515$ at $Z = 0.3$.

Then the evolution of VSAi wave packet intensity during the focusing process can also be analyzed as in **Figure 3**. Where, I_0 is the intensity extreme at the incident plane, and I_{max}/I_0 represents the ratio of the intensity maximum during the propagation with the initial intensity extreme at the plane. It can be seen that the intensity of the VSAi wave packet can be enhanced with the symmetric incident Airy pulse pair in the time domain, and the intensity maximum at focus is about 80 times of that of the initial intensity. This provides a new idea to improve the pulse intensity at a specific position during the application of high intensity pulse processing.

Secondly, by decomposing the nonlinear Schrodinger equation and considering the third-order dispersion effect, we can get.

$$\frac{\partial \boldsymbol{P}}{\partial \boldsymbol{Z}} = \frac{\mathrm{i}}{\mathbf{2}} \frac{\partial^2 \boldsymbol{P}}{\partial \boldsymbol{T}^2} + \frac{\boldsymbol{b}}{\mathbf{6}} \frac{\partial^3 \boldsymbol{P}}{\partial \boldsymbol{T}^3} = \mathbf{0} \tag{5}$$

Where, $b = \beta_3/(|\beta_2|b_t)$ is the third-order dispersion coefficient. Then the influence of the third-order dispersion on the trajectory of the focused pulse can be analyzed by using the split step Fourier method. **Figure 4** shows the influence of positive third-order dispersion coefficients on the evolution trajectory of the focused Airy pulse of $T_0 = 2$ with the different third-order dispersion coefficients as (a) b = 0.1, (b) b = 0.2, (c) b = 0.3; (d) b = 0.4. It can be found that the positive third-order dispersion coefficient

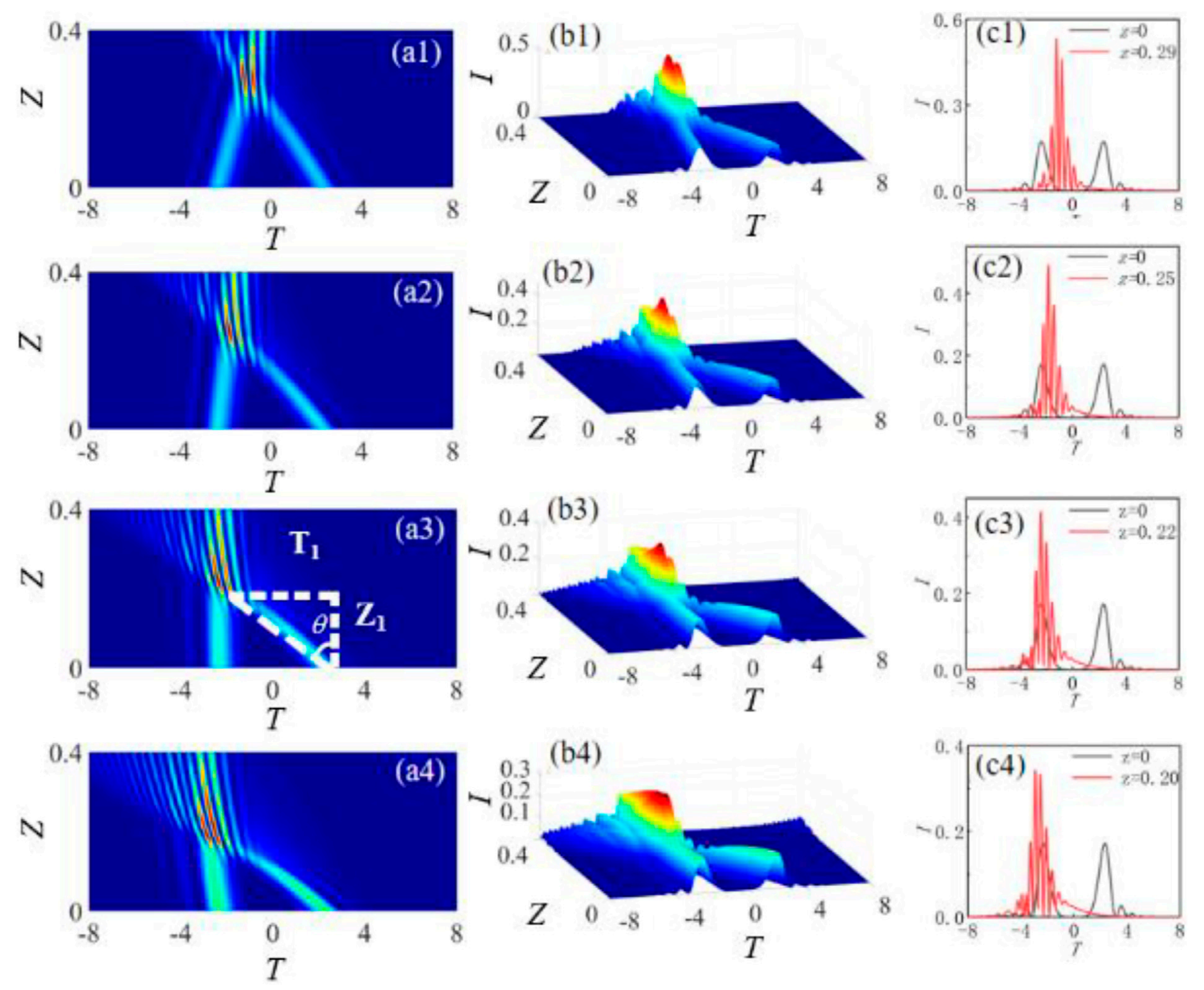

FIGURE 4 | Propagation evolution and intensity distribution of the focused Airy pulse with initial interval T_0 = 2 of the main lobe for different positive third-order dispersion coefficients **(A)** pulse intensity distributions **(B)** pulse evolution versus the propagation distance **(C)** intensity distributions of pulse at the initial plane Z = 0 and the focal point Z = 0.3.

TABLE 1 | Focusing position Z and intensity peak I_{max} of the pulse for different positive third-order dispersion coefficients.

b	*b* = 0.1	*b* = 0.2	*b* = 0.3	*b* = 0.4
Z	0.29	0.25	0.22	0.2
I_{max}	0.5389	0.4915	0.4160	0.3441

causes the forward propagation pulse to travel in the opposite direction, and positive third-order dispersion coefficient will cause a negative acceleration effect on the pulse. In addition, **Table 1** shows the focusing position Z and the intensity peak I_{max} of the pulse for different positive third-order dispersion coefficients. We can see that the evolution trajectory of the focused pulse will deviate from the original trajectory versus the increasing of the third-order dispersion coefficient, the pulse will focus in advance during propagation, and the intensity peak of the focused pulse will also decrease. That's because the increase of the third-order dispersion effect can result in the loss of pulse energy, and the decrease of the pulse energy at the focus will appear. Besides, T_1 and Z_1 in **Figure 4A** describe the change of the time and space position with the propagation pulse in the negative direction from the initial position to the focus for $b > 0$. Here the arctangent value of T/Z is defined as the deflection angle $\theta = \arctan(T/Z)$ of propagation pulse, and it can be used to describe the influence of third-order dispersion effect on the deviation of the evolution trajectory. **Figure 5A** shows the variation of the pulse focusing position Z and deflection Angle θ versus the third-order dispersion coefficient b. It can be seen that the deflection angle of pulse evolution trajectory increases rapidly at first versus the increasing of b, but the growth rate tends to be flat after b = 0.4. The deflection angle of the pulse will increase by 0.2° for every 0.1 increasing of b for the case $b < 0.4$, but the deflection angle θ can't reach 90° obviously, that's because excessive third-order dispersion effecting will lead to excessive

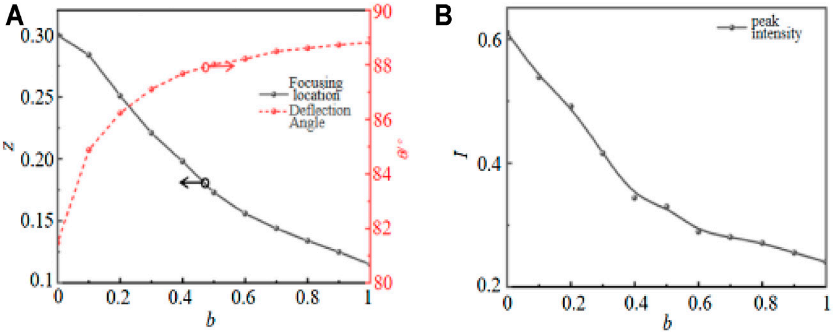

FIGURE 5 | (A) Evolutions of focusing position and deflection angle versus third-order dispersion coefficients; **(B)** Variation of intensity maximum at the focal point versus *b*.

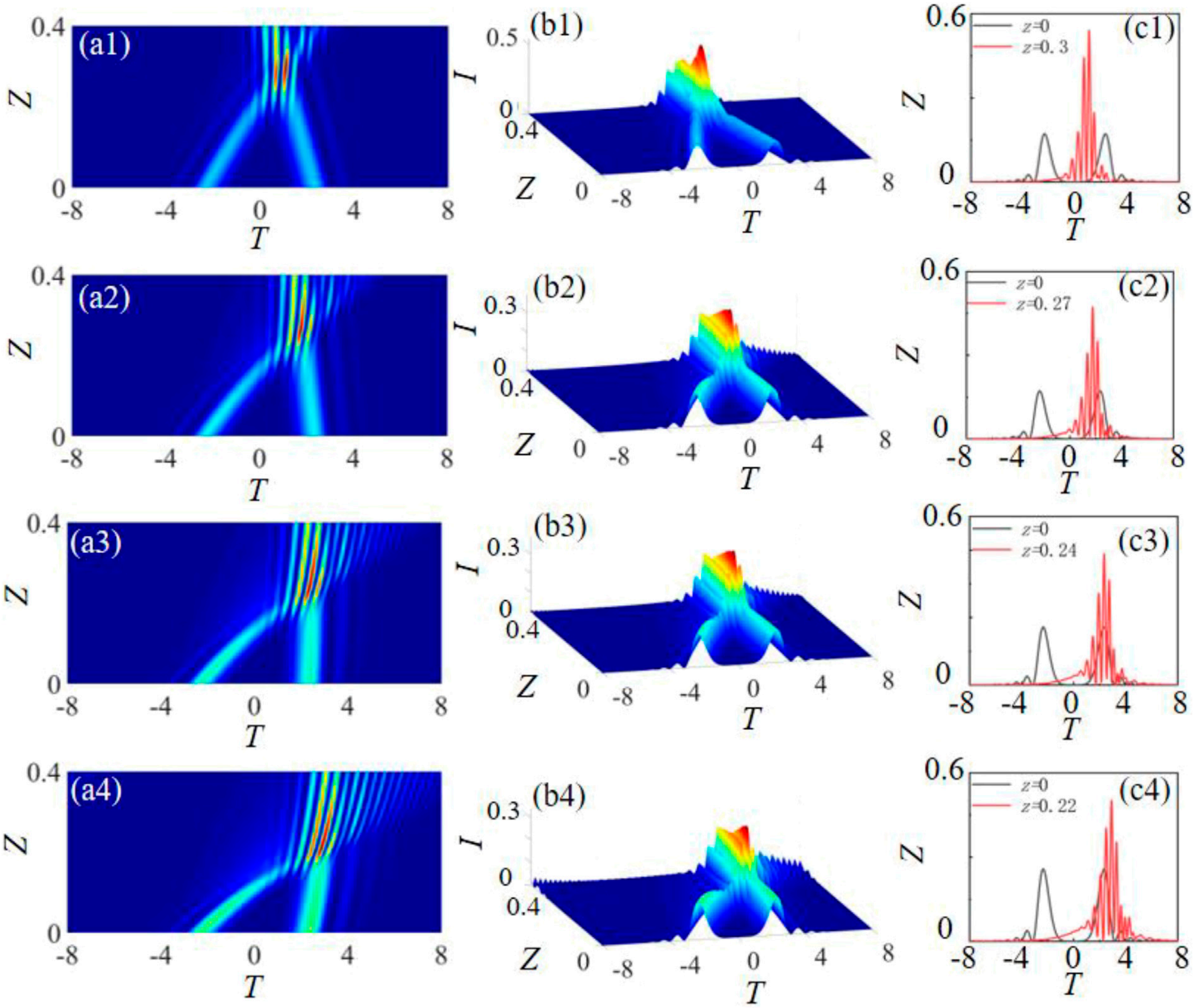

FIGURE 6 | Propagation evolution and intensity distribution of the focused Airy pulse with initial interval $T_0 = 2$ of the main lobe for different negative third-order dispersion coefficients **(A)** Pulse intensity distributions **(B)** pulse evolutions versus the propagation distance **(C)** intensity distributions of pulse at the initial plane Z = 0 and the focal point $Z = 0.3$.

TABLE 2 | Focusing position *Z* and intensity peak I_{max} of the pulse for different negative third-order dispersion coefficients.

b	*b* = -0.1	*b* = -0.2	*b* = -0.3	*b* = -0.4
Z	0.30	0.27	0.24	0.22
I_{max}	0.5456	0.4764	0.3915	0.3376

loss during the pulse propagation and failure to focus. Furthermore, the variation of the evolution trajectory deflection angle with the third-order dispersion coefficient can be approximately described as $y = x^{1/2}$ by fitting, and the focusing position moving in the direction of $Z = 0$ with the increasing of the third-order dispersion coefficient. **Figure 5B** shows the variation of the pulse intensity maximum at the focus versus the third-order dispersion coefficient. The main peak intensity of the pulse at the focal point is closely related to the value of the wave packet equivalent surface. The intensity of the main peak at the focus of the pulse gradually decreases with increasing of *b*, and the intensity of the main peak at the focus is $I_{max} = 0.2408$ with $b = 1$. In conclusion, the deflection angle increases with the increasing of the third-order dispersion coefficients, but the focusing position will move toward Z = 0 and the intensity maximum will decrease.

Based on the analysis above, **Figure 6** presents the influence of negative third-order dispersion coefficients on the evolution trajectory of the focused Airy pulse of $T_0 = 2$ with the different third-order dispersion coefficients as (a) $b = -0.1$, (b) $b = -0.2$, (c) $b = -0.3$ and (d) $b = -0.4$. It can be found that the negative third-order dispersion coefficient causes the reverse propagation pulse to travel in the positive direction, and negative third-order dispersion coefficient will have a positive acceleration effect on the pulse. In addition, **Table 2** shows the focusing position *Z* and the intensity peak I_{max} of the pulse for different negative third-order dispersion coefficients. We can see that the focusing position and intensity maximum are not symmetrical with positive and negative third-order dispersion coefficients.

CONCLUSION

Based on the nonlinear Schrodinger equation, we have established the spatiotemporal decoupling pulse propagation model of the vector field, and analyzed the influence of the initial time interval of focusing pulse on the pulse intensity maximum at the focus. Furthermore, we have also discussed the effects of the third-order dispersion effect at the focus and evolution trajectory of Airy pulses. It is found that the focused airy pulse with the third-order dispersion effect occupies more energy at the sub summit of the focus for the same initial intensity peak. The positive third-order dispersion coefficient causes the forward propagation pulse to travel in the opposite direction, and positive third-order dispersion coefficient will have a negative acceleration effect on the pulse. While the negative third-order dispersion coefficient causes the reverse propagation pulse to travel in the positive direction, and negative third-order dispersion coefficient will have a positive acceleration effect on the pulse. At the same time, it is also found that the intensity maximum of Airy pulse at the focus can be modulated by adjusting the third-order dispersion coefficient, and the evolution trajectory of the pulse can be accurately controlled and processed by adjusting the third-order dispersion effect. In paraxial optical system, the propagation along the Z direction in free space of spatiotemporal decoupled wave packets can be described by the normalized Schrodinger equation. Decoupling the three-dimensional (3D) wave packet as a fundamental spatiotemporal element requires a one-dimensional dispersion-free pulse, that means the wave packet can be decoupled spatiotemporal without dispersion modulation of the pulse, and the spatiotemporal computation can be carried out independently. These results can provide a theoretical basis for accurately controlling the evolution trajectory and intensity peak of the spatiotemporal self-focusing wave packet.

DATA AVAILABILITY STATEMENT

The original contributions presented in the study are included in the article/supplementary material, further inquiries can be directed to the corresponding authors.

AUTHOR CONTRIBUTIONS

Authors DL, XC, and CW are mainly engaged in the calculation and analysis of paper data, as well as the writing and modification of papers. PL and JZ are mainly engaged in the modification and polishing of the paper.

FUNDING

National Key Research and Development Program of China (2017YFA0303800); National Natural Science Foundation of China (61975165, 61405163); Aeronautical Science Foundation of China (201934053001); Natural Science Basic Research Plan in Shaanxi Province of China (2018JQ6029); Fundamental Research Funds for the Central Universities (310201911cx020, 3102017zv019).

REFERENCES

1. McLeod R, Wagner K, and Blair S. (3+1)-dimensional Optical Soliton Dragging Logic. *Phys Rev A* (1995) 52(4):3254–78. doi:10.1103/PhysRevA.52.3254
2. Li D, Chen X, Yang Z, Zhang W, and Zhao J. Velocity Property of an Optical Chain Generated by the Tightly Focused Femtosecond Radially Polarization Pulse. *Appl Opt* (2021) 60(8):2380–7. doi:10.1364/AO.418310
3. Papasimakis N, Raybould T, Fedotov VA, Tsai DP, Youngs I, and Zheludev NI. Pulse Generation Scheme for Flying Electromagnetic Doughnuts. *Phys Rev B* (2018) 97(20):201409. doi:10.1103/PhysRevB.97.201409

4. Shen Y, Hou Y, Papasimakis N, and Zheludev N. *Supertoroidal Light Pulses: Propagating Electromagnetic Skyrmions in Free Space*. arXiv:2103.08431 (2021). doi:10.21203/rs.3.rs-345437/v1
5. Bliokh KY. Spatiotemporal Vortex Pulses: Angular Momenta and Spin-Orbit Interaction. *Phys Rev Lett* (2021) 126. doi:10.1103/PhysRevLett.126.243601
6. Shen Y, Zdagkas A, Papasimakis N, and Zheludev NI. Measures of Space-Time Nonseparability of Electromagnetic Pulses. *Phys Rev Res* (2021) 3. doi:10.1103/physrevresearch.3.013236
7. Zdagkas A, Shen Y, Mcdonnell C, Deng J, Li G, Ellenbogen T, et al. *Observation of Toroidal Pulses of Light*. arXiv:2102.03636 (2021).
8. Hellwarth RW, and Nouchi P. Focused One-Cycle Electromagnetic Pulses. *Phys Rev E* (1996) 54:889–95. doi:10.1103/physreve.54.889
9. Berry MV, and Balazs NL. Nonspreading Wave Packets. *Am J Phys* (1979) 47(4):264–7. doi:10.1119/1.11855
10. Ring JD, Lindberg J, Mourka A, Mazilu M, Dholakia K, and Dennis MR. Auto-focusing and Self-Healing of Pearcey Beams. *Opt Express* (2012) 20(17): 18955–66. doi:10.1364/OE.20.018955
11. Ren Z, Fan C, Shi Y, and Chen B. Symmetric Form-Invariant Dual Pearcey Beams. *J Opt Soc Am A* (2016) 33(8):1523–30. doi:10.1364/JOSAA.33.001523
12. Zhijun R, Chaofu Y, Hongzhen J, and Bo C. Generation of a Family of Pearcey Beams Based on Fresnel Diffraction Catastrophes. *J Opt* (2015) 17(10):105608. doi:10.1088/2040-8978/17/10/105608
13. Liu X-L, Lu X, Liu X, Feng L-B, Ma J-L, Li Y-T, et al. Broadband Supercontinuum Generation in Air Using Tightly Focused Femtosecond Laser Pulses. *Opt Lett* (2011) 36(19):3900–2. doi:10.1364/OL.36.003900
14. Wang H, Shi L, Lukyanchuk B, Sheppard C, and Chong CT. Creation of a Needle of Longitudinally Polarized Light in Vacuum Using Binary Optics. *Nat Photon* (2008) 2(8):501–5. doi:10.1038/nphoton.2008.127
15. Youngworth KS, and Brown TG. Focusing of High Numerical Aperture Cylindrical-Vector Beams. *Opt Express* (2000) 7(2):77–87. doi:10.1364/OE.7.000077
16. Siviloglou GA, Broky J, Dogariu A, and Christodoulides DN. Observation of Accelerating Airy Beams. *Phys Rev Lett* (2007) 99(21):213901. doi:10.1103/PhysRevLett.99.213901
17. Eichelkraut TJ, Siviloglou GA, Besieris IM, and Christodoulides DN. Oblique Airy Wave Packets in Bidispersive Optical media. *Opt Lett* (2010) 35(21): 3655–7. doi:10.1364/OL.35.003655
18. Zhong W-P, Belić MR, and Huang T. Three-dimensional Finite-Energy Airy Self-Accelerating Parabolic-cylinder Light Bullets. *Phys Rev A* (2013) 88(3): 2974–81. doi:10.1103/PhysRevA.88.033824
19. Zhong W-P, Belić M, and Zhang Y. Three-dimensional Localized Airy-Laguerre-Gaussian Wave Packets in Free Space. *Opt Express* (2015) 23(18): 23867–76. doi:10.1364/OE.23.023867
20. Peng X, Peng Y, Li D, Zhang L, Zhuang J, Zhao F, et al. Propagation Properties of Spatiotemporal Chirped Airy Gaussian Vortex Wave Packets in a Quadratic index Medium. *Opt Express* (2017) 25(12):13527–38. doi:10.1364/OE.25.013527
21. Chong A, Renninger WH, Christodoulides DN, and Wise FW. Airy-Bessel Wave Packets as Versatile Linear Light Bullets. *Nat Photon* (2010) 4(2):103–6. doi:10.1038/nphoton.2009.264
22. Driben R, and Meier T. Nonlinear Dynamics of Airy-Vortex 3D Wave Packets: Emission of Vortex Light Waves. *Opt Lett* (2014) 39(19):5539–42. doi:10.1364/OL.39.005539
23. Deng F, and Deng D. Three-dimensional Localized Airy-Hermite-Gaussian and Airy-Helical-Hermite-Gaussian Wave Packets in Free Space. *Opt Express* (2016) 24(5):5478–86. doi:10.1364/OE.24.005478
24. Wu J, Huang F, Chen Y, Cheng L, Li L, and Deng D. Three-dimensional Localized Airy Elegant Laguerre-Gaussian Light Bullets in Free Space. *J Opt Soc Am B* (2017) 34(4):808. doi:10.1364/JOSAB.34.000808

Conflict of Interest: The authors declare that the research was conducted in the absence of any commercial or financial relationships that could be construed as a potential conflict of interest.

ORIGINAL RESEARCH
published: 25 October 2021
doi: 10.3389/fphy.2021.761513

Suppression of Optical Rogue Waves by Dispersion Oscillating Fiber in the Mid-infrared Supercontinuum

Shuo Liu[1,2,3]*, *Xin Han*[1,2,3], *Jiaqi lv*[1,2,3], *Yanhui Feng*[1,2,3], *Yuanqin Xia*[1,2,3] *and Zhenxu Bai*[1,2,3]

[1]*Center for Advanced Laser Technology, Hebei University of Technology, Tianjin, China,* [2]*Hebei Key Laboratory of Advanced Laser Technology and Equipment, Tianjin, China,* [3]*Tianjin Key Laboratory of Electronic Materials and Devices, Tianjin, China*

We further numerically study the mid-infrared supercontinuum (SC) and the rare optical rogue wave (ORW) generated by femtosecond pulse pumping in chalcogenide fibers. Specifically, it is shown via ensembles of numerical simulations that the compression of the spectrum by dispersion oscillating fiber (DOF) effectively controls the generation of ORW. A comparison is made between uniform fiber (UF) and DOF, the spectral bandwidth is compressed from 5,800 nm of UF to 2,300 nm of DOF, and the ORW of high peak power is suppressed. In addition, the oscillation amplitude, oscillation period and initial phase of DOF dispersion are further changed. It has been proved that the suppression effect of ORW is the best when the oscillation amplitude is 300 $\mathrm{ps^2/km}$, the oscillation period is 0.5 cm and the initial phase is 0. We believe that our research results will provide some enlightenment for controlling the direction of ORW by changing the characteristics of optical fiber, improving the performance of SC.

Keywords: optical rogue wave, dispersion oscillating fiber, nonlinear optics, mid-infrared, suppression supercontinuum

Edited by:
Bao-Sen Shi,
University of Science and Technology of China, China

Reviewed by:
Shilong Liu,
University of Ottawa, Canada
Qian Li,
Peking University, China

***Correspondence:**
Shuo Liu
liushuo@hebut.edu.cn

Specialty section:
This article was submitted to Optics and Photonics, a section of the journal Frontiers in Physics

Received: *20 August 2021*
Accepted: *11 October 2021*
Published: *25 October 2021*

Citation:
Liu S, Han X, lv J, Feng Y, Xia Y and Bai Z (2021) Suppression of Optical Rogue Waves by Dispersion Oscillating Fiber in the Mid-infrared Supercontinuum. Front. Phys. 9:761513. doi: 10.3389/fphy.2021.761513

INTRODUCTION

As is known to all, the mid-infrared supercontinuum (SC) has the advantages of wide spectral band, high radiation power and good spatial coherence. It has been widely used in spectroscopy [1], optical coherence chromatography [2], biomedical [3, 4]. In particular, SC broadening at long wavelength has attracted much attention [5]. Petersen et al. extended the long wavelength side of SC spectra to 7 μm in cascaded fibers with semiconductor lasers in 2016 [6]. Years later, the fluoride fiber was pumped by Martinez using a three-stage power amplifier, and obtained SC spectrum coverage of 1.6–11 μm [7]. Subsequently, the diameter of the fiber was reduced to 13 μm by Wang et al., and pumped the 17 cm fiber with an optical parametric amplifier laser to obtain SC spectra from 1.8 to 15 μm [8].

When the fiber is pumped by pulse, new frequency components can be generated continuously due to the interaction of linear and nonlinear effects, making the output spectrum greatly wider [9–11]. During the SC broadening formation, the velocity dispersion of the basic solitons caused by the decay of the higher order solitons is different due to the modulation instability (MI), and the collision between the solitons leads to optical rogue wave (ORW) [12]. ORW was first observed in nonlinear fiber systems by Solli et al. [13]. The ORW is a kind of low probability event with super high intensity and large redshift produced in the long wave length of SC, which seriously degrade the coherence, stability, and flatness of SC [14–16]. Next, a very weak CW trigger was used by Cheung et al. to enhance and stabilize SC generation [17]. Zhao also proposed the method of seed induced MI to control ORW in the process of mid-infrared SC generation [18]. Soon, high order ORW is studied by choosing appropriate nonlinear coefficients [19]. It is demonstrated that cascaded four wave mixing caused by weak continuous wave trigger can accelerate soliton fission and collision [20]. Therefore, how to effectively control the generation of ORW has become an important research hotspot in the field of nonlinear optics.

The periodic change of dispersion oscillating fiber (DOF) characteristics break the traditional limitation of standard MI in uniform fiber (UF). On the one hand, the MI gain side lobes result from quasi-phase-matching relation in DOF provide additional degree of freedom to control generation of ORW. For instance, Finot observed a spectral sideband splitting into different sub-sidebands in a periodically varying DOF [21]. An analytical model was also established by C. Franois et al. to calculate the parametric gain in DOFs and predict the position of the quasi-phase matched MI sidelobes [22]. Soon afterwards, the longitudinal periodic change of DOF is discussed by Mussot, which provided an additional degree of freedom to the system and led to the generation of multiple MI sideband pairs [23]. On the other hand, the dispersion and nonlinear periodic variation of DOF, which further affects the pulse and ORW generation [24]. Using continuous wave and seed signal to pump DOF by Feng in 2014, and compressed the pulse time domain of 37–21 ps [25]. Sysoliatin proved that ORW in the DOF can be controlled by changing the initial pulse and the fiber modulation period [26]. Except for the above, it is also showed an in-depth investigation of ORWs during picosecond SC generations in DOF [27].

To sum up, it is an effective way to control ORW by controlling the variation of dispersion and nonlinearity in mid-infrared DOF. In this paper, we present the in-depth investigation of ORWs during femtosecond SC generation in chalcogenide DOF. The effects of the DOF on ORW are observed by statistical peak power histogram. Then, the SC is generated by DOF with different oscillation amplitude, oscillation period and initial phase along the fiber length, respectively, and the influence of dispersion parameters on ORW is analyzed in detail.

MI ANALYSIS IN DOF

The evolution of optical pulse in DOF can be described by the nonlinear Schrodinger equation in the following form [28]:

$$\frac{\partial A}{\partial z}+\frac{\alpha}{2}A-\sum_{k\geq 2}\frac{i^{k+1}\beta_k}{k!}\frac{\partial^k A}{\partial t^k}=i\gamma\left(1+i\tau_{\text{shock}}\frac{\partial}{\partial t}\right)\left(A(z,t)\int_{-\infty}^{+\infty}R(t')\left|A(z,t-t')\right|^2\mathrm{d}t'+i\Gamma_R(z,t)\right)\tag{1}$$

where $A\ (z, t)$ is the field envelop, $\tau_{\text{shock}} = 1/\omega_0$ and ω_0 is the center frequency, γ is nonlinear coefficient, z accounts for coordinate along the fiber axis. The loss item α is ignored. Noise is included in the frequency domain through one photon per mode spectral density on each spectral discretization bin, and via the term Γ_{R} which describes thermally driven spontaneous Raman scattering [29, 30]. The numerical simulation method is split-step fast Fourier transformation, and the fixed step size used in the simulation is 0.005 cm β_k is the kth-order dispersion coefficient at the center frequency ω_0, the group velocity dispersion (GVD) value is a sine function varying with the transmission distance, which has the following form [31]:

$$\beta_2(z)=\beta_2^0+\beta_2^1\sin\left(\frac{2\pi z}{\Lambda}+\varphi\right)\tag{2}$$

where $\beta_2{}^0$ and $\beta_2{}^1$ are the average GVD value and the oscillation amplitude of GVD value, respectively. Λ is the oscillation period along the transmission distance. The initial values are $\beta_2{}^0 = -144.3\ \mathrm{ps}^2/\mathrm{km}$, $\Lambda = 0.5$ cm, $\varphi = 0$ [32]. The nonlinear response function is:

$$R(t)=\left(1-f_R\right)\delta(t)+f_R h_R(t)\tag{3}$$

where $f_{\mathrm{R}} = 0.115$ is fractional contribution of delayed Raman response to nonlinear polarization, $h_R(t)$ is Raman response function and the formula is usually expressed as [33]:

$$h_R(t)=\frac{\tau_1^2+\tau_2^2}{\tau_1\tau_2^2}\exp\left(-\frac{t}{\tau_2}\right)\sin\left(\frac{t}{\tau_1}\right)\tag{4}$$

where τ_1 relates to the phonon oscillation frequency while τ_2 defines the characteristic damping time of the network of vibrating atoms, taking the value $\tau_1 = 23.1$ fs, $\tau_2 = 195$ fs [34].

Based on the nonlinear Schrodinger equation satisfying the optical pulse transmission in DOF, the gain spectrum of MI in DOF is obtained by linear stability analysis. The MI gain of DOF can be approximately expressed as [35]:

$$g(\Omega_k)=2\gamma P_0\left|J_k\left(\frac{\beta_2^1\Omega_k^2}{2\pi/\Lambda}\right)\right|\tag{5}$$

where J is Bessel function of first kind, k represents the kth harmonic of the MI gain sideband. Ω_{k} is the frequency detuning of the kth-order MI gain sideband. The MI gain in the anomalous dispersion region of UF is considered as:

$$g(\Omega)=\left|\beta_2^0\Omega\right|\left(\Omega_c^2-\Omega^2\right)^{1/2}\tag{6}$$

Here $\Omega_{\mathrm{c}} = 4\gamma P_0/|\beta_2{}^0|$, which is the maximum frequency shift. P_0 is the peak power of pump pulse.

The background material of DOF is chalcogenide glass As_2Se_3. In 2007, Imahoko et al. have implemented a 6–12 μm mid-infrared femtosecond laser source [36]. In 2016, a fiber laser system was designed to generate pulses with a duration of 100 fs and ultra-wide wavelength tunability in the range of 2–5 μm [37]. In this paper, the mid-infrared stray light obtained by Haakestad et al. is selected as the pump light source [38]. The Gaussian pump pulse (pulse width $T_0 = 480$ fs and center wavelength $\lambda_0 =$ 4,000 nm) is propagating in the DOF. The modulated Gaussian input pulse envelope can be expressed as:

$$A(0,T)=\left(\sqrt{P_0}\right)\exp\left(-t^2/2T_0^2\right)\tag{7}$$

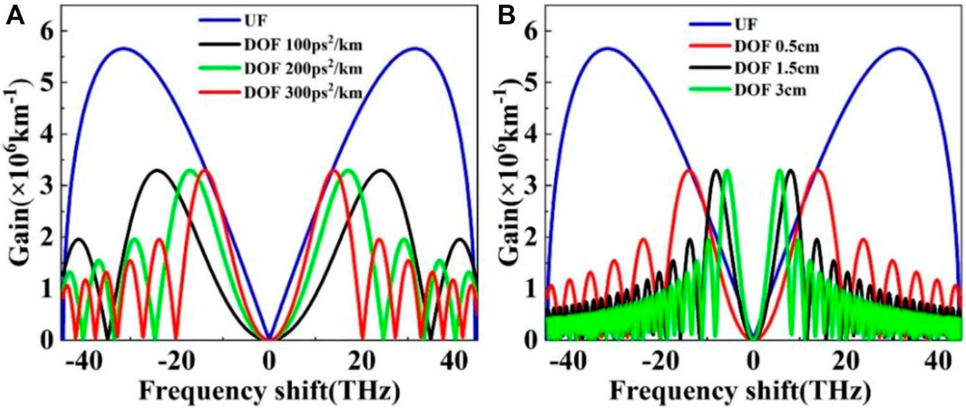

FIGURE 1 | (A) MI gain spectra at the output of DOF with different oscillation amplitudes and UF (P_0 = 1.224 kW, Λ = 0.5 cm, φ = 0), **(B)** MI gain spectra at the output of DOF with different oscillation periods and UF (P_0 = 1.224 kW, β_2^1 = 300 ps^2/km, φ = 0).

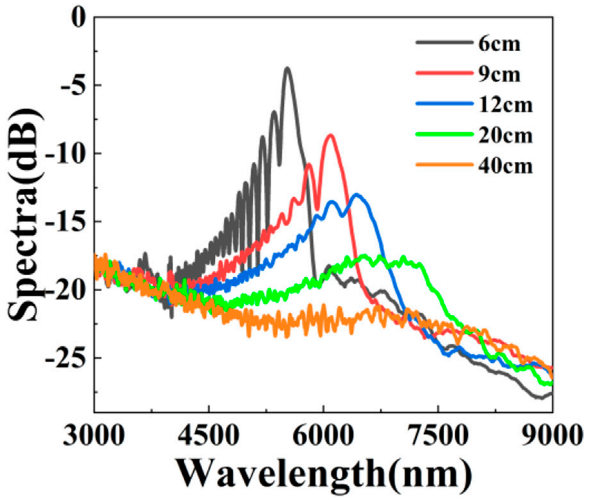

FIGURE 2 | Output mean spectra in different length DOFs (P_0 = 1.224 kW, β_2^1 = 100 ps^2/km, Λ = 0.5 cm, φ = 0).

The pulse peak power is selected as 1.224 kW, and the initial phase is 0, the first order MI gain spectrum of the DOF is drawn. **Figure 1A** corresponds to the MI gain spectrum generated when the oscillation period of DOF is 0.5 cm and the oscillation amplitudes are 100 ps^2/km (black), 200 ps^2/km (green) and 300 ps^2/km (red), respectively, and the MI gain (blue) of the UF is added for comparison. Obviously, the maximum MI gain of UF is 5.6×10^6 km^{-1}, while that of DOF is about 3.3×10^6 km^{-1}. With the increase of oscillation amplitude to 300 ps^2/km, the frequency shift corresponding to the maximum MI gain is reduced from 31 THz to 13 THz. When the oscillation amplitude of DOF is 300 ps^2/km, the oscillation periods are 0.5 cm (red), 1.5 cm (black) and 3 cm (green), respectively, their MI gain spectrum is shown in **Figure 1B**, the maximum MI gain of DOF is also about 3.3×10^6 km^{-1}. When the amplitude period increases to 3 cm, the frequency shift corresponding to the maximum MI gain is reduced from 31 THz to 5.5 THz. It can be seen that the MI gain of the fiber with different oscillation amplitude and period is different.

SIMULATION RESULTS

In the simulation process, higher-order dispersion to tenth-order and the nonlinear coefficient also change along fiber lengths. The MI gain sidelobe contains the spectral bandwidth of noise, it is beneficial to suppress the generation of ORWs in the SC [39]. The input noise with relatively narrow bandwidth near the seed wavelength is enough to simulate the noise bandwidth of the input field. Therefore, according to the MI gain diagram in **Figure 1**, the random noise with limited bandwidth of 13 THz and pump pulse amplitude of 0.01% are selected.

The pump power of the pulse is 1.224 kW, the oscillation amplitude is 100 ps^2/km, the oscillation period is 0.5 cm and the initial phase is 0. In the case of the different initial input noises, we show the output spectral variation of 500 individual simulations. Mean spectra of DOF at different fiber length has been shown in **Figure 2**. With the increase of fiber length, the spectral bandwidth becomes wider, but the spectral amplitude decreases gradually. Until the fiber length reaches 40 cm, the spectrum decays to below −20 dB, but the peak energy of the spectrum moves from 5,500 nm to the long wavelength. Therefore, in the next analysis, in order to further explore the influence of dispersion parameters on ORW in the SC, 9 and 20 cm fibers are selected. It can not only guarantee certain SC bandwidth, but also suppress ORW.

At present, many scholars believe that the emergence of ORW is random and uncertain, usually by analyzing the probability of peak power to determine the generation of ORW. The characteristic of ORW is that the peak power histogram has a long tailed L-shaped distribution structure [40, 41], which is a low probability, high intensity extreme wave phenomenon generated at a long wavelength [18]. Therefore, in this paper, the long-pass filter is used to select the spectral components above a specific wavelength, perform the inverse Fourier transform on the spectral components, count the peak power histogram in the

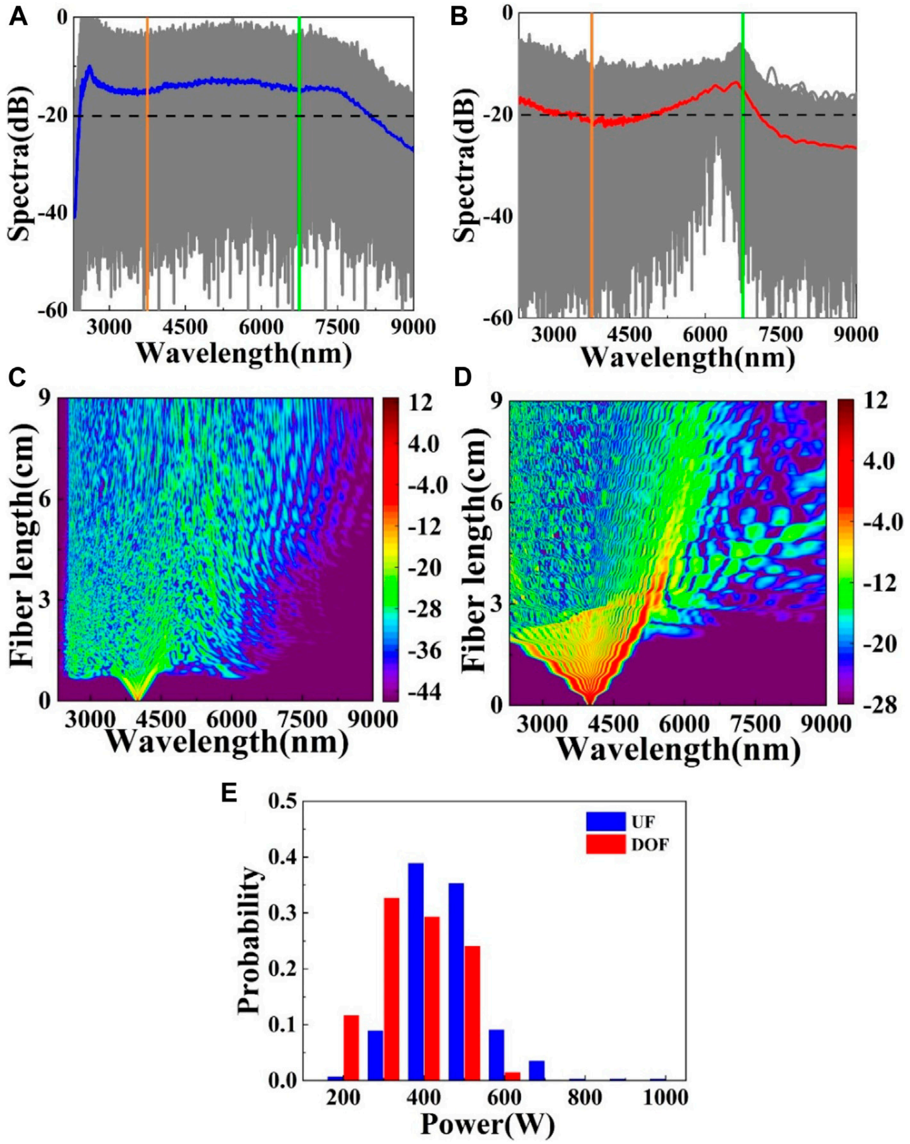

FIGURE 3 | Output mean spectra in **(A)** UF and **(B)** DOF, **(C)** and **(D)** corresponding detailed spectral evolutions dynamics in UF and DOF along the fiber lengths, and **(E)** the histograms of the peak power beyond 7000 nm [green lines in **(A)** and **(B)**]. The yellow lines in **(A)** and **(B)** is the pump wavelength 4000 nm (P_0 = 1.224 kW, β_2^{1} = 300 ps^2/km, Λ = 0.5 cm, φ = 0).

time domain, and observe whether the long tailed distribution diagram is improved. To determine the control effect of ORW.

Under the condition of 1.224 kW pulse pump power, the oscillation amplitude is 300 ps^2/km, the oscillation period is 0.5 cm and the initial phase is 0. **Figure 3A** shows the SC generation in 9 cm UF. The gray line represents the output spectrum of 500 individual simulations, and the blue line represents the average value of the output spectrum in UF. **Figure 3B** also shows the output spectra of 500 individual simulations (gray curves) and the mean spectrum (red curves) in 9 cm DOF. Using −20 dB as the standard, it is found that the spectral width of UF is 5,800 nm and that of DOF is 2,300 nm. In **Figures 3C,D** corresponding detailed spectral evolutions dynamics of a single round trip in UF and DOF along the fiber lengths. The spectral bandwidth of the DOF is much more compressed than that of the UF in long wavelength range. When the fiber length reaches 9 cm, the spectrum of UF and DOF are broadened to the wavelength of 7,200 nm and 6,200 nm. In DOF, the energy transfer occurs when the wavelength is greater than 6,200 nm. A natural idea is that the extreme and rare ORW formed in DOF is suppressed compared with that in UF. In order to verify this conjecture, the statistical histogram of the peak power of the output spectrum (i.e., Raman soliton power) over 7,000 nm in two fibers is calculated, as shown in **Figure 3E**. Specifically, in UF, the peak power histogram is distributed in a wide range of 200–1000 W, and the probability of

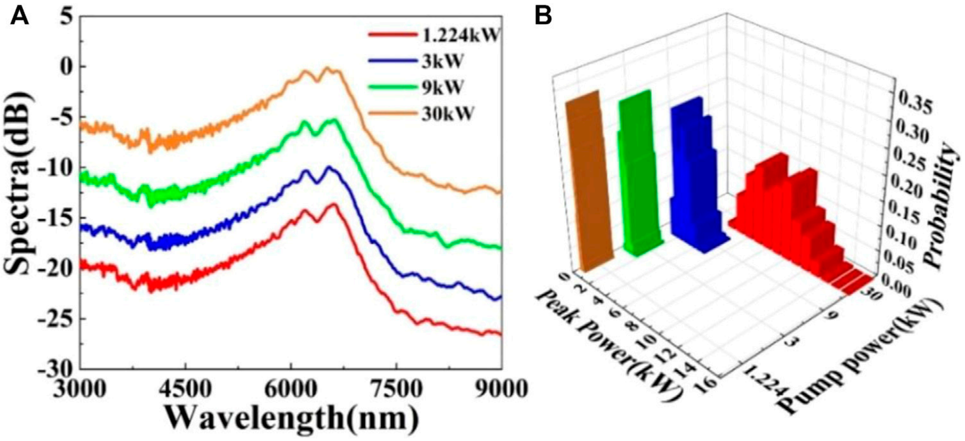

FIGURE 4 | (A) Output mean spectra and **(B)** histograms of the peak power beyond 7,000 nm of the output spectra in DOF with different pump power ($\beta_2{}^1$ = 300 ps^2/km, Λ = 0.5 cm, φ = 0).

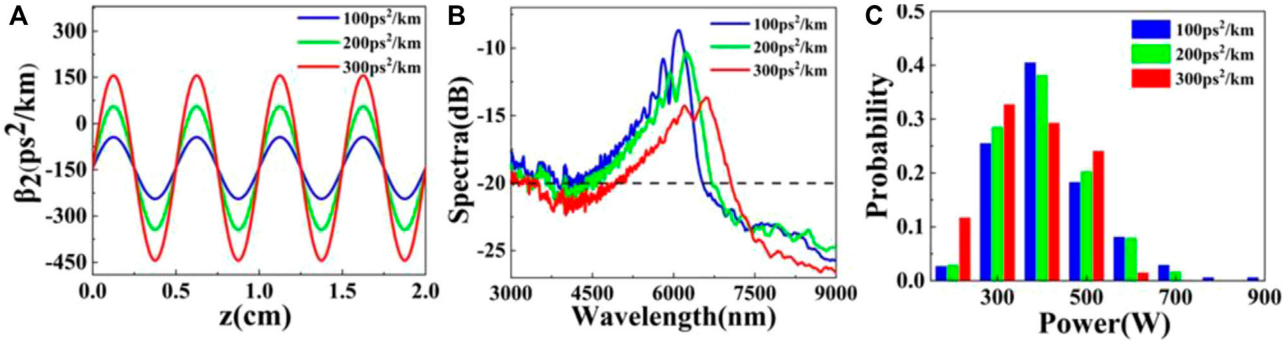

FIGURE 5 | (A) Dispersion curves of DOF, **(B)** output mean spectra of the DOF, **(C)** histograms of the peak power beyond 7,000 nm of the output spectra in DOF with different oscillation amplitudes (P_0 = 1.224 kW, Λ = 0.5 cm, φ = 0).

400 W is 0.39. However, the peak power of 700–1000 W almost disappears in DOF, and the maximum probability intensity at 300 W is reduced to 0.33. The overall probability is scattered in a narrow range of 200–600 W, and the statistical histogram is Gaussian distribution. This phenomenon indicates that the probability of ORW in DOF is much smaller than that in UF. It should be noted that the effective suppression of ORW depends on spectral bandwidth compression.

Then, before discussing different dispersion variables, let's see if the pump power has an effect on ORW. When the oscillation amplitude of DOF is 300 ps^2/km, the oscillation period is 0.5 cm and the initial phase is 0, the simulation results of the different pump power are depicted in **Figure 4A**. It is evident that the shape of SC does not change, but the spectral amplitude increases with the increase of pump power. In order to further know the influence of pump power on ORW, the statistical histogram of soliton peak power under different pump power is calculated, as shown in **Figure 4B**. The results show that as the increase of pump power, the peak power range of soliton pulse gradually increases from 200 - 700 W to 4 - 16 kW, the span range of peak power becomes wider, but the maximum probability intensity decreases from 0.33 to 0.16. When the pump power is 1.224 kW, the peak power is relatively concentrated in the narrow range of 500 W. The disappearance of L-type long tail feature is conducive to the inhibition of ORW. Hence, in the follow-up simulation process, the pump power is still 1.224 kW.

Next, the pump power is determined as 1.224 kW. The changes of different oscillation amplitudes are considered, and the oscillation amplitudes are 100, 200, and 300 ps^2/km, respectively. The oscillation period is set to 0.5 cm and the initial phase is 0. In order to see the variation of dispersion parameters clearly, the variation curve of dispersion with 2 cm DOF is selected and shown in **Figure 5A**. To further exhibit the relation between ORWs and the distinct types of DOFs, we employ three DOFs with different oscillation amplitude in **Figure 5B**. As a comparison, it can be found that with −20 dB as the standard, the spectral width is same, about 2,300 nm, but as the increase of the oscillation amplitude, the corresponding long wavelength at −20 dB increases from 6,500 nm to 7,000 nm, the spectral suppression effect at the long wavelength gradually

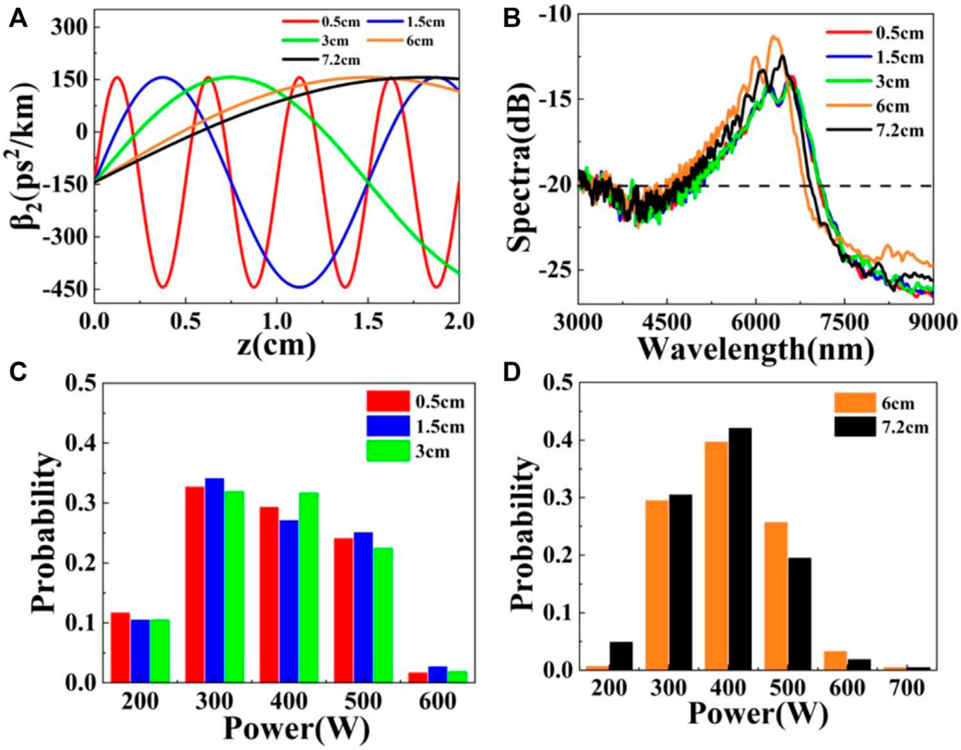

FIGURE 6 | (A) Dispersion curves, **(B)** output mean spectra, **(C,D)** histograms of the peak power beyond 7,000 nm of the output spectra in DOF with different oscillation periods (P_0 = 1.224 kW, $\beta_2{}^1$ = 300 ps^2/km, φ = 0).

becomes better. In order to better understand the influence of oscillation amplitude on ORW, the peak power of solitons in optical fibers with different oscillation amplitudes is counted, as shown in **Figure 5C**. The results show that when the amplitude is 100 ps^2/km, the power is distributed in a wide range of 200–900 W, and the probability of 400 W is 0.41. As the oscillation amplitude increases to 300 ps^2/km, the peak power of 700–900 W disappears, the maximum probability intensity of 300 W gradually decreases to 0.33, and the probability of each peak power disperses in the narrow range of 200–600 W. That is to say, the peak power at the long wavelength decreases, and the long tail of the statistical histogram disappears, so the probability of ORW in SC decreases. In conclusion, when the oscillation amplitude of DOF is large, it can not only ensure a certain SC bandwidth, but also effectively suppress the ORW generation. In the follow-up simulation, the oscillation amplitude of 300 ps^2/km is selected.

Then, the variation of different oscillation periods is considered. The pump power of the pulse is 1.224 kW, the oscillation amplitude is 300 ps^2/km and the initial phase is 0. The oscillation period was changed to integer period 0.5, 1.5, 3 cm and non-integer period 6 cm, 7.2 cm, respectively. The variation curve of dispersion with 2 cm DOF is selected, as shown in **Figure 6A**, it is straightforward that as the oscillation period increases from 0.5 to 7.2 cm, the GVD parameter tends to be flat with the increase of fiber length. Similarly, we carry out an ensemble of 500 individual simulations for each fiber using the parameters mentioned above, and then we can obtain the final output mean spectra in **Figure 6B**. It is obvious that the suppression of SC is basically same with the change of the integral period, taking −20 dB as the standard, the spectral bandwidth is 2,300 nm. While the non-integral period has a certain influence on the spectrum, in the wavelength range of 8,000 nm–9,000 nm, the spectral intensity is increased by about 1 dB. Furthermore, the corresponding statistical histogram of peak power at wavelength over 7,000 nm is calculated, and integer period and non-integer period histogram are shown in **Figures 6C,D**. The suppression effect of non-integer period on ORW is poor, the probability of peak power of about 400 W is 0.42, the peak power distribution is between 200 and 700 W. Relatively speaking, the integer period has a good suppression effect on ORW, the highest probability intensity of 300 W peak power decreases to 0.34, and the overall probability is relatively evenly distributed between 200 and 600 W, but the suppression effect of integer period is basically the same. As a result, in the following simulation, the oscillation period is still 0.5 cm.

In order to consider the different initial phases conditions, and initial phase is increased by 0.25π, 0.5π, 1.25π, 1.5π. The pump power of the pulse is 1.224 kW, the oscillation amplitude is 300 ps^2/km, the oscillation period is 0.5 cm and the initial phase is 0. The variation curve of dispersion with 1 cm DOF is selected, as revealed in **Figure 7A**. Due to different initial phases, the dispersion value at the initial position of the fiber is different, and changes periodically with the length of DOF. **Figure 7B**

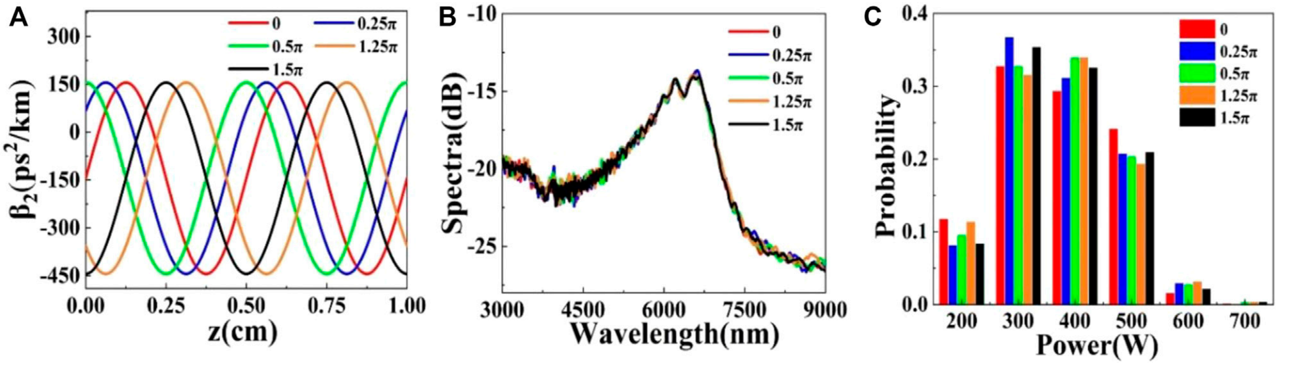

FIGURE 7 | (A) Dispersion curves, **(B)** output mean spectra, **(C)** histograms of the peak power beyond 7,000 nm of the output spectra in DOF with different initial phases (P_0 = 1.224 kW, β_2^1 = 300 ps^2/km, Λ = 0.5 cm).

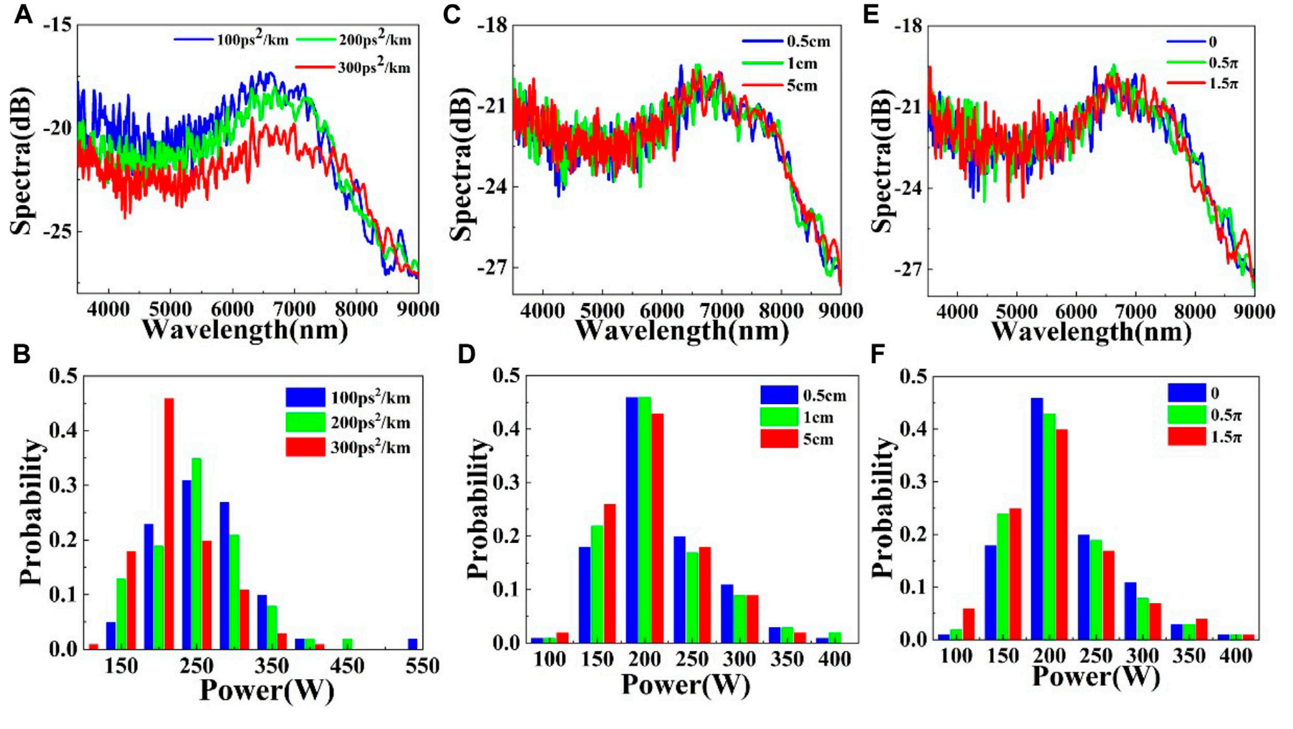

FIGURE 8 | (A,C,E) are the average of 100 output spectra, **(B,D,F)** are the peak power histograms of solitons corresponding to different oscillation amplitudes, periods and initial phases.

shows the gain spectrum, it can be found that the suppression of SC is basically the same with the change of the initial phase of the fiber, the spectral width is about 2,300 nm. Homogeneously, the statistical histograms of different phases are shown in **Figure 7C**, the results show that the probability of each peak power is basically the same, the probability of peak power 300–400 W is the highest, about 0.35, and the peak power distribution is between 200 and 700 W, so to speak, the suppression effect of phase change on ORW is almost the same.

Based on the data presented, an important conclusion can be drawn from the above results. The amplitude of DOF has a significant impact on the suppression of ORW. The greater the amplitude, the better the suppression effect. For changing the oscillation period, the suppression effect of integer period is better than non-integer period, but the suppression effect of different integer period is almost the same. For changing the initial phase, there is no significant difference in the inhibition effect of different phases on ORW. Therefore, based on the previous simulation results, in 9 cm DOF, the best parameters for ORW suppression are oscillation amplitude of 300 ps^2/km, oscillation period of 0.5 cm and initial phase of 0.

In order to verify the correctness and universality of the conclusion, we use the above initial conditions, and change different dispersion parameters in 20 cm DOF. Here, we only simulate the spectrum for 100 individual simulations, and count the corresponding peak power histogram over 7,500 nm, as shown in **Figure 8**. After analyzing the data, the results indicate that the amplitude of DOF increases from 100 ps^2/km to 300 ps^2/km, as the increase of amplitude, the distribution range of peak power decreases from 150–550 W to 100–400 W, and the maximum intensity of probability concentrates from 0.31 of 250 W to about 0.46 of 200 W. The disappearance of high peak power means that the probability of occurrence of ORW decreases. When the oscillation period and initial phase change, the suppression effect of ORW is no evident distinction, the peak power distribution is about 100–400 W, and the probability of 200 W is as high as 0.46. Therefore, a similar result is observed in 9 cm fiber and 20 cm fiber, which verifies the accuracy of the conclusion.

CONCLUSION

In conclusion, the mid-infrared SC and ORW produced by fs pulse pumping chalcogenide fiber are calculated numerically. By comparing 9 cm UF with DOF, the spectral bandwidth of SC is compressed from 5,800 nm to 2,300 nm. The compression of the spectrum by DOF effectively suppresses the generation of ORW and makes the peak power of the output pulse concentrate in a narrow range of 200–600 W. Then, by changing the oscillation amplitude, oscillation period and initial phase of the DOF dispersion, it is found that the variation of the oscillation amplitude of the DOF has a greater influence on the ORW, while the oscillation period and initial phase have no obvious influence on the ORW. The similar conclusion is also obtained in 20 cm DOF. Using the parameters mentions above, it is valid concluded that when the oscillation amplitude is 300 ps^2/km, the oscillation period is 0.5 cm and the initial phase is 0, the ORW suppression effect is the best. We believe that this research conclusion will hopefully serve as useful feedback information for control ORW by controlling the characteristics of optical fiber. It will also further ameliorate the performance of SC.

DATA AVAILABILITY STATEMENT

The original contributions presented in the study are included in the article/supplementary material, further inquiries can be directed to the corresponding author.

AUTHOR CONTRIBUTIONS

SL: Conceptualization, Writing—review and editing, Formal analysis, Supervision, Funding acquisition. XH: Methodology, Formal analysis, Writing—original draft. JL: Investigation, Writing—original draft. YF: Writing—review and editing, Formal analysis. YX: Conceptualization, Supervision. ZB: Conceptualization, Supervision.

FUNDING

National Science Foundation of China (61805067, 61975050, 62005076, 61905061); Science and Technology Research Project of Hebei Province Higher Education (BJ2018047); Natural Science Foundation of Hebei Province (F2020202069).

REFERENCES

1. Kiwanuka SS, Laurila T, and Kaminski CF. Sensitive Method for the Kinetic Measurement of Trace Species in Liquids Using Cavity Enhanced Absorption Spectroscopy with Broad Bandwidth Supercontinuum Radiation. *Anal Chem* (2010) 82(17):7498–501. doi:10.1021/ac1012255
2. Moon S, and Kim DY. Ultra-high-speed Optical Coherence Tomography with a Stretched Pulse Supercontinuum Source. *Opt Express* (2006) 14(24): 11575–84. doi:10.1364/oe.14.011575
3. Tu H, and Boppart SA. Coherent Fiber Supercontinuum for Biophotonics. *Laser Photon Rev* (2013) 7:628–45. doi:10.1002/lpor.201200014
4. He J, Miyazaki J, Wang N, Tsurui H, and Kobayashi T. Biological Imaging with Nonlinear Photothermal Microscopy Using a Compact Supercontinuum Fiber Laser Source. *Opt Express* (2015) 23(8):9762–71. doi:10.1364/oe.23.009762
5. Yang L, Li Y, Zhang B, Wu T, Zhao Y, and Hou J. 30-W Supercontinuum Generation Based on ZBLAN Fiber in an All-Fiber Configuration. *Photon Res* (2019) 7(9):1061. doi:10.1364/prj.7.001061
6. Petersen CR, Moselund PM, Petersen C, Møller U, and Bang O. Spectral-temporal Composition Matters when Cascading Supercontinua into the Mid-infrared. *Opt Express* (2016) 24(2):749–58. doi:10.1364/oe.24.000749
7. Martinez RA, Plant G, Guo K, Janiszewski B, Freeman MJ, Maynard RL, et al. Mid-infrared Supercontinuum Generation from 1.6 to >11 μm Using Concatenated Step-index Fluoride and Chalcogenide Fibers. *Opt Lett* (2018) 43(6):296–9. doi:10.1364/OL.43.000296
8. Wang X, Zhao Z, Wang X, Jiao K, Xue Z, Tian Y, et al. Mid-infrared Supercontinuum Generation in Low-Loss Single-Mode Te-Rich Chalcogenide Fiber. *Opt Mater Express* (2019) 9(8):3487. doi:10.1364/ome.9.003487
9. Tao Y, and Chen S-P. All-fiber High-Power Linearly Polarized Supercontinuum Generation from Polarization-Maintaining Photonic crystal Fibers. *High Pow Laser Sci Eng* (2019) 7(2):e28. doi:10.1017/hpl.2019.15
10. Wang F, Zhou X, Zhang X, Yan X, Li S, Suzuki T, et al. Mid-infrared Cascaded Stimulated Raman Scattering and Flat Supercontinuum Generation in an As-S Optical Fiber Pump at 2 Mm. *Appl Opt* (2021) 60(22):6351–6. doi:10.1364/ao.432394
11. Zhao S, Yang H, Huang Y, and Xiao Y. Generation of Tunable Ultra-short Pulse Sequences in a Quasi-Discrete Spectral Supercontinuum by Dark Solitons. *Opt Express* (2019) 27(16):23539–48. doi:10.1364/oe.27.023539
12. Zhao S, Yang H, Chen N, and Zhao C. Controlled Generation of High-Intensity Optical Rogue Waves by Induced Modulation Instability. *Sci Rep* (2017) 7(1):39926. doi:10.1038/srep39926
13. Solli DR, Ropers C, Koonath P, and Jalali B. Optical Rogue Waves. *Nature* (2007) 450(7172):1054–7. doi:10.1038/nature06402
14. Liu L, Nagasaka K, Suzuki T, and Ohishi Y. Mid-infrared Rogue Wave Generation in Chalcogenide Fibers. In: Proceedings of the SPIE; February 2017; San Francisco, California (2017). p. 369–75.
15. Song YF, Wang ZH, Wang C, and Panajotov K. Recent Progress on Optical Rogue Waves in Fiber Lasers: Status, Challenges, and Perspectives. *Adv Photon* (2020) 2(2):1. doi:10.1117/1.ap.2.2.024001
16. Xu J, Wu J, Ye J, Song J, Yao B, Zhang H, et al. Optical Rogue Wave in Random Fiber Laser. *Photon Res* (2020) 8(1):1. doi:10.1364/prj.8.000001

17. Cheung KKY, Zhang C, Zhou Y, Wong KKY, and Tsia KK. Manipulating Supercontinuum Generation by Minute Continuous Wave. *Opt Lett* (2011) 36(2):160–2. doi:10.1364/ol.36.000160
18. Zhao SL, Yang H, and Xiao YZ. Effects of a Seed Pulse on Rogue-Wave Formation for Midinfrared Supercontinuum Generation in Chalcogenide Photonic crystal Fibers. *Phys Rev A* (2018) 98(4):043817. doi:10.1103/physreva.98.043817
19. Yang Z, Zhong W-P, Belić M, and Zhang Y. Controllable Optical Rogue Waves via Nonlinearity Management. *Opt Express* (2018) 26(6):7587–97. doi:10.1364/oe.26.007587
20. Zhou R, Huang R, Li Q, and Fu HY. Raman Soliton at 2 μm in Picosecond Pumped Supercontinuum by a Weak CW Trigger. *Opt Express* (2019) 27(9): 12976–86. doi:10.1364/oe.27.012976
21. Finot C, Feng F, Chembo Y, and Wabnitz S. Gain Sideband Splitting in Dispersion Oscillating Fibers. *Opt Fiber Tech* (2014) 20(5):513–9. doi:10.1016/j.yofte.2014.06.003
22. Franois C, Alexandre K, Matteo C, Gilbert M, and Arnaud M. Modulation Instability in Amplitude Modulated Dispersion Oscillating Fibers. *Opt Express* (2015) 23(4):3869–75. doi:10.1364/OE.23.003869
23. Mussot A, Conforti M, Trillo S, Copie F, and Kudlinski A. Modulation Instability in Dispersion Oscillating Fibers. *Adv Opt Photon* (2018) 10(1):1. doi:10.1364/aop.10.000001
24. Gochelashvili KS, Konyukhov AI, Melnikov LA, Salganskii MY, and Sysoliatin AA. Controlled Generation of Optical Rogue Waves in Dispersion Oscillating Fiber. In: Proceedings of the SPIE LASE; February 2016; San Francisco, California (2016). p. 331–7. doi:10.1117/12.2212349
25. Sysoliatin A, Feng F, Chembo YK, Fatome J, Wabnitz S, and Finot C. Wavelength Conversion and Temporal Compression of a Pulse Train Using a Dispersion Oscillating Fibre. *Electron Lett* (2014) 50(10):768–70. doi:10.1049/el.2014.0627
26. Sysoliatin AA, Gochelashvili KS, Konyukhov AI, Melnikov LA, and Stasyuk VA. All-optical Fiber Soliton Processing Using Dispersion Oscillating Fiber. *Laser Phys Lett* (2020) 17(6):065105. doi:10.1088/1612-202x/ab8472
27. He Y, Wang S, Yang A, and Zeng X. Dynamics of Optical Rogue Wave Generation in Dispersion Oscillating Fibers. *Opt Express* (2020) 28(14): 19877–86. doi:10.1364/oe.394002
28. Dudley JM, Genty G, and Coen S. Supercontinuum Generation in Photonic crystal Fiber. *Rev Mod Phys* (2006) 78(4):1135–84. doi:10.1103/revmodphys.78.1135
29. Zhao S, Yang H, Zhao C, and Xiao Y. Harnessing Rogue Wave for Supercontinuum Generation in Cascaded Photonic crystal Fiber. *Opt Express* (2017) 25(7):7192. doi:10.1364/oe.25.007192
30. Genty G, Dudley JM, and Eggleton BJ. Modulation Control and Spectral Shaping of Optical Fiber Supercontinuum Generation in the Picosecond Regime. *Appl Phys B* (2009) 94(2):187–94. doi:10.1007/s00340-008-3274-1
31. Conforti M, Trillo S, Kudlinski A, and Mussot A. Multiple Qpm Resonant Radiations Induced by Mi in Dispersion Oscillating Fibers. *IEEE Photon Technol Lett* (2016) 28(7):740–3. doi:10.1109/lpt.2015.2507190
32. Wang XY, Li SG, Liu S, Yin GB, and Li JS. Generation of a Mid-infrared Broadband Polarized Supercontinuum in As_2Se_3 Photonic crystal Fibers. *Chin Phys B* (2012) 21(5):344–51. doi:10.1088/1674-1056/21/5/054220
33. Lin Q, and Agrawal G. Raman Response Function for Silica Fibers. *Opt Lett.* (2006) 31(21):3086–8.
34. Ung B, and Skorobogatiy M. Chalcogenide Microporous Fibers for Linear and Nonlinear Applications in the Mid-infrared. *Opt Express* (2010) 18(8): 8647–59. doi:10.1364/oe.18.008647
35. Finot C, and Wabnitz S. Influence of the Pump Shape on the Modulation Instability Process Induced in a Dispersion-Oscillating Fiber. *J Opt Soc Am B* (2015) 32(5):892–9.
36. Imahoko T, Takasago K, Sumiyoshi T, Sekita H, Takahashi K, and Obara M. Tunable Mid-infrared, High-Energy Femtosecond Laser Source for Glyco-Protein Structure Analysis. *Appl Phys B* (2007) 87(4):629–34. doi:10.1007/s00340-007-2657-z
37. Anashkina EA, Andrianov AV, Dorofeev VV, and Kim AV. Toward a Mid-infrared Femtosecond Laser System with Suspended-Core Tungstate-Tellurite Glass Fibers. *Appl Opt* (2016) 55(17):4522. doi:10.1364/ao.55.004522
38. Haakestad MW, Fonnum H, Arisholm G, Lippert E, and Stenersen K. Mid-infrared Optical Parametric Oscillator Synchronously Pumped by an Erbium-Doped Fiber Laser. *Opt Express* (2010) 18(24):25379–88. doi:10.1364/oe.18.025379
39. Zeng XL, He Y, Wang SF, and Yang A. Optical Rogue Wave Manipulations in Dispersion Oscillating Fibers. *Opt Express* (2020) 28(14):19877–86. doi:10.1364/OE.394002
40. Li Q, and Duan X. Effect of a Weak CW Trigger on Optical Rogue Waves in the Femtosecond Supercontinuum Generation. *Opt Express* (2015) 23(12): 16364–71. doi:10.1364/oe.23.016364
41. Genty G, de Sterke CM, Bang O, Dias F, Akhmediev N, and Dudley JM. Collisions and Turbulence in Optical Rogue Wave Formation. *Phys Lett A* (2010) 374(7):989–96. doi:10.1016/j.physleta.2009.12.014

Conflict of Interest: The authors declare that the research was conducted in the absence of any commercial or financial relationships that could be construed as a potential conflict of interest.

frontiers in Physics

ORIGINAL RESEARCH
published: 26 October 2021
doi: 10.3389/fphy.2021.751860

Angle-Multiplexing Nonlinear Holography for Controllable Generations of Second-Harmonic Structured Light Beams

Wenzhe Yao [1], *Chao Zhou* [1], *Tianxin Wang* [1], *Pengcheng Chen* [1], *Min Xiao* [1,2] *and Yong Zhang* [1]*

[1] *National Laboratory of Solid State Microstructures, College of Engineering and Applied Sciences, School of Physics, and Collaborative Innovation Center of Advanced Microstructures, Nanjing University, Nanjing, China,* [2] *Department of Physics, University of Arkansas, Fayetteville, AR, United States*

Nonlinear multiplexing holography emerges as a powerful tool to produce structured lights at new wavelengths. In this work, we propose and experimentally demonstrate an angle-multiplexing nonlinear holography in an angular noncritical phase-matching configuration. In experiment, various types of structured light beams, such as vortex beam, Airy beam and Airy vortex beam, are simultaneously output at second-harmonic waves along different paths. Because of the large angular acceptance bandwidth of noncritical phase-matching, one can achieve high conversion efficiency of angle-multiplexing nonlinear holography. Our method has potentially applications in high-capacity holographic storage and security encryption.

Keywords: nonlinear holography, noncritical phase matching (NCPM), multiplexing, beam shaping, second harmonic generation

Edited by:
Bao-Sen Shi,
University of Science and Technology of China, China

Reviewed by:
Zhi-Yuan Zhou,
University of Science and Technology of China, China
Youssef Elkouari,
University of Hassan II Casablanca, Morocco
Lixiang Chen,
Xiamen University, China

Correspondence:
Yong Zhang
zhangyong@nju.edu.cn

Specialty section:
This article was submitted to Optics and Photonics, a section of the journal Frontiers in Physics

Received: *02 August 2021*
Accepted: *11 October 2021*
Published: *26 October 2021*

Citation:
Yao W, Zhou C, Wang T, Chen P, Xiao M and Zhang Y (2021) Angle-Multiplexing Nonlinear Holography for Controllable Generations of Second-Harmonic Structured Light Beams. Front. Phys. 9:751860. doi: 10.3389/fphy.2021.751860

INTRODUCTION

Structured light has attracted widespread attentions because of its spatial distributions of amplitude, phase, and polarization [1]. For example, vortex beam has a unique spiral phase $\exp(il\phi)$, featuring a phase singularity at the center and a donut-shaped intensity profile [2–8]. Airy beam is capable to remain its transverse profile during propagation, and it also has self-accelerating and self-healing characteristics [9, 10]. Airy vortex beam has been realized experimentally [11–14], which combines the propagation dynamics of Airy beam and the singularity of vortex beam [15–17]. The rapid development of structured light beam significantly boosts the applications in optical manipulation, quantum communications, and super-resolution microscopy [18, 19].

Holography has many important applications in numerous areas [20–26], including data storage [20], optical encryption [21], holographic interferometry [22], microscopy [23] and dynamic holography [24–26]. Because of its powerful wavefront shaping capability, holography has recently been used in nonlinear optics to enable the generations of various structured light beams at new optical frequencies [27–34]. By utilizing the orthogonal physical dimensions of light, nonlinear holography is capable to reconstruct multiple wavefront information from a single hologram, i.e., nonlinear multiplexing holography [28, 35]. Generally, only one wavefront channel can be output at a time when the corresponding phase matching condition is satisfied in nonlinear holography. It is still difficult for nonlinear holography to output various types of structured light beams efficiently, controllably, and simultaneously.

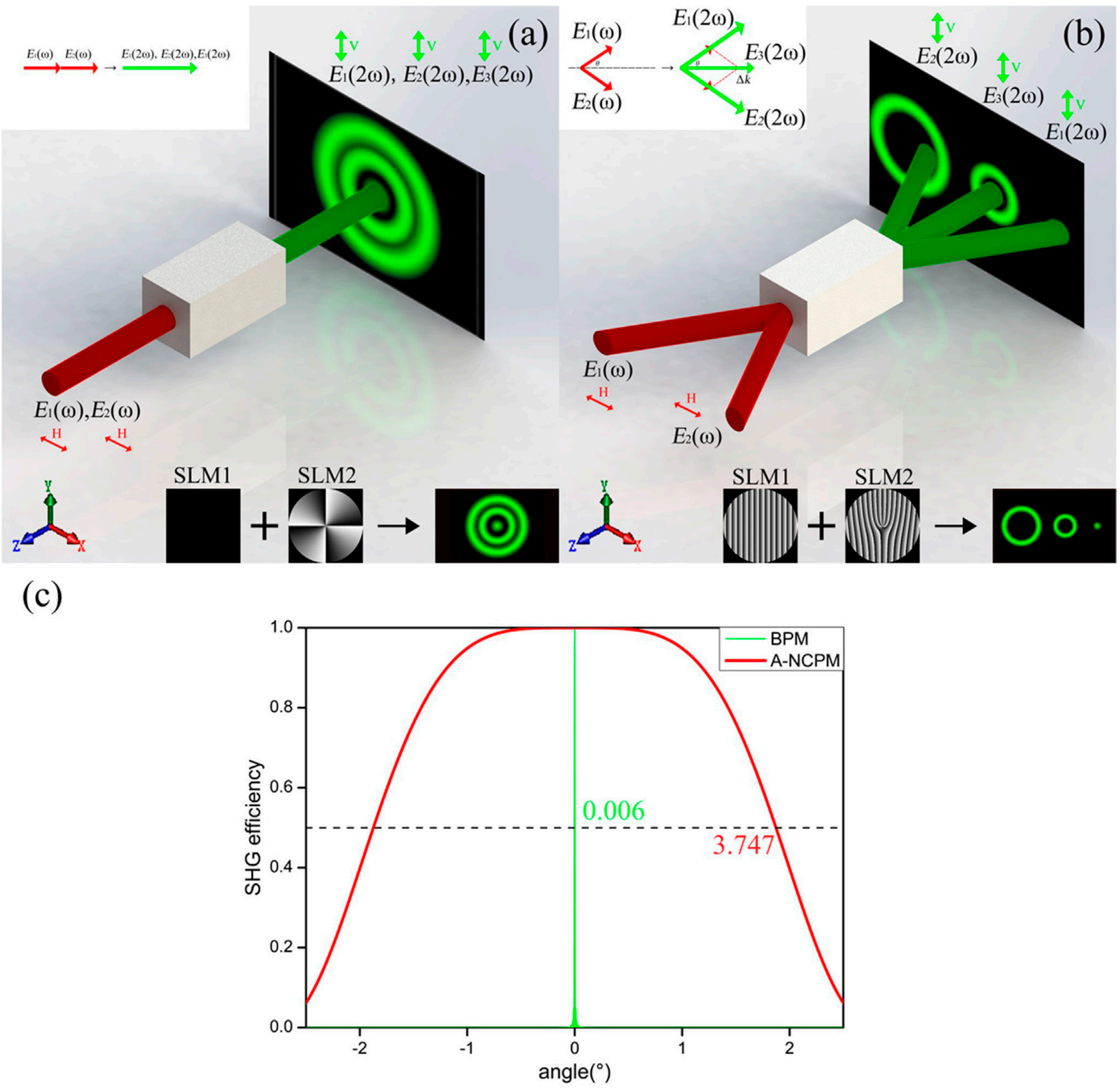

FIGURE 1 | Comparison of collinear and noncollinear BPM configurations. We load the holograms of a plane wave and a l = -4 vortex phase respectively on SLM1 and SLM2 for example. **(A)** shows the collinear BPM process, in which the generated SH fields are mixed together. **(B)** shows the noncollinear case by introducing an additional phase of exp($i\Delta k$) (or exp($-i\Delta k$)) on SLM1 (or SLM2). Clearly, the SH fields can be well separated. **(C)** shows the angle dependence of the normalized SHG efficiency. Here, we use 15-mm-long barium borate (BBO) crystal and lithium boric oxide (LBO) crystal for the calculations of BPM and A-NCPM processes, respectively. The acceptance angular bandwidth is 0.006° in a traditional BPM process, while it is significantly increased is 3.741° in the A-NCPM configuration. Here, we define the angular bandwidth by using the full width at half maximum (FWHM) of the curves.

In this paper, we propose and experimentally demonstrate an angle-multiplexing nonlinear holography in an angular noncritical phase-matching (A-NCPM) configuration. By encoding proper holograms into the fundamental waves, multiple second-harmonic (SH) beams with the desired wavefronts can be simultaneously output along different paths. High conversion efficiency is guaranteed by the large angular acceptance bandwidth of A-NCPM. In experiment, we use the angle-multiplexing nonlinear holography to generate vortex beam, Airy beam and Airy vortex beam at SH waves for example.

METHODS AND EXPERIMENT

We consider two fundamental fields, i.e., $E_1(\omega) = E_1 \exp(i\phi_1)$ and $E_2(\omega) = E_2 \exp(i\phi_2)$, which have the same optical frequencies (ω) but carry different holograms (ϕ_1 and ϕ_2). These fields pass through a nonlinear crystal, which experience three birefringence phase matching (BPM) processes. First, 2 s harmonic generation (SHG) processes happen, in which each fundamental field is frequency-doubled with itself. Second, the two fundamental fields interact with each other through a sum-frequency-generation (SFG) process. Therefore, three fields at SH

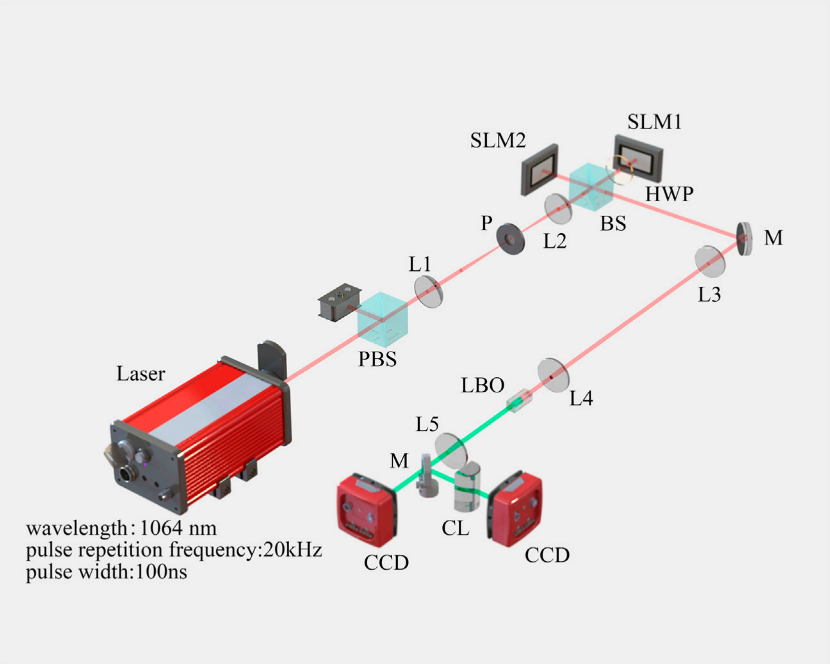

FIGURE 2 | Schematic of the experiment setup. PBS, polarization beam spitter; L, lens; P, pinhole; BS, beam splitter; HWP, half-wave plate; M, mirror; LBO, lithium boric oxide crystal; CCD, charge-coupled device; CL, cylindrical lens.

waves are generated, which can be calculated by using nonlinear three-wave mixing equation,

$$E_1(2\omega) = C(E_1)^2 \exp(2i\phi_1)\exp(-i\Delta k_1(z)z) \quad (1)$$

$$E_2(2\omega) = C(E_2)^2 \exp(2i\phi_2)\exp(-i\Delta k_2(z)z) \quad (2)$$

$$E_3(2\omega) = C(E_1E_2)\exp[i(\phi_1+\phi_2)]\exp(-i\Delta k_3(z)z) \quad (3)$$

Here, $E_i(2\omega)$ with $i = 1, 2, 3, \ldots$ represents the generated SH fields. C is a constant that is proportional to nonlinear coefficient of the nonlinear crystal. z is the propagation direction. The phase mismatch between the interacting fields is defined as $\Delta k_1 = k_1(2\omega) - 2k_1(\omega)$, $\Delta k_2 = k_2(2\omega) - 2k_2(\omega)$, and $\Delta k_3 = k_3(2\omega) - k_1(\omega) - k_2(\omega)$. When the BPM conditions are all satisfied, *i.e.*, $\Delta k_1(z) = \Delta k_2(z) = \Delta k_3(z) = 0$, high conversion efficiency of nonlinear multiplexing holography can be achieved.

Figure 1A shows a collinear type-I BPM configuration, in which two horizontally-polarized fundamental fields propagate collinearly along the z axis. Three vertically-polarized SH fields [$E_1(2\omega), E_2(2\omega)$, and $E_3(2\omega)$ as described in **Eqs 1–3**] are produced through three collinear BPM processes. Because $E_1(\omega)$ and $E_2(\omega)$ have the same wave vectors, it is easy to simultaneously satisfy the phase matching conditions $\Delta k_1(z) = \Delta k_2(z) = \Delta k_3(z) = 0$. However, this leads to overlapping of these SH fields at the image plane, as shown in **Figure 1A**. To effectively separate the generated SH fields, we add an additional term of $\exp(i\Delta k)$ to $E_1(\omega)$, and an additional term of $\exp(-i\Delta k)$ to $E_2(\omega)$, i.e., the fundamental fields of $E_1(\omega)$ and $E_2(\omega)$ are noncollinear. As a result, the SH fields $E_1(2\omega)$ and $E_2(2\omega)$ are output along the axisymmetric direction, while the SH field $E_3(2\omega)$ is still output along the z axis (**Figure 1B**). Clearly, the generated SH fields under such noncollinear configuration propagate along different paths in space, which can be well distinguished on the image plane.

This noncollinear scheme can well solve the problem of SH field overlap. However, the phase mismatch becomes $\Delta k_1(z) = \Delta k_2(z) \neq \Delta k_3(z)$, which cannot be simultaneously compensated in a traditional BPM crystal. Here, we propose A-NCPM to solve this problem [36]. A-NCPM is a popular phase-matching configuration, in which the input field generally propagates along the optical principal axis of nonlinear crystal. Under A-NCPM configuration, one can obtain a large angular acceptance bandwidth. By use of A-NCPM scheme, the conversion efficiency of the SHG process can be well maintained even the input fundamental beam is tilted by a certain angle. **Figure 1C** compares the normalized SHG conversion efficiencies of BPM and A-NCPM at different incident angles [36, 37]. In a traditional BPM process, the angular acceptance bandwidth is typically less than 0.1°. In contrast, the angular acceptance bandwidth is significantly enhanced to about 3.7° under an A-NCPM configuration in our experiment.

Figure 2 shows the experimental setup used in this work. In the optical alignment, the fundamental wave is derived from a 1,064 nm laser with a pulse repetition frequency of 20 kHz and a pulse width of 100 ns A polarizing beam splitter (PBS) is used to select a horizontally-polarized light. The fundamental wave is

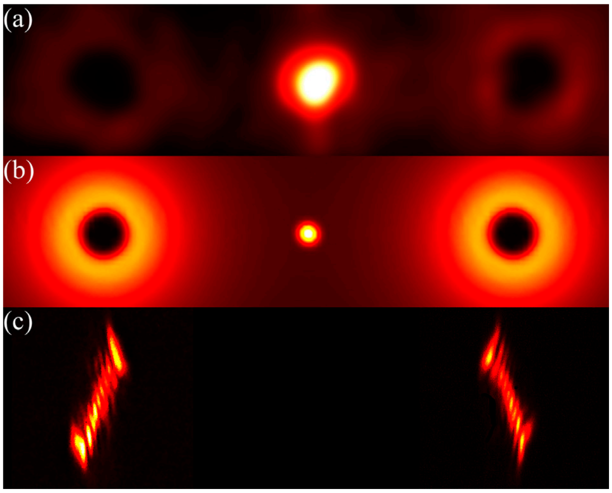

FIGURE 3 | By using two fundamental waves of l = -4 and l = 4, three SH beams of l = -8, l = 0, and l = 8 (from left to right) are simultaneously generated. **(A,B)** show the experimental and simulated results, respectively. **(C)** shows the transformed patterns after a cylindrical lens, from which the OAM number can be measured by counting the dark strips.

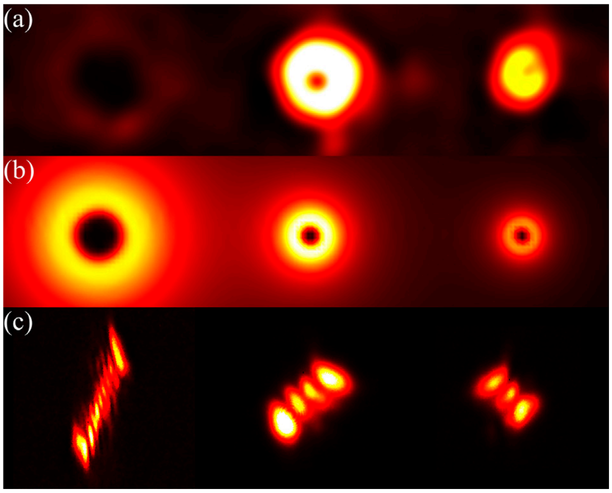

FIGURE 4 | By using two fundamental waves of l = -4 and l = 1, three SH beams of l = -8, l = -3, and l = 2 (from left to right) are produced at the same time. **(A,B)** show the experimental and simulated results, respectively. **(C)** shows the transformed patterns after a cylindrical lens for OAM measurements.

then shaped using a 4-*f* system consisting of two lenses (L1 and L2 with *f*1 = 200 mm and *f*2 = 75 mm) and a pinhole. After passing through a 50:50 beam splitter (BS), the fundamental wave is equally divided into two beams. These two beams are separately modulated by using two spatial light modulators (SLM1, BNS, P1920-600-1300-HDMI; and SLM2, Holoeye, Pluto-2-NIR-011) to carry the designed holograms. Because SLM1 used in the experiment only works for vertically-polarized light, we add a half-wave plate (HWP) between BS and SLM1. After modulation, they are combined via the 50:50 BS and then shaped using another 4-*f* system consisting of lenses L3 and L4 (with *f*3 = 500 mm and *f*4 = 50 mm). Then, the fundamental beams are incident into an LBO crystal (type-I, $\theta = 0$, $\varphi = 90^{\circ}$, $4 \times 4 \times 15\ \text{mm}^3$). A filter is placed after the LBO crystal to filter out the fundamental wave, and a lens L5 (*f*5 = 200 mm) is then used to perform the Fourier transform of the generated SH fields. Finally, the SH beams are recorded using a charge-coupled device (CCD) camera (Newport, LBP2-HR-VIS2). The SH vortex beams is tested by using a cylindrical lens [38].

In experiment, we first demonstrate the generations of multiple SH vortex beams. First, vortex holographic phase holograms with $l = -4$ and $l = 4$ are loaded onto SLM1 and SLM2, respectively. Here, the hologram is designed according to binary computer-generated-hologram (CGH) theory [39]. Besides, a blazed grating phase is superimposed on each hologram to introduce the additional spatial phase $\exp(i\Delta k)$ or $\exp(-i\Delta k)$. Here, Δk is chosen to ensure the incident angle lies in the acceptance angular bandwidth of A-NCPM. In our experiment, the incident angle of the fundamental wave is measured to be 0.78°. Then, the two fundamental waves $E_1(\omega)$ and $E_2(\omega)$ interact in the LBO crystal to produce three SH beams. The conversion of the orbital-angular momentum (OAM) in nonlinear optical process obeys $l(2\omega) = l(\omega) + l'(\omega)$[40, 41]. **Figure 3A** shows the experimental result. The two donut-shaped SH beams on the sides correspond to the SHG processes in which $E_1(\omega)$ (or $E_2(\omega)$) is frequency-doubled with itself. The generated $E_1(2\omega)$ (or $E_2(2\omega)$) carries an OAM of $l = -8$ (or $l = 8$), which is measured by using a cylindrical lens, as shown in **Figure 3C**. The central Gaussian spot results from the SFG process between $E_1(\omega)$ and $E_2(\omega)$. Because the interacting fundamental waves have topological charges of opposite sign, the spiral phase is cancelled in the generated SH wave. In addition, we replace the hologram loaded on SLM2 to a $l = 1$ vortex

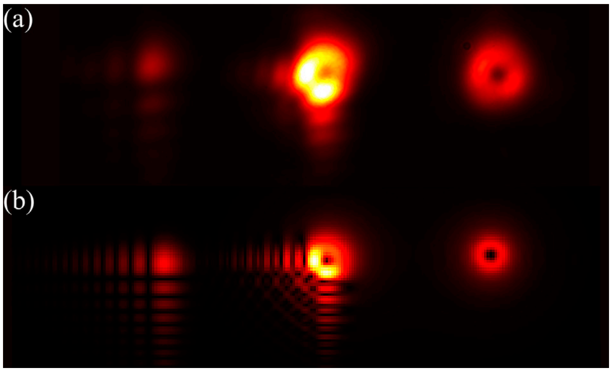

FIGURE 5 | The experimental **(A)** and simulated **(B)** generations of Airy beam, Airy vortex beam and vortex beam (from left to right) at SH waves.

holographic phase hologram while keeping the hologram on SLM1 unchanged. As shown in **Figure 4A**, three SH vortex beams of $l = -8$, $l = -3$, and $l = 2$ present from left to right on the image plane. Their OAMs are also measured by a cylindrical lens as shown in **Figure 4C**, which is consistent with the OAM conservation law. **Figures 3B**, **4B** show the numerical simulations, which are in good agreement with the experimental results in **Figures 3A**, **4A**, respectively.

Next, we produce various types of spatial light beams simultaneously. In this experiment, we load the holograms for the generations of a 2D Airy beam and a $l = 1$ vortex beam on SLM1 and SLM2, respectively. Notably, if a fundamental Airy beam is directly frequency-doubled with itself in the nonlinear crystal, one achieves the product of two Airy beams rather than the SH Airy beam [42]. In the experiment, we use the Fourier transform (FT) of the Airy beam as the hologram on SLM1, which is imaged into the nonlinear crystal and performs SHG. Then, the generated SH field is converted to an SH Airy beam after FT through a lens. Under such experimental configuration, three different types of SH beams, i.e., SH vortex beam, SH Airy beam, and SH Airy vortex beam, are produced along different paths. The experimental results are shown in **Figure 5A**, which agree well with the simulated results as shown in **Figure 5B**. Notably, the SH intensities in **Figures 3–5** are not the same because the conversion efficiencies of SHGs involving various structured light beams are different.

CONCLUSION

In conclusion, we propose an angle-multiplexing nonlinear holography to produce multiple structured light beams simultaneously under an A-NCPM configuration. In experiment, we demonstrate a three-channel output of various SH beams, which can be further extended to more output channels within the angular acceptance bandwidth of A-NCPM. The angle-multiplexing nonlinear holography can also be applied in nonlinear photonic crystals and nonlinear metasurfaces [43–47]. Our work provides a feasible solution to enhance the capacity of nonlinear holography for multi-wavelength display, multi-dimensional optical storage, optical encryption, all-optical diffractive neuron networks [48], and optical communications.

DATA AVAILABILITY STATEMENT

The original contributions presented in the study are included in the article/supplementary material, further inquiries can be directed to the corresponding author.

AUTHOR CONTRIBUTIONS

WY, CZ, TW, and PC performed the experiments under the guidance of YZ and MX, WY, and YZ wrote the manuscript with contributions from all

FUNDING

National Key R&D Program of China (2017YFA0303703), the National Natural Science Foundation of China (NSFC) (91950206 and 11874213), and Fundamental Research Funds for the Central Universities (021314380191 and 021314380105).

REFERENCES

1. Forbes A Structured Light from Lasers. *Laser Photon Rev* (2019) 13(11): 1900140. doi:10.1002/lpor.201900140
2. Allen L, Beijersbergen MW, Spreeuw RJC, and Woerdman JP Orbital Angular Momentum of Light and the Transformation of Laguerre-Gaussian Laser Modes. *Phys Rev A* (1992) 45(11):8185–9. doi:10.1103/PhysRevA.45.8185
3. Coullet P, Gil L, and Rocca F Optical Vortices. *Opt Commun* (1989) 73(5): 403–8. doi:10.1016/0030-4018(89)90180-6
4. Djordjevic IB, and Arabaci M LDPC-coded Orbital Angular Momentum (OAM) Modulation for Free-Space Optical Communication. *Opt Express* (2010) 18(24):24722–8. doi:10.1364/OE.18.024722
5. Yan L, Gregg P, Karimi E, Rubano A, Marrucci L, Boyd R, et al. Q-plate Enabled Spectrally Diverse Orbital-Angular-Momentum Conversion for Stimulated Emission Depletion Microscopy. *Optica* (2015) 2(10):900–3. doi:10.1364/OPTICA.2.000900
6. Chong A, Wan C, Chen J, and Zhan Q Generation of Spatiotemporal Optical Vortices with Controllable Transverse Orbital Angular Momentum. *Nat Photon* (2020) 14(6):350–4. doi:10.1038/s41566-020-0587-z
7. Wei D, Zhu Y, Zhong W, Cui G, Wang H, He Y, et al. Directly Generating Orbital Angular Momentum in Second-Harmonic Waves with a Spirally Poled Nonlinear Photonic crystal. *Appl Phys Lett* (2017) 110(26):261104. doi:10.1063/1.4990527
8. Wei D, Cheng Y, Ni R, Zhang Y, Hu X, Zhu S, et al. Generating Controllable Laguerre-Gaussian Laser Modes through Intracavity Spin-Orbital Angular Momentum Conversion of Light. *Phys Rev Appl* (2019) 11(1):014038. doi:10.1103/PhysRevApplied.11.014038
9. Siviloglou GA, Broky J, Dogariu A, and Christodoulides DN Observation of Accelerating Airy Beams. *Phys Rev Lett* (2007) 99(21):213901. doi:10.1103/PhysRevLett.99.213901
10. Efremidis NK, Chen Z, Segev M, and Christodoulides DN Airy Beams and Accelerating Waves: an Overview of Recent Advances. *Optica* (2019) 6(5): 686–701. doi:10.1364/OPTICA.6.000686
11. Wei B-Y, Liu S, Chen P, Qi S-X, Zhang Y, Hu W, et al. Vortex Airy Beams Directly Generated via Liquid crystal Q-Airy-Plates. *Appl Phys Lett* (2018) 112(12):121101. doi:10.1063/1.5019813
12. Singh BK, Remez R, Tsur Y, and Arie A Measurement of Acceleration and Orbital Angular Momentum of Airy Beam and Airy-Vortex Beam by Astigmatic Transformation. *Opt Lett* (2015) 40(22):5411–4. doi:10.1364/OL.40.005411
13. Zhou J, Liu Y, Ke Y, Luo H, and Wen S Generation of Airy Vortex and Airy Vector Beams Based on the Modulation of Dynamic and Geometric Phases. *Opt Lett* (2015) 40(13):3193–6. doi:10.1364/OL.40.003193
14. Liu Y, Chen W, Tang J, Xu X, Chen P, Ma CQ, et al. Switchable Second-Harmonic Generation of Airy Beam and Airy Vortex Beam. *Adv Opt Mater.* (2021) 9(4):2001776. doi:10.1002/adom.202001776
15. Dai HT, Liu YJ, Luo D, and Sun XW Propagation Properties of an Optical Vortex Carried by an Airy Beam: Experimental Implementation. *Opt Lett* (2011) 36(9):1617–9. doi:10.1364/OL.36.001617

16. Wei B, Qi S, Liu S, Li P, Zhang Y, Han L, et al. Auto-transition of Vortex- to Vector-Airy Beams via Liquid crystal Q-Airy-Plates. *Opt Express* (2019) 27(13):18848–57. doi:10.1364/OE.27.018848
17. Xu C, Wu Y, and Deng D Multioptical Bottles from Second-Order Chirped Symmetric Airy Vortex Beams. *Opt Lett* (2020) 45(13):3502–5. doi:10.1364/OL.388569
18. Hell SW, and Wichmann J Breaking the Diffraction Resolution Limit by Stimulated Emission: Stimulated-Emission-Depletion Fluorescence Microscopy. *Opt Lett* (1994) 19(11):780–2. doi:10.1364/OL.19.000780
19. Klar TA, and Hell SW Subdiffraction Resolution in Far-Field Fluorescence Microscopy. *Opt Lett* (1999) 24(14):954–6. doi:10.1364/OL.24.000954
20. Heanue JF, Bashaw MC, and Hesselink L Volume Holographic Storage and Retrieval of Digital Data. *Science* (1994) 265(5173):749–52. doi:10.1126/science.265.5173.749
21. Li J, Kamin S, Zheng G, Neubrech F, Zhang S, and Liu N Addressable Metasurfaces for Dynamic Holography and Optical Information Encryption. *Sci Adv* (2018) 4(6):eaar6768. doi:10.1126/sciadv.aar6768
22. Powell RL, and Stetson KA Interferometric Vibration Analysis by Wavefront Reconstruction. *J Opt Soc Am* (1965) 55(12):1593–8. doi:10.1364/JOSA.55.001593
23. Gabor D Microscopy by Reconstructed Wave-Fronts. *Proc R Soc Lond A* (1949) 197(1051):454–87. doi:10.1098/rspa.1949.0075
24. Luc J, Bouchouit K, Czaplicki R, Fillaut J-L, and Sahraoui B Study of Surface Relief Gratings on Azo Organometallic Films in Picosecond Regime. *Opt Express* (2008) 16(20):15633–9. doi:10.1364/OE.16.015633
25. Bartkiewicz S, Miniewicz A, Sahraoui B, and Kajzar F Dynamic Charge-Carrier-Mobility-Mediated Holography in Thin Layers of Photoconducting Polymers. *Appl Phys Lett* (2002) 81(20):3705–7. doi:10.1063/1.1512824
26. Matczyszyn K, Bartkiewicz S, and Sahraoui B A New Holographic System: Liquid crystal Doped with Photochromic Molecules. *Opt Mater* (2002) 20(1):57–61. doi:10.1016/S0925-3467(02)00047-2
27. Fang X, Wang H, Yang H, Ye Z, Wang Y, Zhang Y, et al. Multichannel Nonlinear Holography in a Two-Dimensional Nonlinear Photonic crystal. *Phys Rev A* (2020) 102(4):043506. doi:10.1103/PhysRevA.102.043506
28. Chen P, Wang C, Wei D, Hu Y, Xu X, Li J, et al. Quasi-phase-matching-division Multiplexing Holography in a Three-Dimensional Nonlinear Photonic crystal. *Light Sci Appl* (2021) 10(1):1–7. doi:10.1038/s41377-021-00588-5
29. Liu S, Switkowski K, Xu C, Tian J, Wang B, Lu P, et al. Nonlinear Wavefront Shaping with Optically Induced Three-Dimensional Nonlinear Photonic Crystals. *Nat Commun* (2019) 10(1):1–7. doi:10.1038/s41467-019-11114-y
30. Liu S, Mazur LM, Krolikowski W, and Sheng Y Nonlinear Volume Holography in 3D Nonlinear Photonic Crystals. *Laser Photon Rev* (2020) 14(11):2000224. doi:10.1002/lpor.202000224
31. Wang H, Wei D, Xu X, Wang M, Cui G, Lu Y, et al. Controllable Generation of Second-Harmonic Vortex Beams through Nonlinear Supercell Grating. *Appl Phys Lett* (2018) 113(22):221101. doi:10.1063/1.5050423
32. Wei D, Wang C, Xu X, Wang H, Hu Y, Chen P, et al. Efficient Nonlinear Beam Shaping in Three-Dimensional Lithium Niobate Nonlinear Photonic Crystals. *Nat Commun* (2019) 10(1):1–7. doi:10.1038/s41467-019-12251-0
33. Wu Y, Liu H, and Chen X Three-dimensional Nonlinear Optical Holograms. *Phys Rev A* (2020) 102(6):063505. doi:10.1103/PhysRevA.102.063505
34. Zhu B, Liu H, Liu Ya., Yan X, Chen Y, and Chen X Second-harmonic Computer-Generated Holographic Imaging through Monolithic Lithium Niobate crystal by Femtosecond Laser Micromachining. *Opt Lett* (2020) 45(15):4132–5. doi:10.1364/OL.394162
35. Fang X, Yang H, Yao W, Wang T, Zhang Y, Gu M, et al. High-dimensional Orbital Angular Momentum Multiplexing Nonlinear Holography. *Adv Photon* (2021) 3(1):015001. doi:10.1117/1.AP.3.1.015001
36. Liu Y, Wang Z, Yu F, Qi H, Yang X, Yu X, et al. Angular Non-critical Phase-Matching Second-Harmonic-Generation Characteristics of RECOB (RE = Tm, Y, Gd, Sm, Nd and La) Crystals. *Opt Express* (2017) 25(10):11867–93. doi:10.1364/OE.25.011867
37. Wu FT, and Zhang WZ Consideration of Angular Acceptance Angle in BBO crystal on a Highly Efficient Second Harmonic Generation. *Opt Laser Tech* (1998) 30(3-4):189–92. doi:10.1016/S0030-3992(98)00032-2
38. Volyar A, Bretsko M, Akimova Y, and Egorov Y Measurement of the Vortex and Orbital Angular Momentum Spectra with a Single Cylindrical Lens. *Appl Opt.Applied Opt* (2019) 58(21):5748–55. WH. Binary computer-generated holograms1979182136613669. doi:10.1364/AO.58.005748Leedoi:10.1364/AO.18.003661
39. Lee W-H Binary Computer-Generated Holograms. *Appl Opt* (1979) 18(21):3661–9. doi:10.1364/AO.18.003661
40. Courtial J, Dholakia K, Allen L, and Padgett MJ Second-harmonic Generation and the Conservation of Orbital Angular Momentum with High-Order Laguerre-Gaussian Modes. *Phys Rev A* (1997) 56(5):4193–6. doi:10.1103/PhysRevA.56.4193
41. Li Y, Zhou Z-Y, Ding D-S, and Shi B-S Sum Frequency Generation with Two Orbital Angular Momentum Carrying Laser Beams. *J Opt Soc Am B* (2015) 32(3):407–11. doi:10.1364/AO.58.00574810.1364/josab.32.000407
42. Dolev I, and Arie A *Frontiers in Optics*. Rochester, NY, United States: Optical Society of America (2010). p. FThA1. doi:10.1364/FIO.2010.FThA1 Second Harmonic Generation of Airy Beams in Quadratic Nonlinear Photonic Crystals.
43. Wei D, Wang C, Wang H, Hu X, Wei D, Fang X, et al. Experimental Demonstration of a Three-Dimensional Lithium Niobate Nonlinear Photonic crystal. *Nat Photon* (2018) 12(10):596–600. doi:10.1038/s41566-018-0240-2
44. Xu T, Switkowski K, Chen X, Liu S, Koynov K, Yu H, et al. Three-dimensional Nonlinear Photonic crystal in Ferroelectric Barium Calcium Titanate. *Nat Photon* (2018) 12(10):591–5. doi:10.1038/s41566-018-0225-1
45. Li G, Zhang S, and Zentgraf T Nonlinear Photonic Metasurfaces. *Nat Rev Mater* (2017) 2(5):1–14. doi:10.1038/natrevmats.2017.10
46. Zhang Y, Sheng Y, Zhu S, Xiao M, and Krolikowski W Nonlinear Photonic Crystals: from 2D to 3D. *Optica* (2021) 8(3):372–81. doi:10.1364/OPTICA.416619
47. Segal N, Keren-Zur S, Hendler N, and Ellenbogen T Controlling Light with Metamaterial-Based Nonlinear Photonic Crystals. *Nat Photon* (2015) 9(3):180–4. doi:10.1038/nphoton.2015.17
48. Lin X, Rivenson Y, Yardimci NT, Veli M, Luo Y, Jarrahi M, et al. All-optical Machine Learning Using Diffractive Deep Neural Networks. *Science* (2018) 361(6406):1004–8. doi:10.1126/science.aat8084

Conflict of Interest: The authors declare that the research was conducted in the absence of any commercial or financial relationships that could be construed as a potential conflict of interest.

frontiers in Physics

MINI REVIEW
published: 24 November 2021
doi: 10.3389/fphy.2021.768165

Narrow-Linewidth Laser Linewidth Measurement Technology

Zhenxu Bai[1,2,3], Zhongan Zhao[1,2], Yaoyao Qi[1,2], Jie Ding[1,2], Sensen Li[4], Xiusheng Yan[4], Yulei Wang[1,2] and Zhiwei Lu[1,2]*

[1]Center for Advanced Laser Technology, Hebei University of Technology, Tianjin, China, [2]Hebei Key Laboratory of Advanced Laser Technology and Equipment, Tianjin, China, [3]Department of Physics and Astronomy, MQ Photonics Research Centre, Macquarie University, Sydney, NSW, Australia, [4]Science and Technology on Electro-Optical Information Security Control Laboratory, Tianjin, China

A narrow-linewidth laser with excellent temporal coherence is an important light source for microphysics, space detection, and high-precision measurement. An ultranarrow-linewidth output with a linewidth as narrow as subhertz has been generated with a theoretical coherence length over millions of kilometers. Traditional grating spectrum measurement technology has a wide wavelength scanning range and an extended dynamic range, but the spectral resolution can only reach the gigahertz level. The spectral resolution of a high-precision Fabry–Pérot interferometer can only reach the megahertz level. With the continuous improvement of laser coherence, the requirements for laser linewidth measurement technology are increasing, which also promotes the rapid development of narrow-linewidth lasers and their applications. In this article, narrow-linewidth measurement methods and their research progress are reviewed to provide a reference for researchers engaged in the development, measurement, and applications of narrow-linewidth lasers.

Keywords: narrow-linewidth, laser, measurement, high coherence, beat note

Edited by:
Bao-Sen Shi,
University of Science and Technology of China, China

Reviewed by:
Ping Su,
Tsinghua University, China
Tao Peng,
Texas A&M University, United States

****Correspondence:***
Zhenxu Bai
baizhenxu@hotmail.com

Specialty section:
This article was submitted to Optics and Photonics, a section of the journal Frontiers in Physics

Received: *31 August 2021*
Accepted: *01 November 2021*
Published: *24 November 2021*

Citation:
Bai Z, Zhao Z, Qi Y, Ding J, Li S, Yan X, Wang Y and Lu Z (2021) Narrow-Linewidth Laser Linewidth Measurement Technology. Front. Phys. 9:768165. doi: 10.3389/fphy.2021.768165

INTRODUCTION

Narrow-linewidth lasers with extremely low phase noise and a large coherence length have been widely used as a high-spectral-purity light source in gravitational wave detection [1, 2], optical atomic clocks [3, 4], lidar [5, 6], high-speed coherent optical communication [7, 8], and distributed optical fiber sensing [9, 10]. The main reason for the linewidth generation is the phase fluctuation caused by spontaneous radiation [11] and the noise induced by mechanical and temperature factors [12, 13]. Therefore, the laser linewidth reflects the physical and frequency stability of the laser. Scully and Lamb [14] proposed the laser quantum theory. They deduced that the spectral profile of the laser is Lorentzian and calculated its width (full width at half height). The linewidth value, an essential parameter of the laser, directly affects the accuracy of the narrow-linewidth laser in detection [15], sensitivity in sensing [16], and bit error rate in communication [17, 18]. Therefore, precise measurement of the linewidth value is a prerequisite for the application of narrow-linewidth lasers.

Different types of laser produce a broad coverage of linewidths, as large as tens of gigahertz [19, 20] and as small as subhertz [21, 22]. At present, the resolution of a commercial optical spectrum analyzer based on diffraction gratings is approximately 0.05 nm (gigahertz level)[1], and the resolution of Fabry–Pérot interferometers can reach a few megahertz[2]. The rapid development and application

---

[1] https://tmi.yokogawa.com.

[2] https://www.thorlabs.com.

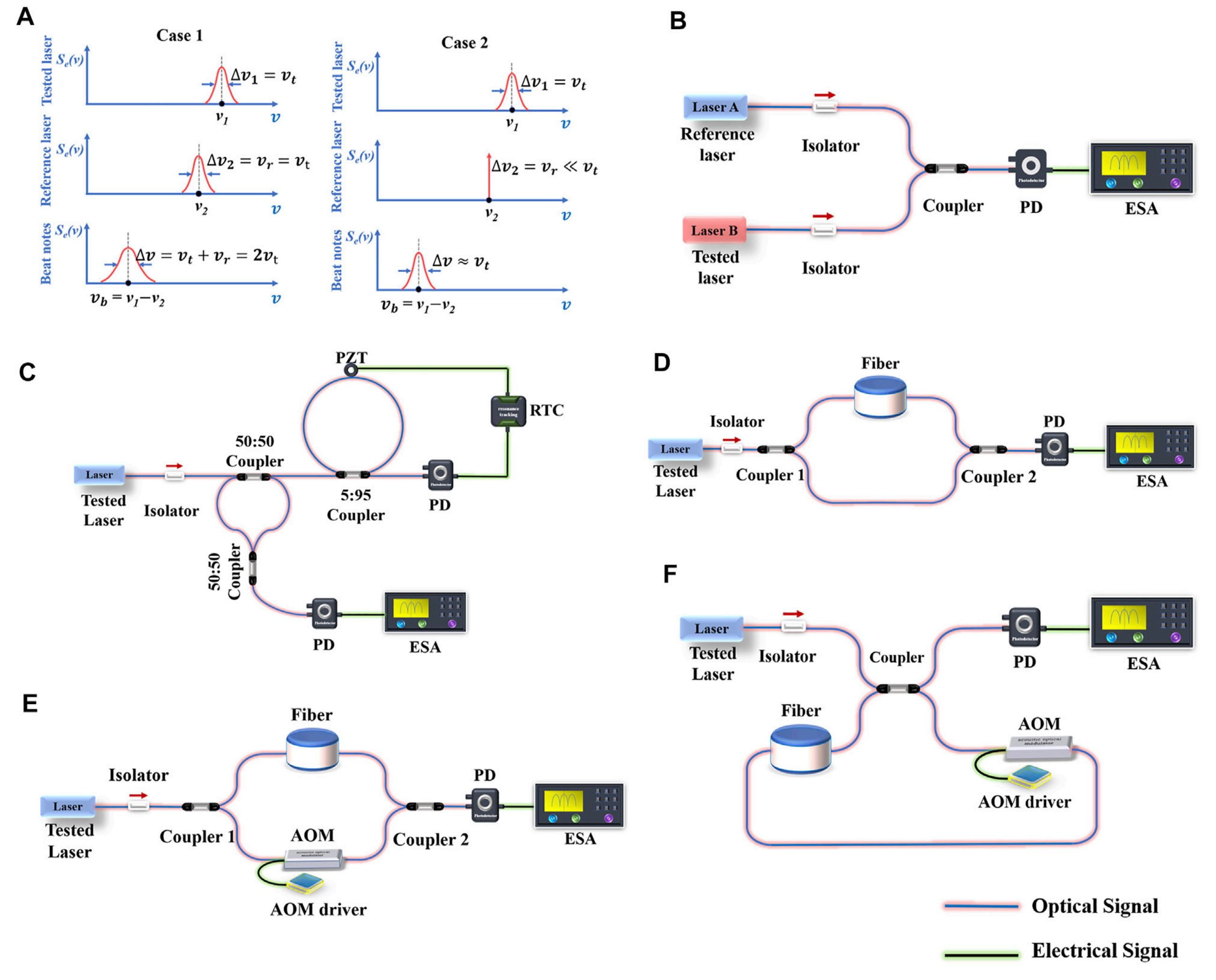

FIGURE 1 | (A) Principle of optical beat notes, **(B)** beating note with a reference laser, **(C)** beating note with the Stokes wave of a Brillouin laser, **(D)** delayed self-homodyne interferometric detection, **(E)** delayed self-heterodyne interferometric detection, and **(F)** recirculating delayed self-heterodyne interferometer detection (PD, photodetector; ESA, electrical spectrum analyzer; RTC, resonance tracking circuit; PZT, piezoelectric transducer; AOM, acoustic optical modulator).

of narrow-linewidth lasers have resulted in higher requirements for laser linewidth measurement technology. Specific devices must be built for lasers with a narrower linewidth (sub-megahertz) to measure the linewidth. In the past few decades, laser frequency stabilization [23, 24] and mode selection [25] have matured, and many narrow-linewidth measurement schemes are constantly being updated.

In this article, typical methods for measuring narrow-linewidth lasers are reviewed, and the characteristics of each method, as well as the status of its development, are summarized. Finally, a summary and an outlook for the future development of narrow-linewidth measurements are provided.

Narrow-Linewidth Laser Measurement Method

Two methods are mainly used for linewidth measurement: directly calculating the laser linewidth using the power spectrum density (PSD) of the laser and deducing the linewidth indirectly based on the relationship between the phase noise and linewidth. The power spectrum contains more-intuitive linewidth information, and it is relatively easy to obtain; therefore, a large proportion of linewidth measurement experiments focus on the former. Optical beat notes are necessary to obtain the PSD. The mixed signal of two incoherent lasers, each with a Lorentzian line shape, still has a Lorentzian line shape, and the PSD of the beat notes can be expressed as [26].

$$s(\nu) = \frac{\Delta\nu}{2\pi\left[(\nu - \nu_b)^2 + (\Delta\nu/2)^2\right]} \tag{1}$$

where $\Delta\nu = \nu_t + \nu_r$, ν_t is the linewidth of the tested laser, ν_r is the linewidth of the reference laser, and ν_b is the difference between the output frequencies of the two lasers mentioned above (also the center frequency of the beat notes). Two lasers with the same or similar frequencies interfere and produce a beat signal with a lower frequency. The linewidth of the beat signal is the sum of the widths of the two lasers participating in the beat. There are usually two cases of beat notes suitable for linewidth measurement, as shown in **Figure 1A**. If $\nu_t = \nu_r$, the linewidth of the beat notes is twice the linewidth of the tested laser ($\Delta\nu = 2\nu_t$, case 1). If $\nu_t \gg \nu_r$, (that is, the output spectrum of the reference laser is exceptionally narrow and the linewidth can be ignored compared with the tested laser), the linewidth value of the beat signal is approximately the value of the linewidth of the tested laser ($\Delta\nu \approx \nu_t$, case 2). These two cases are flexibly used in different measurement structures according to the specific conditions of the tested lasers. In this section, the focus is on four measurement structures based on the above two cases.

Beating Note With a Reference Laser

Figure 1B shows the measurement structure of using an additional laser to generate a reference laser beam and beating with the tested laser. The photodetector (PD) receives the mixed signal and transmits it to an electrical spectrum analyzer (ESA). Based on case 1, a laser with the same linewidth as the test is used to serve as the reference laser. In this case, any linewidth can be measured, but obtaining, measuring, and calibrating a reference laser is difficult. Based on case 2, using a reference laser whose linewidth value is negligible compared with the tested laser can meet the linewidth measurement requirements of most lasers; however, it is difficult to measure the ultranarrow linewidth in this case accurately. In addition, the two lasers participating in the beating should have the same amplitude, the same optical frequency (or a slight difference), and constant phase difference [27], which requires a stable experimental environment, increasing the difficulty and cost of testing.

Although this method has high requirements for the stability of the two lasers and the experimental environment, scientific researchers still favor it. In particular, ultranarrow-linewidth measurement based on case 1 does not require extra algorithm design, such as measuring the ultranarrow linewidth (see *Delayed self-heterodyne interferometric detection*), when analyzing beat notes. This avoids calculation errors, and the results are more convincing. In 1999, Young et al. [28] used a high-precision Fabry–Pérot cavity to realize a narrow-linewidth output. They built a second similar cavity for laser stability measurement (including linewidth measurement) and adjusted the laser frequency difference ν_b between the two cavities to 400 MHz to avoid low-frequency noise. They designed an independent vacuum chamber, temperature control system, and vibration isolation platform to ensure the stability of the two lasers. The measured linewidth was 0.6 Hz. In 2012, Kessler et al. [29] used two traditional cavity-stabilized lasers as reference laser sources to study a test laser. By analyzing the heterodyne signals among the three lasers, they concluded that the stability of the tested laser was the best, so the linewidth of the laser under test was the narrowest. The narrowest linewidth value obtained by the heterodyne signals between the tested laser and the other two lasers was 49 mHz, so they judged the linewidth of the tested laser to be less than 40 mHz. In 2013, Lee et al. [30] reported a chip-based resonator in the form of a spiral. It had a strong resistance to thermal noise and mechanical noise interference. Two identical fiber lasers were locked to the spiral resonator using a Pound–Drever–Hall locking system. The linewidth obtained by analyzing the beat notes of the two locked lasers was less than 100 Hz. In 2015, Liang et al. [31] built a laser identical to the tested laser to measure the narrow linewidth. They designed a thermal package and a sealed environment for the reference resonator to avoid technical noise caused by environmental and temperature fluctuations, and they concluded that the laser has an integrated linewidth of 30 Hz and a subhertz instantaneous linewidth. In 2018, Pavlov et al. [32] achieved a single-frequency output by using self-injection locking. They used a narrow-linewidth tunable fiber laser to perform heterodyne measurement with the tested laser and obtained a 340-Hz Lorentzian width and 1.7-kHz Gaussian width. According to Voigt linewidth theory [33], it was concluded that the laser linewidth was less than 1 kHz.

Beating Note With the Stokes Wave of Brillouin Laser

This approach does not require an additional reference laser, which solves the structural limitation that an additional laser must be used to provide a reference laser beam for linewidth measurement (see *Beating note with a reference laser*). As shown in **Figure 1C**, the tested laser was divided into two beams by a coupler. One beam is injected into the fiber ring cavity to form a Brillouin laser, and the other couples with the first-order Stokes wave propagating backward in the Brillouin laser. The coupling signal enters the PD to beat, and the beat note signal is fed into the ESA. The measurement principle is based on case 2. The tested laser is also the pump used to generate the Brillouin laser. The first-order Stokes beam linewidth ν_r of the Brillouin laser is usually much smaller than the pump linewidth, so the linewidth of the beat notes is approximately the linewidth of the tested laser ($\Delta\nu \approx \nu_r$). Compared with the structure discussed in *Beating note with a reference laser*, this scheme only requires the tested laser to complete the linewidth measurement and makes testing easier. Generally, the Brillouin frequency shift reaches 10–20 GHz [34] in the optical fiber. This frequency shift is the frequency difference ν_b between the Stokes wave and the tested laser. It is also the center frequency of the beat notes. Therefore, a large Brillouin frequency shift causes the center frequency of the beat signal to exceed the measurement range of the ESA, which causes difficulties in the measurement. In principle, this scheme is only suitable for 1–500-kHz linewidth measurement [35]. When the linewidth of the tested laser is extremely narrow, this scheme is no longer applicable, and significant errors occur.

In 1991, Smith [36] verified the good linewidth compression effect of the Brillouin laser by building a Brillouin fiber ring laser. In 1994, Boschung [37] realized a 3.84-Hz linewidth Brillouin laser output in a fiber ring cavity by using an incident laser with a linewidth of 100 kHz. These works provide a theoretical and experimental foundation for the beating frequency with the Stokes wave of the Brillouin laser. In 1996, Kueng [35] built the measurement structure shown in **Figure 1C** for the first time and obtained a linewidth of 4.2 kHz. In 2005, Dong et al. [38]

proposed a scheme using a second-order Stokes wave in the fiber ring as the reference beam, which further improved the accuracy of the Brillouin laser first-order Stokes optical beat method.

Delayed Self-Homodyne Interferometric Detection

The delayed self-homodyne interferometric structure is shown in **Figure 1D**, and the measurement principle is based on case 1. This structure is based on the unbalanced Mach–Zehnder interferometer (UMZI) [39]. It does not have the measurement range limitation of the structure in *Beating note with the Stokes wave of Brillouin laser* and has the advantages of a simple structure, wide measurement range, and low optical transmission loss. However, the center frequency v_b of the beat notes is 0 Hz; therefore, the low-frequency noise in the environment interferes with the measurement results. Considering the sensing characteristics of the optical fiber [40], the disturbance of environmental noise, temperature, pressure, and other factors can seriously affect the test results obtained by the optical fiber [41].

In 1986, Ryu [42] found that this method has the advantages of simple setting and high resolution when measuring narrow-linewidth lasers. In 1989, Nazarathy [43] derived the photocurrent power spectral density for this structure. In 1998, Ludvigsen [44] reported an optimized delay homodyne method in which the photocurrent signal was amplified by a low-noise amplifier and mixed with a stable 200 MHz local oscillator in a double-balanced mixer. They obtained a 460-kHz linewidth value with only 71.7 m of fiber. Because of its poor stability, this structure has rarely been used for direct linewidth measurement in recent years, but it often appears in optical frequency discriminators (OFDs) for linewidth measurement. The measurement principle of OFDs is no longer based on case 1 or case 2, and the linewidth information is calculated from the noise spectrum. In 2019, Gundavarapu [45] et al. reported a narrow-linewidth Brillouin laser output on an integrated Si_3N_4 waveguide platform. They measured the linewidth based on an OFD using a fiber-based UMZI and a balanced PD (the PD in **Figure 1D** is changed to a balanced PD), and the linewidth value was calculated to be 0.7 Hz. In 2021, Chauhan [46] et al. reported a visible-light photonic integrated Brillouin laser, and the measured laser linewidth value was 269 Hz using an OFD.

Delayed Self-Heterodyne Interferometric Detection

Delayed self-heterodyne interferometry (DSHI) overcomes the shortcoming that delayed self-homodyne interferometric structures are susceptible to low-frequency noise. The measurement principle is based on case 1. As shown in **Figure 1E**, an acousto-optic modulator (AOM) is introduced to shift the center frequency of the beat notes to a high frequency that is not affected by the environment to reduce system errors and improve measurement accuracy. Nevertheless, the DSHI method to measure narrow-linewidth lasers must be completed under the condition that the delay time is much longer than the coherence time. In theory, to test a 100-Hz linewidth, the fiber length required is as much as 1,590 km [47]. The long optical fiber increases the experimental volume and attenuation and introduces 1/f noise that can cause spectral line broadening [48], which results in larger measurement errors. Moreover, when the output power of the tested laser is large, the long-delay fiber generates stimulated Brillouin scattering, which is opposite to the direction of laser transmission; in this case, the incident pump energy is converted into Stokes wave and sound wave energy, increasing the transmission loss and even making the PD unable to detect the signal. The DSHI method was first proposed by Okoshi [49] in 1980. In 1986, Richter [50] derived the power spectral density function of the beat notes under the DSHI structure and reported that the measurement result would be more accurate with a delay time much longer than the coherence time of the tested laser. The spectral line of the beat signal is generally fitted by a Lorentzian function [51]. To offset the influence of 1/f noise introduced by long optical fiber, Chen [33] proposed a fitting scheme based on the Voigt profile. The Voigt function is the convolution of the Gaussian and Lorentz functions [52, 53]. Using this function to fit the collected data can effectively filter out the influence of 1/f noise.

To remove the 1/f noise from the root, researchers have proposed a short-fiber delayed self-heterodyne interferometer strategy for linewidth measurement. When the fiber is short, the PSD function is no longer expressed by **Eq. 1**, and the complete PSD function is expressed as [49, 54].

$$\begin{aligned} S(f) = \frac{P_0^2}{4\pi}\frac{\Delta f}{\Delta f^2 + (f - f_1)^2}\Bigg\{1 - exp(-2\pi\tau_d\Delta f) \\ \times\left[\cos(2\pi\tau_d(f - f_1)) + \Delta f\frac{\sin(2\pi\tau_d(f - f_1))}{f - f_1}\right]\Bigg\} \\ + \frac{\pi P_0^2}{2}exp(-2\pi\tau_d\Delta f)\delta(f - f_1) \end{aligned} \tag{2}$$

where P_0 is the power of the beat signal, Δf is the laser linewidth, f_1 is the AOM modulation frequency, τ_d is the delay time (proportional to the fiber length), and $\delta(f)$ is the impact function. According to the PSD function under a short optical fiber delay, different schemes have been designed to calculate the laser linewidth. In 2008, Jia [55] used polynomial fitting to eliminate the defect that caused the measurement accuracy to drop significantly when the delay time was insufficient and measured an 8-kHz linewidth with 25-km fiber. In 2015, Wei [56] obtained a numerical solution for the laser linewidth by measuring the frequency difference between the minimum points next to the maximum at the center frequency of the power spectrum. In principle, measuring a linewidth of 10 kHz requires only 300 m of delay fiber. In 2016, Huang [54, 57] reported an approach for contrasting the difference with the second peak and the second trough (CDSPST) of the coherence envelope to determine the laser linewidth. Only 3 km of fiber was used to measure a linewidth of 150 Hz. In 2018, Bai [58] successfully measured a laser with a linewidth of 98 Hz using

TABLE 1 | Comparison of laser linewidth measurement methods.

Type	Advantages	Disadvantages	Linewidth	Ref
Beating note with a References laser	1. Easy to calculate 2. The measurement results are accurate (especially measuring ultranarrow linewidth according to case 1)	1. Two independent lasers are required 2. The References laser should be adjusted according to the tested laser	0.6 Hz 40 mHz 100 Hz 30 Hz	[28] [29] [30] [31]
		3. Obtaining, measuring, and calibrating the References laser is complicated	<1 kHz	[32]
Beating note with the Stokes wave of Brillouin laser	1. Only one laser can complete the linewidth measurement	1. The Brillouin frequency shift in the optical fiber exceeds the measurement range of some standard ESAs, which causes difficulties for the measurement	4.2 kHz	[35]
	2. The linewidth can be measured within a certain range without adjusting the structure	2. The Brillouin laser has a linewidth that makes the method unsuitable for the case where the linewidth of the tested laser is ultranarrow		
Delay self-homodyne interferometric detection	1. The structure is simple and easy to build 2. It can measure the linewidth within a certain range without adjusting the structure	The measurement results are extremely susceptible to low-frequency noise	460 kHz 0.7 Hz (OFD)	[44] [45]
			269 Hz (OFD)	[46]
Delayed self-heterodyne interferometric detection	1. The structure is simple and easy to build 2. It can measure the linewidth within a certain range without adjusting the structure	A long fiber introduces 1/f noise and causes spectral line broadening	8 kHz 150 Hz	[55] [54]
	3. The measurement structure is stable and not susceptible to external interference		98 Hz 2.53 kHz 458 Hz 151 Hz	[58] [59] [60] [61]

the CDSPST method with a fiber delay of 2,950 m. In 2019, He [59] reported a linewidth demodulation scheme that achieved linewidth measurement by demodulating the coherent envelope of a short-delay self-heterodyne interference spectrum, and used this method to demodulate a 2.53-kHz linewidth. In 2020, Wang [60] reported a dual-parameter acquisition method and used it to calculate a 458-Hz linewidth by obtaining the frequency difference and amplitude difference of the coherence envelope. In 2021, Xue [61] reported a linewidth measurement method that combined long and short fibers. The measurement result of the long-delay fiber was used as the initial value, and the short-fiber self-heterodyne measurement results were demodulated. Xue used this method to demodulate a laser linewidth of 151 Hz successfully.

Other Measurement Methods

In addition to the above approaches, many other structures and optimization algorithms for narrow-linewidth laser measurements have been developed. The recirculating delayed self-heterodyne interferometer (RDSHI) method (see **Figure 1F**) is also widely used [62–65]. The unique fiber ring structure of this approach permits the delay fiber to increase the delay time by several times between two laser beams [66]. It is also an approach for improving the traditional DSHI method. Moreover, there is a close relationship between frequency noise and linewidth. Domenico et al. [67] proposed an approximate formula to show the relationship between the linewidth and frequency noise. Zhou et al. [68] reported a method to estimate the laser linewidth from its frequency power spectral density, called the "power-area method." The β-separation line technique is an application of this relationship, which is convenient for calculating the laser linewidth after obtaining the laser frequency noise data [69]. Xu [70] et al.reported a method to measure the linewidth by using an unbalanced Michelson interferometer composed of a 3 × 3 optical fiber coupler. These structures can achieve a relatively accurate measurement of linewidth at a level of 1,000 Hz.

CONCLUSION AND OUTLOOK

Linewidth measurement technology is an essential part of the research and development process of narrow-linewidth lasers. Here, the typical methods for narrow-linewidth measurement were summarized, and the characteristics of various schemes were analyzed, as shown in **Table 1**. At present, measurement technology based on DSHI methods is developing rapidly, and its application is the most extensive among the methods. The method of beating notes with a reference laser is also used to test some ultranarrow-linewidth lasers owing to its excellent accuracy. The future renewal of linewidth compression technology is expected to place higher requirements on linewidth measurement technology. The RDSHI method has the advantages of the DSHI method. The multiorder beat signal measured by this scheme can avoid random errors and is expected to become the next research focus of narrow-linewidth measurement technology. In addition, Pollnau et al. [71, 72] questioned the traditional linewidth theory in recent studies, and they pioneered the theory that laser linewidth is a classical physics phenomenon, which may have an impact on linewidth measurement technology.

AUTHOR CONTRIBUTIONS

ZB: Investigation, Writing—original draft, Writing—review and editing, Supervision. ZZ: Investigation, Writing—original draft. YQ: Investigation, Writing—review and editing. JD: Investigation, Writing—review and editing. SL: Investigation, Writing—review and editing. XY: Writing—review and editing. YW: Writing—review and editing, Supervision. ZL: Writing—review and editing, Supervision.

FUNDING

This work was supported by the National Natural Science Foundation of China (61905061, and 61927815), Natural Science Foundation of Hebei Province (F2019202337), and National Defense Science and Technology Key Laboratory Foundation (6142107190308).

REFERENCES

1. Abbott BP, Abbott R, Adhikari R. LIGO: the Laser Interferometer Gravitational-Wave Observatory. *Rep Prog Phys* (2009) 72(7):076901. doi:10.1088/0034-4885/72/7/076901
2. Abbott BP, Abbott R, Abbott TD, Abernathy MR, Acernese F, Ackley K, et al. Observation of Gravitational Waves from a Binary Black Hole Merger. *Phys Rev Lett* (2016) 116(6):061102. doi:10.1103/PhysRevLett.116.061102
3. Bloom BJ, Nicholson TL, Williams JR, Campbell SL, Bishof M, Zhang X, et al. An Optical Lattice Clock with Accuracy and Stability at the 10 $^{-18}$ Level. *Nature* (2014) 506(7486):71–5. doi:10.1038/nature12941
4. Ludlow AD, Boyd MM, Ye J. Optical Atomic Clocks. *Rev Mod Phys* (2015) 87(2):637–701. doi:10.1103/revmodphys.87.637
5. Hostetler CA, Behrenfeld MJ, Hu Y, Hair JW, Schulien JA. Spaceborne Lidar in the Study of marine Systems. *Annu Rev Mar Sci* (2018) 10(1):121–47. doi:10.1146/annurev-marine-121916-063335
6. Yang F, Ye Q, Pan Z, Chen D, Cai H, Qu R, et al. 100-mW Linear Polarization Single-Frequency All-Fiber Seed Laser for Coherent Doppler Lidar Application. *Opt Commun* (2012) 285(2):149–52. doi:10.1016/j.optcom.2011.09.030
7. Guan H, Novack A, Galfsky T, Ma Y, Fathololoumi S, Horth A, et al. Widely Tunable, Narrow-Linewidth III-V/silicon Hybrid External-Cavity Laser for Coherent Communication. *Opt Express* (2018) 26(7):7920–33. doi:10.1364/oe.26.007920
8. Zhou K, Zhao Q, Huang X, Yang C, Li C, Zhou E, et al. kHz-Order Linewidth Controllable 1550-nm Single-Frequency Fiber Laser for Coherent Optical Communication. *Opt Express* (2017) 25(17):19752–9. doi:10.1364/oe.25.019752
9. Zhu T, He Q, Xiao X, Bao X. Modulated Pulses Based Distributed Vibration Sensing with High Frequency Response and Spatial Resolution. *Opt Express* (2013) 21(3):2953–63. doi:10.1364/oe.21.002953
10. Juarez JC, Taylor HF. Field Test of a Distributed Fiber-Optic Intrusion Sensor System for Long Perimeters. *Appl Opt* (2007) 46(11):1968–71. doi:10.1364/ao.46.001968
11. Schawlow AL, Townes CH. Infrared and Optical Masers. *Phys Rev* (1958) 112(6):1940–9. doi:10.1103/physrev.112.1940
12. Renk KF. *Basics of Laser Physics*. Dordrecht London New York: Springer Heidelberg (2012).
13. Siegman AE. *Lasers*. Sausalito,CA,United States: University Science Books (1986).
14. Scully MO, Lamb WE, Jr. Quantum Theory of an Optical Maser. 1. General Theory. *Phys Rev* (1967) 159(2):208–26. doi:10.1103/physrev.159.208
15. Li C, Wang T, Zhang H, Xie J, Liu L, Guo J. Effect of Laser Linewidth on the Performance of Heterodyne Detection. *Acta Physica Sinica* (2016) 65(8): 084206. doi:10.7498/aps.65.084206
16. Shi L, Zhu T, He Q, Huang S. Effect of Laser Linewidth on Phase-OTDR Based Distributed Vibration Sensing Regime. *Proc SPIE* (2014) 9157:91576H. doi:10.1117/12.2059448
17. Savory S, Hadjifotiou A. Laser Linewidth Requirements for Optical DQPSK Systems. *IEEE Photon Technology Lett* (2004) 16(3):930–2. doi:10.1109/lpt.2004.823720
18. Honjo T, Inoue T, Inoue K. Influence of Light Source Linewidth in Differential-Phase-Shift Quantum Key Distribution Systems. *Opt Commun* (2011) 284(24):5856–9. doi:10.1016/j.optcom.2011.08.056
19. Bai Z, Williams RJ, Kitzler O, et al. Diamond Brillouin Laser in the Visible. *APL Photon* (2020) 5(3):031301. doi:10.1063/1.5134907
20. O'Reilly JJ, Lane PM, Heidemann R, Hofstetter R. Optical Generation of Very Narrow Linewidth Millimetre Wave Signals. *Electronics Lett* (1992) 28(25): 2309–11. doi:10.1049/el:19921486
21. Al-Taiy H, Wenzel N, Preußler S, Klinger J, Schneider T. Ultra-narrow Linewidth, Stable and Tunable Laser Source for Optical Communication Systems and Spectroscopy. *Opt Lett* (2014) 39(20):5826–9. doi:10.1364/ol.39.005826
22. Hirata S, Akatsuka T, Ohtake Y, Morinaga A. Sub-hertz-linewidth Diode Laser Stabilized to an Ultralow-Drift High-Finesse Optical Cavity. *Appl Phys Express* (2014) 7(2):022705. doi:10.7567/apex.7.022705
23. Drever RWP, Hall JL, Kowalski FV, Hough J, Ford GM, Munley AJ, et al. Laser Phase and Frequency Stabilization Using an Optical Resonator. *Appl Phys B Photophysics Laser Chem* (1983) 31(2):97–105. doi:10.1007/bf00702605
24. Argence B, Chanteau B, Lopez O, Nicolodi D, Abgrall M, Christian C, et al. Quantum cascade Laser Frequency Stabilization at the Sub-hz Level. *Nat Photon* (2015) 9(7):456–60. doi:10.1038/nphoton.2015.93
25. Shaykin AA, Burdonov KF, Khazanov EA. A Novel Technique for Longitudinal Mode Selection in Q-Switched Lasers. *Laser Phys Lett* (2015) 12(12):125001. doi:10.1088/1612-2011/12/12/125001
26. Fang Z, Cai H, Chen G, QU R. Fundamentals of Semiconductor Lasers. *Single Frequency Semiconductor Lasers* (2017) 9(39). doi:10.1007/978-981-10-5257-6_2
27. The Fact Factor. *Global Threat Report* (2021). Available at: https://thefactfactor.com/facts/pure_science/physics/formation-of-beats/6682/ (Accessed August 26, 2021).
28. Young BC, Cruz FC, Itano WM. Visible Lasers with Subhertz Linewidths. *Phys Rev Lett* (1999) 82(19):3799–802. doi:10.1103/physrevlett.82.3799
29. Kessler T, Hagemann C, Grebing C, Legero T, Sterr U, Riehle F, et al. A Sub-40-mHz-linewidth Laser Based on a Silicon Single-crystal Optical Cavity. *Nat Photon* (2012) 6(10):687–92. doi:10.1038/nphoton.2012.217
30. Lee H, Suh MG, Chen T, Li J, Diddams SA, Vahala KJ. Spiral Resonators for On-Chip Laser Frequency Stabilization. *Nat Commun* (2013) 4(1):2468. doi:10.1038/ncomms3468
31. Liang W, Ilchenko VS, Eliyahu D, Savchenkov AA, Matsko AB, Seidel D, Maleki L. Ultralow Noise Miniature External Cavity Semiconductor Laser. *Nat Commun* (2015) 6(1):7371. doi:10.1038/ncomms8371
32. Pavlov NG, Koptyaev S, Lihachev GV, Voloshin AS, Gorodnitskiy AS, Ryabko MV, et al. Narrow-linewidth Lasing and Soliton Kerr Microcombs with Ordinary Laser Diodes. *Nat Photon* (2018) 12(11):694–8. doi:10.1038/s41566-018-0277-2
33. Chen M, Meng Z, Wang J, Chen W. Ultra-narrow Linewidth Measurement Based on Voigt Profile Fitting. *Opt Express* (2015) 23(5):6803–8. doi:10.1364/oe.23.006803
34. Yu J, Park Y, Oh K, Kwon I. Brillouin Frequency Shifts in Silica Optical Fiber with the Double Cladding Structure. *Opt Express* (2002) 10(19):996–1002. doi:10.1364/oe.10.000996
35. Kueng A, Thevenaz L, Robert PA. Laser Linewidth Determination in the Sub-megahertz Range Using a Brillouin Fibre Laser. *Proc Eur Conf Opt Commun* (1996) 2:305–8. https://ieeexplore.ieee.org/abstract/document/715751
36. Smith SP, Zarinetchi F, Ezekiel S. Narrow-linewidth Stimulated Brillouin Fiber Laser and Applications. *Opt Lett* (1991) 16(6):393–5. doi:10.1364/ol.16.000393
37. Boschung J, Robert PA, Thévenaz L. High-accuracy Measurement of the Linewidth of a Brillouin Fibre Ring Laser. *Electronics Lett* (1994) 30(18): 1488–9. doi:10.1049/el:19941053
38. Dong Y, Lu Z, Lu Y, He W. A New Method of Measuring Ultra-narrow Laser Line-Width. *J Harbin Inst Technology* (2005) 37(5):670–3. https://en.cnki.com.cn/Article_en/CJFDTotal-HEBX200505028.htm

39. Mach L. Ueber einen interferenzrefraktor. *Z für Instrumentenkunde.* (1982) 12(3):89–93. https://de.wikipedia.org/wiki/Mach-Zehnder-Interferometer
40. Hocker GB. Fiber-optic Sensing of Pressure and Temperature. *Appl Opt* (1979) 18(9):1445–8. doi:10.1364/ao.18.001445
41. Conforti E, Rodigheri M, Sutili T, Galdieri Flavio J. Acoustical and 1/f Noises in Narrow Linewidth Lasers. *Opt Commun* (2020) 476:126286. doi:10.1016/j.optcom.2020.126286
42. Ryu S, Yamamoto S. Measurement of Direct Frequency Modulation Characteristics of DFB-LD by Delayed Self-Homodyne Technique. *Electronics Lett* (1986) 22(20):1052–4. doi:10.1049/el:19860721
43. Nazarathy M, Sorin WV, Baney DM, Newton SA. Spectral Analysis of Optical Mixing Measurements. *J Lightwave Technology* (1989) 7(7):1083–96. doi:10.1109/50.29635
44. Ludvigsen H, Tossavainen M, Kaivola M. Laser Linewidth Measurements Using Self-Homodyne Detection with Short Delay. *Opt Commun* (1998) 155(1–3):180–6. doi:10.1016/s0030-4018(98)00355-1
45. Gundavarapu S, Brodnik GM, Puckett M, Huffman T, Bose D, Behunin R, et al. Sub-hertz Fundamental Linewidth Photonic Integrated Brillouin Laser. *Nat Photon* (2019) 13(1):60–7. doi:10.1038/s41566-018-0313-2
46. Chauhan N, Isichenko A, Liu K, Wang J, Zhao Q, Behunin RO, et al. Visible Light Photonic Integrated Brillouin Laser. *Nat Commun* (2021) 12(1):4685. doi:10.1038/s41467-021-24926-8
47. Peng Y. A Novel Scheme for Hundred-Hertz Linewidth Measurements with the Self-Heterodyne Method. *Chin Phys Lett* (2013) 30(8):084208. doi:10.1088/0256-307x/30/8/084208
48. Mercer LB. 1/f Frequency Noise Effects on Self-Heterodyne Linewidth Measurements. *J Lightwave Technology* (1991) 9(4):485–93. doi:10.1109/50.76663
49. Okoshi T, Kikuchi K, Nakayama A. Novel Method for High Resolution Measurement of Laser Output Spectrum. *Electronics Lett* (1980) 16(16):630–1. doi:10.1049/el:19800437
50. Richter L, Mandelberg H, Kruger M, McGrath P. Linewidth Determination from Self-Heterodyne Measurements with Subcoherence Delay Times. *IEEE J Quan Electronics* (1986) 22(11):2070–4. doi:10.1109/jqe.1986.1072909
51. Saito S, Yamamoto Y. Direct Observation of Lorentzian Lineshape of Semiconductor Laser and Linewidth Reduction with External Grating Feedback. *Electronics Lett* (1981) 17(9):325. doi:10.1049/el:19810229
52. Abrarov SM, Quine BM, Jagpal RK. A Simple Interpolating Algorithm for the Rapid and Accurate Calculation of the Voigt Function. *J Quantitative Spectrosc Radiative Transfer* (2009) 110(6–7):376–83. doi:10.1016/j.jqsrt.2009.01.003
53. Bruce SD, Higinbotham J, Marshall I, Beswick PH. An Analytical Derivation of a Popular Approximation of the Voigt Function for Quantification of NMR Spectra. *J Magn Reson* (2000) 142(1):57–63. doi:10.1006/jmre.1999.1911
54. Huang S, Zhu T, Cao Z, Liu M, Deng M, Liu J, et al. Laser Linewidth Measurement Based on Amplitude Difference Comparison of Coherent Envelope. *IEEE Photon Technology Lett* (2016) 28(7):759–62. doi:10.1109/lpt.2015.2513098
55. Jia Y, Ou P, Yang Y, Chunxi Z. Short Fibre Delayed Self-Heterodyne Interferometer for Ultranarrow Laser Linewidth Measurement. *J Beijing Univ Aeronautics Astronautics* (2008) 34(05):568. https://en.cnki.com.cn/Article_en/CJFDTotal-BJHK200805021.htm
56. Wei ZP. Measurement of the Narrow Linewidth Laser Spectrum Based on the Delayed Self-Heterodyne. *Opt Optoelectronic Technology* (2015) 13(3):38–40. http://www.cqvip.com/qk/87090x/201503/71887168504849534851484857.html
57. Huang S, Zhu T, Liu M, Huang W. Precise Measurement of Ultra-narrow Laser Linewidths Using the strong Coherent Envelope. *Scientific Rep* (2017) 7(1):41988. doi:10.1038/srep41988
58. Bai Q, Yan M, Xue B, Gao Y, Wang D, Wang Y, et al. The Influence of Laser Linewidth on the Brillouin Shift Frequency Accuracy of BOTDR. *Appl Sci* (2018) 9(1):58. doi:10.3390/app9010058
59. He Y, Hu S, Liang S, Yiyue L. High-precision Narrow Laser Linewidth Measurement Based on Coherent Envelope Demodulation. *Opt Fiber Technology* (2019) 50:200–5. doi:10.1016/j.yofte.2019.03.024
60. Wang Z, Ke C, Zhong Y, Xing C, Wang H, Yang K, et al. Ultra-narrow-linewidth Measurement Utilizing Dual-Parameter Acquisition through a Partially Coherent Light Interference. *Opt Express* (2020) 28(6):8484–93. doi:10.1364/oe.387398
61. Xue M, Zhao J. Laser Linewidth Measurement Based on Long and Short Delay Fiber Combination. *Opt Express* (2021) 29(17):27118–26. doi:10.1364/oe.428787
62. Gao J, Jiao D, Deng X, Liu J, Zhang L, Zang Q, et al. A Polarization-Insensitive Recirculating Delayed Self-Heterodyne Method for Sub-kilohertz Laser Linewidth Measurement. *Photonics* (2021) 8(5):137. doi:10.3390/photonics8050137
63. Dawson JW, Park N, Vahala KJ. An Improved Delayed Self-Heterodyne Interferometer for Linewidth Measurements. *IEEE Photon Technology Lett* (1992) 4(9):1063–6. doi:10.1109/68.157150
64. Han M, Wang A. Analysis of a Loss-Compensated Recirculating Delayed Self-Heterodyne Interferometer for Laser Linewidth Measurement. *Appl Phys B* (2005) 81(1):53–8. doi:10.1007/s00340-005-1871-9
65. Chen X, Han M, Zhu Y, Dong B, Wang A. Implementation of a Loss-Compensated Recirculating Delayed Self-Heterodyne Interferometer for Ultranarrow Laser Linewidth Measurement. *Appl Opt* (2006) 45(29):7712–7. doi:10.1364/ao.45.007712
66. Tsuchida H. Simple Technique for Improving the Resolution of the Delayed Self-Heterodyne Method. *Opt Lett* (1990) 15(11):640. doi:10.1364/ol.15.000640
67. Di Domenico GD, Schilt S, Thomann P. Simple Approach to the Relation between Laser Frequency Noise and Laser Line Shape. *Appl Opt* (2010) 49(25):4801–7. doi:10.1364/ao.49.004801
68. Zhou Q, Qin J, Xie W, Liu Z, Tong Y, Dong Y, et al. Power-area Method to Precisely Estimate Laser Linewidth from its Frequency-Noise Spectrum. *Appl Opt* (2015) 54(28):8282–9. doi:10.1364/ao.54.008282
69. Xu D, Lu B, Yang F, Dijun C, Haiwen C, Qu R. Narrow Linewidth Single-Frequency Laser Noise Measurement Based on a 3×3 Fiber Coupler. *Chin J Lasers* (2016) 43(1):0102004. doi:10.3788/cjl201643.0102004
70. Tran MA, Huang D, Bowers JE. Tutorial on Narrow Linewidth Tunable Semiconductor Lasers Using Si/III-V Heterogeneous Integration. *APL Photon* (2019) 4(11):111101. doi:10.1063/1.5124254
71. Pollnau M, Eichhorn M. Spectral Coherence, Part I: Passive-Resonator Linewidth, Fundamental Laser Linewidth, and Schawlow-Townes Approximation. *Prog Quan Electronics* (2020) 72:100255. doi:10.1016/j.pquantelec.2020.100255
72. Pollnau M. Phase Aspect in Photon Emission and Absorption. *Optica* (2018) 5(4):465–74. doi:10.1364/optica.5.000465

Advantages of publishing in Frontiers

OPEN ACCESS
Articles are free to read for greatest visibility and readership

FAST PUBLICATION
Around 90 days from submission to decision

HIGH QUALITY PEER-REVIEW
Rigorous, collaborative, and constructive peer-review

TRANSPARENT PEER-REVIEW
Editors and reviewers acknowledged by name on published articles

Frontiers
Avenue du Tribunal-Fédéral 34
1005 Lausanne | Switzerland

Visit us: www.frontiersin.org
Contact us: frontiersin.org/about/contact

REPRODUCIBILITY OF RESEARCH
Support open data and methods to enhance research reproducibility

DIGITAL PUBLISHING
Articles designed for optimal readership across devices

FOLLOW US
@frontiersin

IMPACT METRICS
Advanced article metrics track visibility across digital media

EXTENSIVE PROMOTION
Marketing and promotion of impactful research

LOOP RESEARCH NETWORK
Our network increases your article's readership